Rochester Institute of Technology

RIT Digital Institutional Repository

10-2021

Advanced Photovoltaic Devices Enabled by Lattice-Mismatched Epitaxy

Anastasiia Fedorenko
af6673@rit.edu

Follow this and additional works at: https://repository.rit.edu/theses

ROCHESTER INSTITUTE OF TECHNOLOGY

A DISSERTATION SUBMITTED IN PARTIAL FULFILLMENT OF THE
REQUIREMENTS FOR THE DEGREE OF DOCTOR OF PHILOSOPHY
IN MICROSYSTEMS ENGINEERING

Advanced Photovoltaic Devices Enabled by Lattice-Mismatched Epitaxy

Author:

Anastasiia Fedorenko

Advisor:

Dr. Seth M. Hubbard

Microsystems Engineering

October 2021

ABSTRACT

Kate Gleason College of Engineering

Rochester Institute of Technology

Degree: Doctor of Philosophy   **Program:** Microsystems Engineering

Author's Name: Anastasiia Fedorenko

Advisor's Name: Dr. Seth M. Hubbard

Dissertation Title: Advanced Photovoltaic Devices Enabled by Lattice-Mismatched Epitaxy

Thin-film III-V semiconductor-based photovoltaic (PV) devices, whose light conversion efficiency is primarily limited by the minority carrier lifetimes, are commonly designed to minimize the formation of crystalline defects (threading dislocations or, in extreme cases, fractures) that can occur, in particular, due to a mismatch in lattice constants of the epitaxial substrate and of the active film. At the same time, heteroepitaxy using Si or metal foils instead of costly III-V substrates is a pathway to enabling low-cost thin-film III-V-based PV and associated devices, yet it requires to either use metamorphic buffers or lateral confinement either by substrate patterning or by growing high aspect ratio structures. Mismatched epitaxy can be used for high-efficiency durable III-V space PV systems by incorporation of properly engineered strained quantum confined structures into the solar cells that can enable bandgap engineering and enhanced radiation tolerance.

One of the major topics covered in this work is optical and optoelectronic modeling and physics of the triple-junction solar cell featuring planar Si middle sub-cell and $GaAs_{0.73}P_{0.27}$ and $InAs_{0.85}P_{0.15}$ periodic nanowire (NW) top and bottom sub-cells, respectively. In particular, the dimensions of the NW arrays that would enable near-unity broad-band absorption for maximum generated current were identified. For the top

cell, the planarized array dimensions corresponding to maximum generated current and current matching with the underlying Si sub-cell were found to be 350 nm for NW diameter and 450 – 500 nm for NW spacing. For the $GaAs_{0.73}P_{0.27}$, resonant coupling was the main factor driving the absorption, yet addressing the coupling of IR light in the transmission mode in the $InAs_{0.85}P_{0.15}$ nanoscale arrays was challenging and unique. Given the nature of the Si and bottom NW interface, the designs of high refractive index encapsulation materials and conformal reflectors were proposed to enable the use of thin NWs (300 – 400 nm) for sufficient IR absorption. A novel co-simulation tool combining RSoft DiffractMOD^{TM} and Sentaurus Device^{TM} was established and utilized to design the p-i-n 3D junction and thin conformal GaP passivation coating for maximum $GaAs_{0.73}P_{0.27}$ NW sub-cell efficiency (16.5%) mainly impacted by the carrier surface annihilation.

Development of a highly efficient GaAs solar cell enhanced with $In_xGa_{1-x}As/GaAs_yP_{1-y}$ quantum wells (QWs) is also demonstrated as one of the key parts of the dissertation. The optimizations including design of GaAsP strain balancing that would support efficient thermal (here, 17 nm-thick $GaAs_{0.90}P_{0.10}$ for 9.2 nm-thick $In_{0.10}Ga_{0.90}As$ QWs) and/or tunneling (4.9 nm-thick $GaAs_{0.68}P_{0.32}$) carrier escape out of the QW while maintaining a consistent morphology of the QW layers in extended QW superlattices were performed using the principles of strain energy minimization and by tuning the growth parameters. The fundamental open-circuit voltage (V_{oc}) restraints in radiative and non-radiative recombination-limited regimes in the QW solar cells were studied for a variety of $In_xGa_{1-x}As$ compositions (x=6%, 8%, 10%, and 14%) and number of QWs using spectroscopic and dark current analysis and modeling. Additionally, the design and use of distributed Bragg reflectors for targeted up to 90% QW absorption enhancement is demonstrated resulting in an absolute QW solar cell efficiency increase by 0.4% due to

nearly doubled current from the QWs and 0.1% enhancement relatively to the optically-

thick baseline device with no QWs.

iv

Advanced Photovoltaic Devices Enabled by Lattice-Mismatched Epitaxy
by
Anastasiia Fedorenko

Committee Approval:

We, the undersigned committee members, certify that we have advised and/or supervised the candidate on the work described in this dissertation. We further certify that we have reviewed the dissertation manuscript and approve it in partial fulfillment of the requirements of the degree of Doctor of Philosophy in Microsystems Engineering.

_____   Date
Dr. Seth M. Hubbard
Associate Professor, Physics and Microsystems Engineering

_____   Date
Dr. Parsian K. Mohseni
Assistant Professor, Microsystems of Engineering

_____   Date
Dr. James E. Moon
Professor, Electrical and Microelectronic Engineering

_____   Date
Dr. Jing Zhang
Associate Professor, Electrical and Microelectronic Engineering

_____   Date
Dr. Scott Williams
Professor, Chemistry and Materials Science

Certified by:

_____   Date
Dr. Stefan F. Preble
Director, Microsystems Engineering Program

Dedication

This work is a part of my life-long devotion to the world of the free and independent thinkers, strong people, who stand for the truth, discipline, personal evolution, strength of character, aesthetics, and dignity despite the seeming prevalence of the forces ignorantly demolishing the sophisticated beauty of the world and civilization of the creators who follow the universal principle of fine balance.

Acknowledgments

First, I would like to thank my advisor Dr. Seth M. Hubbard for being there for me when his immense expertise and knowledge were necessary and, at the same time, for giving me freedom to shape my Ph.D. process and to never feel like an employee and for encouraging me to express my thoughts and ideas openly. I have always appreciated Dr. Hubbard's strict, reasonable, and productive criticism and our good, fulfilling scientific debates - I will miss those the most! It was a great pleasure to be his student and it was the most intellectually enriching and liberating experience to work on the research projects with Dr. Hubbard and, on a personal level, through challenge and responsibility, it allowed me to acquire my voice and helped to solidify leadership skills.

I would like to thank my committee members who each made unique contributions into my professional development and helped me to successfully accomplish the Ph.D. I was lucky to work closely with Dr. Parsian K. Mohseni for almost two years on the Nanowire Solar Cell project, and his broad and thorough expertise in Materials Science and Nanotechnology were incredibly useful for directing my simulation work and giving me exposure to the nuances and manufacturing details that were sparking my curiosity and inspiration. I would like to thank Dr. James E. Moon whom I met in my first year as a Professor teaching Advanced Carrier Injection Devices. Such an elegant and rigorous way of delivering this complex subject along with regular exercises in mathematical art rooted my appreciation for the semiconductor devices physics and I am very happy to have had Dr. Moon as a part of my committee as an expert in this discipline and a professional to look up to. I would like to thank Dr. Jing Zhang for her curiosity and invigorating, lively feedback on my work. It was so much fun to discuss and debate the same fundamental concepts, but applied to, in principle, inverse phenomena when

applied to the devices with Dr. Zhang! I would like to thank Dr. Scott Williams for his outside-of-the-box feedback and contributions into my work and for thought-provoking questions that made me appreciate the bigger picture and the context of my research!

My senior and fellow colleagues who also grew into good friends were a tremendous gift throughout these four years. I would like to thank Dr. Yushuai Dai, Dr. George Nelson, Dr. Zac Bittner, Dr. Stephen Polly, Dr. Thomas Wilhelm, Dr. Elisabeth McClure, Dr. Mohadeseh Baboli, Dr. Dylan McIntyre, Julia D'Rozario, Emily Kessler-Lewis, Salwan Omar, and Mitsul Kacharia. Each of you were influential in your own special way and much more than just research partners with your strong, admirable characters and personal histories! I learned a lot from each of you.

I would like to express gratitude to the students Yoshiaki Shiba and Brandon Bogner who I was lucky to work with as a mentor and who were able to reciprocate my teaching style and achieve amazing results by quickly gaining independence, professionalism, and confidence to shape and design the research and by not settling for simply operational roles. Thank you for giving me feelings of pride and fulfillment from watching you grow and uncover your talents!

Contents

List of Figures

Chapter 1

Introduction

Single-junction crystalline silicon (Si) solar cells are approaching their Auger theoretical efficiency limit of 29% [1] reaching up to 26.3% efficiency under AM1.5 illumination [2]. On the solar cell level, the further improvements in the area-specific power output
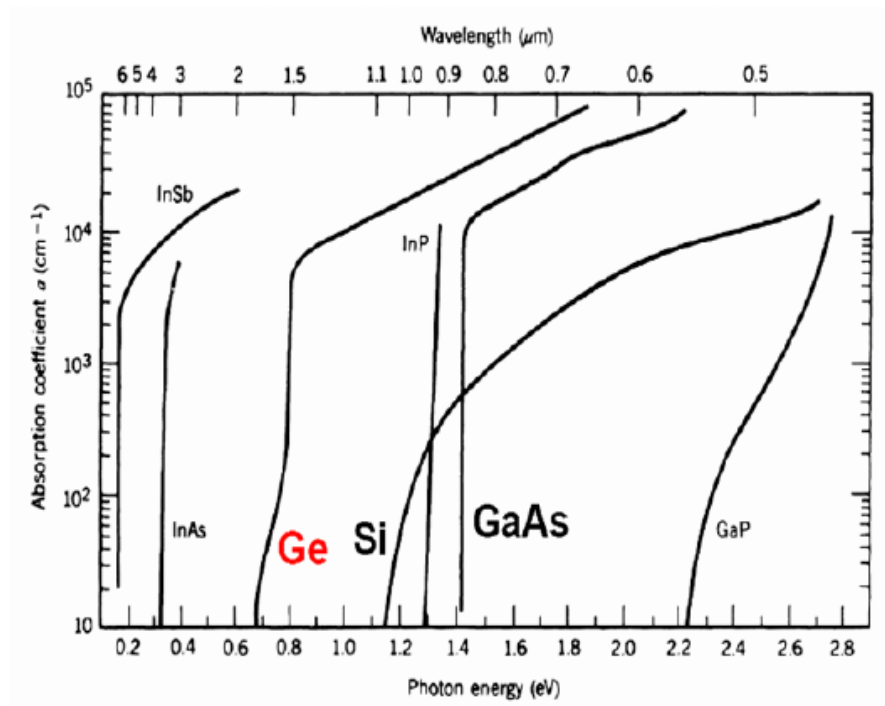
FIGURE 1.1: Absorption coefficient (α) chart.
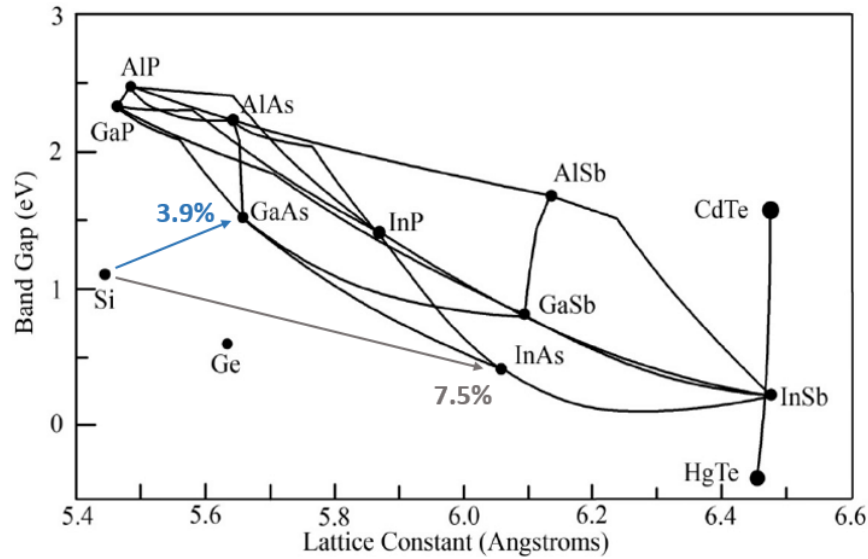
FIGURE 1.2: Bandgap/lattice constant diagram of III-V compounds. Si and Ge are denoted. Colorful lines guide to the lattice constant values of Si, GaAs, and InP. The numbers indicate the %-mismatch of GaAs and InP with Si, respectively.

from terrestrial Si modules can be enabled by transitioning to the multijunction Si-based photovoltaics (PV) as this approach allows to use the incident solar energy more efficiently by minimizing the main fundamental losses: thermalization and transmission of the photons. Even though Si bandgap of 1.12 eV is nearly ideal for the single-junction (1J) solar cells [3], placing additional wide- and narrow-bandgap solar cells on the front and rear sides of the Si absorber, respectively, can boost the overall efficiency of the device. In this case, power of the incident short-wavelength photons will be converted into electrical work in the wide-bandgap subcells(s) instead of being lost as heat in Si. At the same time, narrow-bandgap subcell placed below Si solar cell will be responsible for the conversion of the infrared photons, that are otherwise not used. In this regard, the possibility of enabling Si-based multijunction solar cells has been extensively studied due to the low cost of electronic grade Si and well-established manufacturing of the Si PV devices.

The main barrier preventing successful realization of Si-based multijunction systems is the limited choice of materials that would meet the requirements for environmental
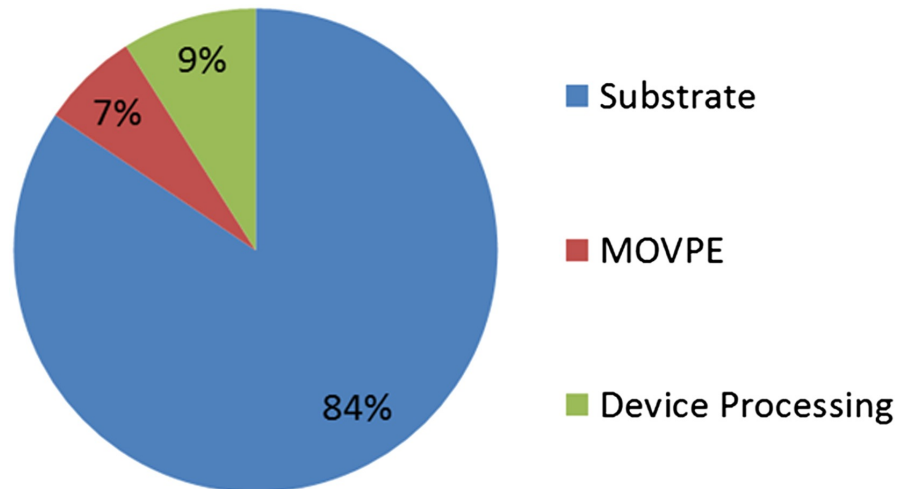
FIGURE 1.3: Cost breakdown of the single-junction GaAs solar cell manufacturing process. [4]

stability and the feasibility of integration with Si. One of the options for integrating Si into the multijunction architectures is deposition of the perovskite compounds that are capable of absorbing light in the UV and visible range dependent on their composition [5]. Metal halide perovskites (hybrid organic-inorganic lead or tin-based materials), on the one hand, offer low cost, wide bandgap tunability, scalable printing-based deposition, and high absorption coefficient [6, 7, 8]. At the same time, environmental stability of perovskite films limits their commercialization and hardening of these compounds against heat and illumination is still a matter of research [9, 10].

The other material group that can serve as a candidate for Si-based multijunction cells is III-V alloys. The use of III-V alloys for partitioning the solar spectrum leading to enhanced efficiency of Si-based solar cells has been an alternative to perovskites. As can be seen on Fig. 1.2, a family of III-V alloys provides broad-range bandgap tunability (from $\sim$0.1 eV of antimony-based alloys to 2.48 eV of AlP) and selection of materials with strong direct-bandgap absorption allowing to use ultra-thin films of III-V materials as shown on Fig. 1.1 (for example, a simple optically-thick GaAs solar cell is only $\sim$ 3.5 μm [11]). In addition, multijunction III-V solar cells grown by metal organic vapor

phase epitaxy (MOVPE) on Ge or GaAs substrates hold the record of efficiency and are leaders in the space PV industry due to their light weight in combination with high efficiency and radiation hardness [12, 13, 14]. As of 2021, the record efficieny of the dual junction InGaP/GaAs tandem solar cell is 32.9% measured under ASTM AM1.5 G terrestrial spectrum [15] and commercially available space solar cells feature beginning-of-life efficiencies ranging from 30 % to 33% under AM0 illumination with the end-of-life (after exposure to the 1 MeV electrons with fluence of 5×10^{15} e/cm2) and post-annealing remaining efficiency factor up to 78% (https://solaerotech.com/space-solar-cells-cics/).

The main limitation for using such devices terrestrially is their high cost that is mainly driven by the cost of III-V substrates (Fig. 1.3). While retail price of the 2-inch Si wafer is less than $ 10, the cost of the 2-inch GaAs substrate is $\sim$ $100 - 150 (https://order.universitywafer.com/default.aspx?cat=Gallium%20Arsenide). It seems to be an ideal solution to combine the benefits of III-V PV with low-cost Si for creating hybrid multijunction devices, however, there is a significant lattice mismatch between Si and majority of the III-V compounds. Figure 1.2 shows the bandgap/lattice constant diagram denoting binary III-V alloys, Si, and Ge. The lines stretched down to the lattice constant axis correspond to GaAs and InP (two most used III-V epitaxial substrate materials). It can be seen that percent lattice mismatch of GaAs with Si is 3.9%, while for InP it reaches 8%. Considering that lattice mismatch >1% results in epitaxial film relaxation and associated formation of threading dislocations propagating through the body of the epitaxial film (which is also an active part of the future device), GaAs films cannot be directly grown on Si without incorporation of the threading dislocations, which in turn have detrimental impact on the minority carrier lifetimes [16, 17].

For decades, the scientific focus was on pursuing the solutions that could allow to overcome the severe lattice mismatch between Si and most III-V materials offering use of
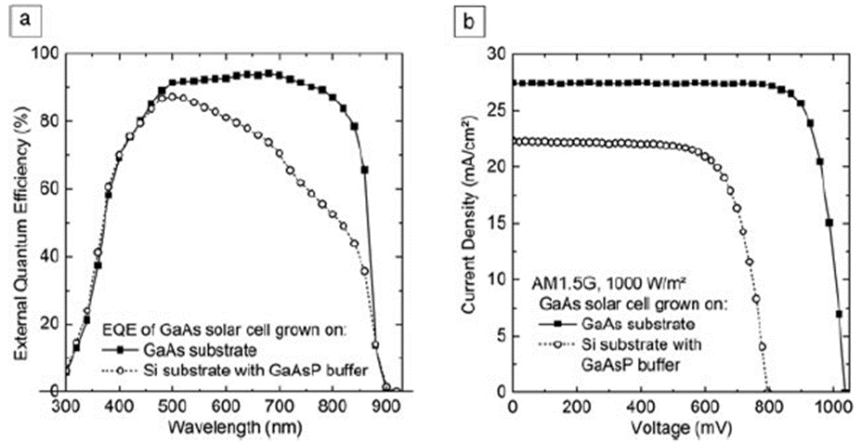
FIGURE 1.4: (a) EQE spectra and (b) illuminated J-V characteristics of the 1J GaAs solar cell grown on the GaAs substrate (dark points) and on Si via $GaAs_xP_{(1-x)}$ metamorphic buffer (open circles) [18].

metamorphic grade buffers for monolithic growth of III-V on Si [18]. This can be achieved either by growing GaP on Si first and grading the alloy composition from GaP (mismatch with Si is 0.36%, Fig. 1.2) to the $GaAs_xP_{(1-x)}$ with stoichiometry corresponding to the active device region bandgap value (Fig. 1.5)[19, 20]. Alternatively, since GaAs can be lattice matched to Ge by adding only 1% In, growth of GaAs on Si can be enabled by grading the lattice parameter from Si to Ge via SiGe alloy [21]. In the second case, however, Si cannot be used as a part of the solar cell, since thick, narrow-bandgap SiGe buffer is highly absorbing. Figure 1.4 shows external quantum efficiency (EQE) spectra, that indicate the number of electron-hole pairs per incident photon with given wavelength, and current-voltage (J-V) characteristics of the GaAs solar cells grown on GaAs substrate and on Si substrate with graded $GaAs_xP_{(1-x)}$ metamorphic buffer. Even qualitative analysis of the EQE of both types of cells (Fig. 1.4a) indicates that long-wavelength carrier collection efficiency drops in the solar cell grown metamorphically corresponding to the degraded diffusion length of minority carriers in the base of the device compared to the solar cell grown by homoepitaxy (epitaxial GaAs on GaAs substrate). The same trend is observed in the J-V curves (Fig. 1.4b) exhibiting drop in

both short-circuit current density (J_{sc}) and open-circuit voltage (V_{oc}). The reason for the inferior performance of the metamorphic cells is propagating threading dislocations resulting from lattice mismatch with the substrate. Figure 1.5 shows transmission electron microscopy of cross-sectional view of the $GaAs_yP_{1-y}$ metamorphic buffer grown on Si via step-grading (lattice constant in the buffer changes in a discrete fashion by the growth of layers with constant composition). Horizontal lines correspond to the interfaces between the 250 nm-thick layers with constant lattice parameter. In this structure, one can notice the defect lines propagating at an angle to the growth direction (threading dislocations) that do not contribute to the lattice relaxation (misfit dislocations that relieve the strain propagate along the film plane). Present in the active part of the device, threading dislocations reduce the minority carrier diffusion lengths by introducing trap states and scattering cites. For comparison, GaAs epitaxial substrates' threading dislocation density (TDD) is in the order of 10^3 $1/cm^2$, while in the metamorphic material TDD can reach $10^6 - 10^8$ $1/cm^2$. This change results in minority electron lifetimes, τ_e, drop up to three orders of magnitude and minority holes lifetimes, τ_h, drop up to two orders of magnitude as shown on Fig. 1.6 [16].

An alternative that allows to integrate high crystalline quality III-V films with Si is wafer bonding [22, 23]. This method is essentially a combination of lattice-matched growth of III-V device structures on expensive GaAs substrates (in an inverted configuration) followed by surface-activated wafer bonding to Si and further GaAs substrate removal by wet chemical etching [24]. Figure 1.7 shows the comparison between the EQE spectra of the dual-junction (2J) InGaP/GaAs solar cells grown inverted on GaAs substrates and wafer-bonded to Si and grown on Si via $GaAs_yP_{1-y}$ metamorphic grade [25]. While in terms of device performace, wafer bonding is much more viable than direct growth
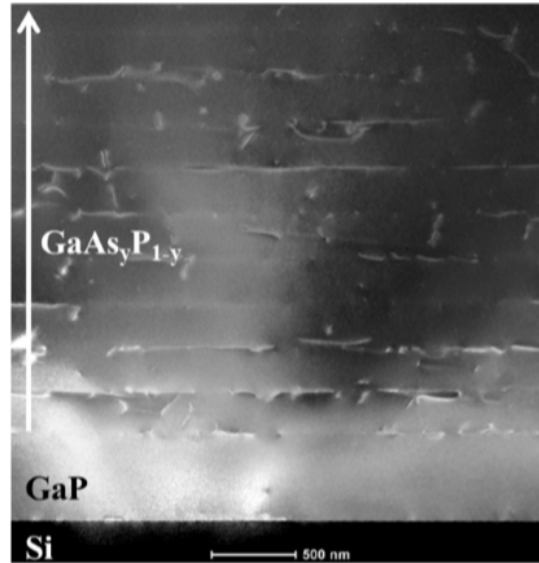
FIGURE 1.5: Transmission electron microscopy cross sectional image of the $GaAs_yP_{1-y}$ metamorphic buffer on Si. [20]
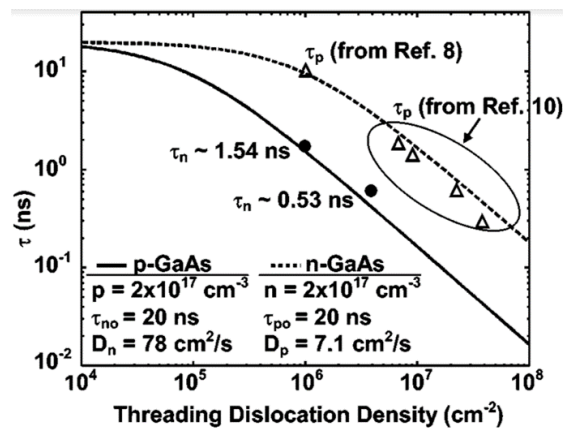
FIGURE 1.6: Electron and hole lifetimes in the p- and n-type GaAs, respectively, in dependency on the TDD. [16]

on Si, as it allows to retain high crystalline quality, it does not fulfill the cost requirement because it relies on the GaAs substrate use. Another important limitation of the wafer bonding method is low manufacturing scalability making it non-viable for bulk production [23].

As thin-film III-V-on-Si integration in perspective might be disregarded due to either inevitable loss of the III-V material quality or low cost efficiency of stacked systems, the parallel approach exploiting direct growth of 3-dimensional III-V structures, such as
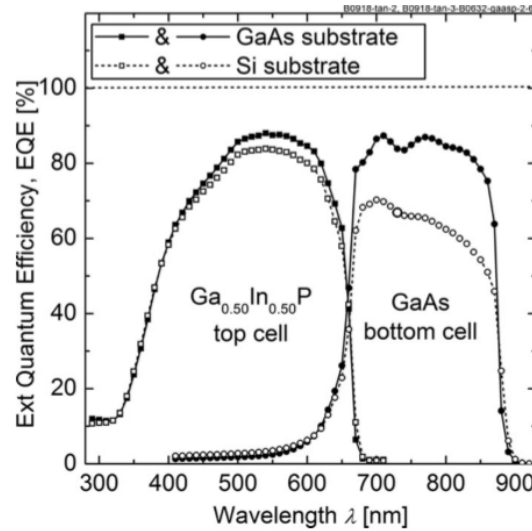
FIGURE 1.7: EQE spectra of the 2J InGaP/GaAs solar cells grown inverted on GaAs substrates and wafer-bonded to Si (dark circles) and grown on Si via $GaAs_yP_{1-y}$ metamorphic grade (open circles) [25].

nanowires (NWs), on Si can be considered. An efficient approach to mitigate the lattice mismatch-induced threading dislocations formation in the III-V hetero-epitaxial films is to laterally confine the epitaxial crystal and allow relaxation via its facets [26]. Radial spatial confinement of nanowires (NWs) allows for efficient strain relaxation that enables direct epitaxy of a broad range of lattice-mismatched materials on Si, thereby allowing unprecedented bandgap tunability and heterogeneous integration [27, 28, 29]. Figure 1.8 shows cross-sectional high resolution TEM (HRTEM) image of the GaAs NW grown on Si. A pristine atomic arrangement with no stacking faults and bulk crystalline defects in the body of a NW.

To show the potential of heterogeneous integration of III-V NWs on Si, the first chapter of this work focuses on simulation-based study of the III-V-Nanowire-on-Si triple-junction solar cells and offers design guidelines for overcoming the effects of high surface-to-volume ratio in the NW subcells, as well as demonstrates optical enhancement systems for elevated absorption in NWs.

Associated with the methodology of growing III-V NWs on Si, a selective light sensing
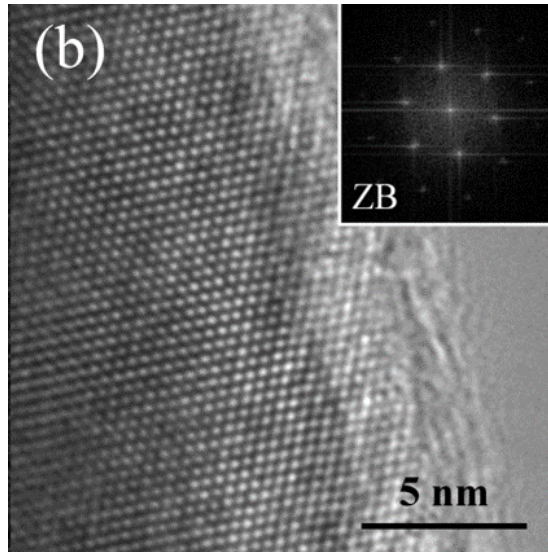
FIGURE 1.8: Cross-sectional HRTEM image of the GaAs NW grown on Si substrate.

system was proposed. Despite the capabilities for spectral tunability of the absorption in the NW arrays due to their waveguide properties allowing to couple light with specific wavelengths dependent on the NW width, for the infrared applications implementation of the NWs with diameters that would be sufficient for long-wavelength light coupling on heterosubstrates (Si) might be associated with an occurence of crystalline defects. The mechanism for selective IR sensing by NWs relies on filtering the short-wavelength light. In the previous works, the NW diameter-dependent spectral responsivity in InP NWs was demonstrated for the NWs grown on InP substrates for which lattice mismatch is not a concern, while the cost of such substrates is high. Integrating NW and Si can be efficient (i.e., provide desired optical and structural properties of the NW material with minimal bulk defect density in the NWs) if NWs are sufficiently thin, with the NW diameter not exceeding critical width. In this case, the wavelength selectivity can be in part achieved by designing Si substrates in a form of one-sided or two-sided diffraction gratings with anti-reflective coating on the light-incidence side for the following growth of NWs on the textured rear side. In this case, NW arrays become optically passive as the light with specific wavelengths is forced into the array. The simplicity of such approach

is that for IR operation, the feature size of the grating laterally is in the micrometer range making standard UV lithography applicable for fabricating such devices, while the depth of the grating can vary by tuning the etching duration. The proposed work includes modeling part demonstrating the wavelength selectivity in the InAsP NWs on the rear side of Si diffraction grating with various grating feature sizes. The experimental implementation of such structure and analysis of the absorption in dependency on the Si grating properties is in progress.

While the approaches to adapt III-V PV to the terrestrial use still mostly remain in the research scope (except for the concentration III-V PV that until recently was present in the market [30]), the full potential of the III-V materials for photovoltaic applications can be fully realized in the space industry. Not largely restricted by cost-per-watt requirements, the demand for radiation-tolerance and low specific power determined as a mass specific power output of solar cells for space applications becomes critical [31].

Multijunction III-V solar cells are leaders on the space PV market due to their high efficiency [32]. The newest 4-junction III-V solar cell grown on Ge developed by So-lAero features 30.0% minimum efficiency in the beginning of life and previous 3-junction model achieves 29.5% minimum efficiency. The challenge is to retain stable performance of the multijunction cells under electron and proton radiation in space. The end-of-life (conventionally, end of life corresponds to the exposure to 1 MeV 1×10^{15} electrons/cm^2 radiation) efficiency of the solar cell relies on maintaining current matching between the subcells that are prone to the influence of non-ionizing radiation. The necessity to main-tain current matching comes from the subcells being connected in series and dramatic reduction in current generated by one of the cells overtime can result in premature wear-off of the space module. In a 3-junction InGaP/GaAs/Ge or InGaP/GaAs/InGaAs solar cell (Fig. 1.9), GaAs middle cell is the most vulnerable to the radiation [33]. Exposure
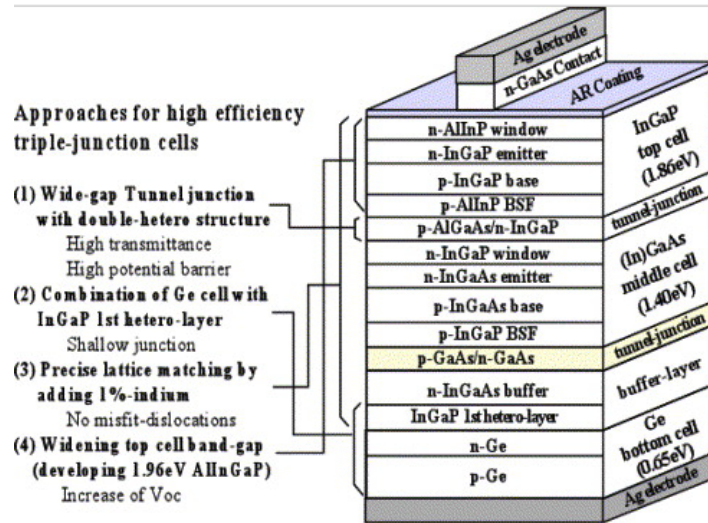
FIGURE 1.9: Schematics of the 3J solar cell for space applications [34].

of the solar cell to the incident flux of charged particles leads to the formation of lattice defects affecting the mean-free path of the minority charge carriers and reducing their diffusion length.

Thinning the subcells can be beneficial for their radiation tolerance as, first, the degree of damage from particles bombardment gets reduced, and second, the dependency of the carrier collection efficiency on the large diffusion length becomes smaller with the junction being closer to the carrier generation region. Engineering of the ultra-thin space solar cell relies on photon management and epitaxial lift-off or substrate removal and has been implemented [35, 36, 37, 38].

With short-circuit current density (J_{sc}) linearly dropping with the diffusion length [3], the thick sub-cells radiation tolerance in terms of maintaining current matching can be also achieved by introducing of low-dimension structures, such as quantum dots (QDs) and quantum wells (QWs) that have shown great potential for bandgap engineering in solar cells [40, 41, 42, 43, 44]. The main idea of using quantum-confined structures is to enhance current density of the limiting GaAs subcell by providing extra absorption
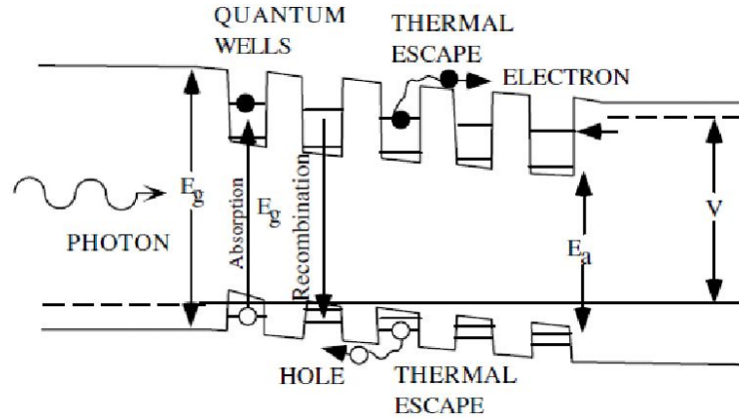
FIGURE 1.10: Band diagram of the solar cell with the QW superlattice in the intrinsic region. Dark circles represent electrons and open circles correspond to holes. The arrows show absorption and radiative recombination events, as well as carrier escape mechanisms. [39]

below its bandgap to maintain current matching towards the end of life. QDs and QWs are realized in a form of superlattices of strained quantum-confined structures and separating barriers to form quantum boxes (Fig. 1.11a) incorporated into the high electric field region (intrinsic region) of the solar cell that is prone to the radiation damage (Fig. 1.11b) [45, 46]. The band diagram showing QW superlattice in the i-region in given on Fig. 1.10. QDs, due to their dimensionality and discrete morphology, might offer higher radiation resistance due to reduced capture cross-section, however, QWs inherently have overall higher number of available transition states resulting in higher sub-bandgap photon absorption in the solar cell and can be preferred over the QDs for space applications [47, 48, 49].

With the outlook to the future applications for the tandem devices, in this work, implementation of high-efficiency GaAs solar cells with QW superlattices, where strained $In_{0.08}Ga_{0.92}As$ QWs separated by the GaAs barriers, is considered and preliminary results proving an increase in the beginning-of-life efficiency of the single-junction (1J) GaAs QW solar cell compared to the baseline device are shown. The proposed advancements that would further enhance the QW solar cell efficiency will include increased
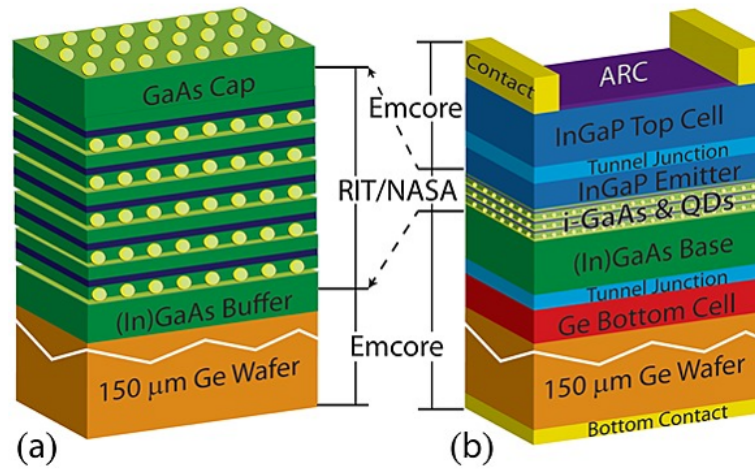
FIGURE 1.11: (a) QD superlattice; (b) Layer structure of the 3J solar cell with QDs in the middle GaAs junction [45].

number of QWs associated with the necessity of strain balancing development, as well as adding distributed Bragg reflectors on the rear side of the cell for increased absorption in the QW region.

Chapter 2

Novel III-V-Nanowire-on-Silicon Devices: from Physical Modeling to Prototype

2.1 Summary

Design guidelines for creating triple-junction (3J) bifacial Si-based solar cell with top GaAs$_{0.73}$P$_{0.27}$ NW subcell and bottom InAs$_{0.85}$P$_{0.15}$ subcell were established by rigorous coupled wave analysis (RCWA) simulations in RSoft (Synopsys). The electrical modeling using the co-simulations in Sentaurus and RSoft were carried out for the top wide-bandgap cell, however, the development of the complete 3J device model is in progress.

The concept of the narrow-band wavelength-selective NW-based IR light detector was demonstrated using optical RSoft modeling. The idea of using Si diffraction grating for wavelength selectivity as a substrate for the growth of absorbing narrow-bandgap

NWs (InAsP or, alternatively, InGaAs) was exploited. The preliminary optical RCWA simulation results suggesting the viability of the concept are shown as well as possible device fabrication route.

Proposed novel and viable structures based on the use of III-V NWs grown on Si substrates for solar and sensing applications were proposed. A multidimensional model of the peel-off NW stackable solar cell system alternative to the NW-on-Substrate device was performed.

2.2 III-V-Nanowire-on-Silicon Devices

2.2.1 Motivation and Background

The rod-like shape of the NWs alters photonic properties of semiconductor materials compared to the bulk (planar) counterparts making III-V NWs versatile building blocks for optoelectronic device applications. The mechanisms determining the interaction of NWs with different wavelength light are near-field evanescent wave coupling, transverse mode resonances, and Fabry-Perot cavity formation [50, 51]. Varying thicknesses and spatial distribution of NWs, their optical response can be tuned to provide either wavelength-selective sensing or broad-band absorptivity guiding the interaction between transverse components of the incident electromagnetic waves, NWs, and adjacent medium[52]. For solar-cell applications, NW geometry-driven broad-band enhancement in light absorption can promote high short-circuit current density even without an anti-reflective coating [53, 54]. At the same time, high anisotropy of the NWs increases the thermodynamic limit of open-circuit voltage due to the enforced directionality in the light emission from the NWs and reduction in substrate emission losses (the mechanism
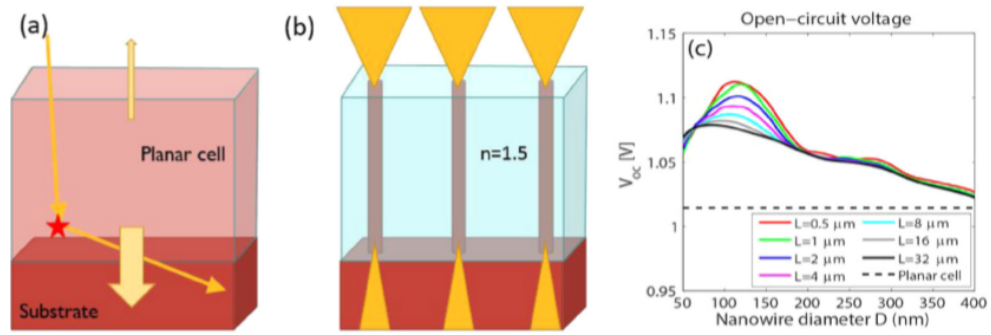
FIGURE 2.1: (a) Black body emission from the solar cell loss into the semi-infinite substrate; (b) restriction of the emission cone in NWs due to the restricted optical density of states; (c) predicted V_{oc} in the NW solar cells with different NW lengths and diameters (solid lines) compared to the planar cell (dashed line) [55, 56].
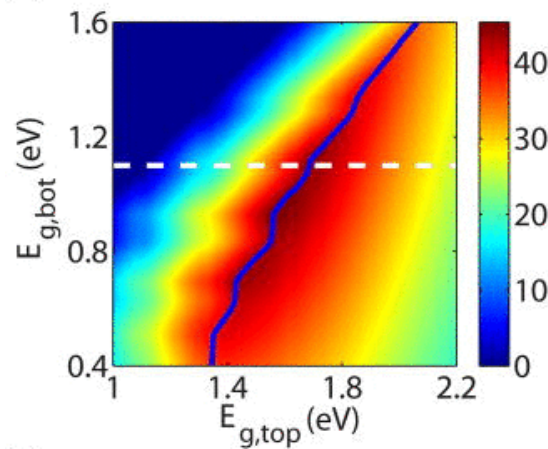
FIGURE 2.2: Detailed balance efficiency map for the 2J solar cell assuming unity absorption in the top cell [58].

of radiative loss in the planar cell into the substrate is illustrated on Fig. 2.1a and, in contrast, Fig. 2.1b is showing the emission restriction in the vertically aligned NWs which results in increased radiative efficiency limit as shown on Fig. 2.1c) [55, 56].

These factors coupled with the enhanced carrier extraction (the junction can be designed radially, surrounding the base of the NW solar cell, thus diffusion length of minority carriers becomes a non-critical parameter) can enable the NW solar cell device with theoretical efficiency exceeding the efficiency limit of thin-film planar devices. Removing the substrate and placing encapsulated NWs onto the reflective handle can further increase the achievable V_{oc} of the NW cells [57].

The cost efficiency of using the NWs instead of planar film does not only come from the capability of using the heterogeneous substrates, but also from the MOVPE growth regime favoring formation of the NWs. The use of NWs not only provides higher photo-conversion efficiency compared to the planar solar cells with no anti-reflective coating, but also allows for dramatic reduction in material volume (i.e., compared to lattice-mismatched thin film GaAsP-on-Si growth which may also include thick metamorphic buffers).Maximum current from both the top and middle cells can be provided with only $30 - 40\%$ of the solid material otherwise required for planar devices. Converted to the mass of metalorganic precursors required for metalorganic vapour phase epitaxy (MOVPE) of NWs, this corresponds to an overall material savings of 93% (not including the cost of several micrometres-thick metamorphic buffer in case of thin film).

The possibility of heterogeneous III-V NW integration on Si led to the concept of the tandem III-V-Nanowire-on-Si solar cells design [58]. The detailed balance efficiency calculations [3] for such tandem solar cell carried out in the assumptions of unity absorption in the top cell above the bandgap (Fig. 2.2) show that for the NW on Si (bandgap, $E_g(\text{Si}) = 1.12$ eV), the optimal top cell bandgap value is ~ 1.7 eV resulting in the limiting efficiency near 40% [58]. This bandgap value can be targeted with $GaAs_{0.77}P_{0.23}$ NWs. The experimental implementation of such tandem device (Fig. 2.3 c) was demonstrated in 2017 with tandem GaAsP/Si tandem solar cell efficiency reaching 3.51% (for comparison, efficiency of the 1J Si solar cell depicted on Fig. 2.3a was 9.33% and 1J GaAsP-NW solar cell shown on Fig. 2.3b efficiency was 0.75%) [59]. The suspected issues leading to the poor performance of the tandem device were indicated to be low Te doping of the n-type NW shell (emitter) and tunnel junction, as well as elevated surface recombination velocity and presence of a thick axial emitter region. In addition to the manufacturing-related complications, fundamental design concerns need
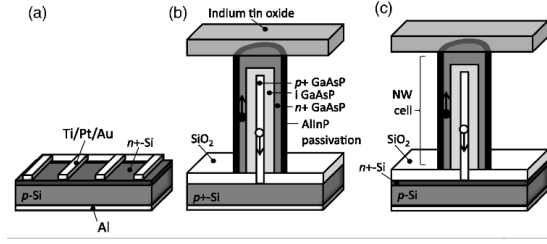
FIGURE 2.3: (a) Simple planar Si solar cell; (b) Layer structure of the GaAsP-NW solar cell diode on the Si handle with ITO deposited as a contact layer; (c) Full GaAsP-NW-on-Si tandem solar cell[59].

to be addressed. In particular, the previous NW-on-Si tandem and multijunction structure concepts [60] do not consider the transmission loss occurring below Si band edge. Thus, triple-junction bifacial design was proposed and is in detail described in the next section.

Another application of the III-V NWs that can as well be implemented by the low-cost manufacturing using Si substrates is light sensing. III-V Nanowire-based photodetectors are an attractive alternative to the existing thin-film devices due to the potential for increased response speed due to the junction geometry [61]. The photodetectors are operated under reverse bias to increase the depletion region width that assists in carrier capture and reduction of the response time. The response time is defined as:

$$\tau_{RC} = RC = \frac{\epsilon A R}{t_A}, \tag{2.1}$$

where C is the depletion capacitance expressed through the parallel plate capacitor formula using t_A, thickness of the absorbing material and A, area of the device. R is the amplifier resistance (Fig. 2.4). On the other hand, carrier collection time, or transit time, for the carriers moving with the velocity v can be written as:

$$\tau_{tr} = \frac{t_A}{v}. \tag{2.2}$$
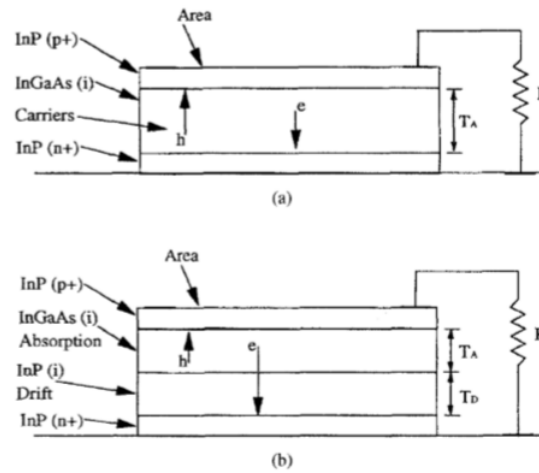
FIGURE 2.4: Schematics of (a) p-i-n InGaAs/InP photodetector and (b) dual-depletion region InGaAs/InP high-speed detector [62].

Equations 2.1 and 2.2 [62] suggest that in the planar detector depicted on Fig. 2.4a for achieving both fast carrier transit and response, on the one hand, the area of the detector needs to be minimized and, on the other hand, the thickness of the absorbing layer should be minimal. Alternatively, an additional drift region can be introduced, as shown on Fig. 2.4b [62]. In a NW detector, these issues can be solved by using core-shell geometry (i.e. cylindrical capacitor geometry for the depletion capacitance, Eg. 2.3) and adjusting doping in the components to increase the depletion region width and enable radial collection of the carriers. In the Eq. 2.3, capacitance per length, C/L, in the cylindrical capacitor is expressed in terms of the radii of the inner and outer depletion region borders, R_{inner} and R_{outer}, respectively:

$$\frac{C}{L} = \frac{2\pi\epsilon}{ln\left(\frac{R_{outer}}{R_{inner}}\right)}. \tag{2.3}$$

The waveguide properties of the NWs can be used for narrow-band sensing as was demonstrated in previous works [63, 64, 65]. However, while in the short-wavelength range the tunability in the NW absorption can be easily achieved by the variations in

the NW diameter in the below target wavelength range [66], selectivity in the IR range is not as trivial. To ensure a near-unity absorption in the IR range, the diameter of the absorbing NWs must be in the order of micrometers which increases the number of allowed waveguide modes inside the NW [67]. So for enabling the efficient selectivity, the IR NW absorbers can be equipped with the wide-bandgap light filter that can be realized in a form of an epitaxial substrate. Such structure was shown in [68]. Active $InAs_{0.73}Sb_{0.27}$ NWs grown on InAs substrates (Fig. 2.5a) and fabricated into the photodiode (Fig. 2.5b) with the NWs being illuminated from the substrate side (Fig. 2.5c). Lattice mismatch between InAs and $InAs_{0.73}Sb_{0.27}$ is only ∼2%, however, the substrate cost remains a concern. At the same time, growth of the thick (beyond critical diameter) NWs on the lattice-mismatched cheap Si substrates can be associated with incomplete relaxation of the NW crystal lattice and inclusion of the crystalline defects. Measured for InAs and InP gold-catalyzed NW growth, the critical diameter changes with misfit as shown on Fig. 2.6 [69, 70]. Thus, the optimization problem for the IR NW sensors is to achieve high narrow-band absorption in the IR region while keeping the diameter of the NW and substrate contact region minimal.

2.2.2 Modeling of the Bifacial III-V-Nanowire-on-Silicon Triple Junction Solar Cells

III-V-on-Si multijunction solar cells can be made using 1.75 eV $GaAs_{0.73}P_{0.27}$ NWs on the front side of a bulk-type, planar Si solar cell and 0.5 eV $In_{0.81}Ga_{0.19}As$ NWs on the rear side (the ideal bandgaps (E_g) are based on Shockley-Queisser detailed balance efficiency calculation for a fixed middle cell with $E_g = 1.12$ eV, Fig. 2.7).
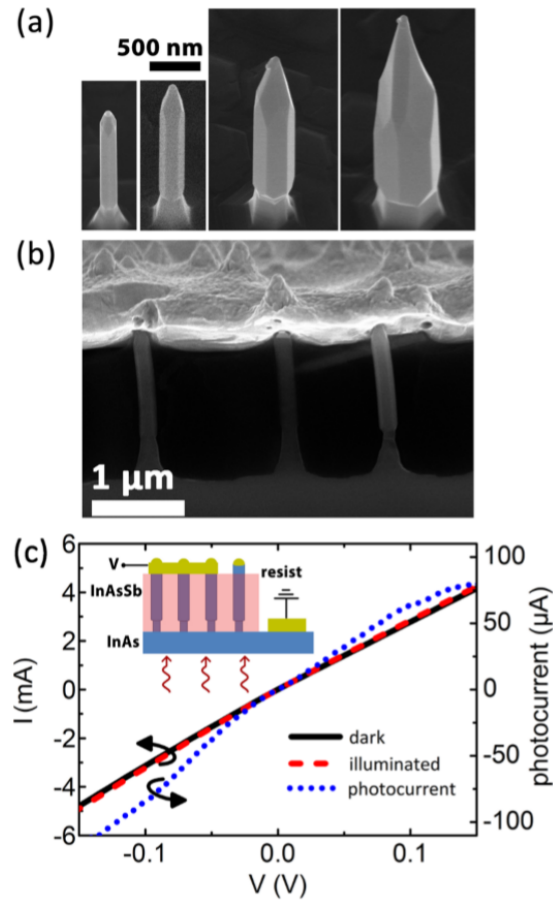
FIGURE 2.5: (a) SEM of the InAs/InAsSb NWs grown on InAs substrate; (b) cross-sectional view SEM of the fabricated device featuring encapsulating photoresist and metal contact (bright); (c) current-voltage characteristics of the InAs/InAsSb photodiode measured at 5 K, the inset cartoon shows the device schematics with the incident illumination depicted [68].
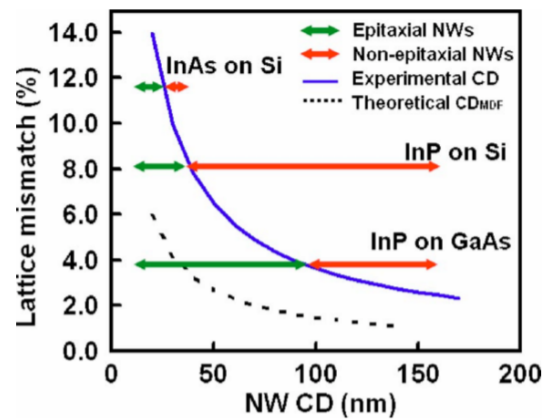
FIGURE 2.6: Critical diameter of the III-V NWs grown on the lattice-mismatched substrates as a function of lattice mismatch[69].
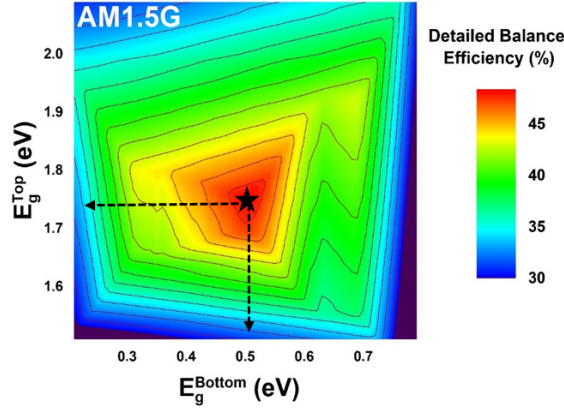
FIGURE 2.7: Detailed balance efficiency map for the triple-junction (3J) solar cell with the middle Si cell corresponding to the bandgap of 1.12 eV. This calculation was carried out assuming AM1.5 incident illumination.

Absorption and limiting short-circuit current density (J_{sc}) in wide-bandgap $GaAs_{0.73}P_{0.27}$ top-side NW arrays are highly geometry-sensitive. The J_{sc} in an underlying Si cell also becomes a function of the diameter and pitch of the top array for a fixed NW length of 1.5 μm. Thus, an optimization of the dimensions of NWs relatively to their spatial distribution in array configurations is needed to achieving absorption enhancement promoting current matching between sub-cells. A top-side NW array geometry that was optimized for maximum efficiency operation of a dual-junction solar cell as a part of a $GaAs_{0.73}P_{0.27}/Si/In_{0.81}Ga_{0.19}As$ triple-junction NW-based device (Fig. 2.8a) was performed. Additionally, adjustment of the rear-side 0.5 eV NW sub-cell was necessary, since unlike bulk materials, the diameter of the NWs affects the fundamental light scattering mechanism. For longer wavelengths, transmission of electromagnetic waves due to field screening can occur, thereby reducing the absorption in substantially thin $In_{0.81}Ga_{0.19}As$ NWs compared to the planar films. At the same time, from the growth perspective, the use of thinner NWs would be preferable. Thus, modelling of the bottom array configurations focused on finding minimal NW diameters and reasonable pitch values that enable current matching between all three sub-cells.
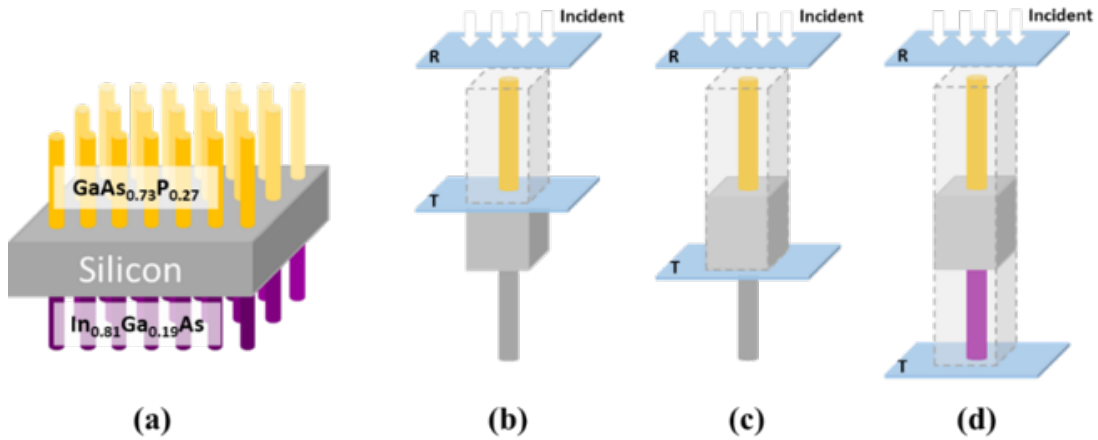
FIGURE 2.8: (a) Scheme of the bifacial 3J NW-on-Si solar cell (not to scale); Simulation domain (unit cell) with the reflection (R) and transmission (T) measurement planes for calculating absorption in (b) top NW array, (c) top array and Si middle cell, and (d) full 3J device.

2.2.3 RCWA Algorithm for Nanowire Arrays Simulations

RCWA wave analysis algorithm has been widely used for modeling diffraction structures [71, 72, 73, 74]. The general solution principle can be shown for the structure depicted on Fig. 2.9. Note that the same approach can be applied to the structure with periodicity in 2 dimensions within a single layer as well.

The basic principle of the RCWA algorithm relies on finding the semi-analytical solutions of Maxwell's equation for the electromagnetic waves propagating through the matter with lateral non-homogeneity of refractive index, for which the analytical solution is found only in the direction along which the refractive index remains constant (by convention, Z-axis). The incident, reflected, and transmitted electromagnetic field is written as a superposition of the coupled waves and Fourier transforms of the refractive indices along X- and Y-directions is used. In 3D case in real space,

$$\frac{\partial E_z}{\partial y} - \frac{\partial E_y}{\partial z} = i\omega\mu_r H_x, \tag{2.4}$$
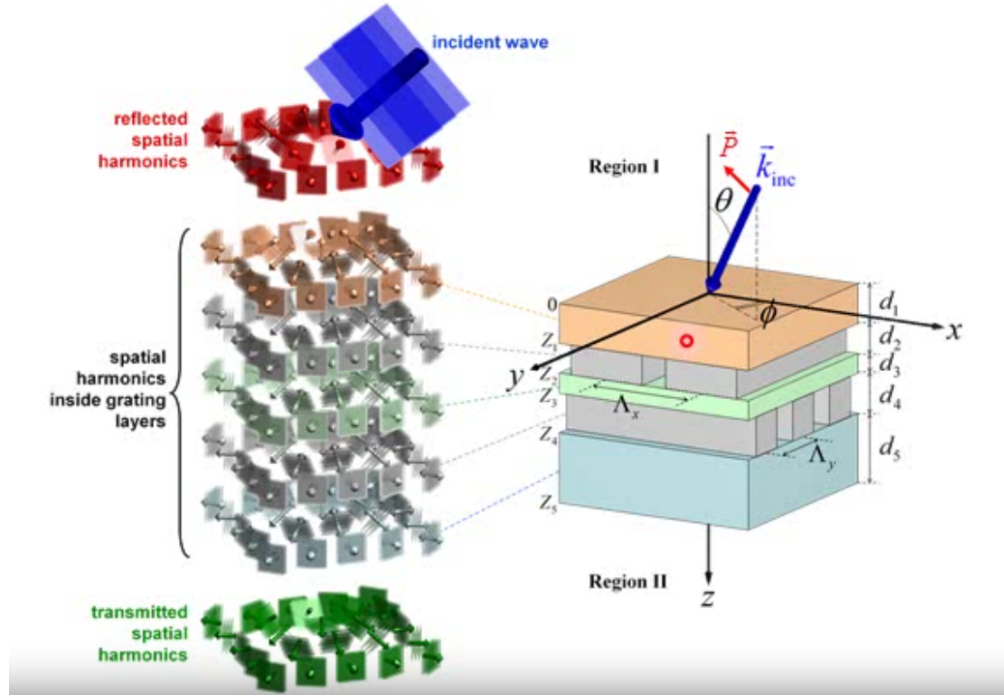
FIGURE 2.9: The wave harmonics representation of the physical structure comprising homogeneous along Z-axis layers and periodic inclusions along X and Y axes (the physical layers and their modal representations are connected with lines).

$$\frac{\partial E_x}{\partial z} - \frac{\partial E_z}{\partial x} = i\omega\mu_r H_y, \tag{2.5}$$

$$\frac{\partial E_y}{\partial x} - \frac{\partial E_x}{\partial y} = i\omega\mu_r H_z, \tag{2.6}$$

and

$$\frac{\partial H_z}{\partial y} - \frac{\partial H_y}{\partial z} = -i\omega\epsilon_0\epsilon_{r,x} E_x, \tag{2.7}$$

$$\frac{\partial H_x}{\partial z} - \frac{\partial H_z}{\partial x} = -i\omega\epsilon_0\epsilon_{r,y} E_y, \tag{2.8}$$

$$\frac{\partial H_y}{\partial x} - \frac{\partial H_x}{\partial y} = -i\omega\epsilon_0\epsilon_{r,z}E_z. \tag{2.9}$$

Within a single homogeneous layer (along Z-axis), the electric $(\epsilon_{r,\vec{j}})$ and magnetic $(\mu_{r,\vec{j}})$ permittivities can be written in a form of their Fourier expansions along X and Y axes:

$$\epsilon_r(x,y) = \sum_{m=-\infty}^{\infty}\sum_{n=-\infty}^{\infty} a_{m,n} e^{i\left(\frac{2\pi m x}{\Lambda_x} + \frac{2\pi n y}{\Lambda_y}\right)} \tag{2.10}$$

and

$$\mu_r(x,y) = \sum_{m=-\infty}^{\infty}\sum_{n=-\infty}^{\infty} b_{m,n} e^{i\left(\frac{2\pi m x}{\Lambda_x} + \frac{2\pi n y}{\Lambda_y}\right)}. \tag{2.11}$$

For calculating the transmission and reflection at the interfaces, solving this system in the real-space domain will be computationally costly: it involves breaking the structure down into the fine unit cells with the solutions being found along the grid. On the other hand, transitioning to the frequency space allows to exploit X- and Y-periodicity of the diffraction grating minimizing the computation time [75]. Substitution of the Fourier series of the matter permittivity components forming diagonal tensor to the Maxwell's equations results in a system of transverse Maxwell's equations:

$$\frac{\partial}{\partial z}E_x = \frac{-i}{\omega\epsilon_0}\frac{\partial}{\partial x}\frac{1}{\epsilon_{r,z}}\frac{\partial}{\partial y}H_x + \left(\frac{i}{\omega\epsilon_0}\frac{\partial}{\partial x}\frac{1}{\epsilon_{r,z}}\frac{\partial}{\partial x} + i\omega\mu\right)H_y, \tag{2.12}$$

$$\frac{\partial}{\partial z}E_y = \frac{i}{\omega\epsilon_0}\frac{\partial}{\partial y}\frac{1}{\epsilon_{r,z}}\frac{\partial}{\partial x}H_y + \left(\frac{-i}{\omega\epsilon_0}\frac{\partial}{\partial y}\frac{1}{\epsilon_{r,z}}\frac{\partial}{\partial y} - i\omega\mu\right)H_x, \tag{2.13}$$

$$\frac{\partial}{\partial z}H_x = \frac{i}{\omega\mu}\frac{\partial}{\partial x}\frac{\partial}{\partial y}E_x + \left(\frac{-i}{\omega\mu}\frac{\partial}{\partial x}\frac{\partial}{\partial x} - i\omega\epsilon_0\epsilon_{r,y}\right)E_y, \qquad (2.14)$$

$$\frac{\partial}{\partial z}H_y = \frac{-i}{\omega\mu}\frac{\partial}{\partial y}\frac{\partial}{\partial x}E_y + \left(\frac{i}{\omega\mu}\frac{\partial}{\partial y}\frac{\partial}{\partial y} + i\omega\epsilon_0\epsilon_{r,x}\right)E_x. \qquad (2.15)$$

Applying Bloch's Theorem, the electromagnetic field components in a periodic structure replicated along X and Y axes can be expressed as:

$$E_x = e^{i(k_{x,0}x+k_{y,0}y)}\sum_p\sum_q e^{i\left(\frac{2\pi}{\Lambda_x}px+\frac{2\pi}{\Lambda_y}qy\right)}\sum_m a_{x,m,p,q}\left(f_m e^{i\kappa_m z} + g_m e^{-i\kappa_m z}\right), \qquad (2.16)$$

$$E_y = e^{i(k_{x,0}x+k_{y,0}y)}\sum_p\sum_q e^{i\left(\frac{2\pi}{\Lambda_x}px+\frac{2\pi}{\Lambda_y}qy\right)}\sum_m a_{y,m,p,q}\left(f_m e^{i\kappa_m z} + g_m e^{-i\kappa_m z}\right), \qquad (2.17)$$

$$H_x = e^{i(k_{x,0}x+k_{y,0}y)}\sum_p\sum_q e^{i\left(\frac{2\pi}{\Lambda_x}px+\frac{2\pi}{\Lambda_y}qy\right)}\sum_m b_{x,m,p,q}\left(f_m e^{i\kappa_m z} - g_m e^{-i\kappa_m z}\right), \qquad (2.18)$$

$$H_y = e^{i(k_{x,0}x+k_{y,0}y)}\sum_p\sum_q e^{i\left(\frac{2\pi}{\Lambda_x}px+\frac{2\pi}{\Lambda_y}qy\right)}\sum_m b_{y,m,p,q}\left(f_m e^{i\kappa_m z} - g_m e^{-i\kappa_m z}\right). \qquad (2.19)$$

Substituting the expressions for periodic wave components into the system of transverse Maxwell's equations, taking partial derivatives, and cancelling terms containing dependency on Z results in an eigenvalue problem for the field amplitudes:

$$\mathbf{A}\mathbf{x} = \lambda\mathbf{x} \tag{2.20}$$

where $\mathbf{A}$ is an operator (Eq. 2.12 - 2.15), λ is the eigenvalue (κ_m^2). Amplitudes a and b are found for the corresponding eigenvalues. The operator form of the equation allows to further carry out the solution in a matrix form for the incident ("+"), reflected ("-"), and transmitted waves [76]. The extension of the RCWA model onto the multilayer structures involves the use of scattering matrices [77]. RSoft DiffractMOD exploits this algorithm for the complex structures using transmission-line treatment of boundary conditions [78, 79]. For the jth layer within the simulation domain, the modal voltage and current amplitudes can be written as:

$$v_m^{(j)} = f_m^{(j)}e^{i\kappa_m z} + g_m^{(j)}e^{-i\kappa_m z}, \tag{2.21}$$

$$i_m^{(j)} = f_m^{(j)}e^{i\kappa_m z} - g_m^{(j)}e^{-i\kappa_m z}. \tag{2.22}$$

Then, for the $(j+1)^{th}$ layer, using the boundary condition for the wave recurrent relation can be defined:

$$\sum_m \begin{pmatrix} a_{x,m,p,q} \\ a_{y,m,p,q} \end{pmatrix}^{(j)} v_m^{(j)}(z_j^{j+1}) = \sum_m \begin{pmatrix} a_{x,m,p,q} \\ a_{y,m,p,q} \end{pmatrix}^{(j+1)} v_m^{(j+1)}(z_j^{j+1}) \tag{2.23}$$

$$\sum_m \begin{pmatrix} b_{x,m,p,q} \\ \\ b_{y,m,p,q} \end{pmatrix}^{(j)} i_m^{(j)}(z_j^{j+1}) = \sum_m \begin{pmatrix} b_{x,m,p,q} \\ \\ b_{y,m,p,q} \end{pmatrix}^{(j+1)} i_m^{(j+1)}(z_j^{j+1}). \tag{2.24}$$

The accuracy of the simulation (solution) is determined by the number of the refractive index and field upon Fourier series decomposition with the optimal number of modes corresponding to the complete convergence of the simulations. Full convergence of the simulation with respect to the Fourier mode number is defined for the number of harmonics N for which further increase of N results in none-to-negligible deviation of the diffraction efficiency for each frequency of the incident field.

2.2.3.1 Optical Simulation Details

The DiffractMOD simulation engine of Synopsys TCAD RSoftő software was used employing the RCWA technique for calculating absorption in $GaAs_{0.73}P_{0.27}$ NW arrays. A 3-dimensional unit cell with cubic arrangement of cylindrical NWs was created (Fig. 2.8b-d). A shallow, 2 nm-thick, underlying Si substrate was included in the simulation of the top NW array to consider the possible impact of the NW/Si interface on the optical path of photons escaping the NW through transmission. Light absorption by NWs within the simulation domain was calculated as a difference between normalized incident, transmitted, and reflected components of linearly polarized normally incident light, which was enabled by the symmetry of the array making X- and Y-polarized waves indistinguishable resulting in identical absorption spectra. The accuracy of the simulations was evaluated by increasing the number of the plane wave harmonics from 25 to 196 and examining the convergence of the diffraction efficiency spectra. This analysis
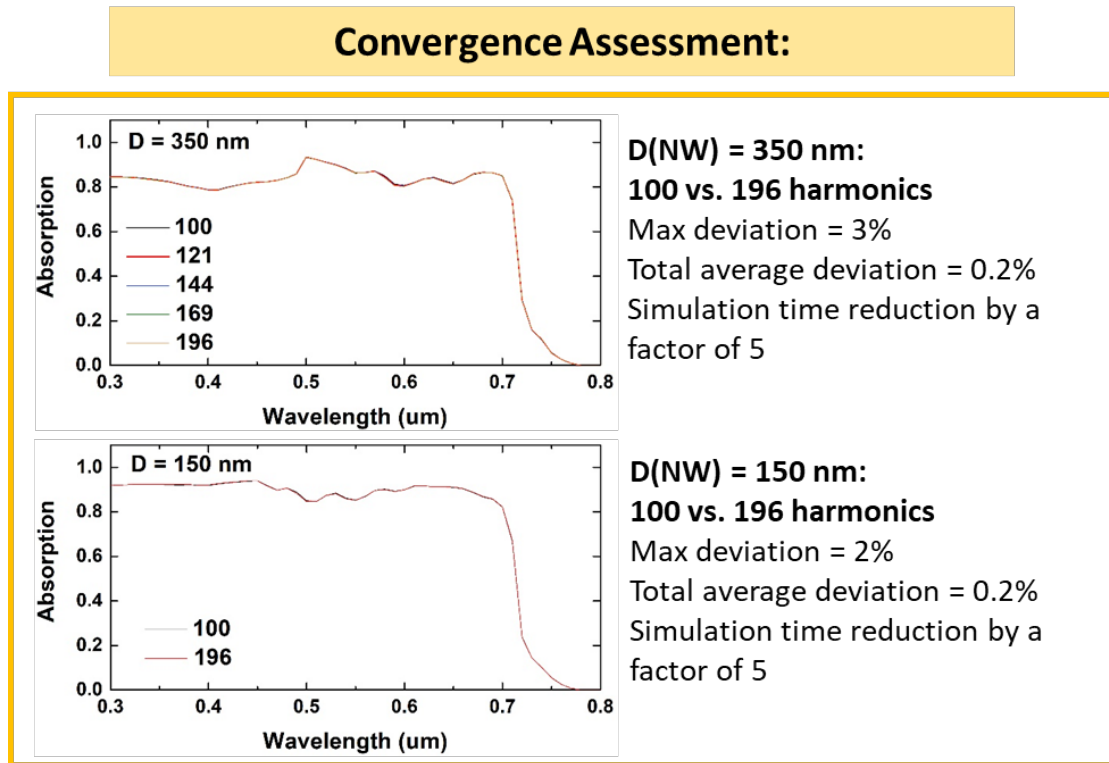
FIGURE 2.10: Absorption spectra of the GaAsP NWs with diameters of 350 nm and 150 nm simulated for various numbers of plane wave harmonics for convergence assessment.

was carried out for the two diameters of the NWs, 150 nm and 350 nm. Using 10 harmonics per dimension (along X and Y where arrays are periodic), or total of 100, results in convergence of the total integrated absorption within 0.2% (Fig. 2.10). The error might be further minimized to 0.006% by transitioning to 13 harmonics per coordinate, however, in this case the computational speed would increase by a factor of 5 which was an important consideration for the batch simulations used in this work.

The diameters (D) of the NWs were varied from 100 nm to 550 nm in conjunction with the pitch (P) from 250 nm to 800 nm, both with a step of 50 nm. The optimal length of the NWs mostly corresponds to the band edge absorption depth of $GaAs_{0.73}P_{0.27}$, so that an ideal length for the NWs alone would be several microns (Fig. 2.11). However, the maximum efficiency of the multijunction solar cell requires not only maximization of J_{sc}, but current matching between the sub-cells. Therefore, from the perspective
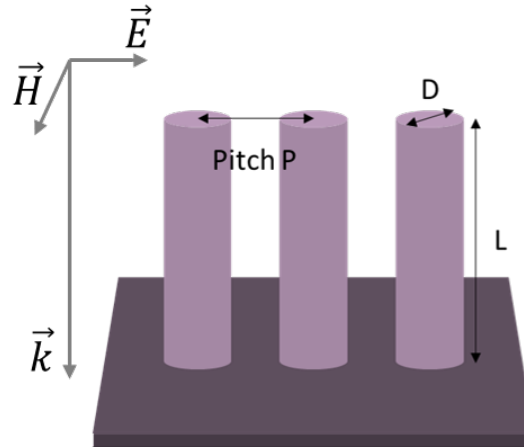
FIGURE 2.11: Illustration of the NW geometrical parameters: diameter, D, pitch, P, and length, L.

of both experimental feasibility and current matching, L = 1.5 μm was used. In the multijunction cell, essentially representing a set of in-series connected diodes, equating the generation currents (ideally translated onto the short-circuit and maximum power point currents at the device level) is one of the main engineering problems as the whole device is limited by the smallest current. Maximization of the open-circuit voltages of the subcells and equating the output currents are principle for achieving highly efficient multijunction solar cell.

To simulate the absorption in the middle Si cell with thickness of 200 μm, corresponding to a typical single-crystalline Si solar cell thickness, in relation to the pitch and diameter of the top NWs, the simulation unit cell was extended to comprise both the Si and top NW sub-cells. The total absorption in such stack was modeled for each geometry of the top array, and then the absorption in the middle cell was found by subtracting the initial top NWs absorption from the total absorption of the dual junction stack. The same approach was used to calculate the parameters of the bottom cell, except that the top array was included in the domain only in selected simulations where the pitches of the top and bottom NW arrays could be easily adjusted (for example, P_{Top} = 500 nm, P_{Bot} = 1000 nm). No anti-reflective coating, embedding polymer (for example

benzocyclobutene, BCB, with refractive index of ~1.552), and ITO coatings were added to the simulated structure for the preliminary geometry optimization study in order to minimize the number of simulation parameters. For the current study, the thickness of the Si sub-cell was kept constant. The refractive indices and extinction coefficients of the ternary compounds used in simulations were calculated using the Kramers-Kronig model [80].

Limiting short-circuit current density, $J_{sc,lim}$, calculations were performed based on the assumption that each absorbed photon generates an electron-hole pair and that 100% collection efficiency is realized, which can be described as generation current density, J_{Gen}. Thus, J_{Gen} values were calculated for the Air Mass 1.5 global (AM1.5G) incident spectrum with spectral irradiance $I_{AM1.5G}(\lambda)$ taken from ASTM G173-03 Tables and solar cells absorption, $A(\lambda)$ extracted from simulation as:

$$J_{sc,lim} \equiv J_{Gen} = \int_{\lambda_1}^{\lambda_2} \frac{q\lambda}{hc} I_{AM1.5G}(\lambda)A(\lambda)d\lambda. \tag{2.25}$$

In Eq. 2.25, the values of spectral irradiance of the AM1.5G spectrum were interpolated to match the wavelengths step of the simulated absorption spectra ($5 - 10$ nm). This integral was then solved numerically for individual sub-cells with wavelengths from λ_1 to λ_2 corresponding to the absorption range of the sub-cell.

While simulations of absorption and calculations of the generation currents in top array and middle Si cell were relatively straightforward, direct simulations of an entire 3J device as shown on Fig. 2.8d were associated with the necessity of matching the periodicities, or pitches, in top and bottom arrays within a single simulation domain (Fig. 2.12). Thus, in order to map the J_{Gen} of the bottom cell over a broad range of diameters and pitches, significantly more computational resources would be required.
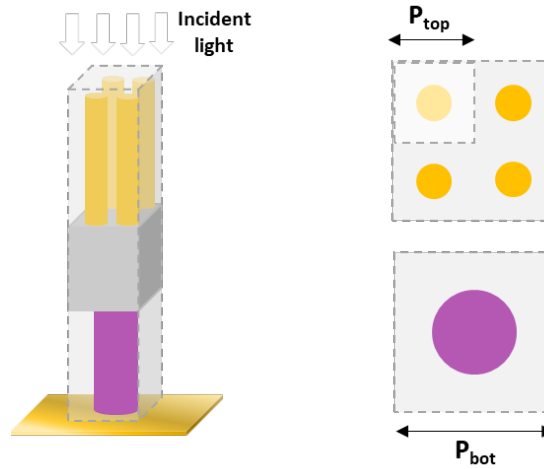
FIGURE 2.12: Illustration of the simulation domain matching principle in the cases of non-equal NW periodicities in top and bottom arrays.

To facilitate the process and get a general guideline for the bottom NWs' parameters, an initial adjustment of the bottom $In_{0.81}Ga_{0.19}As$ NW sub-cell's geometry was performed without a top-side array added on the Si surface to avoid the mismatch between the periodicity in top and bottom arrays. Using this approach, the diameters and pitches of the bottom NWs were swept from 300 nm to 1200 nm and from 350 nm to 1500 nm, respectively. However, since the front NW array acts as an antireflective coating, its impact on the absorption in the bottom array was evaluated as well by comparing the reflectivity spectra of the bare Si, R_{bare}, and Si with the NW array on top, R_{ARC}, in the absorption range of the bottom array (i.e. from ~ 1.2 μm to 2.5 μm). Short-wavelength absorption in the top array was not included in the analysis, since this portion of light is readily absorbed in 200 μm-thick Si and does not have any influence on the bottom NWs. Thus, the maximum generation current that could be gained by the bottom NWs by including top array was calculated. For some cases where pitches of the top and bottom arrays are $P_{Top} = 500$ nm and $P_{Bot} = 1000$ nm, the whole structure was directly modelled by increasing the number of the top NWs inside the domain to form 2×2 array. In this work, the effects of a back-surface reflector (BSR) on the long-wavelength

absorption in the solar cell were also studied. In all cases, the BSR was represented by a flat Au slab in contact with the rear-side of the InGaAs NWs.

For the next part of the study, optical simulations were performed including the embedding media and ITO coating. As was done previously, for simulating the top NW array absorption, a 3D cubic unit cell was designed, however, the NWs were encapsulated in BCB. The thickness of the planar ITO layer value of 300 nm was sourced from literature [81]. An increased thickness of the ITO contact layer would provide lower series resistance (R_{series}) by reducing the lateral conduction path cross-sectional area (for current traveling between the metal grid fingers), however, ITO has a non-zero absorbance in the UV region which introduces another optimization parameter which so far has not been studied. The length of the top NWs was preserved at 1.5 μm and pitch and diameter were varied. Calculations of the generated current density were performed by subtracting the parasitic absorption in the ITO layer from the total absorption in the domain. While both refractive index (n) and extinction coefficient (k)of the ITO refractive index were used explicitly for each incident wavelength, the BCB medium optical constants were approximated as having n = 1.552 and k = 0.

2.2.3.2 Opto-Electrical Simulation Details

Two-dimensional NW device simulations and multifaceted optimizations of the NW solar cell parameters (i.e. thicknesses of the base, intrinsic region, and emitter and doping levels) were carried out using TCAD Sentaurus^{TM}. Since coupling interaction between the NWs alters electromagnetic wave propagation and optical generation profiles in the NWs compared to the planar device, where absorption follows Beer-Lambert law, the spatial carrier generation rate profiles computed for the AM1.5G spectrum were sourced from RCWA RSoft engine integrated in the Sentaurus^{TM} work flow. Two-dimensional
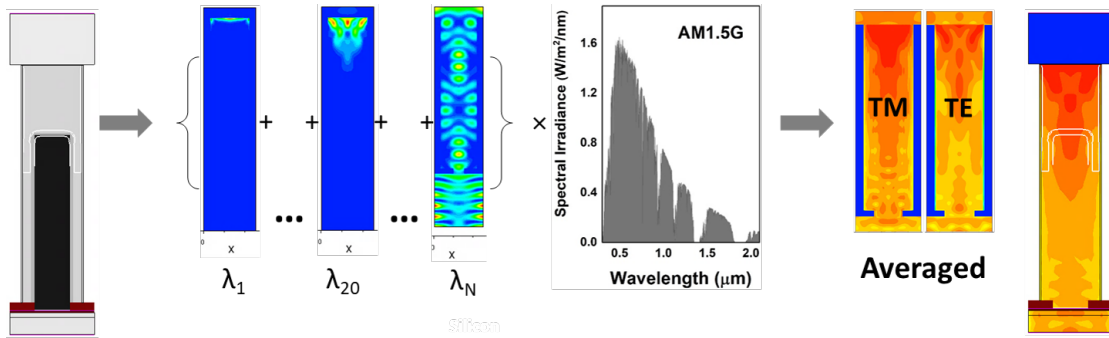
FIGURE 2.13: Co-simulation flow chart: the CAD model of the NW is created in Sentaurus Structure Editor, imported to the RSoft tool which computes spatially resolved absorption spectra for TE and TM light polarizations modulated by the incident solar spectrum. The average product of thus obtained optical generation is imported to Sentaurus Device computing current-voltage characteristics.

NW representation was created in TCAD Sentaurus Structure Editor and explicitly imported to the RSoft tool. Spatially resolved absorption profiles were computed for two polarizations of the incident plane wave and averaged. Average spatial absorption was then convolved with the incident AM1.5G spectrum resulting in the optical generation profile serving as an input for the Optical Solver in Sentaurus Device. The sequence of the processes is shown on the diagram (Fig. 2.13)

The combination of the core-shell and axial junction geometries, as illustrated by Fig. 2.14a-c, was chosen in a pursuit of possible benefits of the two: while core-shell geometry alone provides independency of the carrier collection efficiency on the minority carrier diffusion length, isolation of the depletion region from lossy surface, addition of the axial component allows an *in-situ* homogeneous passivation of the NWs with doped wide-bandgap material (here, GaP) and also facilitates fabrication of the top contact. Such a combined design was analyzed in terms of the overall performance, potential design concerns, and elevated surface recombination velocity tolerance and its dependence on the thicknesses and doping.

As a passivation (window) layer, 10 nm-thick GaP was conformally deposited onto the NW. Driven by the Si middle cell processing resulting in n-on-p planar Si middle cell,
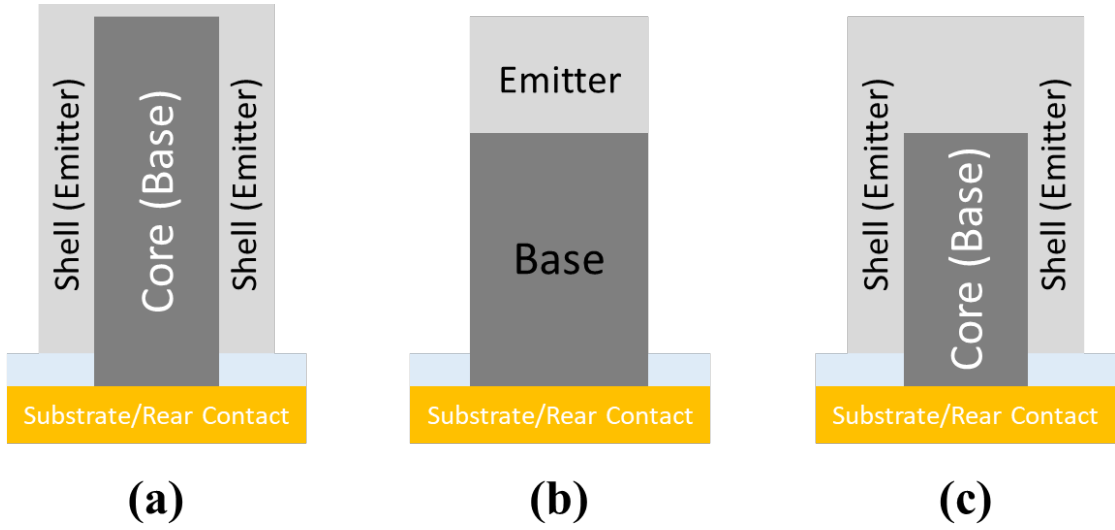
FIGURE 2.14: (a) Core-shell NW junction; (b) Axial NW junction; (c) Combined, core-shell and axial NW junction. The spacer (light blue) represents an insulator preventing shortening of the diode formed by the core and the shell (a and c).

the polarity of the top NW cell was n-i-p corresponding to the p-type core (base) and n-type shell (emitter), so that the passivation was n-doped. The total diameter of the NW including the passivation on the sides was 370 nm and pitch was 500 nm. The total length of the NWs was 1.5 μm. Axially, the junction depth was changed by adjusting by mutually adjusting emitter and base thicknesses with the axial i-region thickness of 50 nm such that the total NW length was preserved (except for the cases specified in Results and Discussion). At the same time, tuning of the radial junction parameters was performed. First, the base radial width was fixed at 210 nm and mutual variations of the core i-region and emitter radially (the sum of radial emitter and radial i-region thicknesses was fixed at 70 nm) were performed (Fig. 2.15). The insertion of the thin i-region in the radial direction serves as a diffusion buffer and memory effect reduction measure for the dopant species (currently, Zn and Si are available for p- and n-type dopants), rather than for extending the electric field region for enhanced collection. The carrier mobilities were sourced for the bulk GaAs$_{0.73}$P$_{0.27}$ material values [82]. Based on the literature source, electron mobility, μ_e, is 9.40×10^3 cm^2/V-sec, hole mobility,
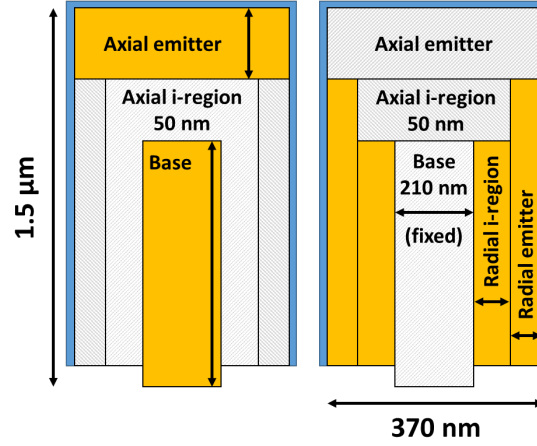
FIGURE 2.15: Schematics of the axial and radial components of the top $GaAs_{0.73}P_{0.27}$ NW junction.

μ_h, is 81 cm^2/V-sec. Effective masses of carriers were derived from Vegard's law: for electron, $m_e = 0.107m_0$, and for the heavy and light holes, respectively, $m_{hh} = 0.948m_0$ and $m_{lh} = 0.089m_0$. Radiative recombination coefficient, C_{rad}, is 1.7×10^{-10} cm^3/sec. Auger coefficient is 1.0×10^{-30} cm^6/sec.

2.2.3.3   Results and Discussion

Fig. 2.16a shows the maps of limiting J_{sc} extracted for the top NW array for the AM1.5G solar spectrum; Fig. 2.16b shows the difference between the J_{sc} values of the top GaAsP NW cell without embedding and ITO coating and middle Si cell in consideration that all absorbed flux is converted into electrical current. Absorption in the arrays where diameter of the NWs is equal or exceeds pitch was not simulated since it is not physical. In Fig. 2.16a, two local J_{sc} maxima at $D_A = 150$ nm, $P_A = 250$ nm and $D_B = 300$ nm, $P_B = 500$ nm are observed for the AM1.5G spectrum. However, minimization of the difference between the current output from top and middle cell is critical for approaching the maximum possible efficiency of the full triple-junction cell, assuming that the bottom cell with its 0.5 eV bandgap is not current-limiting. Although
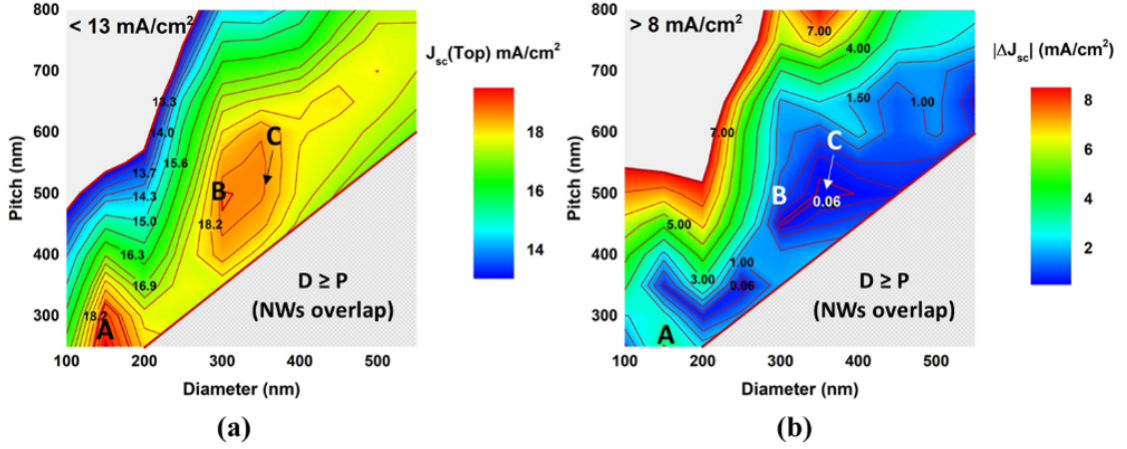
FIGURE 2.16: (a) Limiting short-circuit current density of the GaAsP NW cell (J_{sc}(Top)) mapped as a function of diameter and pitch of the NW array; (b) difference between J_{sc} of the top GaAsP NW and middle Si cells (ΔJ_{sc}). Arrays A, B, and C correspond to the dimensions $D_A = 150$ nm and $P_A = 250$ nm, $D_B = 300$ nm and $P_B = 500$ nm, $D_C = 350$ nm and $P_C = 500$ nm, respectively.

arrangement A ($D_A = 150$ nm and $P_A = 250$ nm) would allow realization of a maximum J_{sc}(AM1.5G) $= 19.65$ mA/cm^2, this configuration would not be preferable for a tandem-junction solar cell design, as it would make the middle cell current-limiting with 3.05 mA/cm^2 overproduction from the top cell.

Adding 300 nm-thick ITO on top, however, slightly alters the distribution of the diameters and pitches optimal for current matching. This is due to the non-zero parasitic absorption in short-wavelength range and thin-film interference. Fig. 2.17 shows the top NWs generation current and top and middle cells current difference maps modified by ITO coating and BCB encapsulation surrounding the NWs. The maxima inherent to the uncoated arrays (Fig. 2.16a) are shifted towards lower pitch values (450 nm) and get less pronounced. Additionally, the highest J_{sc} is characteristic to the thicker NWs ($J_{sc,max} = 17.19$ mA/cm^2 at the D $= 350$ nm and P $= 450$ nm). The close current matching is satisfied in a broad range of diameter (Fig. 2.17b) and pitch values allowing to use thicker NWs. Despite thin NWs (D $= 200$ nm) being optically suitable for achieving high current densities, the impact of surface recombination velocity (S) on the effective
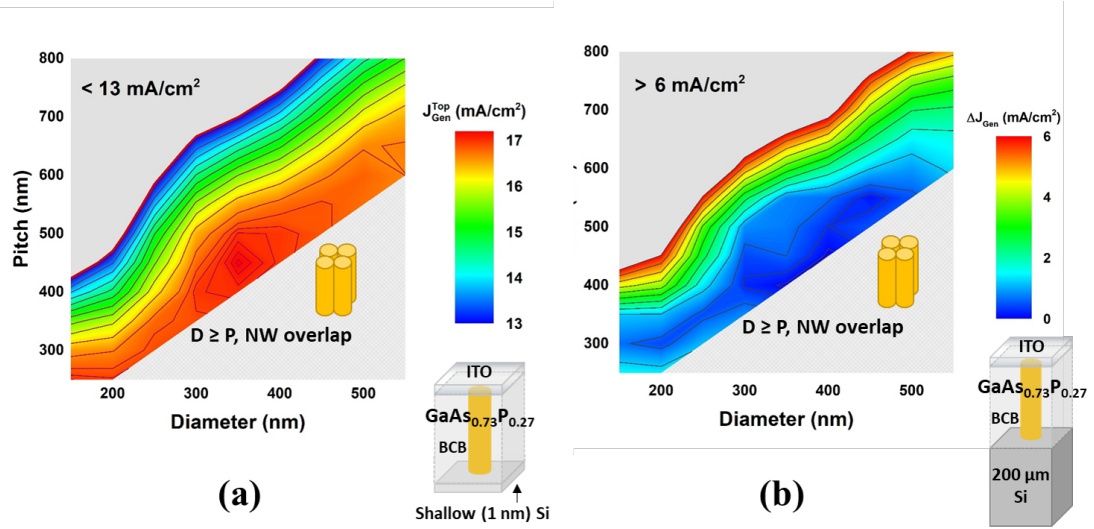
FIGURE 2.17: (a) Limiting short-circuit current density of the embedded and ITO-coated GaAsP NW cell (J_{sc}(Top)) mapped as a function of diameter and pitch of the NW array; (b) difference between J_{sc} of the top GaAsP NW and middle Si cells (ΔJ_{sc}). The cartoons show the simulation domains comprising the BCB encapsulation and ITO layer.

minority carrier lifetime (τ_{eff}) and carrier collection becomes more significant 2.26 [83]:

$$\frac{1}{\tau_{eff}} = \frac{1}{\tau_{Bulk}} + \frac{4S}{D}, \qquad (2.26)$$

where τ_{Bulk} is the minority carrier lifetime in bulk material and D is diameter of the NW. Based on the optical simulations results obtained for the embedded arrays, the dimensions used for the electrical model were chosen to be 370 nm diameter and 500 nm pitch (including the passivation).

While the concern arising in the case of purely axial junction NW is the space charge region being in contact with the surface, having core-shell junction imposes requirements on the doping of NW core and shell to avoid fully depleting the base and/or emitter. First, doping study was performed. For this, base (core) diameter was fixed at 210 nm, axial thickness of the i-region was 50 nm, the sum of radial thicknesses of the i-region and emitter was bound to 70 nm, and depth of the axial junction was varied. Surface
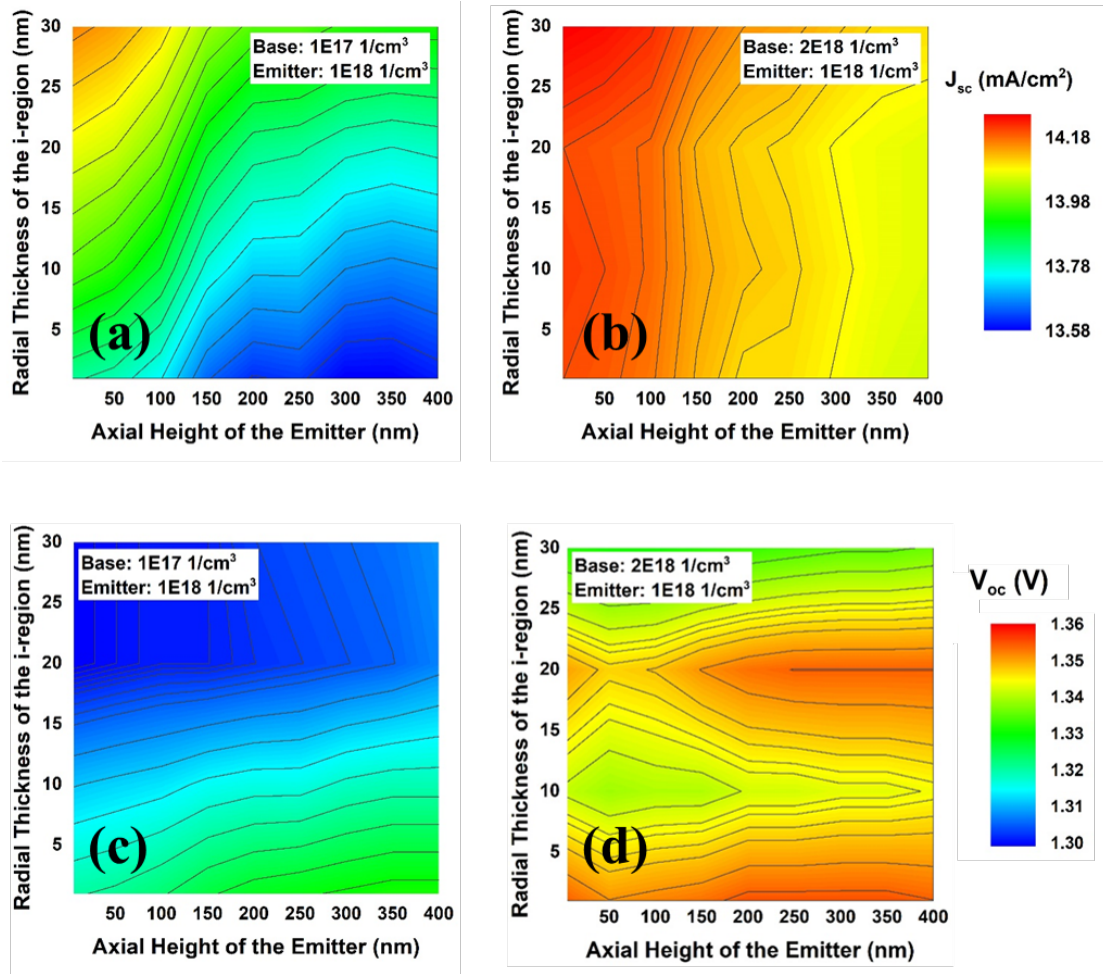
FIGURE 2.18: Short-circuit current density of the top NW cell mapped for different axial junction depths and radial emitter/i-region thicknesses at standard doping (a) and elevated core (base) doping (b); corresponding open-circuit maps (c, d).

recombination velocity was neglected assuming perfect passivation. The J_{sc} and V_{oc} of the top NW solar cell were mapped in dependency on the axial emitter/base height and radial i-region/emitter thicknesses for various doping levels. Fig. 2.18 shows the extracted parameters for the typical planar solar cell base and emitter doping values used for the optically GaAs solar cells [84] and for an elevated base doping.

The observed trends in the J_{sc} and V_{oc} suggest that an increase in the p-doped base is necessary to minimize the depletion region width which, given the optimized geometry, allow to gain up to 1 mA/cm^2 of J_{sc} and 60 mV of V_{oc}. At the same time, it can be evident that deep axial junction does not favor high J_{sc} due to the reduced collection

probability in the high optical generation region at the tip of the NW and while with zero surface recombination velocity (SRV) this effect is less pronounced, considering that V_{oc} remains relatively constant with variations in the axial junction depth, as SRV increases the impact of the axial emitter thickness becomes more dramatic. Note, that the minimal axial emitter thickness on the maps is 5 nm with the axial i-region reduced to 5 nm as well. In other cases, the reduction in the axial i-region did not have significant impact on the top NW cell efficiency.

Elevated SRV on the surface of the GaP passivation layer showed negligible effect on the simulated electrical parameters of the top NW solar cell, however, the recombination at the interface between the emitter and passivation layer is a critical parameter. The increased recombination at the emitter-window can occur due to the 1.89% lattice misfit between $GaAs_{0.73}P_{0.27}$ and GaP that can be partially mitigated via the NW facets edges. The changes in J_{sc} and V_{oc} induced by increased interface recombination velocity (labeled as SRV) were investigated for the range of SRV from 0 to 2×10^5 cm/sec (Fig. 2.19a,b). These data was generated with base width of 210 nm and radial emitter and i-region thicknesses of 50 nm and 20 nm, respectively, corresponding to the region where V_{oc} reaches its maximum values (Fig. 2.18d).

The critical SRV value for both designs at which V_{oc} starts rapidly dropping is 10^2 cm/sec, so for the given NW diameters performance of the solar cell is heavily dominated by the surface losses implying the necessity of nearly perfect passivation. At the same, minimization of the axial depth can help in recovery of J_{sc} up to 37% (at SRV $= 10^5$ cm/sec) by increasing the carrier collection probability to ensure relative reliability of the top NW cell performance if surface is not perfectly passivated. Considering that for well-passivated GaAs NWs the SRV is 1300 cm/sec [85], similar range of values can be expected for the $GaAs_{0.73}P_{0.27}$. As Fig. 2.19c, d illustrate, higher carrier collection
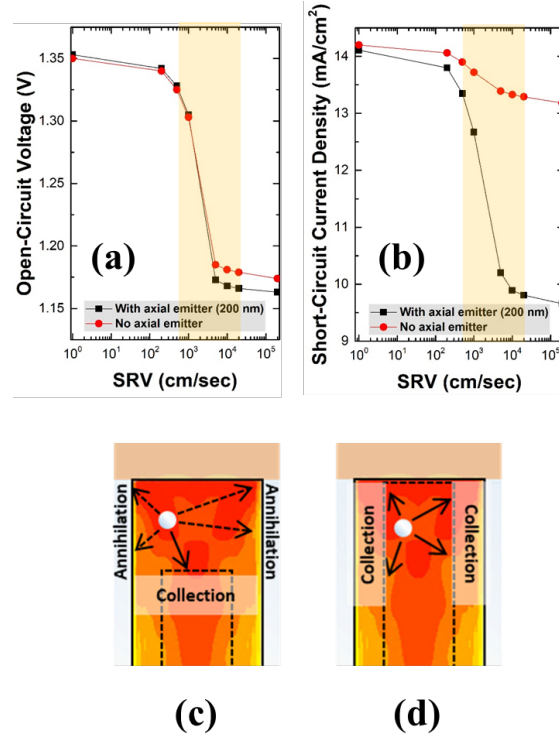
FIGURE 2.19: (a) Open-circuit voltage and (b) short-circuit current density of the top NW cell in dependency on the surface recombination velocity for deep axial junction (black line) and no axial emitter (red line); the cartoon (c) depict the carrier loss mechanism in the deep-junction cell where generation and diffusion can result in surface annihilation, while in the case of radial junction (d) the collection of the minority carriers is more efficient.

is expected with the junction parallel to the NW sides. Despite the enhanced J_{sc} in the radial junction configuration, the degradation in V_{oc} is more less dependent on the geometry. The breakdown of the contributions of dark current components to the V_{oc} can explain the observed trends. From the ideal diode law, it follows

$$V_{oc} = \frac{nkT}{q} ln\Big(\frac{J_{sc}}{J_0}\Big),\tag{2.27}$$

where n is an ideality factor and reverse saturation dark current J_0 is expressed as

$$J_0 = \frac{qn_i^2\sqrt{D_p/\tau_p}}{N_D} + \frac{qn_i^2\sqrt{D_n/\tau_n}}{N_A}\tag{2.28}$$

with D_n and D_p being diffusion coefficients of the electrons in the p-type base and holes in the n-type emitter, respectively, τ_n and τ_p their lifetimes, intrinsic carrier concentration n_i , donor and acceptor concentrations N_D and N_A, and elementary charge q. Considering very narrow depletion region in the base due to the enhanced core doping, there are several scenarios where recombination in the core emitter can dominate. From the Eq. 2.26,

$$\frac{1}{\tau_{eff}} = \frac{1}{\tau_{SRH}} + \frac{1}{\tau_{Rad}} + \frac{4S}{D}. \qquad (2.29)$$

For the NW diameter of 350 nm and SRV of 1300 cm/sec, the surface recombination lifetime is 6.7 ns, so SRV becomes dominant, especially if the volumetric fraction of the space-charge region is comparable to the surface depletion width. This observation indicates that it is important to push dopant concentration in the passivation layer as high as possible to reduce the near-surface band bending while keeping the axial emitter minimal.

The sweep of the radial base, i-region, and emitter thicknesses within cumulative 370 nm including 10 nm-thick GaP layer was performed to find the conditions promoting the maximum efficiency considering increased SRV. Figure 2.20 shows efficiency of the top cell mapped for various combinations of radial base width (220 nm – 300 nm) and radial intrinsic (or diffusion stop) layer (10 nm – 30 nm) bound to the radial emitter thickness. No emitter region corresponds to the set of dimensions resulting in degeneracy of the junction such that the sum of the base, i-region, and passivation widths is equal or exceeds the total diameter of the NW. The highest efficiency region of $\sim 16.5\%$ corresponds to the emitter thickness of 15 nm reaching maximum of 16.53% as the diameter of the base increases along with narrowing of the intrinsic region. In terms

of the preferred wider core (base), the associated increase in efficiency occurs from the volumetric increase in base collection. At the same time, there is a noticeable maximization of the efficiency along the isoline corresponding to the emitter width of 15 nm. An increase in the emitter width (towards the left side of the map) leads to the relative reduction in the efficient core carrier collection that ideally should prevail, since the space-charge region on the base side is isolated from the high-loss interface.

Considering this, the alternative structure for the top NW cell can be a heterojunction with i-region and GaAsP emitter being completely removed to utilize the full advantage of the base collection. To demonstrate that, the base doping was preserved and its width was increased to 350 nm. The simulated heterojunction solar cell consisted of the GaAsP base and 10 nm-thick GaP emitter. Its electrical parameters were compared to those of the cell with base width of 300 nm, i-region of 10 nm, and emitter width of 15 nm. By switching to the heterodesign, the J_{sc} reduced by 0.1 mA/cm^2, while V_{oc} got increased from 1.301 V to 1.318 V by eliminating the additional carrier losses within the native depletion region and at the interface. The total efficiency was preserved within 0.01%. This shows that simplified design can be also adopted for manufacturing the top cell with high resistance to surface recombination.

The heterojunction structure can be further improved by optimizing the doping and geometry of the emitter and base. Figure 2.21a shows the map of efficiency of the heterojunction solar cell for varied doping and thickness of the GaP n-type layer. For the later, base width changes correspondingly within the 370 nm limit. The SRV is preserved at 1300 cm/sec for demonstrating the trends in efficiency. Figure 2.21a shows efficiency of the GaP/GaAsP solar cell as a function of the GaP layer thickness and doping with fixed dopant concentration in the GaAsP base (5×10^{18} cm^{-3}). The maximum efficiency of 16.90% is reached with a thicker GaP shell ranging from 25 nm to 31 nm. At the same
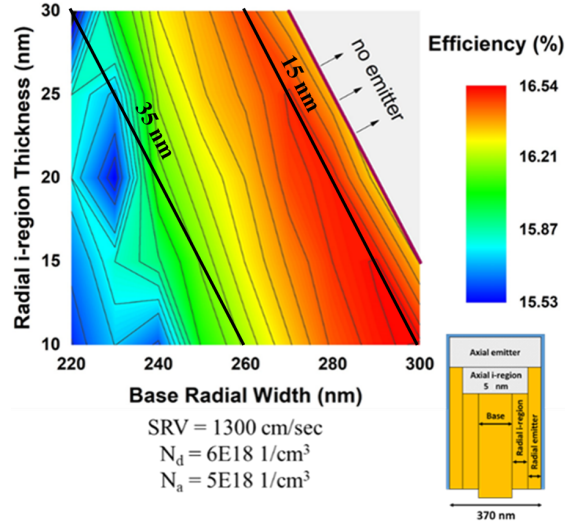
FIGURE 2.20: AM1.5G 1 sun efficiency of the top NW solar cell mapped for varied base width and radial i-region/emitter thicknesses. Grey area corresponds to the not allowed range of dimensions where emitter thickness is zero. Cartoon shows mutually changed components in yellow.

time, doping of the emitter below 6×10^{18} cm^{-3} is preferred. Doping of the base was also increased to 6×10^{18} cm^{-3} to investigate the change in the efficiency as a function of the GaP layer doping. Both results are presented in Figure 2.21b. It can be seen that an increase in the base doping might be beneficial in the range of the GaP shell doping between 2×10^{18} cm^{-3} to 1×10^{19} cm^{-3} indicating that the ratio between the core and shell dopant concentrations defines the efficiency. At the same time, from the growth perspective the interest is in lowest possible doping for both core and shell. For a fixed GaP doping of 1×10^{18} cm^{-3}, base doping was swept from 1×10^{18} to 6×10^{18} cm^{-3}. These data points are outlined on Figure 2.21b. It can be seen that the maximum deviation in efficiency within this range of base dopant concentrations is 0.12% suggesting that lowered doping of the core can be targeted as well in a heterojunction configuration.

Optical simulations of the bottom 0.5 eV NW subcell absorption were done to find the tools enabling the use of thin and sparse NW arrays capable of providing sufficient generation current densities for current matching. Two ternary materials that can be successfully grown via self-assembly on Si could be used for targeting this bandgap
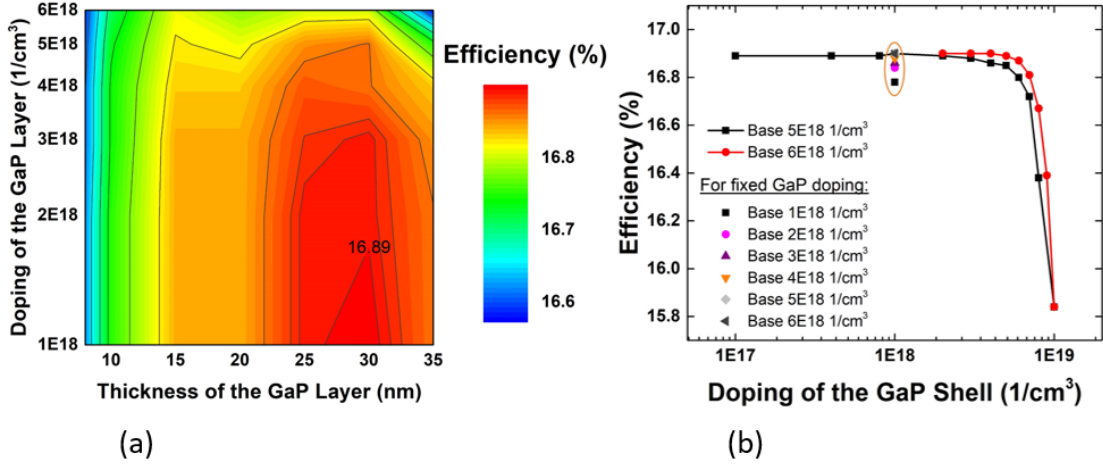
FIGURE 2.21: (a) Efficiency of the GaP/GaAsP NW solar cell dependent on the GaP thickness and doping. GaAsP base doping is fixed at 5×10^{18} cm^{-3}. (b) Efficiency of the GaP/GaAsP NW solar cell as a function of 30 nm-thick GaP layer doping. Plots in black and red symbols correspond to the base doping of 5×10^{18} cm^{-3} and 6×10^{18} cm^{-3}, respectively. An ellipse outlines the data points generated for various base dopant concentrations and GaP doping fixed at 10^{18} cm^{-3}.

(InGaAs and InAsP), however, since InAsP has lower achievable surface recombination velocity it was used for modeling and further experimental implementation [86]. The self-assembly epitaxy mechanism is specifically attractive as it allows to bypass the pre-growth lithography steps for manufacturing the bottom NW cell. The possible fabrication flow following the top cell growth includes protection of the front-side NWs by encapsulating them in the SiO$_x$ to provide necessary rigidity of the front array for the rear-side growth. Any excessive handling and advanced surface preparation including additional exposure to chemicals and requiring lithography preceding the narrow-bandgap NW growth are undesirable. The nuances that need to be taken into account while optimizing the geometry of the bottom NWs are that self-assembly results in the arrays without long-range ordering, such that center-to-center distance becomes a statistical parameter for a given NW, and that this mechanism favors formation of either high-density arrays of thin NWs (50 - 100 nm) or in more sparse arrays of thicker NWs which can be interchangeably tuned by adjusting the growth parameters [87].

To evaluate the optimal diameter and spacing of the InAsP NWs, the simulation-based

study of the generation current density was performed. Since there are top and bottom NW arrays with mismatched periodicity, the simulation domain size would need to be adjusted to comprise multiple NWs for performing explicit modeling. While top NWs exhibit noticeable anti-reflective properties in the IR range compared to the bare Si surface, planarized array IR reflectivity is mostly dominated by the ITO film (Fig. 2.22). Computation time can be reduced by approximating the ARC properties of the top NW arrays with those of planar encapsulation and ITO laterally continuous films and significantly reduce the computational time. Alternatively, for calculating generated current densities solar spectrum data can be modified to account for the ARC effects, however, the thin-film approximation allows to simulated the full structure with all interfacial phenomena included. Approximating the top array with only its planar encapsulation, the bottom cell generation current map was created in the range of NW diameters from 300 nm to 700 nm and spacing from 450 nm to 1400 nm (Fig. 2.23). The yellow rectangle frames the approximate range of the dimensions of the NWs achievable via self-assembly suggesting that such arrays would not be applicable for the current-matched 3J cell applications.

Despite the volumetric density of the InAsP NWs being the same, the use of thinner NWs was found to be associated with dramatic reduction in the IR absorption being illuminated through the 200 μm-thick Si slab showing the inapplicability of the effective medium approximation [88]. The reasons for such low generation current densities are poor IR absorption past 1500 nm in thinner NWs that was found to be due to reflection at the interface between Si substrate and the bottom of the NWs as well as transverse electric field screening caused by the refractive index contrast between the NWs and surrounding dielectric (vacuum was used in a preliminary study). Based on this, the light management strategies that would enable use of sparsely distributed several-hundred
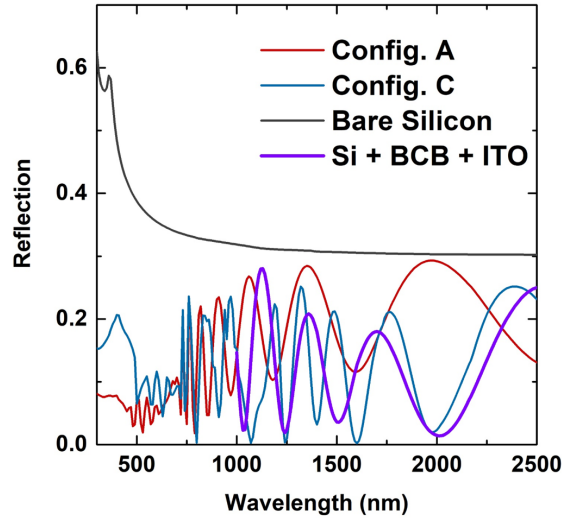
FIGURE 2.22: Reflectivity spectra of the bare Si (black line) and Si with non-embedded GaAsP NWs in the arrangements A and C as indicated in Fig. 2.16. Thick purple line shows the reflection from the Si slab with planar 1.5 μm-thick BCB and 300 nm ITO layers on top.

nanometers-thick NWs were proposed. The range of diameters of the bottom NWs that would allow efficient long-wavelength light coupling into the NWs resulting in the near-unity IR absorption starts at ~ 600 nm, where a NW properties become comparable to those of a bulk material and spacing of the NWs starts having direct impact on the absorption [89]. Considering that a more realistic diameter goal would be 300 - 400 nm with a spacing above 1 micron, two phenomena need to be realized: first, light needs to be forced through the arrays, and second, transmitted light can be deflected to pass though the sides of the NWs.

Thus, two main modifications to the rear-side arrays of thin and sparse NWs need to be implemented. To reduce the electric field screening, the NWs can be embedded in the dielectric with high refractive index. There are two readily available candidates, HfO_2 and Si_3N_4, with refractive index of $\sim$2 in the wavelength range of the bottom cell absorption (1.2 - 2.5 μm). The deflection of the light passing through the inter-nanowire regions can be implemented by equipping the rear side of the NWs with shallow dish-like metal mirror (Fig. 2.24). The fabrication process of such structure is demonstrated
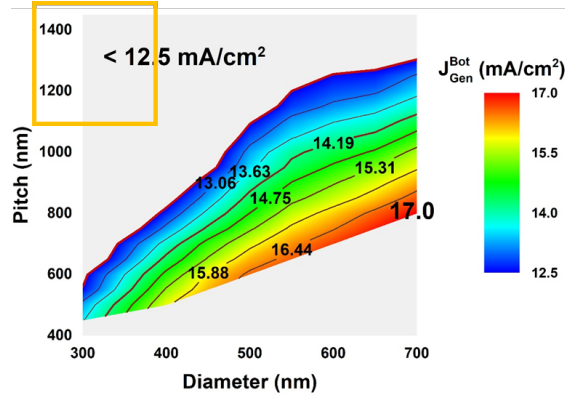
FIGURE 2.23: Generated current density in the bottom $InAs_{0.85}P_{0.15}$ NW array under AM1.5G illumination filtered through the top array encapsulation, 300 nm-thick planar ITO, and middle Si cell plotted in dependency on the diameter and pitch of the NWs. The outlined region corresponds to the range of dimensions achievable with the NW self-assembly on Si.

on Fig. 2.25 and includes deposition of encapsulation material (BCB or high-refractive index dielectrics) and back etching to expose tips of the NWs (back-etching depth here will determine the mirror curvature) followed by conformal deposition of ITO and metal (Au). Besides having a benefit of using the light that otherwise would be normally back-reflected at the rear metal surface and escape from the front side of the solar cell, the long-wavelength light incident onto the side of the NWs will face larger cross-sectional area which will also increase the probability of it being absorbed. The mold used to form and model the curved Au reflector is a thin non-absorbing ITO layer. The curvature radius of the mirror used to demonstrate the principle was 0.75 μm. To increase the simulation efficiency and take advantage of the RCWA algorithm implying continuity within the structures along Z axis, for IR simulations the dish mirror was approximated with the Fresnel lens-like structure (Fig. 2.24b) sufficient for the simulated diffraction efficiency convergence. To simulate the absorption in the arrays enhanced with the curved reflectors the refractive index of the embedding medium was set to 1 (vacuum) and 2 for comparison. The curved mirror NW absorption data was overlayed with the baseline (no rear-side reflector, no embedding) and planar reflector data. The generation current density calculations in the embedded rear NW arrays with reflectors
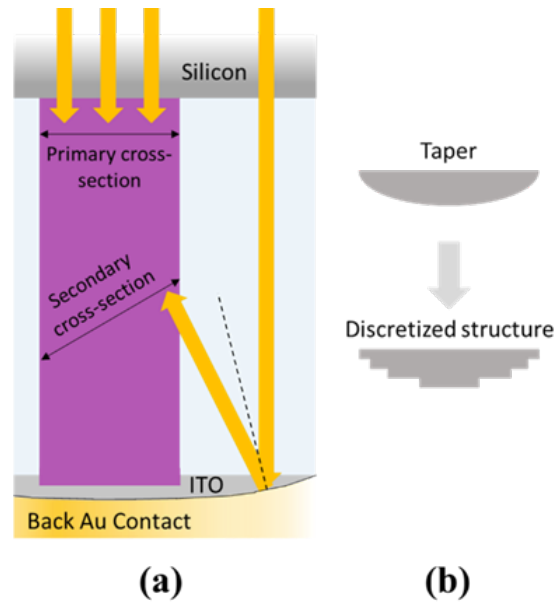
FIGURE 2.24: (a) Schematics of the light deflection system with the NW cross-sectional area depicted for the primary incident light and for the second-pass deflected waves; (b) discretized representation of the continuous smooth curved mirror with Fresnel-lens-like structure.

were performed the same way as in the vacuum-suspended (extinction coefficients of the embedding media were set to 0).

Fig. 2.27 shows the generation current densities extracted from the rear NWs with 300 nm and 400 nm diameters for the spacing swept from 400 nm to 1500 nm and from 500 nm to 1700 nm, respectively. The baseline data (no embedding, no reflector) is shown with blue line, the data corresponding to the NW suspended in the low-refractive index media and n = 2 material with planar BSR are shown in yellow and red, respectively. The black lines correspond to the combination of the n = 2 embedding and concave BSR. The specifics of the simulation domain setting that regulates both the pitch and geometry of the BSR with preserved curvature radius explains that at low pitch values the discrepancy between the absorption in the arrays with planar BSR and curved BSR is very small and noticeable changes can be visible when the arrays become more sparse. For both diameters, rapid drop of the current is observed as spacing between non-embedded NWs increases. An increase in the generated current is clear when refractive
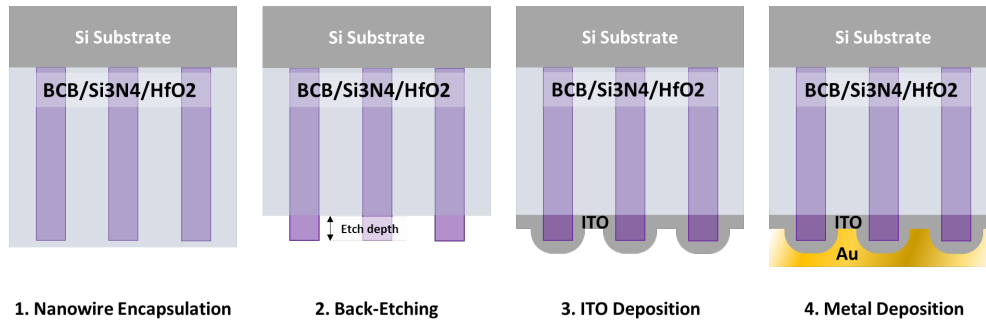
FIGURE 2.25: Concave mirror fabrication flow. Encapsulation, back-etching to expose NW tips with desired depth, conformal ITO deposition, and conformal metal deposition.

index of the surrounding medium becomes 2 and while in the case of 400 nm-thick NWs the change arising only due to the embedding medium modification is $\sim$1.2 mA/cm^2 in dense arrays, in thinner NW arrays the increase in absorption and consequently the current is up to 2.5 mA/cm^2. The most benefit, however, can be achieved from combination of the high-refractive-index encapsulation and deflecting concave mirror, allowing to recover 4 mA/cm^2 of generated current density and maintain the current almost independent on the pitch of the arrays making it possible to utilize relatively thin NWs for the rear-side subcell in the 3J device. These results are generated for a single configuration of the rear mirror to prove the conceptual validity of such design for enhancing the absorption in the sparse NW arrays, however, there is a room for more optimizations of the mirror parameters. The experimental feasibility of similar structure was shown for the front-side ITO coatings conformally following the shape of the embedded NW arrays [90] SEM image and diagram illustrating the conformal ITO coatings deposited onto the encapsulated NW arrays are shown on Fig. 2.26a and b, respectively.

The desired geometry can be achieved by back etching the embedding medium to expose the tips of the NWs and deposition of ITO to create curved mold for the following Au coating as shown on Fig. 2.25. Considering the disordered nature of the self-assembled
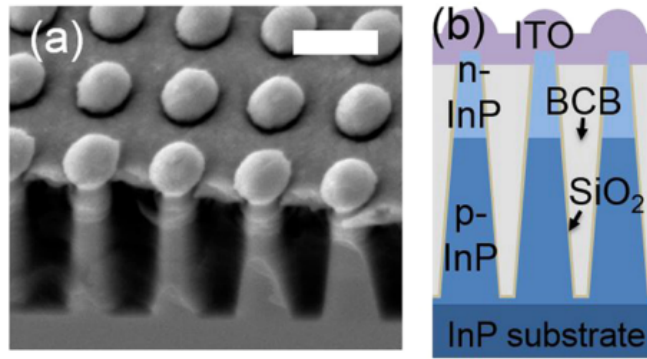
FIGURE 2.26: (a) SEM image of the encapsulated NWs with scattering ITO structures with the shape defined by the depth of encapsulation back etching which is schematically shown on (b). [90]
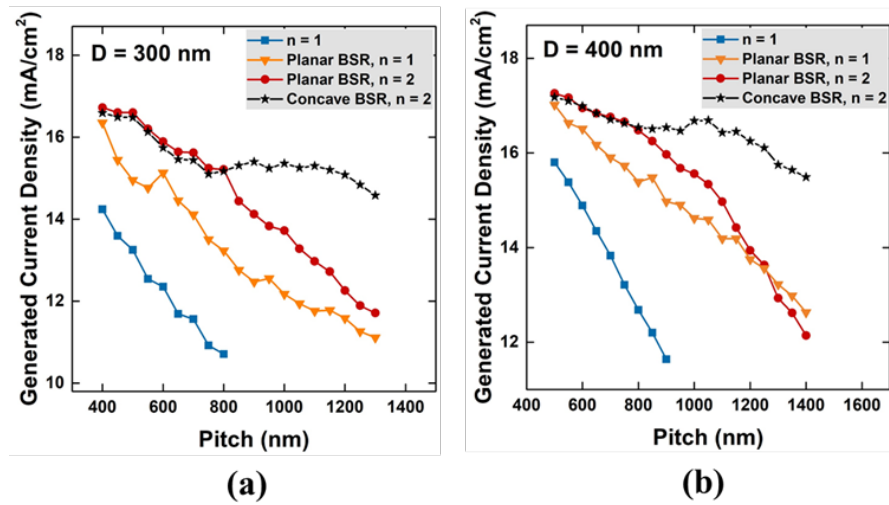
FIGURE 2.27: Generation current densities plotted for varied pitch of the NW arrays, non-embedded without and with planar BSR, embedded in the medium with refractive index of 2 with planar and concave BSR; diameters of the simulated NWs are (a) 300 nm and (b) 400 nm.

arrays, the wide range of the rear reflector geometries can be obtained by employing this method so one of the further steps can be a study of the disordered arrays behavior by creating a simulation unit cell consisting of several NWs with chaotic placement to compare the absorption and performance of the curved mirrors with the perfectly periodic system.

2.2.3.4 Some Notes on the Middle Silicon Sub-Cell Design

The middle Si cell design proposed for this 3J device is inherited from the standard commercial c-Si single-junction bulk solar cell. The n-on-p Si cell with 180 nm-deep arsenic-implanted and annealed junction, however, will be subjected to the high-temperature growth of the top cell NWs (900°C for 45 - 60 min), while rear-side NWs are grown at ∼550 ° and have negligible impact on the As redistribution. The diffusion of the As species under the top-cell growth conditions and evolution of the junction depth was simulated using Athena^{TM} (Silvaco) to ensure the predictability of the middle cell junction parameters after the NW cells manufacturing. Figure 2.28 shows the changes in the doping profile in the Si middle cell exposed to the NW growth conditions. Fig. 2.28a and b illustrate the initial as-implanted and annealed junction respectively and Fig. 2.28c corresponds to the post-NW growth state of the middle cell n-p junction. The difference between the junction depths shown on Fig. 2.28c and b is only 20 nm resulting in the final emitter thickness of 200 nm with doping level of which suggests that no special preliminary dose and annealing modifications would be required for the middle cell prior to the NW growths. The resulting average emitter doping of $1.5 \times 10^{20} 1/\text{cm}^3$ is reduced to $1.3 \times 10^{20} 1/\text{cm}^3$. Thus, the final parameters of the middle cell used as an epitaxial substrate for the NW growth are not notably changed.

2.2.4 Wavelength-Selective Infrared Nanowire-Based Detectors on Si Diffraction Gratings

The complications associated with achieving broad-band absorption in the rear-side thin InAsP NWs inspired an idea of the wavelength-selective NW absorbers with selectivity in the sensing wavelength achieved by growing the NWs on Si diffraction grating filters.
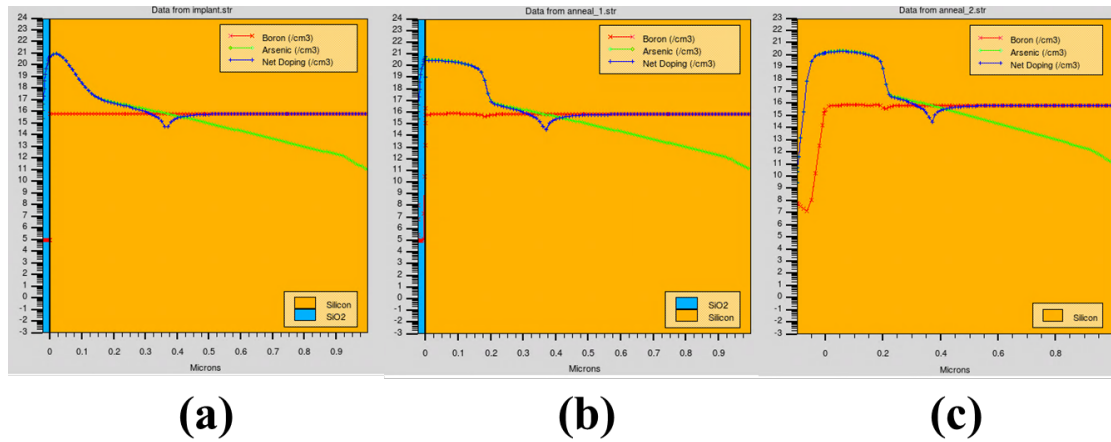
FIGURE 2.28: (a) As-implanted arsenic doping profile in the boron-doped p-type Si; (b) the junction profile after the junction annealing in nitrogen atmosphere at 1000°C for 10 min; (c) the middle cell junction profile after exposure to the conditions of the top NWs growth (900°C for 1 hour).

While selectivity can be achieved by tuning the geometries of the NWs themselves, for IR operation, as was shown before, the diameters of the NWs should be sufficiently large, comparable to the target wavelengths [63, 67, 61]. One of the issues arising with thin-NW IR absorption is the reflection at the interface between the rear-side of the planar Si filter and the NW array base[89]. Since fabrication of the thin-film antireflection coatings at such interfaces is not feasible, the problem can be solved by implementing diffraction gratings on the front and back faces of the Si wafer that in turn will serve as a growth substrate for the absorbing NWs. However, for simplicity, the spectral selectivity in the NW absorption was demonstrated for the Si filters with the rear-side gratings only (Fig. 2.29a). Formation of the gratings with varied lateral and axial dimensions can be implemented by combining photolithography technique and dry etch of the voids as shown on Fig. 2.29b. It was shown before that texturing Si solar cell surfaces can assist in increasing the light trapping [91] implying that the reduction in rear-side reflection by cancelling the phase-shifted waves can allow to force the light out of the Si slab that can be tuned by the depth and width of the gratings. In turn, equipping the structure with the front-side grating can further refine the passing spectrum. In addition, the top
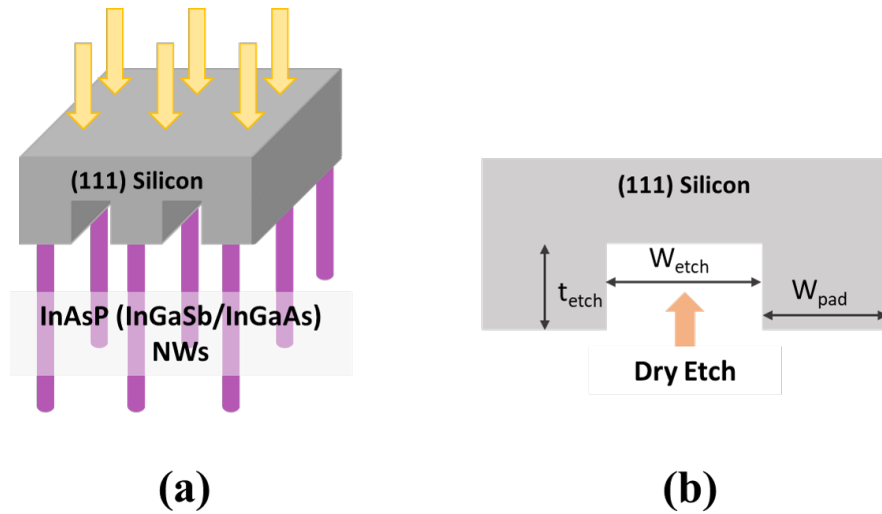
FIGURE 2.29: (a) Simulated structure schematics: planar Si substrate with diffraction grating on the rear side with the InAsP NWs grown directly on the pads of the grating; (b) parameters of the grating varied in the model to achieve the desired wavelength bandwidths.

surface of the substrate can be enhanced with an anti-reflective coating designed for IR transmission.

The first step of the proposed study was to model the structure and demonstrate the selectivity in the NW absorption wavelength in dependency on the gratings geometry. Two-dimensional RCWA simulations were performed in DiffractMOD RSoft. InAsP NWs with the bandgap of 0.5 eV and diameters of 400 nm and length of 2.5 μm were placed onto the exposed Si facets (diffraction grating pads) such that a single NW was on each pad while the voids between the pads were filled with SiO_2 which in the actual structure will serve as a protection from the parasitic growth of the III-V material on the scalloped sidewalls of the grating pads. The front side of Si wafer is coated with 300 nm of ITO for reduced reflectivity. The thickness of the grating (t_{etch} on Fig. 2.29b) was varied from 0 nm (representing flat Si back surface without texturing) to 1500 nm. At the same time, the lateral widths of the diffraction grating pads and spacing between the neighboring pads were set to 1000 nm, 1500 nm, and 2000 nm. The results of these three modeling experiments are shown on Fig. 2.30. Absorption in the NWs was calculated by
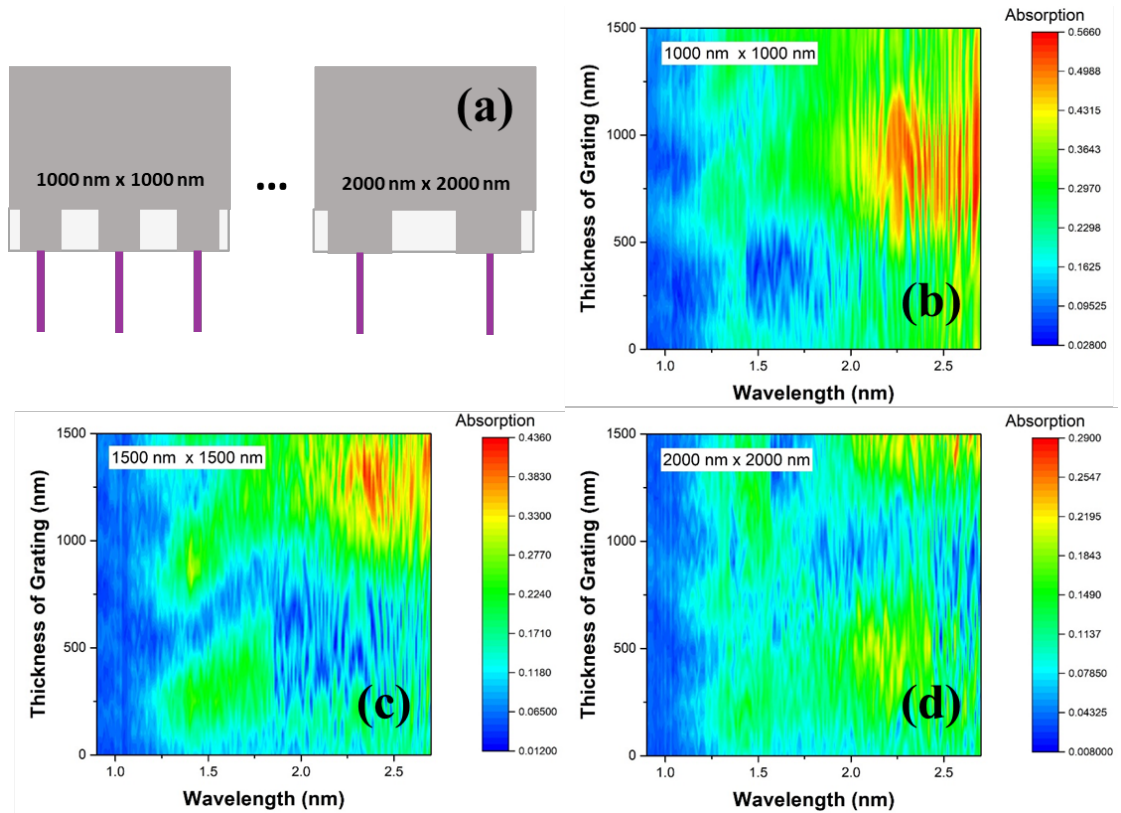
FIGURE 2.30: (a) Scheme of the grating width variations with the NWs; (b-d) absorption in the NWs mapped for each wavelength and varied thicknesses of the gratings with grating pad widths and spacing of 1000 nm (b), 1500 nm (c), 2000 nm (d).

subtracting the absorption in the ITO and Si from the total absorption in the simulation domain comprising all components of the structure as described in the previous section.

The absolute values of absorption (unitless, absorption here represents a fraction of absorbed power ranging from 0 to 1) get reduced as period of the diffraction grating increases, since the density of the absorbing medium reduces. This, however, can be addressed by increasing the number of the NWs per pad. At the same time, for each configuration there are modes of higher absorption around 2.4 μm that are achieved by varying the thickness of the diffraction gratings along with the width. The wavelengths at which absorption is maximized lay near the NW band edge. An increase in the lateral period of the gratings implies an increase in the grating depth. However, for the largest period of the grating (2 μm), the emergence of two modes of high absorption

can be seen corresponding to the grating thicknesses of 500 nm and beyond 1500 nm. It can be seen that the primary strong absorption mode experiences red shift with increase in the grating lateral period. Refining the step size and moving to the grating feature widths, modifying the grating pad width relatively to the spacing can result in an assortment of the available wavelengths. To enhance the absorption that does not exceed 0.57 achievable at the maximum density of the NWs in case of the 1000 nm × 1000 nm grating, the transmission can be mitigated by adding the reflective metal on the rear side of the NWs which in turn can lead to new optical phenomena in this structure. At the same time, the number of the NWs per pad can be increased as well to maintain consistent material density. Enhancing the filter with the front-side grating can also assist in increasing the response. The further optimization can be done by using embedding media. In addition, the NW material can be changed to the antimony-containing alloys for broadening the sensing region.

2.2.5 Design of Future Work and Ideas

The objectives of the proposed work are to provide the guidelines for the 3J NW-on-Si two-terminal monolithic solar cell parameters via optical and electrical modeling using RSoft and Sentaurus software from Synopsys. Using these modeling tools, design of the wavelength-selective NW-based IR detector is to be developed, followed by the device fabrication and testing.

The default proposed design of the middle Si cell is a standard crystalline Si cell with n-on-p polarity, total thickness of 200 μm and implanted emitter with $\sim$180 nm [92]. Reference base doping is 7×10^{15} cm^{-3}, while emitter doping is 1.5×10^{20} cm^{-3}. These parameters, however, can vary if Si cell is a part of the 3J device. To find proper doping and thicknesses, the additional device modeling will be performed.

While compete opto-electronic modeling study of the top NW array has been accomplished, the similar study of the rear-side narrow-bandgap NW subcell has not been done yet and using modified approach to the co-simulations can be further done. Important parameter to take into account, considering tremendous impact of the surface recombination velocity and diode polarity of the bottom subcell, are the junction design that needs to include the effective passivation. In addition, the use of heterojunction as was demonstrated to be beneficial for the top cell operation can be applied to the bottom cell. The following steps will include an investigation of the available material systems that would allow to alleviate the dramatic impact of surface recombination.

III-V-Nanowire-on-Si is an attractive system due to the use of Si as both substrate and operational subcell of the multijunction device. At the same time, there are apparent complications with monolithic integration of the NWs and Si with the main problem being design and growth of tunnel diode that would result in minimal resistive losses at the subcells' electrical connections [59]. Degenerate doping of the tunnel diode components required for reliable operation is challenging given relatively high NW growth temperatures due to the diffusion of the dopant species [93]. One of the solutions that can not only eliminate the necessity of epitaxial tunnel junctions, but also broaden the scope of the tunable parameters is to use stackable NW arrays grown on Si substrates, but fabricated by peel-off and metallized separately. A peel-off technique steps are illustrated on Fig. 2.31 [94]. The as-grown NW arrays on substrate are shown on Fig. 2.31a. The substrate with NWs is then covered with polydimethylsiloxane (PDMS) dispersion which is then cured in vacuum to remove the solvent. Alternatively, the polymer can be spin-coated and thermally cured. Cured PDMS film with encapsulated NW is then mechanically stripped off of the substrate breaking the bases of the NW (Fig. 2.31b). Figures 2.31c - e illustrate the final product, i. e. NWs encapsulated in the polymer
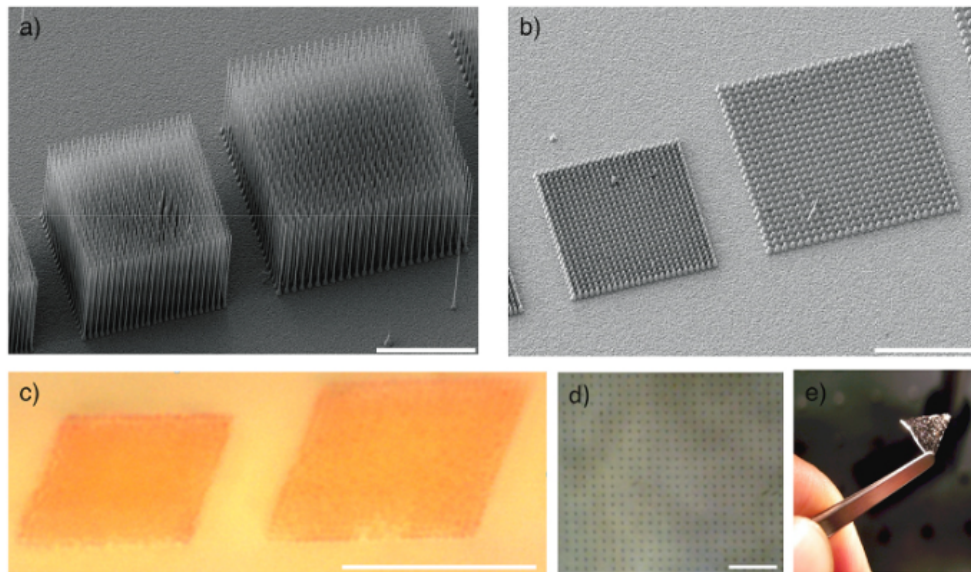
FIGURE 2.31: Scanning electron micrographs of (a) GaP NW arrays on the substrate; (b) Remaining NW nucleation sites on the substrate after the NW transfer into PDMS. (c, d) Optical microscopy images after transfer of the NW embedded in PDMS, and (e) photograph of the PDMS film with the NWs [94].

membrane. Such approach can be quite beneficial for the device manufacturing allowing free-standing flexible NW arrays.

The sensitivity bandwidths of such arrays can be tuned not only by choosing the alloys band gaps, but also by varying the geometrical parameters. The example of such structure is shown on Fig. 2.32. The fabrication of the stacked multiterminal multijunction cell would include deposition of transparent conductive oxides on the front and rear sides to enable transmission of light through the top arrays to let the light in the underlying subcells [95, 96, 97]. Not only independent geometrical parameters (diameter, length of the NWs and spacing between them) can be tuned, but also the relative placement of the NW stacks as underlying NWs can be located either underneath the top NWs or in the voids between them. It can lead to the multijunction device that achieves current matching at the higher values than planar tandem cells. Optical modeling establishing the multidimensional set of the arrays forming the subcells of this stacked multijunction cells will be performed. Additionally, this study can be expanded to cover electrical
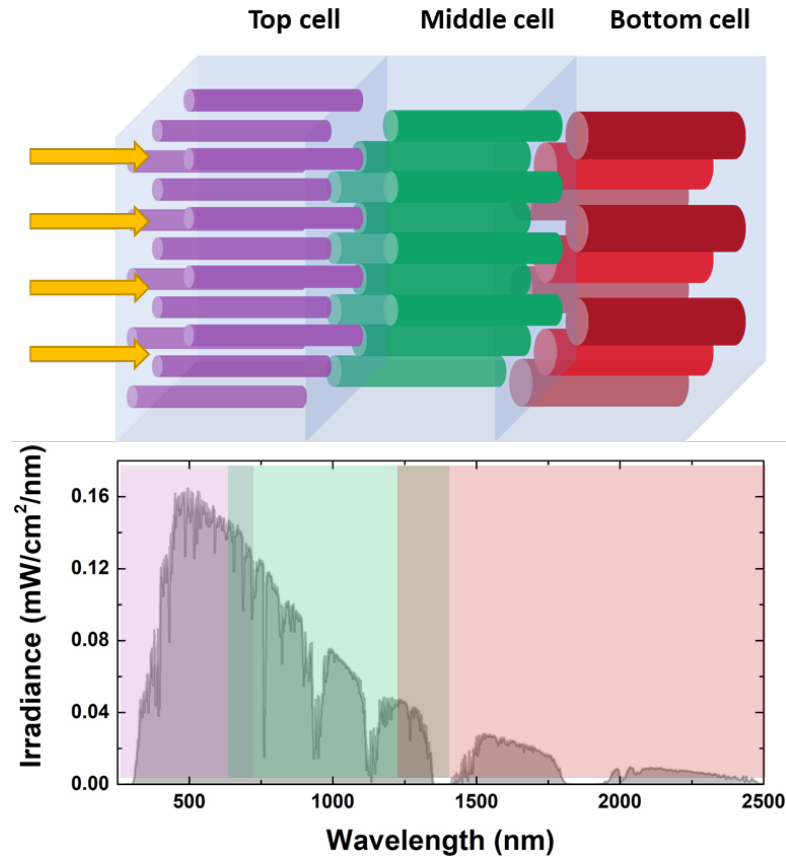
FIGURE 2.32: Concept of the multijunction stacked peel-off NW solar cell with the corresponding solar spectrum regions available for each subcell color-coded.

simulations for junctions optimizations.

An experimental implementation of the wavelength-selective photosensor design based on the $InAs_xP_{(1-x)}$ NWs grown on Si diffraction gratings is proposed as well allowing new dimension in the IR photoresponse tuning in NW absorbers by combining them with Si diffraction filter. The viability of such concept was verified with preliminary modeling, however, the number of parameters that can be modified for achieving the desired bandwidth is high which implies the expansion of the study if simulated results are supported by experimental observation. The subsequent step is realization of the photodetector device requiring a non-trivial metallization process. The complication comes in isolating optical Si filter from the active NW part of the structure. One of the routes enabling the independent metallization of the NW arrays can be a combination of

direct growth, embedding in PDMS, peel-off [98, 99], deposition of contacts, and bonding to the rear side of the Si filter. Alternatively, such photodetector can be fabricated in the bottom-bottom configuration featuring cathode and anode on the back of the arrays. An experimental implementation of this work would initially include a proof of concept by demonstrating the differences in absorption spectra of Si with the InAsP NWs on the rear side directly grown the plain surface and on the variety of the gratings fabricated in one lithography step and crystallographic etch to form the grating features. In addition to the 2D gratings, the lithography mask should comprise patterns for symmetrical 3D gratings insensitive to the light polarization or anisotropic patterns. As optical properties of the NW-on-grating are confirmed and absorption selectivity is established for each subset of gratings, fabrication of the device (adding a junction and metallization) can be performed.

Chapter 3

High-Efficiency Quantum Well Solar Cells

3.1 Summary

An extensive amount of work was performed to, first, develop extended high-quality QW superlattices with two types of strain balancing. The observations and analysis of the QW structure and morphology influence on the solar cells dark current and open-circuit voltage was documented and used, in combination with spectroscopy analysis and reciprocity, to derive the fundamental limitations imposed on the QW solar cells' performance and empirically-supported design guidelines were established. QW solar cells with distributed Bragg reflectors were fabricated and tested as well showing over 95% rear side reflectivity and nearly doubled light conversion efficiency in the QW region.
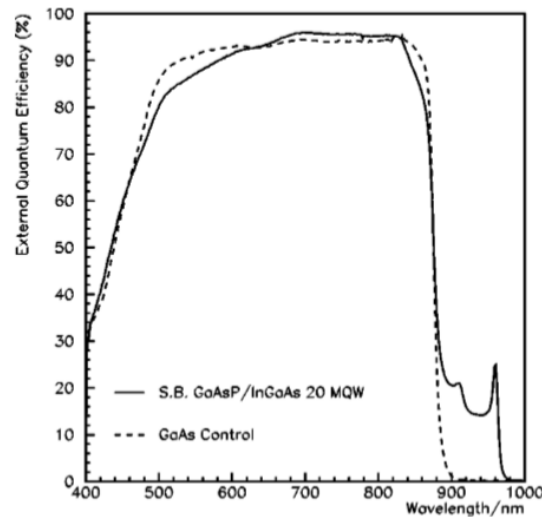
FIGURE 3.1: EQE spectra of the GaAs solar cell with no QWs (dashed line) and of the GaAs solar cell with 20 periods of InGaAs QWs with GaAsP strain balancing [101].

3.2 Motivation and Background

An incorporation of the narrow-bandgap quantum structures is a way to extend the absorption range in the solar cells below the band edge [41, 100, 45, 46]. Adding QWs in the intrinsic region, on the one hand, enables absorption of the sub-band edge photons and at the same time allows for efficient carrier extraction [101, 102]. Figure 3.1 shows EQE spectra of the GaAs solar cell with InGaAs/GaAsP QWs (solid line) in comparison with the baseline device (no QWs) where noticeable extension of the carrier collection wavelength range was achieved by adding the QWs [101]. The main challenges arising from incorporating the QW structures into the solar cells, however, are associated with the potential increase in, primarily, non-radiative and radiative recombination which can lead to reduced overall device efficiency despite the boost in J_{sc} due to lowered carrier lifetimes and/or impeded carrier transport causing the V_{oc} and fill factor of the cell to get reduced.

There are several major parameters that can be tuned to enable efficient InGaAs QW light conversion with minimal losses in V_{oc} (limited to possible fundamental restraints

that will be discussed in the subsequent section):

- Depth of QW by varying In content allowing to red-shift the QW absorption edge [103]

- QW region volume that can be extended to reduce long-wavelength photons transmission loss [104, 105]

- Depletion region and strain balancing design boosting escape and collection of carriers optically generated in the QWs [106, 107, 108]

- Accurate strain balancing for preventing local and extended strain-related defects formation [109]

At the same time, deepening the QWs is associated with higher lattice mismatch between the QW and the host material which requires strain balancing to be designed to account for the extra strain energy. For the $In_xGa_{(1-x)}As$ QW system incorporated into the GaAs device, compressive strain in the QWs resulting from the mismatch can cause relaxation with formation of misfit dislocations in the subsequent layers. To offset the compressive strain energy building up in the $In_xGa_{(1-x)}As$ QWs, thin interlayers with the opposite type of strain can be grown between the wells. Figure 3.2 shows the sequence of the tensile-strained GaAsP and compressively strained $In_xGa_{(1-x)}As$ on GaAs resulting (ideally) in a net zero strain [102]. The strain-balancing layer thickness (t_b) for the specific lattice constant of the $In_xGa_{(1-x)}As$ QW material, a_{QW}, and QW thickness, t_{QW} can be calculated for various compositions of strain balancing $GaAs_yP_{(1-y)}$ using Eq. 3.1, where a_b is a lattice parameter of the strain balancing layer [101]. The strain balancing approach has been previously successfully implemented in high-efficiency single- and multijunction solar cells allowing to increase the number of QW superlattice periods up to 80 [110, 111, 112, 15].
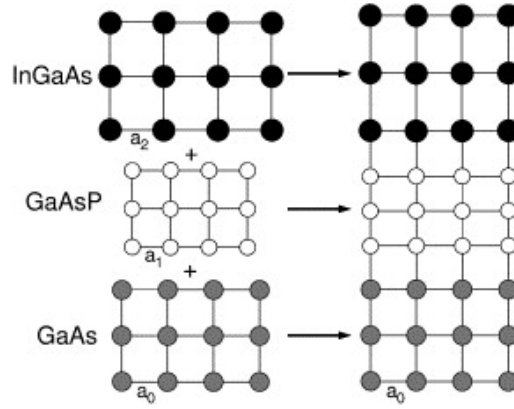
FIGURE 3.2: Strain balancing in the InGaAs/GaAsP QW superlattice [102].

$$a_b = \frac{t_b a_b + t_{QW} a_{QW}}{t_b + t_{QW}} \tag{3.1}$$

Equation 3.1 is derived from the energy (tension and compression) balance equation. For grown on GaAs, compressively strained $In_xGa_{(1-x)}As$ QW with fixed thickness, tensile $GaAs_yP_{(1-y)}$ strain balancing layer can be designed as thin, tunneling barriers with high lattice mismatch of a_b relatively to the host GaAs material or, alternatively, thicker strain balancing can be employed using $GaAs_yP_{(1-y)}$ with low lattice constant offset corresponding to phosphorous-poor material as shown on Fig. 3.3 [113]. In an ideal material system *not* affected by spontaneous local relaxation or thickness modulations due to the substrate offcut and growth conditions [114, 115, 116, 117], for each $In_xGa_{(1-x)}As$ composition the choice of strain balancing type enabling efficient carrier escape via predominantly tunneling or thermal escape is an optimization problem that can be solved specifically for every x and electric field that can be established across the depletion region containing N periods of QWs. The later depends not only on the emitter doping, width of the intrinsic region, mainly determined by the QW region width, but also on the background doping and is a function of the growth temperature and can be modified by compensation doping, especially when low-temperature QW growth is
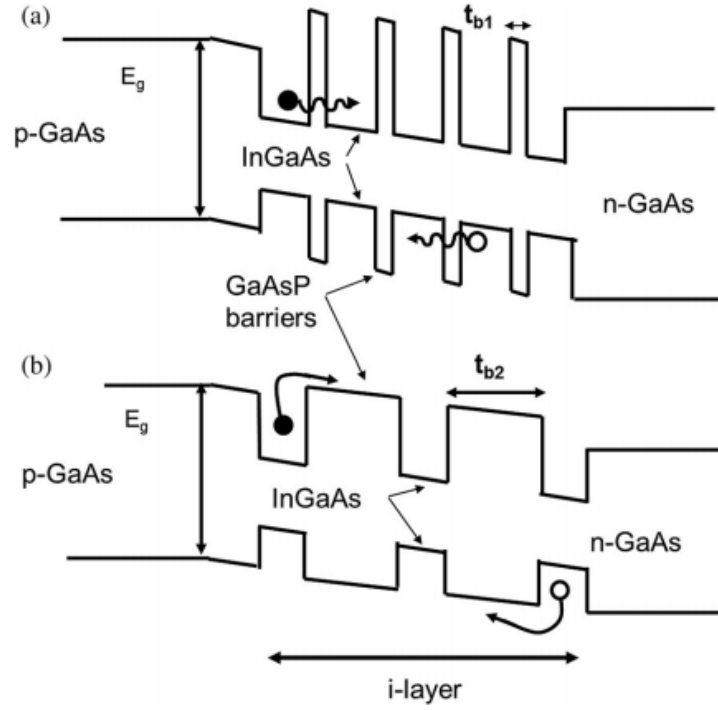
FIGURE 3.3: (a) QW superlattice with high-phosphorous thin strain balancing tunneling barriers and (b) with low-phosphorous strain balancing promoting carrier escape via thermalization [113].

implemented [112, 118].

Thermal escape rate, R_{th}, or in terms of lifetime $1/\tau_{th}$ is calculated as:

$$R_{th} = \frac{1}{\tau_{th}} = \frac{1}{L_{QW}}\sqrt{\frac{kT}{2m_{QW}\pi}}exp\Big(-\frac{E_b}{kT}\Big),\qquad(3.2)$$

where electron or hole barrier height is E_b, QW width is L_{QW}, m_{QW} is effective mass of electrons or holes in the QW, and T is temperature [119]. The cumulative escape rate can be calculated for each type of carriers and energy state resolved in the QWs (E_{b1}, E_{b2}, E_{b3}, etc.) determined by the QW confinement, depth, width, and coupling.

Tunneling escape rate, R_{tun}, or $1/\tau_{tun}$ can be expressed as:

$$R_{tun} = \frac{1}{\tau_{tun}} = \frac{1}{L_{QW}^2} \frac{n\pi\hbar}{2m_{QW}} exp\left(-\frac{2}{\hbar}\int_0^b \sqrt{-2m_b(E_b - qFz)}dz\right), \qquad (3.3)$$

dependent on the electric field strength, F, barrier height, E_b, and barrier width, b, carrier effective masses in the strain balancing material, m_b [120]. It is noteworthy to mention that carrier escape from the QWs can and in most cases is via both thermal and tunneling mechanisms at room temperature (Fig. 3.4). Quantum structures' energy states, in particular, can be designed to support resonant tunneling under specific electric field (or bias) applied [121, 122]. Even though this mechanism does not necessarily apply to the shallow QW systems (convention for defining shallow InGaAs QWs as QWs with $< 12\%$In [123]) reported in this work, resonant tunneling principle is a nice illustration of the hybrid controllable carrier transport across the QW region before collection. Under established non-zero electric field, carriers can tunnel between the individual QWs from deeper energy levels to available shallow states in the adjacent QW where they will have sufficient thermal energy to thermalize out and get collected. The choice of the barrier type is in a sense a self-optimized problem, since thin, tunneling barriers allow to embed extended superlattices while maintaining an electric field enabling tunneling carrier escape, and thick thermalization barriers increasing the superlattice period and causing the potential across the QW region to drop allow carriers to thermalize regardless of the field magnitude (it is essential that F is non-zero though).

Internal quantum efficiency and consequently extra current provided by the QW superlattice of N QWs incorporated in the solar cell can be assessed in terms of cumulative escape (R_{escape}) and recombination (R_{recomb}) rates signifying the probability of the generated carrier collection before it recombines, either radiatively or non-radiatively [113]:
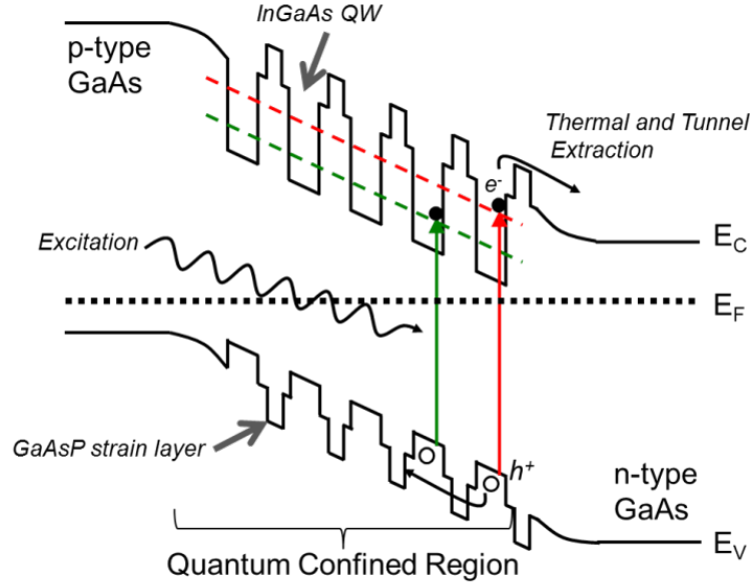
FIGURE 3.4: Carrier generation, recombination, and escape in the InGaAs/GaAsP QWs in the intrinsic region of a GaAs solar cell.

$$IQE_{QWSL} = \left(\frac{R_{escape}}{R_{escape} + R_{recomb}} \right)^{N}. \tag{3.4}$$

From Eq. 3.4, quantum efficiency in the QW region can be limited by the recombination rate, since $R_{recomb} = R_{rad} + R_{non-rad}$ and deterioration of the crystalline quality in the QW region either through introduction of parasitic interfacial layers between the QW and strain balancing layers or because of formation of stacking fault defects caused by aggravation of localized strain in the QWs grown on offcut substrates, carrier loss via non-radiative recombination in the superlattice can occur. However, since under short-circuit conditions electric field F across the depletion region is the strongest, efficient carrier collection (Eq. 3.3,3.2), especially in shallow QWs, is highly likely compared to the recombination events, so J_{sc} of the solar cell could be less impacted by the quality and morphological properties of the QWs and relies mainly on the position of the confined energy states relatively to the barrier height. It can be concluded that QW solar cell's J_{sc} is mostly determined by carrier generation and escape.
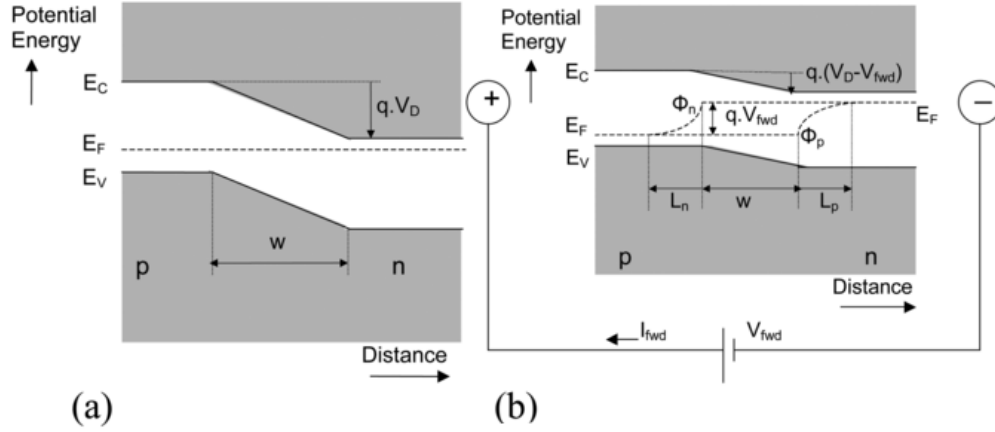
FIGURE 3.5: (a) Equilibrium p-n junction band diagram; (b) p-n junction under applied forward bias causing the electron and hole Fermi levels to split.

To truly gain from the current enhancement V_{oc} and fill factor have to be minimally affected by the incorporation of the QWs and must be comparable to the bulk values ($Eff = \frac{J_{sc}V_{oc}FF}{P_{inc}}$). Quantum wells are placed in the depletion region and can significantly contribute to the non-radiative dark current J_2 if they become a source of high-density defects and trap centers. Even on a fundamental, idealistic level, inserting a narrow-bandgap $E_{g,QW}$ material instead of the same volume of intrinsic GaAs already should reduce the magnitude of the quasi-Fermi level splitting V_F (Eq. 3.5) under non-equilibrium conditions dependent on the intrinsic and non-equilibrium carrier densities (Fig. 3.5a, b). Without considering any quantum effects, the intrinsic concentration exponentially dependent on the bandgap (in a bulk material, $n_i = \sqrt{N_c N_v} exp\left(-E_g/2kT\right)$), increasing, will lower the V_F and maximum achievable V_{oc} (radiative limit of open-circuit voltage).

$$V_F = \frac{kT}{q} ln \left(\frac{np}{n_i^2} \right). \tag{3.5}$$

An expression for the non-radiative saturation dark current in a solar cell with QWs

with the effective offset of the bandgap relatively to the host material ΔE_g occupying fraction f_{QW} of the intrinsic region of a solar cell can be written as [124]:

$$J_{02,QW} = qWR_{NR,B}n_{i,B}\left(1 + f_{QW}\left[\gamma_{NR}exp\left(\frac{\Delta E_g}{2kT} - 1\right)\right]\right), \quad (3.6)$$

where $\gamma_{NR} = \frac{\tau_B}{\tau_{QW}}$ is a non-radiative lifetime ratio in host and QW materials, $R_{NR,B}$ is an average recombination rate in the host material, $n_{i,B}$ is host material intrinsic carrier density, q is elementary charge, and density of states across the space charge region is assumed to be preserved [124, 125]. Thus, non-radiative saturation current density in the solar cell with QWs can be compared to a baseline device, i.e. device with no QWs and equivalent volume of intrinsic host material sandwiched between base and emitter and their ratio can be expressed as:

$$\frac{J_{02,QW}}{J_{02,B}} = 1 + f_{QW}\left[\frac{\tau_B}{\tau_{QW}}exp\left(\frac{\Delta E_g}{2kT} - 1\right)\right]. \quad (3.7)$$

Using this metrics, careful dark current analysis can allow to extract the carrier non-radiative lifetime reduction in the QW compared to the bulk and correlate the measured V_{oc} with not only effective bandgap reduction, but with the material quality in the QW region. The supplementary measurement and analysis that allows to extract the concentrations and activation energies of the traps is temperature-dependent photoluminescence which will be described in detail in the subsequent chapters.

From the theoretical basis outlined above, the concept behind the voltage suppression in the QW solar cells even if QW structures are pristine and do not contribute to the concentration of non-radiative centers lays in the effective bandgap reduction inside the i-region where quantum structures are placed. On the one hand, the dark current

model given by Eq. 3.7 operates with the bandgap offset as it is defined in a bulk material convention, however, if we consider a system of strain-balanced QWs where low-bandgap material alternates with the high-bandgap materials what will represent ΔE_g? In particular, what energy state in a QW with multiple discretized levels is responsible for the quasi-Fermi level splitting (QFLS)?

To investigate the inherent QFLS offset in the QW region, an electroluminescence (EL) and EQE reciprocity relation formulated by U. Rau [126] can be used. Conceptually, the reciprocity theorem is a representation of the detailed balance model [127] correlating the energy absorbed and emitted by the solar cell with electric work that the system can perform through the energy conservation principle and can be written as:

$$\phi_{EL}(\lambda_\xi, J_{inj}) = EQE(\lambda_\xi)\phi_{BB}(\lambda_\xi)\left[exp\left(\frac{qV_{0F}(J_{inj})}{kT}\right) - 1\right], \qquad (3.8)$$

where $\phi_{EL}(\lambda_\xi, J_{inj})$ and $\phi_{BB}(\lambda_\xi)$ are EL and black body radiation fluxes (at solar cell operational temperature T), $EQE(\lambda_\xi)$ is external quantum efficiency at each λ, and qV_{0F} is a quasi-Fermi potential corresponding to the injected current density J_{inj} at which EL spectrum was collected. In a solar cell with quantum-confined structures the reciprocity relation might not hold in the quantum region indicating the suppression of the emission resulting from the radiative recombination in the QW region under applied forward bias which can be explained, dependent on the properties of specific QW system, by carrier thermalization, non-isotropic emission from the QWs, or by strain-induced emission polarization selection rules [128, 129, 123, 130]. Thus, to match reciprocated and measured EL spectra in the QWs, a correction factor of ΔV_F indicating the reduction in QFLS (in radiative limit) in the QW region needs to be introduced to Eq. 3.8. The corrected reciprocity relation in QW region can be written as:
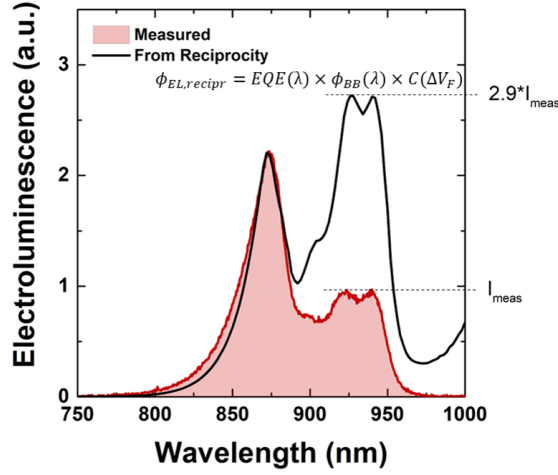
FIGURE 3.6: Measured EL spectrum (red, shaded) of a QW solar cell with suppressed QW radiative recombination and EL calculated from reciprocity relation (black line).

$$\phi_{EL,QW}^{measured} = EQE\phi_{BB} \left[exp\left(\frac{q(V_{0F} - \Delta V_F)}{kT} \right) - 1 \right]. \tag{3.9}$$

Then, radiative efficiency factor (REF) in the QW region can be expressed as was demonstrated in [131]:

$$REF_{QW} = \frac{I_{EL,QW}^{measured}}{I_{EL,QW}^{reciprocity}}, \tag{3.10}$$

where $I_{EL,QW}^{reciprocity}$ is the intensity of QW EL peak derived from continuous reciprocity relation assuming steady QFLS qV_{0F} across the space charge region (SCR) (Eq. 3.8) and $I_{EL,QW}^{measured}$ is measured EL peak intensity as shown on Fig. 3.6.

For example, in [131], the REF analysis was performed to analyze the influence of the $In_{0.08}Ga_{0.92}As/GaAs$ QW GaAs barrier width (determining the degree of coupling between the QWs) on the radiative emission from the QWs under applied forward bias. It was shown that increased coupling between the QWs results in a suppressed radiative recombination and lower REF (Fig. 3.7). The initial hypotheses for the REF reduction in
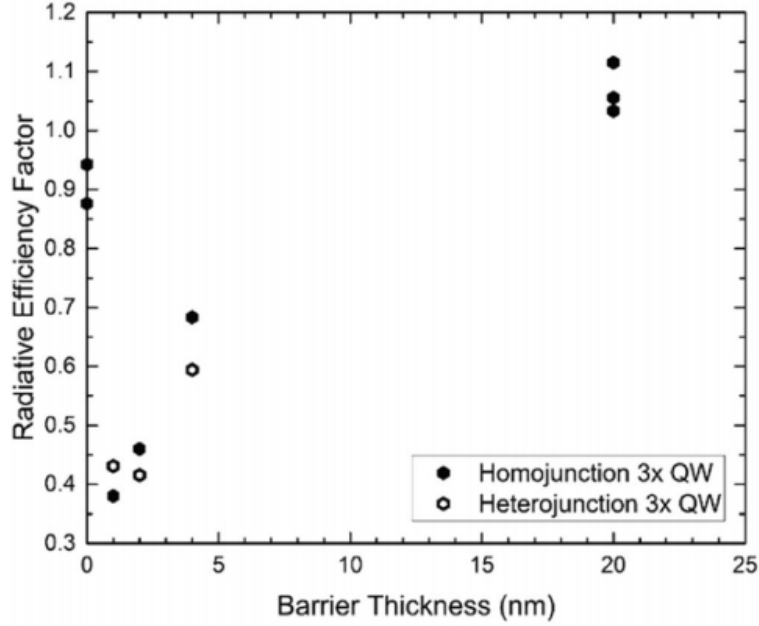
FIGURE 3.7: REF of the InGaAs QWs dependent on the GaAs barrier width. [131]

strongly coupled QWs were enhanced thermal carrier escape and possible contribution of quantum-confined Stark effect, however, in more detail this behavior is further discussed and analyzed in Results and Discussion section below establishing the limiting factors determining the QFLS in the QWs.

Radiative recombination suppression can be diagnosed using EL, PL, and EQE spectroscopy techniques, however, on a device performance level, solar cells are likely to be primarily limited by non-radiative recombination (n_2, J_{02}):

$$J = J_L - J_{01} exp\left(\frac{qV}{n_1 kT} - 1\right) - J_{02} exp\left(\frac{qV}{n_2 kT} - 1\right),$$ (3.11)

or

$$J_{sc} = J_{01} exp\left(\frac{qV_{oc}}{n_1 kT} - 1\right) + J_{02} exp\left(\frac{qV_{oc}}{n_2 kT} - 1\right).$$ (3.12)

Ideality factors n_1 and n_2 are 1 and 2, respectively. In a device where maximum power point is in the n_2 or mixed regime, slight variations in J_{01} due to the radiative recombination suppression in the QW region will not affect the overall device's V_{oc} and efficiency. To observe the *measurable* changes due to the modulated radiative recombination in the QWs, the superlattices and bulk regions must be engineered to minimize the concentration of non-radiative recombination centers, so a special focus has to be placed on material development. Analyzing the existing advancements in QW solar cell technologies, the parametric space for design of experiment was selected to be studied in this work.

To date, one of the most significant advancement in incorporating an extended (60 and 80 periods) QW superlattices ($In_{0.10}Ga_{0.90}As/GaAs_{0.90}P_{0.10}$) into the inverted GaAs solar cell with rear reflector with 60 mV V_{oc} loss and reduction of fill factor from 86% to 83% due to adding 60 QWs compared to the device with no QWs was demonstrated by M. A. Steiner *et al.*, National Renewable Energy Laboratory (NREL) [15]. The current pay-off due to the added QW absorption was 2 mA/cm^2 resulting in total efficiency reduction from 27.81% to 27.18% coming from the baseline to QW device (given that efficiency of the single-junction GaAs QW solar cell is not the most representative figure and the primary goal is to provide extra current in the GaAs sub-cell as a part of a multi-junction solar cell). The result demonstrated in this work by NREL is notable and the details of the device structure deserve closer investigation. In particular, the choice of 17 nm-thick $GaAs_{0.90}P_{0.10}$ strain balancing which was likely enabling for preserving the superlattice quality throughout the QW stack. Previously reported studies performed by the groups from Imperial College London and The University of Tokyo reported on using both, ultra-low phosphorous content strain balancing, as well as over 30%P $GaAs_yP_{(1-y)}$ barriers for the solar cells with InGaAs QWs. For example, in a study by Imperial College

London analyzing radiative properties of $In_{0.15}Ga_{0.85}As/GaAs_{0.91}P_{0.09}$ QW GaAs solar cells with only up to 10 QW periods the V_{oc} is on the order of 0.9 V [132]. In a 2011 study by J. Adams *et al.* 50 strain-balanced $In_{0.10}Ga_{0.90}As/GaAs_{0.93}P_{0.07}$ were added to the p-i-n tandem InGaP/GaAs solar cell's GaAs sub-cell resulting in 30-fold increase in J_{02} in the GaAs sub-cell [123]. In a strain-balancing study carried by K. Watanabe *et al.* in 2014, the $60 \times In_{0.11}Ga_{0.89}As/GaAs_{0.76}P_{0.24}$ QW GaAs solar cell with AM1.5G efficiency of 24.35% and drop in V_{oc} of only 43 mV compared to the reference device with no QWs was demonstrated and this result was attributed to minimization of strain by properly adjusting the strain balancing composition and good quality of the superlattice interfaces as indicated by X-ray diffraction (XRD) [133]. Another impressive result was achieved by M. Sugiyama *et al.* where incorporation of $112 \times In_{0.14}Ga_{0.86}As/GaAs_{0.57}P_{0.43}$ QW superlattice (only 3.1 nm-thick strain balancing barriers) in GaAs cell with excellent crystalline and interface quality demonstrated by high-resolution transmission electron microscopy (HRTEM) led to V_{oc} retention at 0.94 V (only 30 mV drop compared to the baseline) under 1 sun AM1.5G illumination, while J_{sc} enhancement due to the added QW photo-conversion was 3 mA/cm^2 [104]. The important nuance associated with the works where high phosphorous content strain balancing was used is that the samples were grown at 610°C and 600° as compared to 650°C growth temperatures used in other works. This deserves special attention, since it was shown that increase in QW growth temperature can lead to either a significant disruption of 2-dimensional growth and cause local material aggregation at the growth steps resulting in wavy, 3-dimensional quantum dot-like growth [117] and rapid accumulation of strain along the growth direction or, otherwise, to the reduction in interface roughness dependent on the epitaxial substrate offcut [114, 115]. The higher order issues that can lead to increased non-radiaitive carrier losses throughout the QW-strain-balancing sequences are primarily
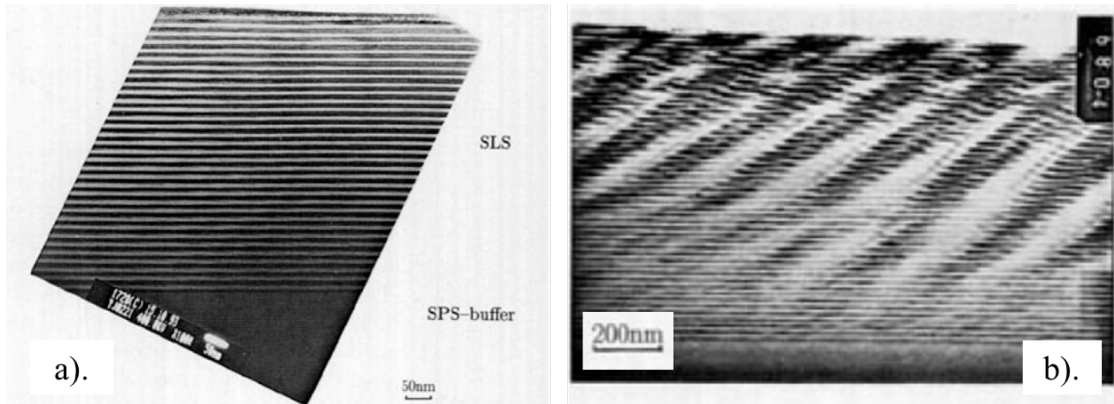
FIGURE 3.8: Cross-sectional TEM images of the InGaAs/GaAsP QW superlattices grown on (a) on-axis and on (b) $2° \to$[110] offcut (100)GaAs substrates [138].

at the interfaces between InGaAs and GaAsP where parasitic diffusion of species can lead to smearing of the abrupt QW/barrier transition by forming graded quaternary $In_xGa_{1-x}As_yP_{1-y}$ mixed compounds [134]. Minimization of interface smearing can be achieved by employing proper switching sequence and by adding thin interfacial GaAs layers [135, 136, 137].

In summary, morphology of the QW superlattices may depend on the interplay of the following parameters:

- Substrate offcut angle and direction [114, 117]

- Growth temperature [115, 116, 117]

- Composition (and associated thickness) of strain balancing layers

- Number of QW periods [116]

- Switching sequence on transition from TMIn to PH_3 and other interface management techniques [134, 136, 135, 137]
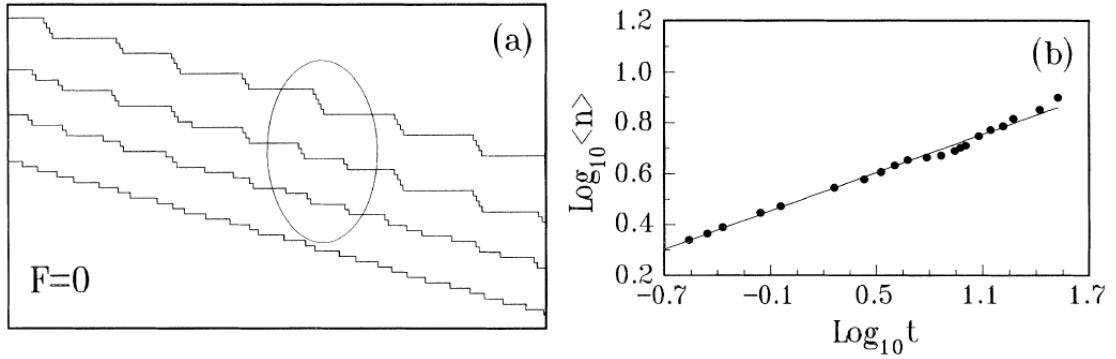
FIGURE 3.9: (a) Surface morphology profile evolution with time (5 steps coalescing into 1 bunch); (b) characteristic bunch size $\langle n \rangle$ change over time [140].

All of the above determine a probability and severity of *step bunching* [139, 140, 141]. One of the earliest observations of thickness modulation in strained films (InGaAs/-GaAsP QW on GaAs) grown on offcut (100)GaAs substrates was reported by T. Marschner *et al.* [138]. While growth on on-axis substrate results in planar QW layers (Fig. 3.8a), the authors claim that compressively strained layers grown on offcut vicinal substrates are responsible for initiating the processes leading to surface roughening, while strain balancing layers are preferentially deposited in the areas where the QW layers are the thinnest stabilizing the lateral growth and allowing some elastic strain relaxation and eventually resulting in large-order steps (Fig. 3.8b). A theoretical model for this behavior in strained films was developed by J. Tersoff *et al.* appealing to the periodic spontaneous perturbations in the step growth [140]. Thinking of a strained film growth macroscopically the lateral atomic uniformity of the epitaxial surface is assumed following the 2×4 or 4×2 (001) GaAs surface reconstruction pattern, however, surface of the offcut substrates acquires periodic discontinuities, terraces with width determined by the offcut angle. The variations in height along the growth plane in a presence of strain in the epitaxial film ($In_xGa_{1-x}As$ or $GaAs_yP_{1-y}$ on GaAs) cause the uncompensated lateral force equal to the magnitude of stress multiplied by the step height resulting in the instability of the step bunching (Fig. 3.9a, b) [140].

Laterally periodic local relaxation and thickness modulation in the QW layers propagate at $\sim30°$ - $\sim45°$ to the surface and dependent on the offcut, QW and strain balancing layer thicknesses and degree of relaxation can cause morphological changes to the superlattice ranging from the onset of wavy structures to a complete disruption of the superlattice. In the work by M. Steiner *et al.* (NREL), the cross-sectional TEM images of the $In_{0.10}Ga_{0.90}As/GaAs_{0.90}P_{0.10}$ superlattice clearly show ripple-like features propagating at an angle starting from $\sim20^{th}$ period along with a variation in QW thickness by at least a factor of 2 (Fig. 3.10). This observation can be correlated to the fundamental cause of excessive step bunching and wavy growth of strained materials - accumulation of strain, such that at some critical value σ the QW layers start relaxing at the growth steps. The period of the ripples is ~200 nm whereas the terrace width of the bulk GaAs grown on 2° off substrate at the same 650°C temperature is ~40 nm (Fig. 3.11a) [142]. Terrace widening occurs at elevated temperatures due to the increased adatom diffusion. Figure 3.11b shows relation between the Ga adatom concentration, n_{step}, and substrate offcut. When $n_{step} < n_e$, where n_e is equilibrium adatom concentration at the step, steps are bunched and n_{step} increases from curve (a) to curve (b) until $n_{step} = n_e$. Then, the terrace width retains a constant value W_b [142].

QW superlattices grown on on-axis substrates do not exhibit such behavior and the steady step-flow growth mode is maintained, however, it is not an option to use small-offcut substrates for growing multijunction devices (either growth of GaAs on Ge substrates, ordering of the InGaP and InAlP, or even growth of metamorphic InGaAs subcell all show improved material quality grown on the offcut substrates). Thus, determining what growth conditions will allow to minimize the formation of excessive step bunching in strained QW layers is one of the goals of this study. From the diagram (Fig. 3.11b), it is evident that maintaining a step-flow growth is nearly impossible in
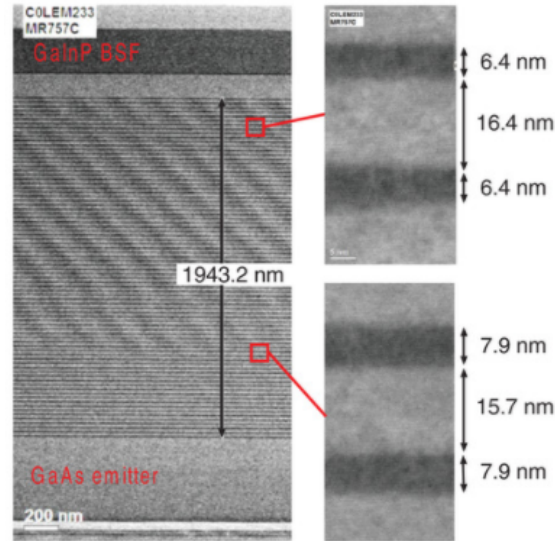
FIGURE 3.10: Cross-sectional TEM of the $80 \times \text{In}_{0.10}\text{Ga}_{0.90}\text{As}/\text{GaAs}_{0.90}\text{P}_{0.10}$ super-lattice; thickness of the QW and strain balancing layers becomes non-uniform and formation of ripples proceeds starting from $\sim 20^{th}$ period [15].

the offcut systems, and growing the films at low T is a way to prevent an excessive step bunching resulting in a non-uniform QW growth and formation of strain relaxation sites leading to the propagation of uncompensated strain due to non-uniform growth of the strain-balancing layers. A critical number of QW layers corresponding to the maximum number of wells that can be grown before the wavy growth initiates was shown to be in exponential relation with growth temperature (Fig. 3.12) which further supports the case [116].

From a device operations perspective, it is difficult to separate the contributions into the dark current, typically increasing in its non-radiative J_{02} component when the QWs are introduced. Would resolving the thickness modulation issue observed in the NREL study from 2021 [94] recover some of the V_{oc} by growing the superlattices at lower T (University of Tokyo group demonstrated only 30 mV V_{oc} drop in solar cells with thinner strain balancing layers and 112 QWs grown at low T [104])? In other words, what do these propagating ripples (the contrast occurring in the electron microscopy
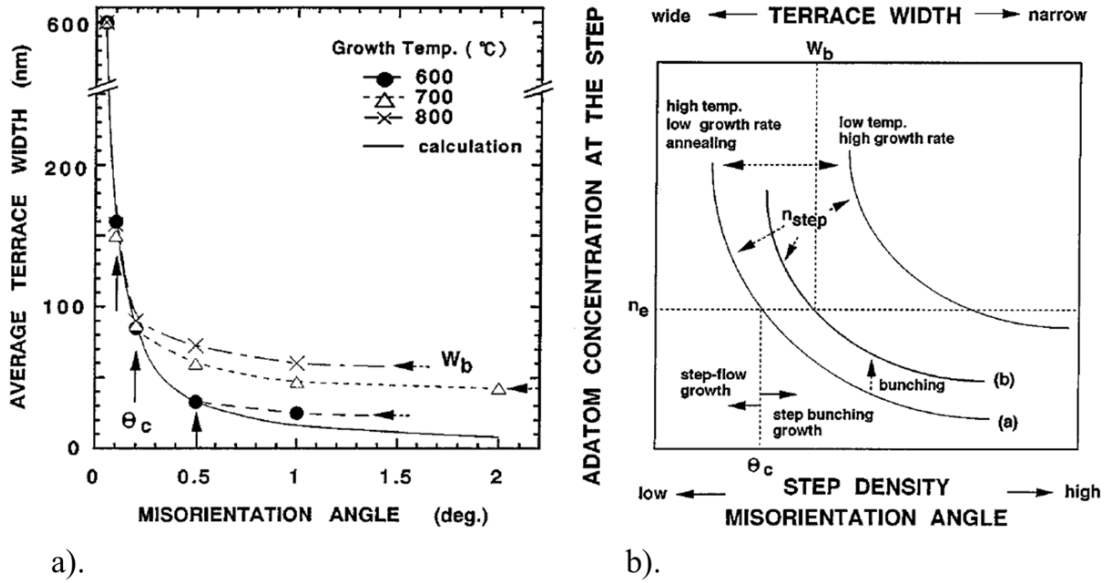
a).   b).

FIGURE 3.11: a). Epitaxial 300 nm-thick GaAs terrace width dependent on the substrate offcut grown at different temperatures and calculated from the monolayer thickness and angle (solid line); b). a diagram representing the relations between Ga adatom concentration at the steps (n_{step}) and step density related to the substrate misorientation angle. [142].
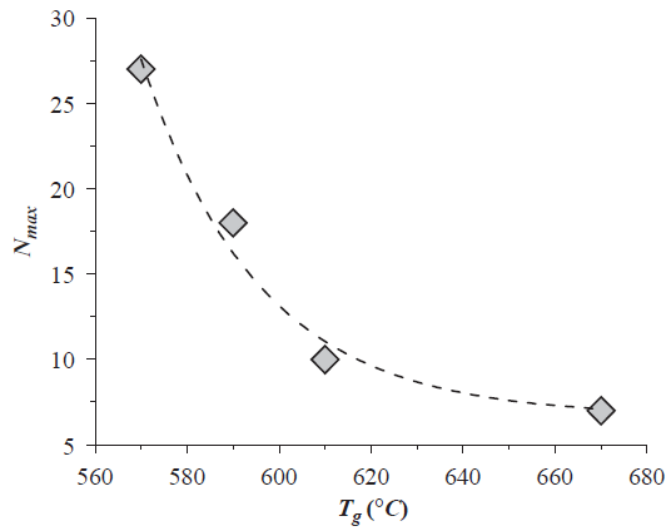
FIGURE 3.12: Experimental values of N_{max} as a function of the growth temperature T_g, at constant strain energy per period. The dashed line represents the exponential decay fit. [116].

images which makes these defects visible is associated with local strain) and irregularities throughout the QW sequences represent electronically? Is the period of thickness modulation modes directly related to the reduction of the carrier lifetimes introducing parasitic electronically active capture sites? How do strain balancing layer properties influence the severity of the SL disruption? How many periods of QW SL can be grown uniformly at each set of growth conditions before the rippling initiates and how is this metrics related to the strain type and magnitude? These and other experimentally relevant questions can and are answered fully or in part using a combination of spectroscopic analysis and dark current analysis and modeling in the Results and Discussion section applied to the devices designed and manufactured at RIT. It is suspected that degradation of superlattices might be responsible for the drop of V_{oc} and fill factor, thus addressing this issue by selecting proper substrate offcut, growth temperature, maximum number of QW periods for each set of growth parameters and strain balancing, and interface management strategies is the key for offsetting the limiting recombination type towards radiative, where quantum well radiative properties can be utilized for further enhancement of solar cell efficiency.

An increase in the number of QWs essential for approaching a near unity internal quantum efficiency and effective bandgap offset in the GaAs cell (optimal bandgap for a middle sub-cell is 1.35 eV) can be associated not only with the increase in non-radiative current, but also can lead to an impeded carrier transport and poorer carrier extraction from the QWs resulting in progressively smaller gain in J_{sc} per QW, since IQE is a strong function of R_{escape} (Eq. 3.4) [112]. Expanding the QW region will lead to the reduction in F, thus lowering the probability of tunneling escape (this would increase the residence time of the carriers promoting higher chance of their recombination) and, in an extreme case can lead to the dampened carrier separation inside of the depletion

region. One of the alternative ways to boost absorption in the QW region is optical enhanced by adding rear-side mirrors [38, 143]. This can be enabled by growing solar cells in an inverted configuration and by etching away the epitaxial substrate or by performing epitaxial lift-off (ELO) for future substrate reuse. The inverted design was actually implemented in the NREL's study as well demonstrating the dual junction 0.25 cm^2 devices [15]. The alternative approach is to use distributed Bragg reflectors (DBR) [144]. In this case, an upright solar cell structure is grown on top of the DBR mirror consisting of Al$_z$Ga$_{1-z}$As layers. DBR structures composed of the alternating thin films with various refractive indices designed to reflect light with a desired wavelength and bandwidth [144]. Reflectivity in the bi-layer DBR stack can be expressed as [145, 146]:

$$R(\lambda) = \left(\frac{n_0(\lambda)(n_2(\lambda))^{2N} - n_s(\lambda)(n_1(\lambda))^{2N}}{n_0(\lambda)(n_2(\lambda))^{2N} + n_s(\lambda)(n_1(\lambda))^{2N}} \right)^2, \tag{3.13}$$

where refractive index of the light incidence material is n_0, substrate, n_s, and layers, n_1 and n_2. N is the number of the repeated DBR periods. Figure 3.13a shows the schematic representation of the solar cells with multiple QWs (MQW) and with combination of the MQW and DBR structures. The comparative analysis of the optoelectrical characteristics of these two devices clearly shows an enhanced J_{sc} (Fig. 3.13b) due to increased IR absorption as indicated by EQE spectra (Fig. 3.13b) and reflectivity and electroluminescence spectroscopy (Fig. 3.13c, d) [144]. The bandwidth Δf_0 of the DBR reflectivity centered around the frequency f_0 is also expressed in terms of refractive indices of the adjacent layers:

$$\frac{\Delta f_0}{f_0} = \frac{4}{\pi} arcsin \left(\frac{n_2 - n_1}{n_2 + n_1} \right). \tag{3.14}$$
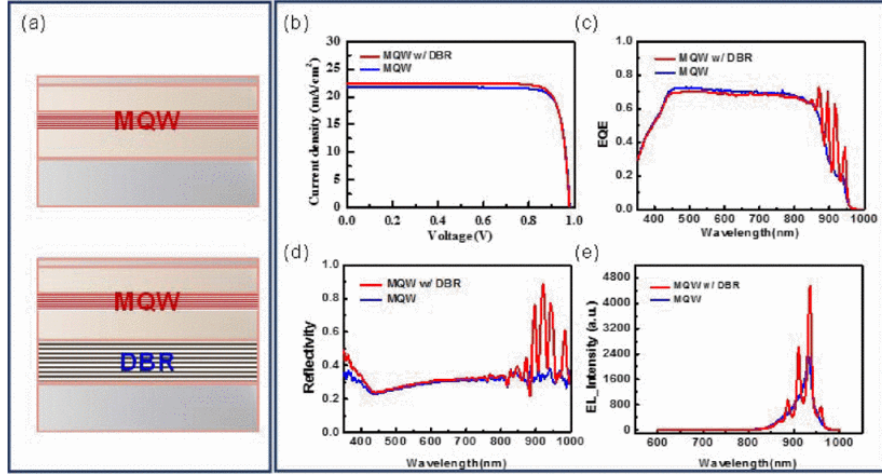
FIGURE 3.13: (a) Schematics of the MWQ solar cell and solar cell with combined MQW and DBR structures; (b) Illuminated J-V characteristics; (c) EQE spectra; (d) Reflectivity spectra; (e) Electroluminescence spectra [144].

Transfer matrix modeling can be used to obtain the thicknesses of each DBR layer for tuning it to the f_0 frequency of interest. For QW solar cell applications, the peak reflectivity wavelength should be centered close to the QW absorption peak, and can be further adjusted if bulk photon recycling phenomenon is targeted [147].

3.3 Methods

3.3.1 Experimental Techniques

Growth of the QW test structures and solar cell devices is done by metal organic vapor phase epitaxy (MOVPE) using $3 \times 2''$ Aixtron close-coupled showerhead reactor on (100) GaAs substrates with $2°$ towards $\langle 110 \rangle$ offcut. Additionally, on-axis and other substrate offcuts and offcut directions were employed for growth of SL test structures and some devices: $2° \rightarrow \langle 111 \rangle A$, $2° \rightarrow \langle 111 \rangle B$, and $6° \rightarrow \langle 111 \rangle A$.

Trimethylindium (TMIn), trimethylgallium (TMGa), and trimethylaluminum (TMAl) were used as group III precursors and arsine (AsH$_3$) and phosphine (PH$_3$) as group

V sources. Diethylzinc (DEZn) and carbon tetrachloride (CCl$_4$) were used as p-type dopant precursors and n-type layers were doped using diethyltellurium (DETe) or disilane (Si$_2$H$_6$). The monitored (using an *in situ* Laytec pyrometer system) substrate growth temperature was 650° for base, emitter, and front and rear surface field layers, and temperature was adjusted as indicated further in the text for growing some QW superlattices. Fabrication of the 1×1 cm^2 solar cells is performed via standard III-V processing with electroplated metal contacts (Zn and Au for p-type annealed contacts and non-annealed Au for n-type contacts).

The next**nano** software is used to model the QW superlattices for composition and thickness calibration including simulations under applied electric field for carrier and recombination escape rates calculations. The verification of the modeled QW properties, composition calibrations of epitaxial layers, as well as comparative studies are done or assisted by photoluminescence (PL) spectroscopy and voltage-biased PL for which 256 W/cm^2 532 nm laser source with Princeton Instruments Acton SpectraPro SP-2300 spectrometer are used. To investigate carrier collection efficiency from both base and QW region of the solar cells at J$_{sc}$ and near the maximum power point, voltage-biased external quantum efficiency (EQE) measurements are performed using Newport IQE 200 quantum efficiency measurement system calibrated against silicon (Newport 818-UV-L) and germanium (Newport 818-IR-L) detectors. Carrier collection efficiency (CCE) methodology and validity are described in [148]. Radiative recombination suppression and quasi-Fermi level splitting offset in QWs are analyzed by electroluminescence (EL) and EQE reciprocity relation [126]. For EL measurements, an ASD FieldSpec 3 spectroradiometer and OceanOptics HR2000 (high-resolution spectral sensitivity range is 250 - 1050 nm) are used.
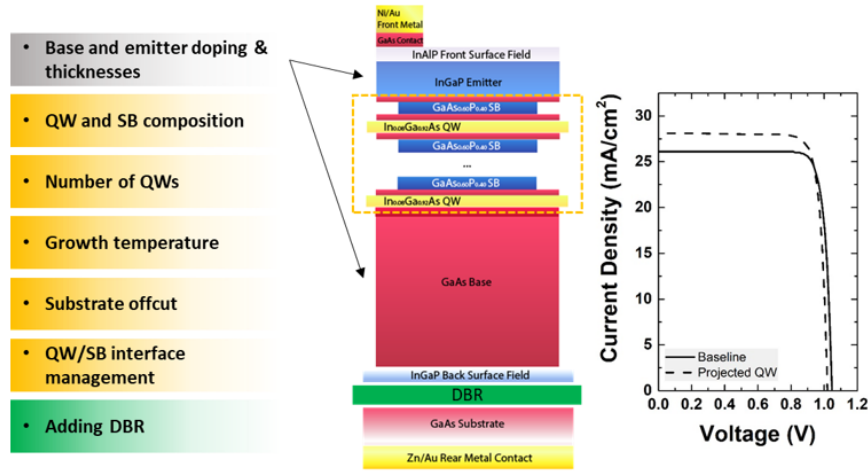
FIGURE 3.14: The key components of the design of experiment for achieving high efficiency QW solar cell device structure including bulk and strained material development, electric field adjustments, and implementing optical enhancement DBR structures. The projected IV curve is interpolated from [104] based on the best baseline result achieved at RIT to date.

3.3.2 Design of the Study

Figure 3.14 shows the main routes identified to enhance the QW device performance and the projected IV curve (dashed line) is created based on the current and voltage offsets from [104] and on the limitations of the record efficiency bulk baseline device fabricated at RIT. Minimization of non-radiative dark current increasing due to adding the QWs and adjusting the doping in bulk base and emitter, as well as the thickness of absorbing GaAs, modulating the quantum properties of the QWs and electric field across the QW region, and increasing light absorption in the QWs are the priorities. The secondary mechanisms including minimization of radiative recombination in the QWs and photon recycling in the GaAs base are contingent upon recovery of non-radiative current.

Ultimately, the goal of this study is to further exploit the capabilities of QWs for achieving higher efficiency of the GaAs solar cell. The study needs to be followed with growth of the devices with extended QW region to further push the sub-bandgap photons utilization which will require the analytic approaches successfully applied to the demonstration

set of devices.

Considering the key requirement for achieving high efficiency of the QW solar cell to be an increase in sub-bandgap absorption, minimization of the radiative recombination probability, i.e. low residence time in the QW region, while preserving non-radiative recombination rate comparable to the baseline (with no QWs) device's values, the design of the QW superlattices need to be optimized. In particular, finding the maximum number of strain balanced $In_{0.08}Ga_{0.92}As$ QW superlattice periods that do not block carrier transport through the depletion region is a subject of the study. It will be accompanied with the $GaAs_xP_{(1-x)}$ strain balancing design [149] and growth optimization. Inclusion of the strain-balancing, however, will introduce the energy barriers between the QWs, so refining of the model with careful electric field adjustment and tunneling effects that can become critical with strain balancing will be performed to find proper QW placement and balance between strain compensation layers bandgap and lattice constant. This can also be assisted with additional QW barrier engineering to ensure efficient carrier thermalization. MQW solar cells with DBR structures will further be designed and fabricated as well to demonstrate increased absorption in the QW region. The DBR will consist of the epitaxially grown $Al_{0.10}Ga_{0.90}As/Al_{0.90}Ga_{0.10}As$ pairs.

Fabrication of the devices will be refined. In particular, studying the dependency of the V_{oc} on the device area is relevant for assessing the sidewall recombination rate influence (the depletion region being in contact with the sidewalls). If it is found to be substantial, the sidewall passivation strategies can be implemented [150]. These findings in future can be applied to the dual-junction structure with InGaP top cell (development of 2J devices is in detail described in Chapter 4).

At the same time, temperature-dependent spectral characteristics of the solar cells will

be investigated as well to derive the minority carrier lifetimes attributed to the recombination in the space charge region and quasi-neutral region. Electron microscopy studies will be used for determining the morphological properties of the QWs.

3.4   Results and Discussion

3.4.1   Device Fabrication Study

The initial study intended to rule out the suppression of non-radiative lifetime by sidewall recombination and to determine the minimal device area-to-perimeter ratio at which sidewall recombination impact is negligible. This study also includes an investigation of various etchants for III-V materials and mesa etch depth.

The fabrication process is schematically shown on Fig. 3.15 - 3.18. Consistency of metallization process and contact resistivity on the order of 10^{-5} $\Omega - cm$ ensures that fill factor is not reduced due to the series resistance, and adding Zn dopant and annealing of the rear contact allows to create a low-resistance rear contact (Fig. 3.15-2, 3). Front Au contacts are directly electroplated onto the tellurium-doped GaAs contact layer (Fig. 3.16-6).

To maximize the yield and quality of the devices, the proper manufacturing approaches need to be established. In particular, from the solar cell fabrication standpoint, there are the following parameters to be tested:

- Mesa etch chemistry (impact on the yield and sidewall roughness, lateral etch rate, etc.)

- Mesa etch depth (back surface field or substrate).
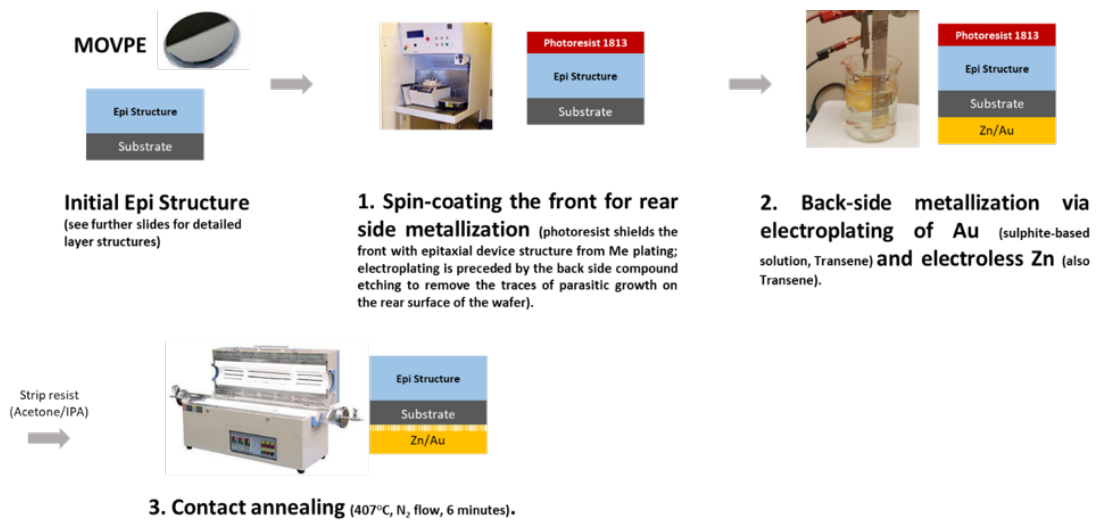
FIGURE 3.15: REAR SIDE METALLIZATION. 1. The front side is protected with photoresist that is spin-coated and soft-baked. Prior to metal electroplating, the rear surface is cleaned using chemical wet etch (H_3PO_4:H_2O_2:H_2O and HCl). 2. To form a low-resistance contact, the rear surface (p-type) of the wafer is additionally doped with Zn via electroless deposition. Then, $\sim$300 nm-thick gold is plated using sulphite gold plating solution and platinum-coated titanium mesh as a counterelectrode. Electroplating is performed at $50 - 55$°C and at current density of 0.31 mA/cm^2. 3. After the deposition of metal, the protective photoresist is removed with acetone and the residue is washed away with isopropanol. The annealing in nitrogen atmosphere is performed to diffuse Zn. Annealing temperature is 407°C for 6 minutes.
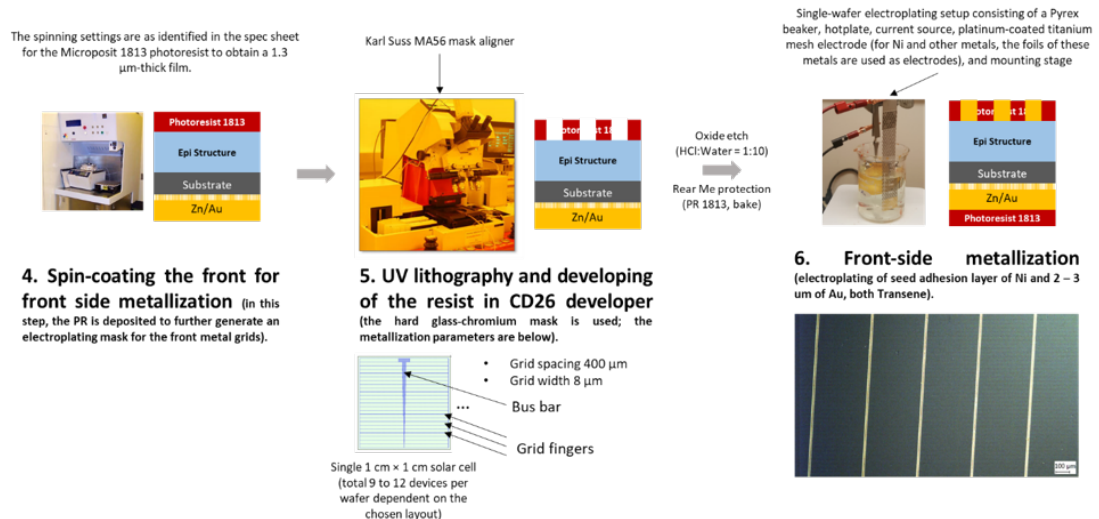
FIGURE 3.16: FRONT METAL CONTACTS DEPOSITION. 4. The positive photoresist is again spin-coated on the front side of the wafer for a lithography step. 5. Exposure of photoresist is performed using a mercury light source calibrated with 2 radiometers (365 nm and 436 nm) and a hard mask (chromium on glass) with the metal grids defined as openings. The picture below step 5 is showing a single solar cell grid design (total 12 devices per wafer). Each cell features 8 micron-wide grids 400 micron apart. Cell area is 1 cm^2. The photoresist is then developed using CD-26 developer to open up the contact layer of the solar cell for the following metal deposition. 6. Nickel adhesion layer is electroplated (using a piece of nickel foil as a counter electrode) preceding the gold layer yielding up to 4 micron thick features. The microscopy image below step 6 shows Au grids after the photoresist is removed.
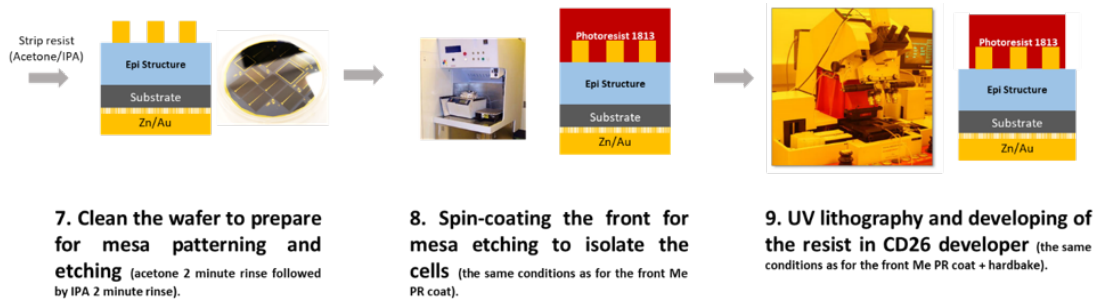
FIGURE 3.17: DEFINING THE CELLS AREA (MESA LITHOGRAPHY). 7. Solvent cleaning (acetone and isopropanol) to remove the photoresist before the next lithography step. 8. The new layer of photoresist is spin-coated onto the wafer's front surface. 9. A mask with defined cell areas is used to expose and remove the resist between the cells for the following semiconductor etching. The resist is hard-baked after development (removal of exposed resist with CD-26) to further solidify it prior to the mesa etching.
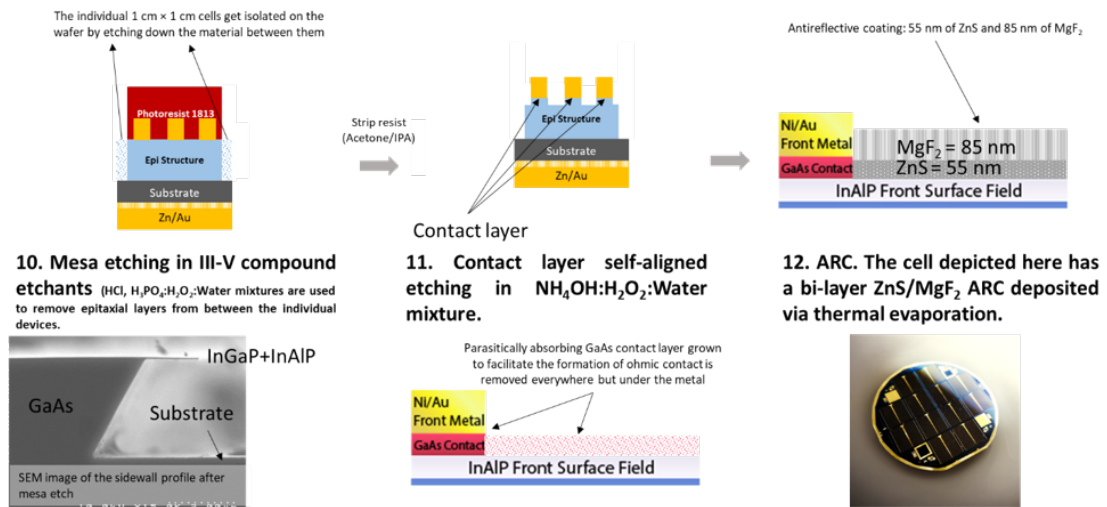
FIGURE 3.18: MESA ETCHING, CONTACT ETCHING, ANTI-REFLECTIVE COATING. 10. Removal of the epitaxial layers between the mesa-defined solar cells by wet chemical etching (HCl for InGaP, InAlP and $H_3PO_4:H_2O_2:H_2O$ or $NH_4OH:H_2O_2:H_2O$ for GaAs, InGaAs, AlGaAs (where applies)). The scanning microscopy image below step 10 is showing the cross-sectional view of the solar cell after mesa etching with the respective layers denoted. After the mesa etching, the photoresist is removed with acetone and isopropanol. 11. Highly doped epitaxially grown GaAs contact topmost layer serves to make an ohmic contact and it is highly absorbing. It is removed everywhere, but under the metal (as shown on the diagram). Contact etch is self-aligned (metal grids serve as an etching mask). $NH_4OH:H_2O_2:H_2O$ mixture is used. 12. Antireflective coating is deposited to dramatically reduce front-surface reflectivity. Bi-layered, consisting of ZnS and MgF_2, antireflective coating is deposited by thermal evaporation. The final product is shown on the photo under step 12 description.
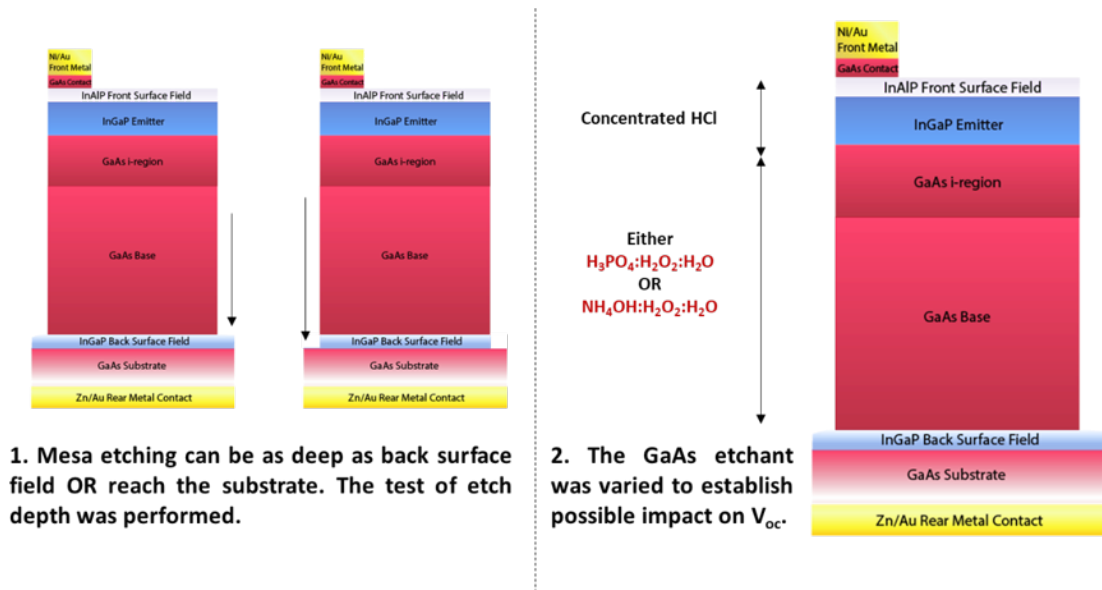
FIGURE 3.19: 1. Mesa etch depth test and 2. GaAs etching chemistry test.

The mesa etch used to isolate the individual solar cells on a substrate is inevitably associated with a crystallographic lateral etch of the sidewall besides the desired vertical etch. This, depending on the choice of chemicals, their concentrations, and time of etching, can result in excessive roughness of the sidewall and/or significant undercut (refer to the SEM image shown in Fig. 3.18, item 10). The set of fabrication test structures was labelled as R0 and consisted of 2 wafers with identical epitaxial baseline structures (no quantum wells, QWs) grown, that are exact replicas of the structures that are in detail described here (InGaP/GaAs heterojunction single junction solar cell). Figure 3.19 summarizes the tests that were performed on these samples. To test the impact of the mesa etch depth, one of the wafers was split in 2 halves (GaAs contact and base layers were etched with H_3PO_4:H_2O_2:H_2O = 3:4:1) and an alternative GaAs etch chemistry (NH_4OH:H_2O_2:H_2O = 1:1:8) was tested on a full sample set of the other wafer. The roughness of the sidewall, on the device level, would manifest itself primarily in the increase in dark current and consequently in the open-circuit voltage (V_{oc}).

To investigate the impact of the sidewall properties on the V_{oc} of the cells, multiple solar

cells with varied perimeter-to-area ratio were added to the layout resulting in total 18 solar cells per wafer and including 9 1 cm × 1 cm standard solar cells (Fig. 3.20a) and 2 solar cells designed for concentrated light operation (more closely spaced grid fingers). However, performance of the 1 cm × 1 cm devices was in focus of this study. The solar cells were measured under 1 sun AM0 illumination and their open-circuit voltages are summarized on Fig. 3.20b. Given that for the mesa etch depth study the wafer was split into halves, the number of large cells per test was small, so the statistical data shown on Fig. 3.20b is taken across only a couple of devices considering the outliers that were removed from each sample set. This plot shows the highest V_{oc}'s. A brief comparison indicates that using the ammonia-based GaAs etch solution resulted in a relatively poor yield of the cells compared to the standard phosphoric acid-based mixture (broad data distribution even in a small sample set) as well as a reduction in V_{oc} by up to 10 mV, so for the next rounds, H_3PO_4:H_2O_2:H_2O was used for the mesa etch. At the same time, the mesa depth study showed that etching down to the substrate supports higher V_{oc} and would be a preferential procedure for manufacturing the high-efficiency solar cells. However, retaining the back surface field layer has an important application for the solar cells with distributed Bragg reflectors (DBR) for enhanced QW absorption. In particular, since DBR consists of the pairs of alternating layers of $Al_xGa_{1-x}As$ with X = 10% and X = 90%, exposing the AlGaAs with high Al content to air causes rapid oxidation that can proceed both vertically and laterally degrading the optical and electrical properties of DBR. This means that InGaP back surface field in this case would serve as a passivation layer preventing the exposure of the DBR to the ambient environment. Additionally, InGaP facilitates the fabrication serving as an etch stop that prevents accidental etch through the DBR stack during base mesa etch. In this context, the V_{oc} data can be viewed as having the back surface field (BSF) does
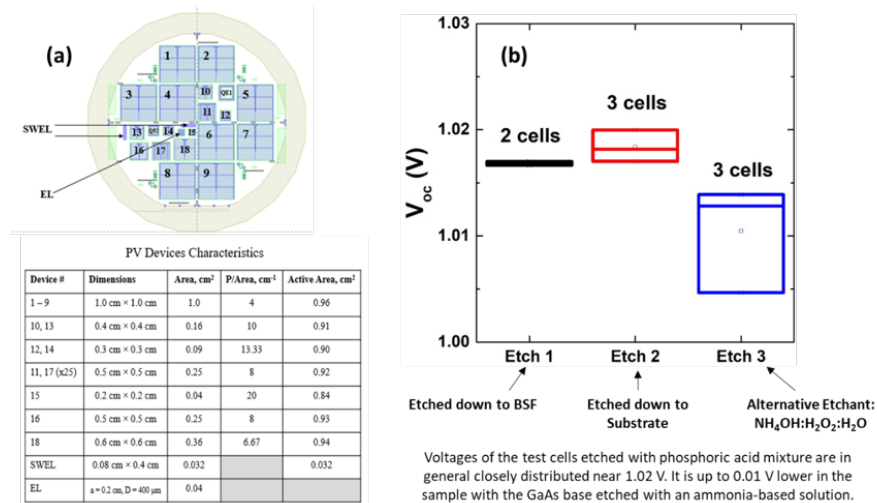
FIGURE 3.20: (a) Mask layout featuring multiple solar cells with varied perimeter-to-area ratio. The solar cells parameters are summarized in the table. (b) Open-circuit voltage distributions for every set of sample dependent on the etch scheme/chemistry.

not cause much reduction in V_{oc} compared to that of solar cells mesa-isolated down to the substrate and such procedure can still be used when it is necessary to provide a passivation for the optical structures under the solar cell potentially reducing the V_{oc} only by 2 mV.

The sample etched with ammonia-based solution was excluded from the further analyses. An investigation of the dark current in dependency on the perimeter-to-area ratio (the higher perimeter-to-area ratio, P/A, gets, the more is the sidewall contribution, so for the inferior quality sidewall non-radiative dark current increase is expected) was performed. Figure 3.21b is showing the dark current curves obtained from the cells etched down to the substrate with P/A of 4 and 13.33 are compared to the dark current of the cells etched down to the BSF with P/A of 4 and 8. Analysis of these curves did not indicate a consistent change in non-radiative dark current with reduction in device size and as well can be related to the naturally occurring growth or fabrication non-uniformities.

Considering the findings obtained in R0, fabrication of the subsequent rounds including the cells with quantum wells was performed with the mesa etch down to the BSF and
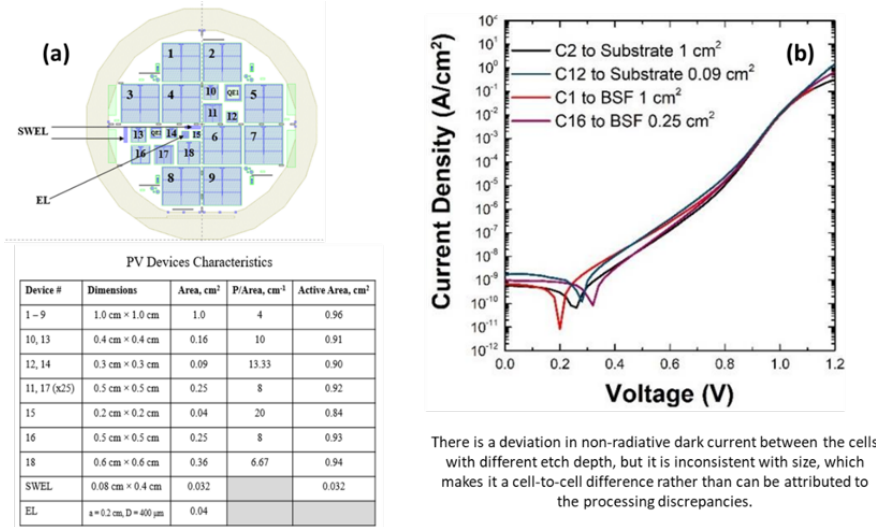
FIGURE 3.21: (a) Mask layout featuring multiple solar cells with varied perimeter-to-area ratio. The solar cells parameters are summarized in the table. (b) Dark current-voltage curves of the cells etched down to the substrate and down to the back surface field with various perimeter-to-area ratios.

phosphoric acid-based GaAs etchant. Some other modifications are denoted where apply (switching GaAs base dopant from Zn to C, changing the base dopant concentration, using higher offcut substrates, etc.).

3.4.2 Modeling of the Baseline Solar Cell (Carrier Lifetime Assessment)

Modeling of the solar cells was performed using Synopsys Sentaurus TCAD software using optical constants of the corresponding films grown at RIT. Input doping and thicknesses were set to accurately represent the experimental values derived from the Hall measurements of calibration samples and selected to maintain a sufficient electric field across the depletion region and to have sufficient electron mobility in the base (the values are specified later in the chapter) and in-situ reflectivity measurements during growth. The goal of the modeling was to establish the diffusion lengths of the minority carriers in the base and emitter of the baseline device. However, an important note is that for a good material (with diffusion length of carriers exceeding the thickness of

the layer) the variations in the diffusion length will not be noticeable in the EQE/IQE (for diffusion lengths greater than 3 times the layer thicknesses). The fit shown on Fig. 3.22a is achieved in an assumption of dominant recombination mechanism to be radiative recombination, such that the non-radiative carrier loss is negligible. Radiative lifetime, τ_{Rad}, can be calculated as:

$$\tau_{Rad} = \frac{1}{B_{Rad} N_{Layer}}, \tag{3.15}$$

where B_{Rad} is radiative recombination coefficient and N_{Layer} is either donor or acceptor concentration, N_d or N_a, respectively, in the emitter and the base. Substituting the $B_{Rad}(\text{InGaP}) = 1.0 \times 10^{-10}$ cm^3/s and $B_{Rad}(\text{GaAs}) = 1.7 \times 10^{-10}$ cm^3/s, doping $N_a = 3 \times 10^{17}$ 1/cm^3 and $N_d = 2 \times 10^{18}$ 1/cm^3, results in $\tau_{e,Rad}(base) = 3$ ns and $\tau_{h,Rad}(emitter) = 33$ ns which represents a higher estimate of the effective lifetime, since zero trap density is assumed. For the minority electrons in the GaAs base, the diffusion length was 37.8 μm, while diffusion length of the minority holes in the InGaP emitter was 1.5 μm. Both values provided a very closely matched fit indicating that the diffusion length of the minority carriers in the solar cell greatly exceeds the thicknesses of the base (2.7 μm) and emitter (50 nm) and the density of traps with high capture cross section determining the non-radiative recombination rate is insufficient to impact the lifetimes and cause the carrier collection to drop. The light I-V modeling (shown on Fig. 3.22b) shows an excellent match using the radiative limit assumption as well. The simulation is performed in 1D, so to account for lateral resistance losses a lump resistance was added at the metal-semiconductor interface.

To determine the limiting thickness of the QW region, simulations of the QW solar cells with different values of the intrinsic region, which is effectively an unintentionally doped
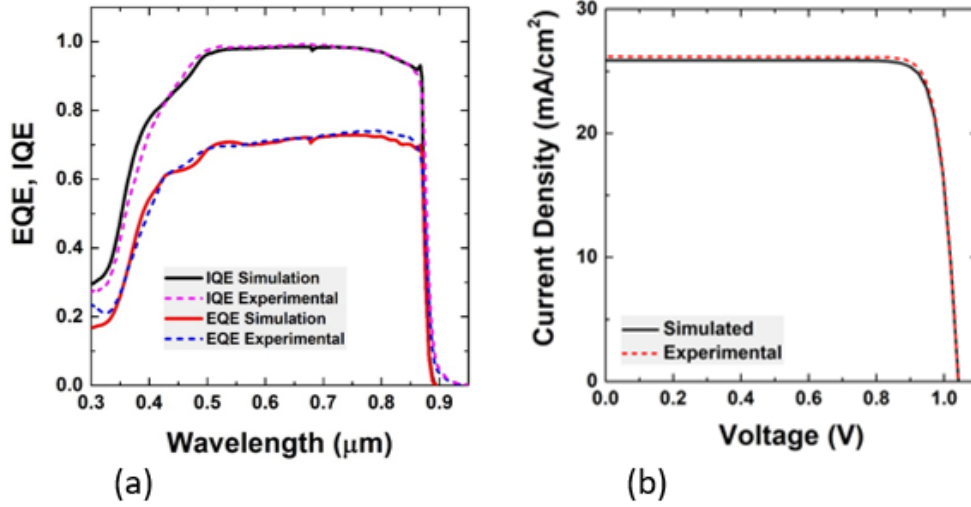
FIGURE 3.22: Simulated (solid lines) and experimental (dashed lines) (pre-ARC) (a) internal and external quantum efficiency data and (b) AM0 light I-V curves.

(UID) region, since incorporation of parasitic dopant species occurs in a real system, background doping (N_{bg}) were performed. Figure 3.23(a) shows band diagram of the intrinsic region of the QW solar cell with 19 nm-thick barriers between the QWs (here, no strain balancing is assumed and thickness of the GaAs interlayers is brought to the expected 17 nm-thick GaAs$_{0.90}$P$_{0.10}$ SB values added to 1 nm-thick GaAs interlayers) for 5×10^{14}, 2×10^{15}, and 2×10^{16} 1/cm^3 background doping at maximum power point. Background doping can vary dependent on the growth temperature and is driven by the memory effect or presence of impurities inside the reactor and it can significantly impact carrier transport across the QW region due to dampened electric field, which changes the number of QWs that can be added to the i-region. Typical unintentional doping for RIT growths is $\sim 5 \times 10^{14}$ cm^{-3}, so maximum number of QWs with 17 nm-thick strain balancing and 1 nm-thick interface GaAs layers to target can approach 60 which is what was reported by NREL [15]. The alternative QW structure is simulated for the background doping of 2×10^{15} as well, and Fig. 3.23b shows a comparison of two strain balancing types: 10%P (19 nm total) and 32%P (5 nm total). A rapid cut-off of the E-field limiting the maximum number of QWs that would support efficient carrier transport
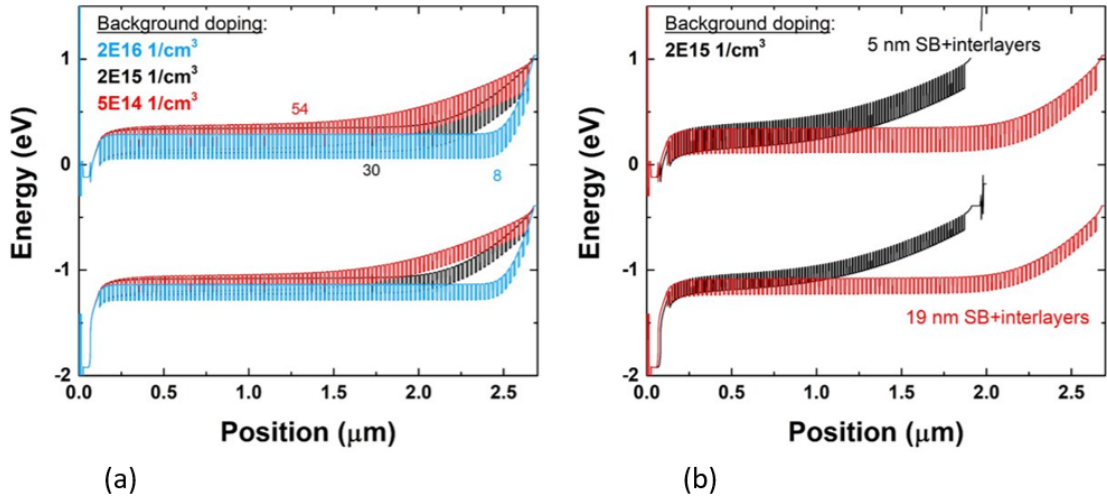
FIGURE 3.23: (a) Simulated band structure of the strain balanced QWs (100 periods are simulated) for 5×10^{14}, 2×10^{15}, and 2×10^{16} 1/cm^3 background doping. (b) Comparison between the band diagrams of the QW regions with 5 nm and 19 nm-thick SB barriers and background doping of 2×10^{15}.

by drift is observed as background doping increases resulting in 54, 30, and 8 QWs as N_{bg} increases from 5×10^{14} to 2×10^{16} (Fig. 3.23a). For the structures with thinner GaAs$_{0.68}$P$_{0.32}$ tunneling barriers, as shown on Fig. 3.23b, definitely can support over 100 QWs even with slightly elevated unintentional doping, but more careful investigation of the tunneling rate might be necessary to determine whether carrier escape could suffer from adding extended QW superlattices.

3.4.3 Solar Cell Structures, Baseline vs. QW Solar Cells

For the second round labelled as R1, the main focus was on comparing the performance of the baseline devices with the devices in which the QW superlattices were added in the intrinsic region. Figure 3.24 shows the layer structures of the baseline (a) and of the solar cell with triple quantum wells (3 × QW) (b). The 9.2 nm-thick nominally In$_{0.08}$Ga$_{0.92}$As QWs (and actually In$_{0.06}$Ga$_{0.94}$As QWs) are separated with 4 nm-thick GaAs barriers with no strain balancing applied (Fig. 3.24c), since the target thickness of the triple-well stack is under the critical thickness of In$_{0.08}$Ga$_{0.92}$As grown on GaAs. For
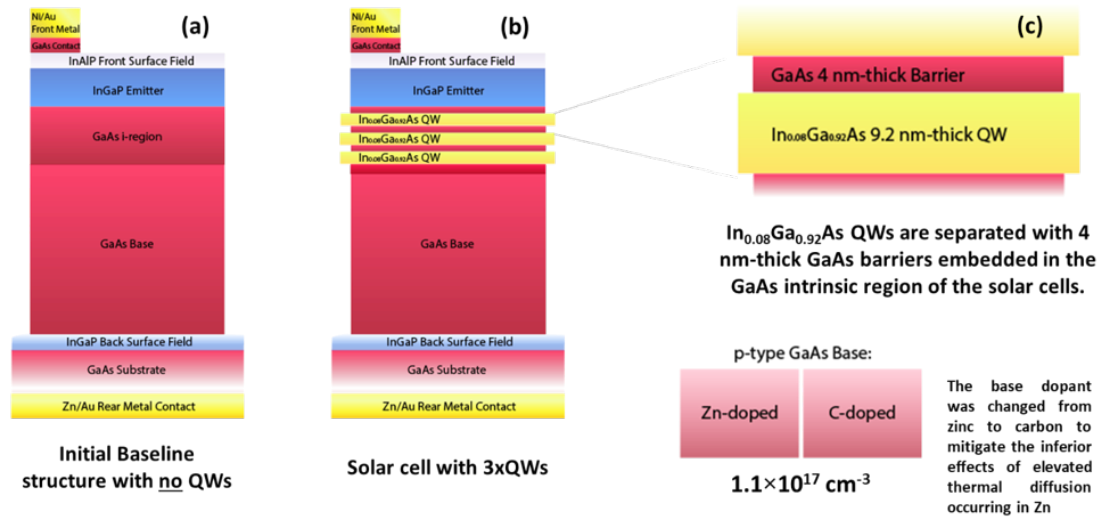
FIGURE 3.24: (a) Baseline cell layer structure. (b) QW solar cell layer structure. (c) QW region detailed view (9.2 nm-thick $In_{0.06}Ga_{0.94}As$ QWs separated with 4 nm-thick GaAs barriers).

the QW device, the base dopant was changed from zinc to carbon that has lower rate of thermal out-diffusion compared to Zn allowing to create more abrupt junction. The nominal QW composition, i.e. 8%In, was actually 6% due to lowered pick-up efficiency of TMIn species from the bubbler which is not instrumentally controlled, and in the further studies.

Figure 3.25 shows the representative metrics of the baseline and $3 \times$ QW solar cells. Comparison of the quantum efficiency spectra (Fig. 3.25a) demonstrates that changing the dopant type from Zn to C increases the mid-wavelength region EQE. An inset is showing the sub-bandgap EQE with the QW quantum efficiency up to 2.1% resulting in extra up to 0.05 mA/cm^2 of current. In combination with the enhanced bulk carrier collection, the resulting total increase in short-circuit current density, J$_{sc}$, in the QW cells (Fig. 3.25b) is 0.5 mA/cm^2. It is seen from the light current-voltage characteristics shown on Fig. 3.25b that the V$_{oc}$ increased by $\sim$20 mV due to replacing Zn with C. Hence, for the advanced devices (with increased number of QWs, strain balancing, DBR) this type of dopant is preferred to ensure the maximum achievable efficiency.
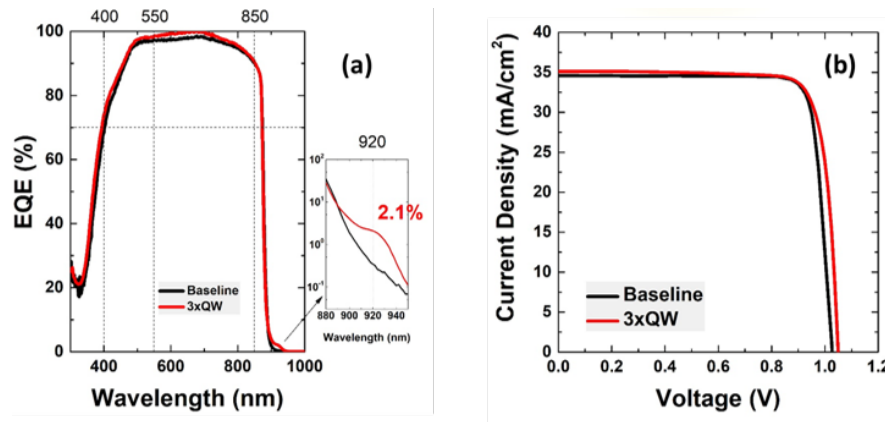
FIGURE 3.25: (a) External quantum efficiency (EQE) of the baseline and QW solar cells. The sub-bandgap region is shown on the inset. (b) One sun AM0 current-voltage characteristics of the cells.
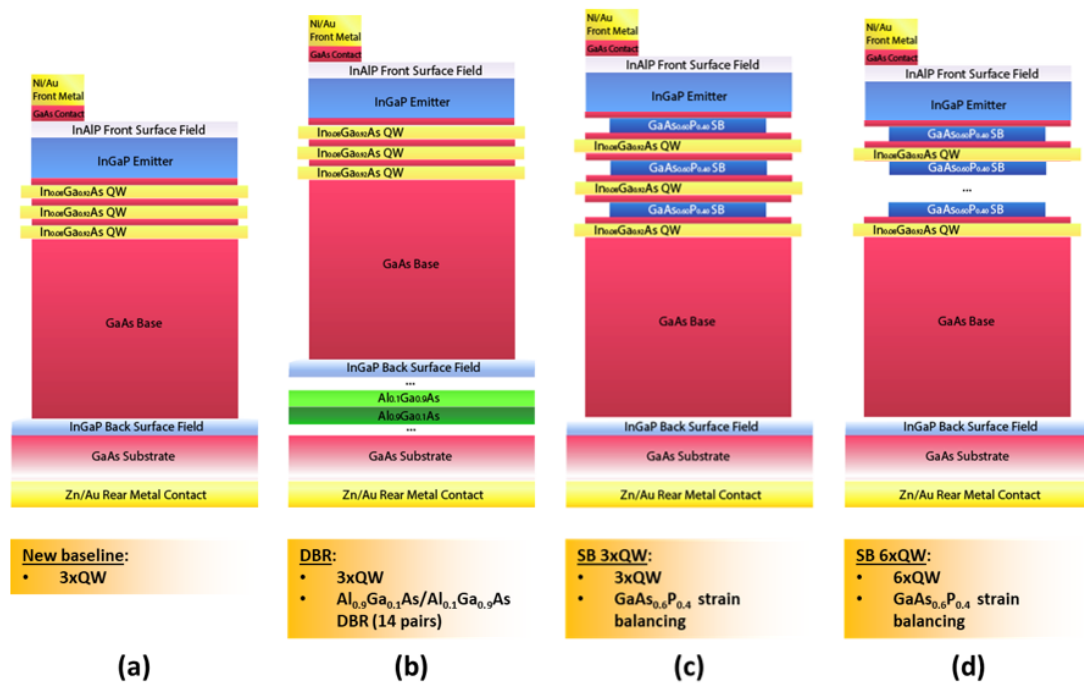
FIGURE 3.26: (a) New baseline device structure featuring triple strained QW superlattice. (b) Solar cell structure with DBR. (c) Triple QW cell with $GaAs_{0.68}P_{0.32}$ strain balancing. (d) Solar cell with 6 strain balanced QWs.

3.4.4 Advanced Solar Cells (Strain Balancing, DBR, Increased Number of QWs - Design Evaluation)

In Round 2, some advancements were implemented pursuing an increase in the current available from the QWs. To increase the number of QWs pushing the width of the QW region beyond critical thickness is inevitably associated with implementation of

strain balancing to prevent the propagation of the strain-induced effects through the upper layers of the solar cell. Additionally, an effective increase in absorption in the QW region was achieved by adding the DBR tuned to selectively reflect light in the QW absorption range allowing to nearly double the number of light passes through the QWs. This optical enhancement is equivalent to almost doubling the number of QWs. DBR design ($Al_x Ga_{1-x}$As layers compositions were fixed at %Al of 10 and 90 and thicknesses were tuned to target peak reflectivity at ~915 nm to not only provide extra absorption in the QWs, but near the band edge of GaAs) was developed using TFCalc. The resulting structure consisted of 12 65 nm-thick $Al_{0.10}Ga_{0.90}$As and 75 nm-thick $Al_{0.90}Ga_{0.10}$As pairs. The chosen number of DBR pairs was determined by modeling the J_{sc} in the solar cell and the minimum number of DBR pairs at which J_{sc} starts to saturate was chosen (Fig. 3.27). As simulated results suggest, the total increase in J_{sc} due to adding DBR is 0.4 mA/cm^2 which is partially driven by the enhanced bulk near-band edge absorption. Minimization of the DBR thickness is desired for reducing the growth time and minimization of the precursors used for making an efficient back mirror. Figure 3.28a shows measured reflectivity of the DBR test structure (14 pairs of 65 nm-thick $Al_{0.10}Ga_{0.90}$As and 75 nm-thick $Al_{0.90}Ga_{0.10}$As capped with 10 nm GaAs to prevent oxidation of the Al rich layer) and reflectivity spectra of the identical solar cell structures with QWs and 12 pair-DBR grown on GaAs substrates with $2° \rightarrow \langle 110 \rangle$ and $6° \rightarrow \langle 110 \rangle$ offcuts are plotted on Fig. 3.28b. The 14-pair test structure reaches 96% peak reflection and in the solar cell DBR reflection is ~90%. The 21 nm shift is observed with changing substrate offcut and it is related to the variations in the $Al_x Ga_{1-x}$As growth rate. Figure 3.29a shows simulated (TFCalc) reflection of the 12-pair DBR composed of target, 65 nm and 75 nm-thick, layers and layers with thicknesses varied by 3%. The corresponding spectra of the DBR-enhanced solar cell structures are shown on Fig.
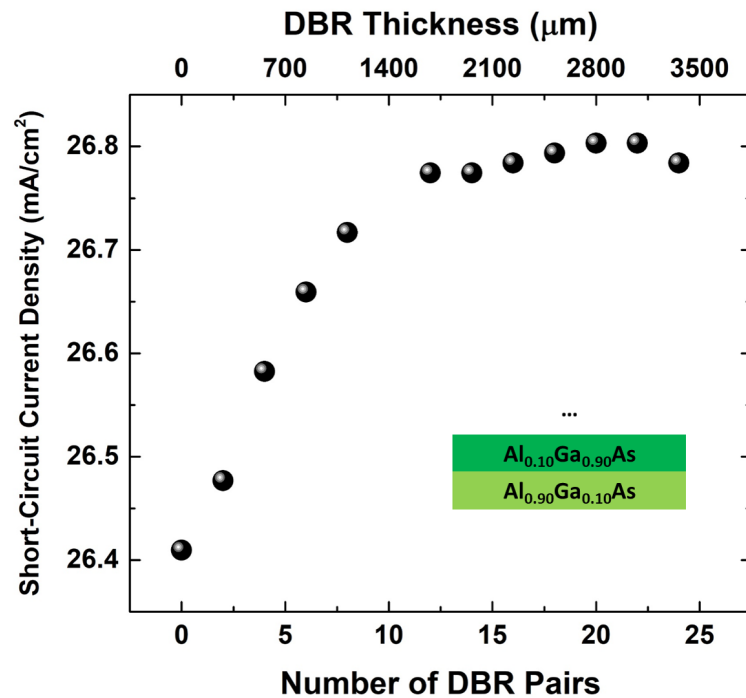
FIGURE 3.27: Simulated J_{sc} as a function of number of DBR pairs with the total DBR stack thickness corresponding to each number of pairs shown on top.
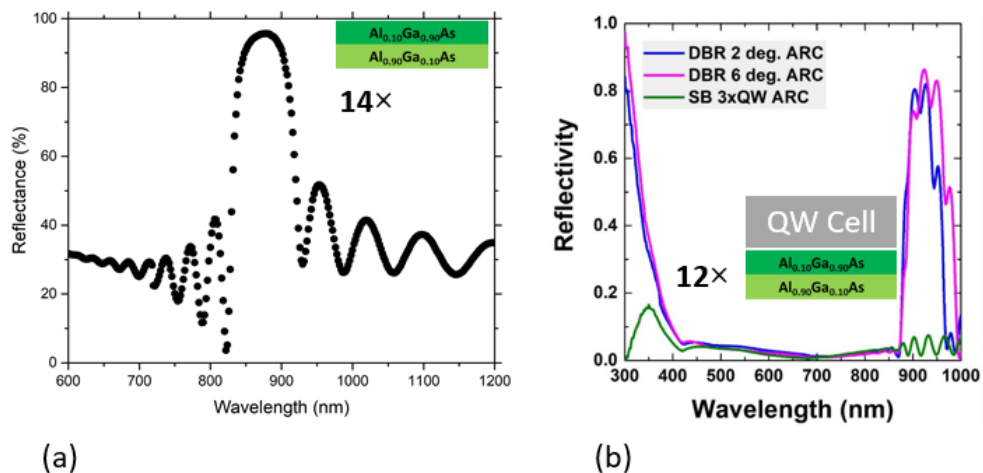
FIGURE 3.28: (a) Measured DBR reflection spectrum of the test structure; (b) measured reflectivity of the solar cell structures with 12-pair DBR grown on $2° \to \langle 110 \rangle$ and $6° \to \langle 110 \rangle$ offcuts.

3.29b.

Figure 3.26 summarizes the Round 2 structures including the previously optimized triple-quantum well solar cell (Fig. 3.26a), solar cell with triple wells and 14 pairs of DBR
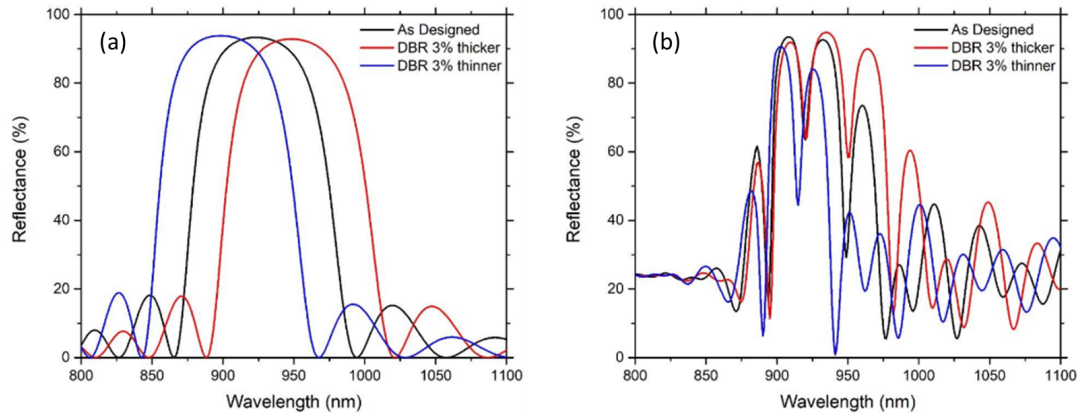
FIGURE 3.29: (a) Simulated reflection of the 12-pair DBR composed of target, 65 nm and 75 nm-thick, layers and layers with thicknesses varied by 3% and (b) simulated reflection spectra of the solar cell structures with the corresponding DBR structures.
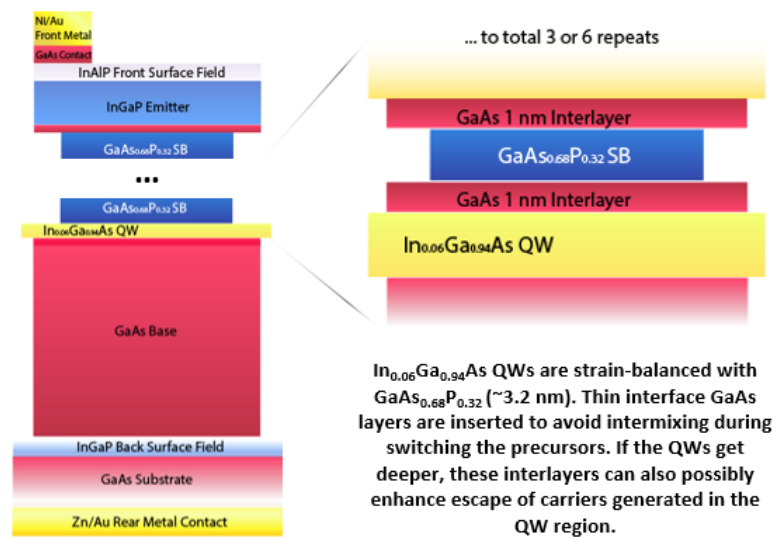
FIGURE 3.30: Schematics of the QW region with $GaAs_{0.68}P_{0.32}$ strain balancing and 1 nm-thick GaAs interlayers.

consisting of alternating layers of $Al_{0.10}Ga_{0.90}As$ and $Al_{0.90}Ga_{0.10}As$ tuned to have maximum reflection at 915 nm (Fig. 3.26b), solar cell with triple strain balanced QWs is shown in Fig. 3.26c and with 6 QWs in Fig. 3.26d. The detailed view of the strain balanced QWs is shown in Fig. 3.30. The 9.2 nm-thick $In_{0.06}Ga_{0.94}As$ QWs are separated with the 3.2 nm-thick $GaAs_{0.68}P_{0.32}$ layers with the 1 nm-thick GaAs interlayers which serve to potentially preserve abrupt interfaces. Both strain balanced QW solar cells were grown on $2° \rightarrow \langle 110 \rangle$ offcut substrates and where applies, $6° \rightarrow \langle 110 \rangle$ offcut is specified as 6 deg., since offcut direction was unchanged in this experiment.

All supplementary sample-to-sample data breakdown from the Round 2 presented below is **without** anti-reflective coating (ARC) (Fig. 3.31). In Figure 3.31, the dopant types are denoted on the left side and all supplementary labelling is given on the right. The record (pre-ARC) efficiency achieved in the sample with DBR and is greatly attributed to the current and fill-factor enhancement and is 17.2% (AM0). It is also clearly seen that carbon doping used for the GaAs base promoted an enhancement in the V_{oc} by up to 20 mV compared to the Zn-doped base devices. The Fig. 3.31 presents the values gathered from the best performing cells in each device batch. The statistical efficiency data of the Round 2 cells is given in Fig. 3.32. The statistics is gathered from 12 1 cm × 1 cm cells per wafer. The maximum average efficiency is measured in the DBR-enhanced cells. Another observation is that the distribution of efficiencies is narrower in strain-balanced QW cells (SB 3 × QW and SB 6 × QW). Adding strain balancing makes the devices less sensitive to the possibly occurring variation in the QW thickness across the wafer that nominally is at the critical thickness, so an accidental increase in the QW thickness can cause a buildup of the strain energy. Adding strain balancing alleviates this effect and spatial voltage and current uniformity improves. Doubling the number of QWs was performed with minimal losses in efficiency opening up a route for further investigation of the limiting number of QWs for extended and efficient light absorption beyond the bandgap of GaAs.

The observations made in Round 2 clearly indicate the path to take for the next rounds in pursuit of the highest efficiency of the single-junction solar cell. The benefits of strain balancing that will allow to further increase the number of QWs and potentially vary the content of In to deepen the wells combined with the DBR structures are the avenue to boosting the short-circuit current density with preserved open-circuit voltage and fill factor.
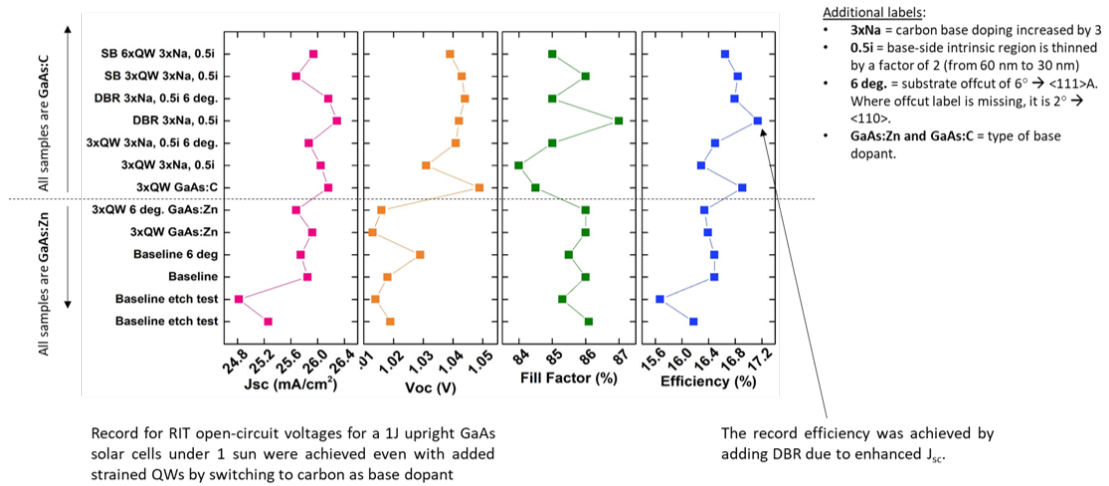
FIGURE 3.31: Round 0, 1, and 2 data summary. All metrics are collected BEFORE anti-reflective coating (ARC) deposition to enable direct comparison of the impact of changing device parameters.
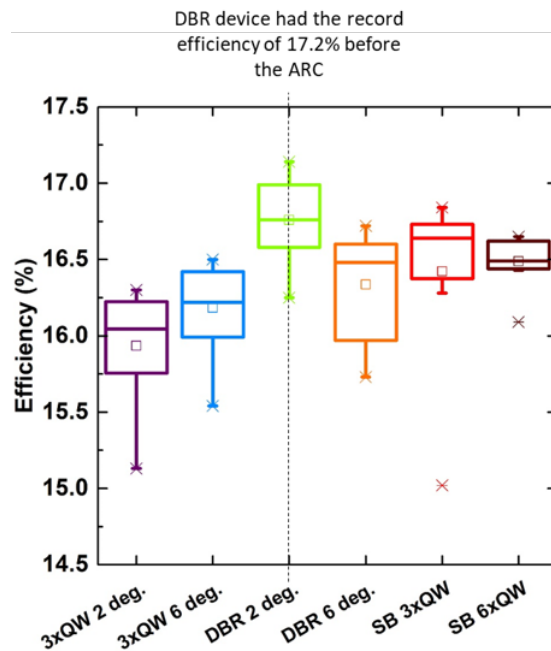
FIGURE 3.32: Statistical summary of AM0 efficiency of the solar cells from Round 2. All data is collected before the ARC. The offcut of the substrates (2 deg. or 6 deg.) is specified.

Taking a closer look at the data (Fig. 3.31), an increase in number of 6%In SB QWs from 3 to 6 led to an average reduction in V_{oc} by 6 mV and fill factor reduction by 1% absolute was observed as well which are relatively insufficient changes, but some concerning aspects associated with strain-balanced QWs are revealed in quantum efficiency spectra. Figure 3.33 shows IQE curves corresponding to the QW conversion region for the samples with strained $3 \times \text{In}_{0.06}\text{Ga}_{0.94}\text{As}$ QW separated with 4 nm-thick GaAs barriers (Previous Champion), the same QW structure, but with thinned intrinsic region framing the QW region and 3 times increased base doping (BL - 2 deg.), and strain balanced QW structures, $3 \times$ SBQW and $6 \times$ SBQW (same tripled doping and i-region layer thicknesses as in the BL sample). Comparing the spectra of the Previous Champion cell and BL, the apparent QE drop of the curve can be observed. On a fundamental level, this can be caused by alterations in the quantum confinement and density of states in the QWs (i.e., absorption spectrum) or by carrier extraction efficiency (i.e., electric field). For these samples without strain balancing specifically, the IQE reduction can be caused by the changes in E-field, since narrowing the base-shifted intrinsic region from 62 nm down to 31 nm could have resulted in a placement of the QWs where E-field is not steady.

A more dramatic change in IQE is observed in the strain-balanced QWs where blue shifting of the spectral curves by up to 15 nm was observed. On a manufacturing level, uncontrollable reduction in In incorporation efficiency could cause the actual QW composition to get In-depleted (the suspected reason is gradually reducing TMIn pick-up efficiency as the precursor bubbler is approaching its end of life), so the subsequent InGaAs growths performed with a sufficient time difference are likely to need a composition adjustment by calibration, however, it is highly unlikely for these samples, since they were grown back to back. To investigate and demonstrate the spectral absorption
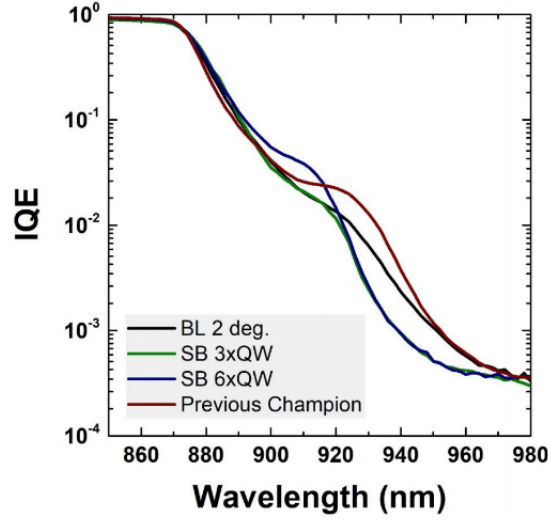
FIGURE 3.33: QW IQE of the samples with strained $3 \times \text{In}_{0.06}\text{Ga}_{0.94}\text{As}$ QW separated with 4 nm-thick GaAs barriers (Previous Champion), the same QW structure, but with thinned intrinsic region framing the QW region and 3 times increased base doping (BL - 2 deg.), and strain balanced QW structures, $3 \times$ SBQW and $6 \times$ SBQW (same tripled doping and i-region layer thicknesses as in the BL sample).

range dependency on the QW parameters (QW thickness, QW composition, and barrier thickness), parametric modeling of the QW structures was performed using next**nano**. Figure 3.34 shows dependency of the simulated transition spectra on QW composition, thickness, and barrier thickness. The cumulative transition intensity spectra are a superposition of all allowed transitions determined by non-zero electron and hole wave function overlap $|\langle\phi_e|\phi_h\rangle|^2$. Equation 3.16 shows band-to band recombination rate:

$$R_{Rad} = \frac{q^2 E_p \omega n}{2 m_0 \epsilon_0 h c_0^3} |\langle\phi_e|\phi_h\rangle|^2, \tag{3.16}$$

where q is electron charge, E_p is Kane energy, m_0 is electron mass, n is refractive index, c_0 is the speed of light, and ω is a frequency corresponding to the transition energy [151]. As Figure 3.34a shows, $\text{In}_x\text{Ga}_{1-x}\text{As}$ QW composition with increasing In content leads to the red shift of the main excitonic transition, whereas QW thickness varied within a possible growth error ($\pm$ 1 nm from target 9.2 nm) has minimal effect (Fig. 3.34b). The dependence of the main transition peak wavelength plotted for varied In

content in comparison to the QW and barrier thicknesses are shown on Fig. 3.34c and d, respectively. Assuming the possibility of the %In variations from growth to growth resulting in the absorption edge change rate of ∼10 nm per each %In change and relatively slow dependency of the transition peak position with varied QW and barrier thickness, it is a fair assumption that fluctuating In content is the factor driving the QW band edge shift. Figure 3.35 showing measured PL spectrum of the $In_{0.09}Ga_{0.91}As$ QW structure and simulated spectrum validates the accuracy of this model and assumptions made given that the offset between the modeled and experimental data is only 2 nm which can be attributed to the composition fluctuation within tens of a percent absolute.

Returning to the strain-balanced $In_{0.06}Ga_{0.92}As/GaAs_{0.68}P_{0.32}$ QW structures exhibiting a blue shift compared to the QWs separated by GaAs barriers, the reduction in In incorporation efficiency does not seem to be a satisfactory explanation. At the same time, changing the barrier height by replacing GaAs with 3.2 nm-thick GaAsP layers also result in minimal deviation in the peak position. The answer might be inspired by the XRD spectroscopy.

Figure 3.36 shows a multitude of the (004) reflection XRD spectra of the solar cell structures without QWs (control samples), with strained triple QWs separated by 4 nm-thick GaAs layers, and with QWs strain balanced with $GaAs_{0.68}P_{0.32}$ layers. The InGaAs composition is varied in some samples (6%, 10%, and 14%In are shown and indicated for each spectrum on the right; all samples are grown on the offcut (100)GaAs substrates and the magnitude of the offcut angle, 2° or 6°, is specified in the legend as well). If QW superlattice is formed, in addition to the interference of the waves scattered by the atomic planes, a higher order diffraction from the repeated nanolayers results in the occurrence of the Pendellosung fringes as shown on Fig. 3.37a [152] and a high-quality InGaAs/GaAsP QW superlattice structure's XRD spectrum is shown on Fig. 3.37b
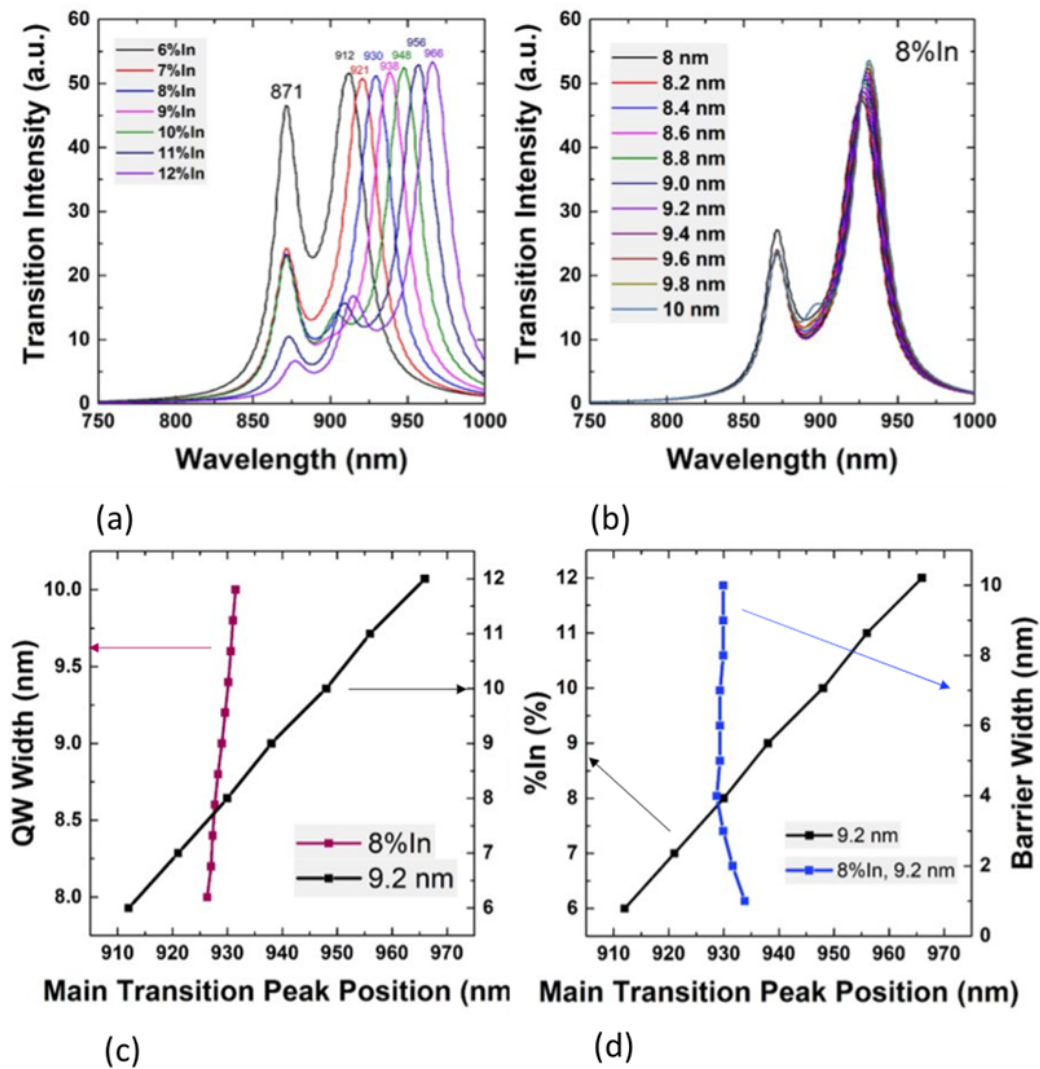
FIGURE 3.34: Transition intensity spectra in the $3 \times$ QW superlattices for $In_xGa_{1-x}As$ with (a) varied In content (QW thickness 9.2 nm and fixed) and (b) varied QW thickness (composition is fixed at 8%). (c) Dependence of the main peak transition wavelength on the fixed width QW composition (black points) and on the fixed composition QW width (purple points); the lines are added as guides; and (d) peak position vs. QW separating barrier thicknesses (blue line) for fixed QW thickness and composition.

with superlattice peak orders denoted (the sample is from one of the later calibration sample series and is shown here as an example). On Fig. 3.36, the superlattice peaks are present only in the spectra produced by the structures with strained $3 \times$ QW (i.e., separated by the GaAs layers). In contrary, adding strain balancing with 32%P (curves labeled as SBQW) content results in smearing of the superlattice fringes irrespective of the number of QWs.
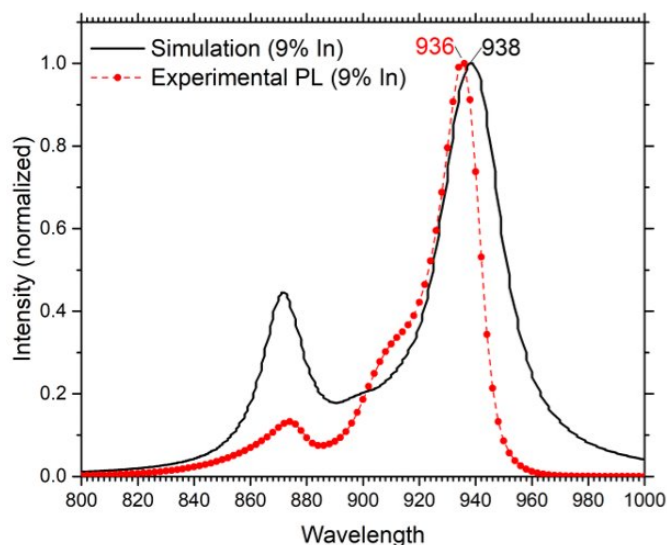
FIGURE 3.35: Photoluminescence of the $In_{0.09}Ga_{0.91}As$ QW structure (composition was additionally confirmed with XRD) shown in red in comparison with the predicted transition intensity spectrum for $In_{0.09}Ga_{0.91}As$ QW structure shown in black.
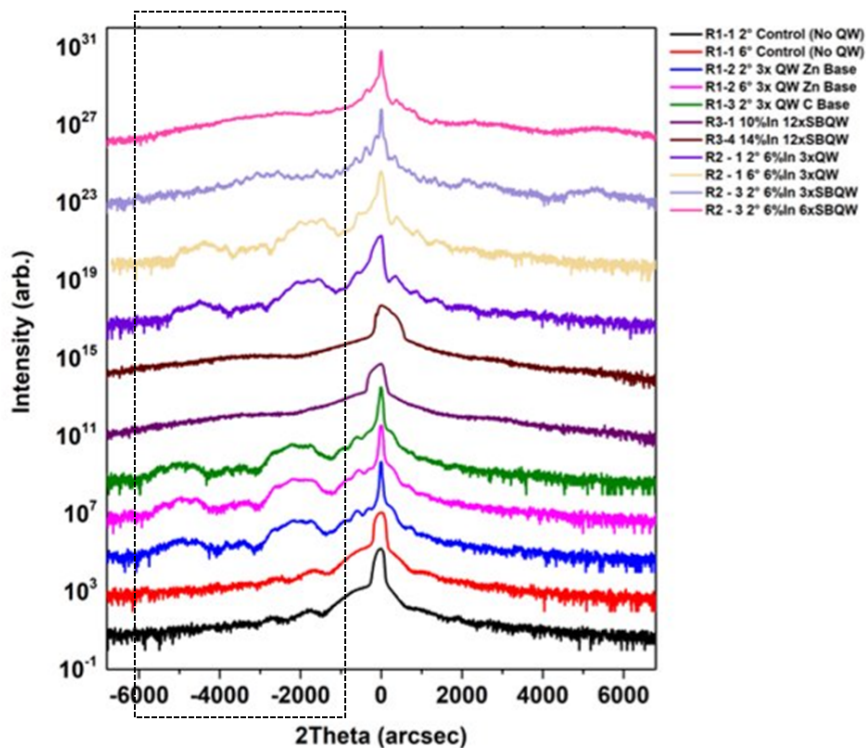
FIGURE 3.36: XRD spectra of the QW solar cells including the baseline devices with no QWs, devices with strained QWs separated by 4 nm-thick GaAs barriers and with $GaAs_{0.68}P_{0.32}$ strain balancing layers. The outline shows the region where the occurrence of the Pendellosung fringes is expected if QW superlattice is formed.

A known reason for increased full-width half-maximum (FWHM) of the SL fringes, and essentially, the broad features that are seen at the angles below the Bragg peak can be interpreted as widened, is interface smearing which can be caused by diffusion of In from the QWs into the barriers and P from the barriers into the QWs. The high angle annular dark field (HAADF) scanning transmission electron microscopy (STEM) and energy dispersive spectroscopic (EDS) study performed by J. Samberg *et al.* [134] shows the cross-sectional profile of the $In_{0.23}Ga_{0.77}As/GaAs_{0.2}P_{0.8}$ superlattices with 7 nm-thick GaAs interlayers coming from GaAsP to InGaAs and 0.7 nm-thick GaAs coming from InGaAs to GaAsP clearly demonstrating the interdiffusion of the In and P species across the QW/SB interfaces (Fig. 3.38). From the crystallographic analysis perspective, this can be interpreted either as alternating graded layers. In addition, it can be associated with elevated interface roughness. In particular, the FWHM of the superlattice fringes is determined by the relative interface roughness $\frac{\sigma}{\Lambda_0}$ as:

$$W_n = W_0 + (ln2)^{1/2}n\Delta\theta_M\frac{\sigma}{\Lambda_0}, \tag{3.17}$$

where W_n and W_0 are the FWHM of the nth order satellite peaks and $\Delta\theta_M$ is the angular distance between the adjacent satellite peaks [114]. In the extreme case, degeneracy of the peaks can progressively occur when interface roughness increases. While photoluminescent properties of the QW structures with roughened interfaces cannot be efficiently simulated requiring atomic resolution and 3D workflow, the transitions in the QWs with non-abrupt transitions from QW to strain balancing and vice versa, as shown with the material profile and band structure on Fig. 3.39a can be evaluated. Comparing the simulated transition spectrum of such diffuse superlattice to the spectrum of the ideal
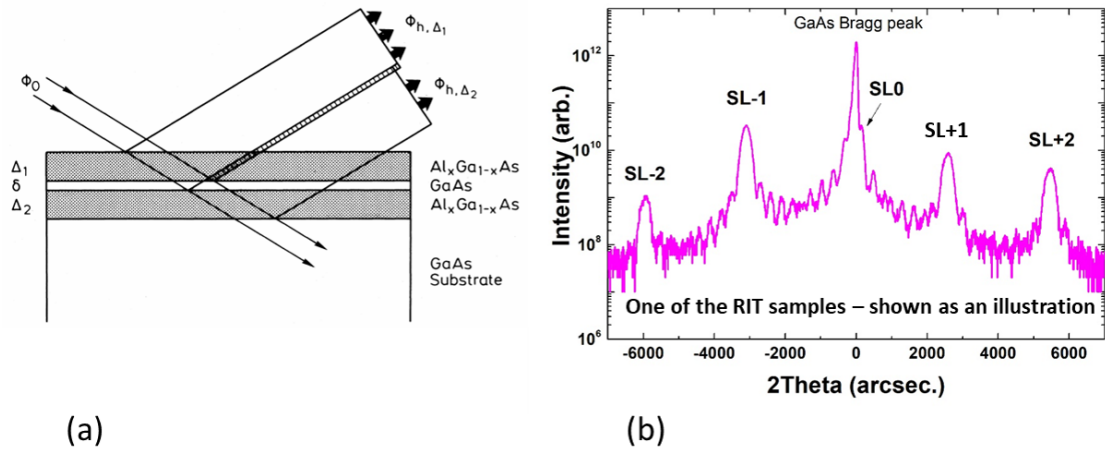
FIGURE 3.37: (a) A diagram showing X-ray scattering and interference on an AlGaAs/-GaAs heterointerface [152]. (b) XRD spectrum of an InGaAs/GaAsP superlattice.

SBQW superlattice's shown on Fig. 3.39b, there is a clear 15 nm blue shift originating from the graded material profiles. It is important to understand that the structure modeled in this simulation study is not immediately representative of the actual structure, but assessing the impact of the QW/SB imperfections on the quantum structure specifically is useful to not rule out the influence of the structural non-uniformity on the spectral properties of the quantum wells manifesting in quantum efficiency and PL spectra.

Correlating the XRD, QE, and modeling observations, it becomes clear that transitioning to strain balanced $In_{0.06}Ga_{0.94}As/GaAs_{0.68}P_{0.32}$ QW superlattices causes morphological disruption of the superlattice and interface degradation compared to the $In_{0.06}Ga_{0.94}As/GaAs$ QWs. Disappearing superlattice fringes in the SB QW XRD do not even allow to determine the impact of the offcut on FWHM, however, since $6 \times$ SBQW devices exhibit minimal losses in V_{oc} (only up to 6 mV), so the next attempt to integrate the SB QWs was done. In the next set of experiments, solar cells with 12 periods of $In_{0.10}Ga_{0.90}As/GaAs_{0.68}P_{0.32}$ and $In_{0.14}Ga_{0.86}As/GaAs_{0.68}P_{0.32}$ grown on $6° \rightarrow \langle 110 \rangle$ offcut substrate with and with no 12-pair $Al_{0.1}Ga_{0.9}As/Al_{0.9}Ga_{0.1}As$ DBR were manufactured to study how In content and number of QWs affects dark current
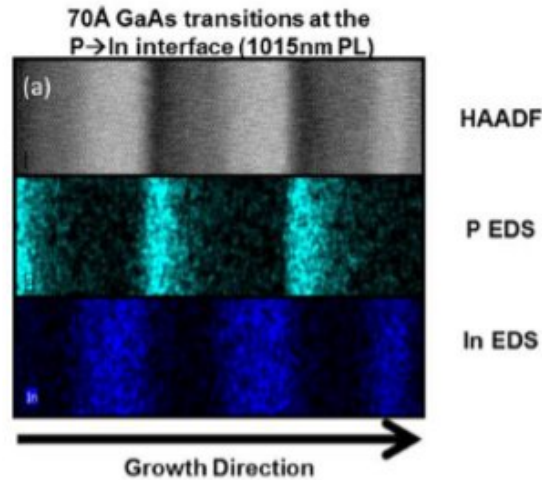
FIGURE 3.38: HAADF STEM images and EDS plots for two $In_{0.23}Ga_{0.77}As/GaAs_{0.2}P_{0.8}$, 20 period MQW structures with GaAs transitions of 7 nm at the Ga(As,P) to (In,Ga)As transition and 0.7nm at the (In,Ga)As to Ga(As,P) transition [134].

and V_{oc}. The DBR structure and properties remained the same as in the preceding round of devices (Fig. 3.28).

3.4.5 Impact of the QW Depth and Number on Solar Cell Dark Current and V_{oc}

Summary of the device structures is shown on Figure 3.40. The study consisted of 4 types of solar cells with 12 periods of QW superlattices ($In_{0.10}Ga_{0.90}As/GaAs_{0.68}P_{0.32}$ and $In_{0.14}Ga_{0.86}As/GaAs_{0.68}P_{0.32}$) and DBR structures and concluded the series of QW solar cells with phosphorous-rich strain balancing.

It is expected (Eq. 3.6) that increasing QW depth can lead to the increase in non-radiative dark current, and it can lead to the reduced fill factor and V_{oc}. Table 3.1 summarizes the AM0 parameters of the solar cells. Efficiencies of all devices with extended QW superlattices do not exceed 15% (the maximum baseline cell efficiency was 17.1%) and go below 12% in devices with 14%In QWs which are affected by both voltage and fill factor reduction.

(a)   (b)
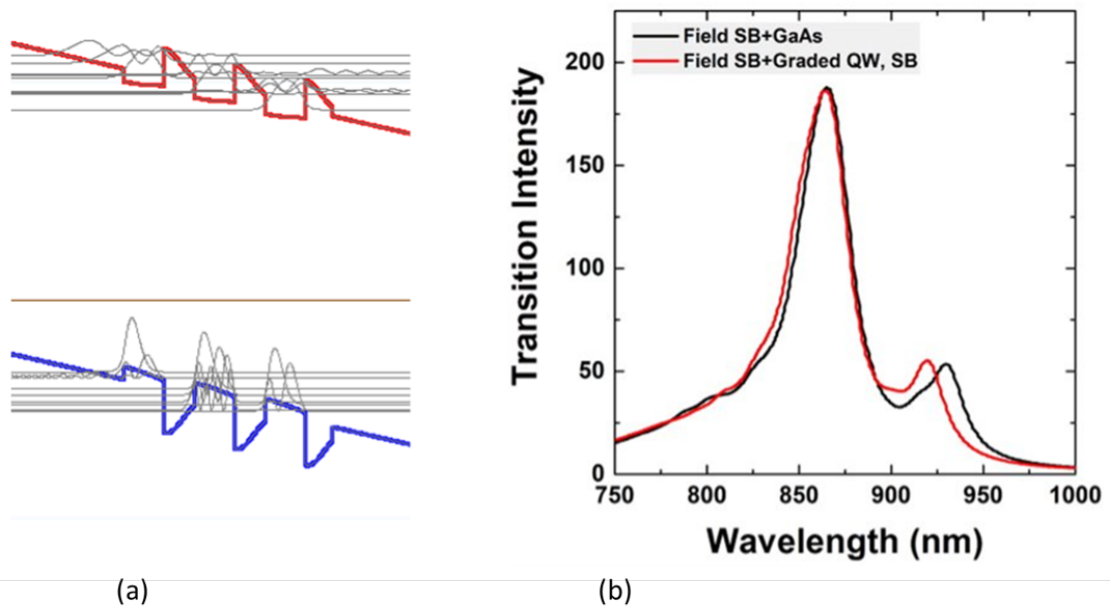
FIGURE 3.39: (a) Band structure and energy states of the graded 3 - 8%In QWs separated by the 0 - 32%P strain balancing and (b) corresponding transition intensity spectrum of the structure with graded material profile (red line) in comparison with the ideal abrupt-interface structure's spectrum (black line).
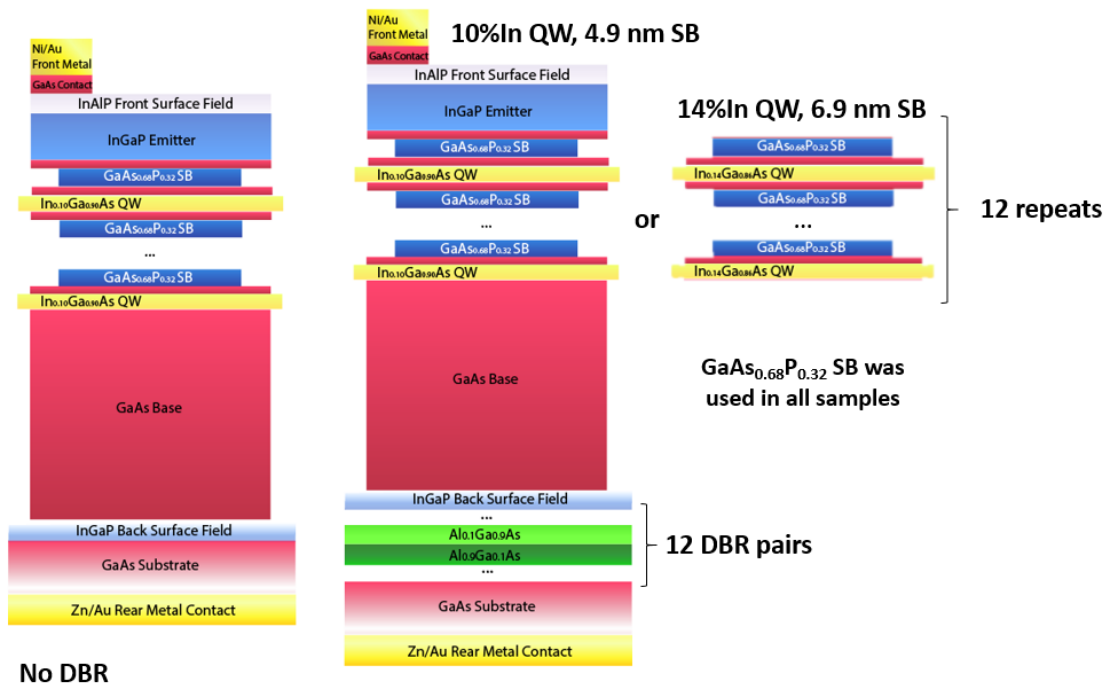
FIGURE 3.40: Deep QW solar cell study structures including devices with $In_{0.10}Ga_{0.90}As/GaAs_{0.68}P_{0.32}$ and $In_{0.14}Ga_{0.86}As/GaAs_{0.68}P_{0.32}$ QWs with or without the DBR consisting of 12 $Al_{0.1}Ga_{0.9}As$ pairs. All structures were grown on $6° \rightarrow \langle 110 \rangle$ offcut (100)GaAs substrates.

Parameter:	10%In	10%In, DBR	14%In, DBR	14%In
J_{sc}, mA/cm^2	26.28 ± 0.17	26.44 ± 0.17	26.58 ± 0.18	26.10 ± 0.18
V_{oc}, V	0.719 ± 0.190	0.982 ± 0.025	0.824 ± 0.008	0.831 ± 0.009
FF, %	58.7 ± 14.4	74.3 ± 1.2	72.0 ± 2.9	74.9 ± 1.25
Efficiency, %	8.52 ± 3.94	14.13 ± 0.48	11.55 ± 0.55	11.90 ± 0.36

TABLE 3.1: $12 \times$ QW solar cell parameters under 1 sun AM0 illumination.

The IV characteristics of the cells with the highest efficiency out of each type of the device are shown on Figure 3.41a. A notable drop in V_{oc} is observed upon increasing the In content in the QWs. Surprisingly, the lowest J_{sc} is observed in the 14%In device, and resonant DBR absorption enhancement in the near-band edge bulk and QW regions resulted in an increase of $\sim$0.2 mA/cm^2. Fill factors of the cells with tunneling strain balancing barriers and deeper $12 \times$ QWs reduced by over 6% absolute compared to the cells with 6%In QWs where only 3 or 6 QWs are present, which may be a consequence of either the transport problems or of the excessive non-radiative recombination rate inside the QW region. Quantum efficiency spectra shown on Fig. 3.41b feature minimal bulk response alterations below 650 nm indicating no residual strain from the QWs, however, the 10%In sample with no DBR surprisingly has lower GaAs base response, which can be specific to the cell measured. DBR reflectivity spectrum (Fig. 3.28) FWHM is $\sim$100 nm, so oscillations near the band edge in the bulk region are also observed, however, the base thickness in these devices was increased from 2.9 μm to 3.5 μm, so optical bulk EQE enhancement is not as pronounced as in the thin-base devices. In the In$_{0.14}$Ga$_{0.86}$As/GaAs$_{0.68}$P$_{0.32}$ QW cells, a 25 nm red shift of the EQE is observed closely matching the simulated results (Fig. 3.34c). After the ARC deposition, the strong cavity resonance peaks from 880 nm to 950 nm coming from the DBR will be gone.

Figure 3.42a shows a comparison of the QW region EQE spectra of the cells with no
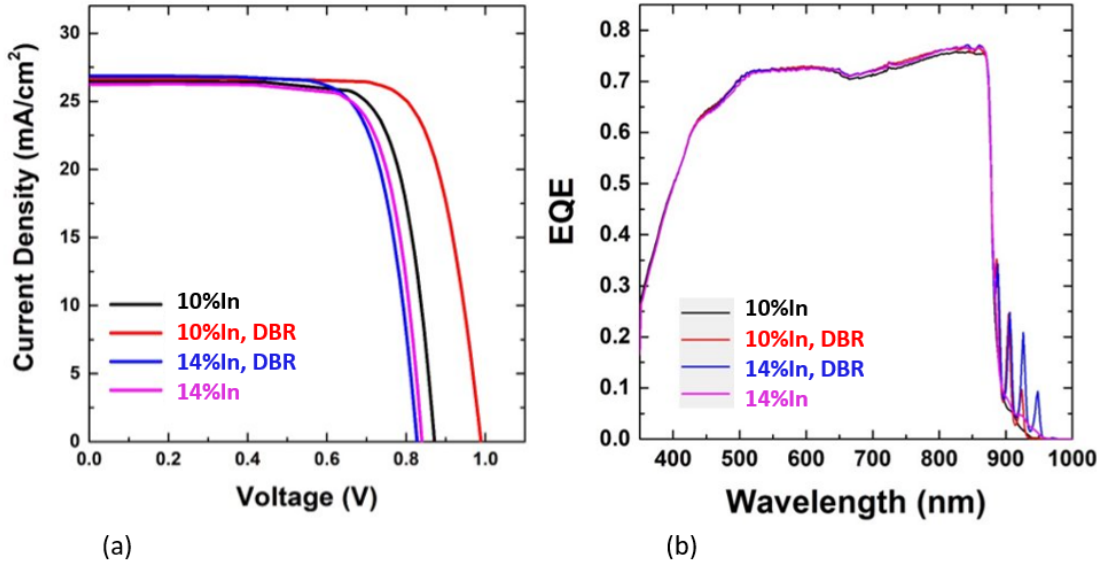
FIGURE 3.41: (a) AM0 light IVs and (b) EQE spectra of the $12 \times$ QWs: $In_{0.10}Ga_{0.90}As/GaAs_{0.68}P_{0.32}$ and $In_{0.14}Ga_{0.86}As/GaAs_{0.68}P_{0.32}$ (strain balancing layer thicknesses were adjusted to meet nominally net zero strain in a superlatiice as shown in Eq. 3.1) with and without the DBR.

DBR to the baseline (no QWs) and with different %In and Fig. 3.42b illustrates the change in QW EQE for varied number of QW periods. Broader absorption range in the 14%In compared to the 10%In converted to the extra current results in 0.08 mA/cm^2 J_{sc} enhancement. At the same time, an increase in the number of QW periods does not necessarily follow an expected linear change. First, one can observe $\sim$7 nm of the QW absorption edge red shift moving from 3 to 12 periods (Fig. 3.42b) indicating possible composition fluctuations which are a result of the growth control limitations discussed in the previous chapters. An increase in the EQE peak intensity is spectrally non-uniform, so for each QW structure extracted total $J_{sc}(QW)$ and associated ΔJ_{sc} per single QW period was extracted and summarized in Table 3.2. While current per QW increases in strain-balanced structures with deepening the QWs from 10% to 14%, it is clear that adding strain balancing reduces the current gain per QW as can be seen from the data acquired for the $3 \times$ QW 8%In sample with no SB and for the same number of QWs with 10%In with GaAs$_{0.68}$P$_{0.32}$ strain balancing added, so the current enhancement due to
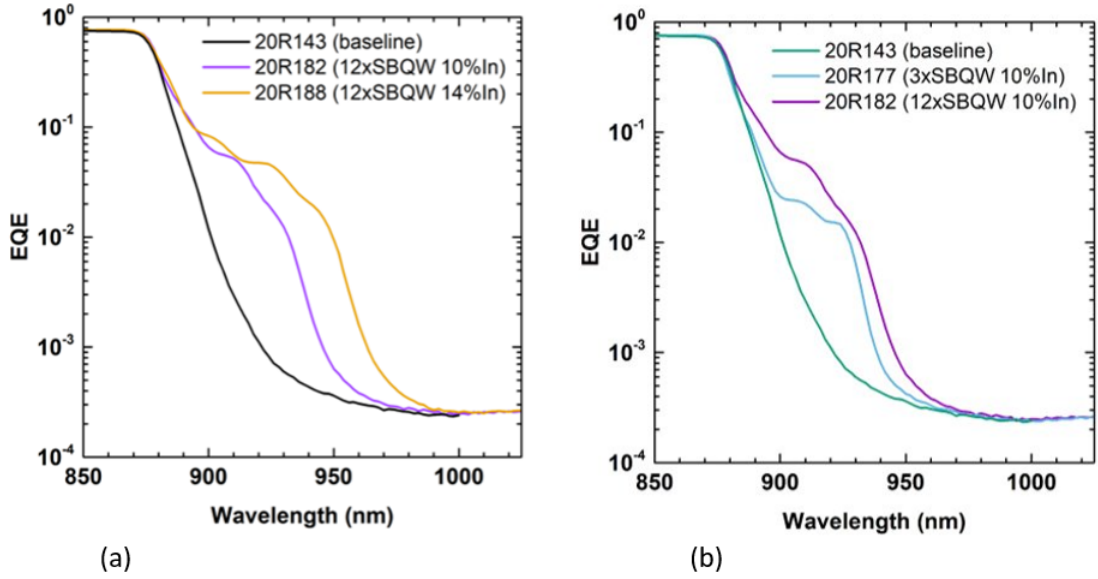
FIGURE 3.42: QW region of the EQE spectra of the cells with (a) 12 × In$_{0.10}$Ga$_{0.90}$As/GaAs$_{0.68}$P$_{0.32}$ and In$_{0.14}$Ga$_{0.86}$As/GaAs$_{0.68}$P$_{0.32}$ QWs and (b) 3 vs. 12 periods of In$_{0.10}$Ga$_{0.90}$As/GaAs$_{0.68}$P$_{0.32}$ QWs compared to the baseline device.

increasing the QW depth is overtaken by the reduction due to the GaAs$_{0.68}$P$_{0.32}$ barriers. An assumption that can be drawn from solely EQE spectroscopy and modeling can be that the interface between the QW and SB causes a blue shift and that carrier escape might be impeded, however, combining the spectroscopic results with the V_{oc} and J_{02} analysis can lead the reader to a fuller picture before the explicit explanation for the deterioration of the QW solar cells performance as strain balancing is added.

Dependency of the V_{oc} on the number of QWs for GaAs$_{0.68}$P$_{0.32}$-strain-balanced In$_{0.06}$Ga$_{0.94}$As, In$_{0.10}$Ga$_{0.90}$As, and In$_{0.14}$Ga$_{0.86}$As QW solar cells is shown on Figure 3.43. A direct correlation between the V_{oc} and the QW depth is seen resulting in up to 150 mV loss coming from 10%In to 14%In QW composition. At the same time, the rate of the V_{oc} reduction following the increase in the QW number changes with the QW depth. For 10%In QWs, 12-period superlattice device shows V_{oc} reduction by 40 mV compared to the 3-period structure. Unfortunately, at the moment of writing this work the intermediate data for a full spectrum of QW numbers was unavailable, so completion of this work to separate

J_{sc}, mA/cm² :	12× 10%In, SB	12× 14%In, SB	3× 8%In, no SB	3× 10%In, SB
QW total	0.16	0.24	0.09	0.03
Per period	0.013	0.020	0.030	0.010

TABLE 3.2: Extra J_{sc} originating from the QW region in total and ΔJ_{sc} per QW for various QW superlattice structures.
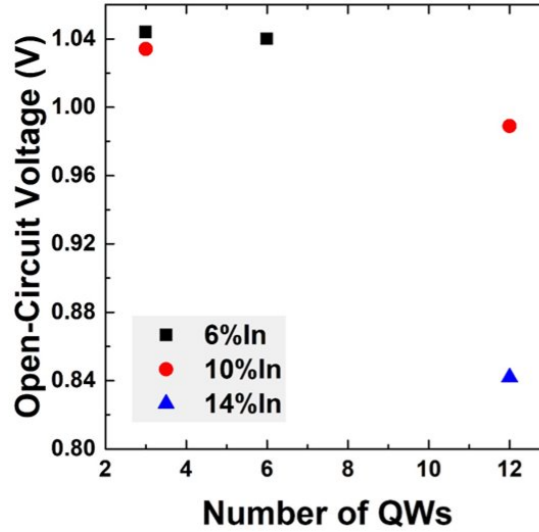
FIGURE 3.43: V_{oc} of the solar cells with GaAs$_{0.68}$P$_{0.32}$-strain-balanced In$_{0.06}$Ga$_{0.94}$As, In$_{0.10}$Ga$_{0.90}$As, and In$_{0.14}$Ga$_{0.86}$As QWs dependent on the number of QWs.

and correlate the influences of the QW depth and number can be addressed in the future. However, if the QW bandgap reduction was directly responsible for the V_{oc} offset, such a dramatic V_{oc} reduction would not be observed (the main transition energy lowers by 52 mV coming from 10% to 14%), so excessive non-radiative recombination is responsible for the voltage loss.

Figure 3.44 shows V_{oc}'s of the various solar cells vs. their J_{sc} (the sample attributes for each data point are shown on the sides). The equation representing the V_{oc} shown in the inset is derived from the two-diode equation for a device in a non-radiative limit (ideality factor n = 2), and blue line represents calculated V_{oc} values by substituting the measured J_{sc} and J_{02} extrapolated from the dark current measurements. Measured V_{oc} values of the solar cells with extended superlattices of 10%In and 14%In QWs accurately fall on the calculated non-radiative V_{oc} line, while the group of QW samples and baseline solar
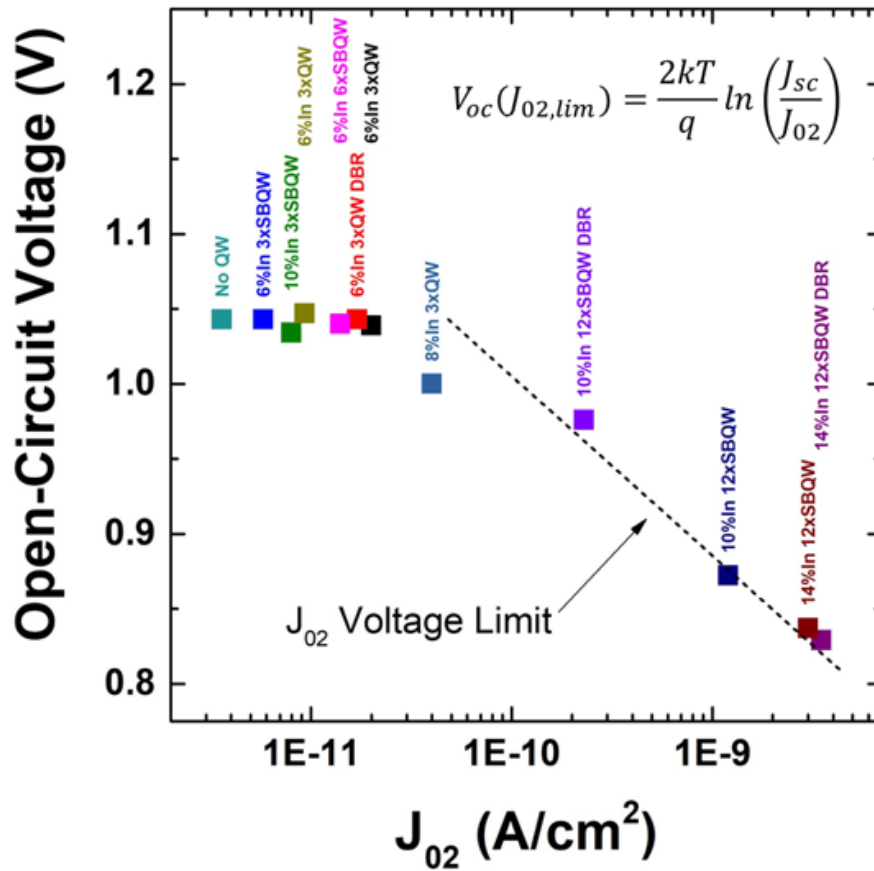
FIGURE 3.44: Dependency of the measured V_{oc} on measured J_{02}. The dashed line shows the V_{oc} calculated using the equation in the inset using the J_{sc} and J_{02} measured for the corresponding cells. The sample attributes are denoted for each data point.

cell exhibit a mixed behavior with the ideality factor $1 < n < 2$. The critical J_{02} value is 1.1×10^{-10} A/cm^2 at which V_{oc} becomes dominated by non-radiative recombination.

Using Eq. 3.7 by substituting the effective bandgap offset and measured $J_{02,QW}$ and $J_{02,Bulk}$ an increase in non-radiative lifetime can be extracted as shown on Fig. 3.45. Fig. 3.45 shows an increase in the J_{02} due to the added QWs into the intrinsic region and occupying a fraction f_{QW} of the i-region volume plotted for various bandgap energy offsets between the QW and host material, $\Delta E/kT$, and lifetime reduction inside the QW region. This extrinsic added loss is a quantitative measure allowing to compare the density of traps and trap capture rates coming from the interface defects. In accordance
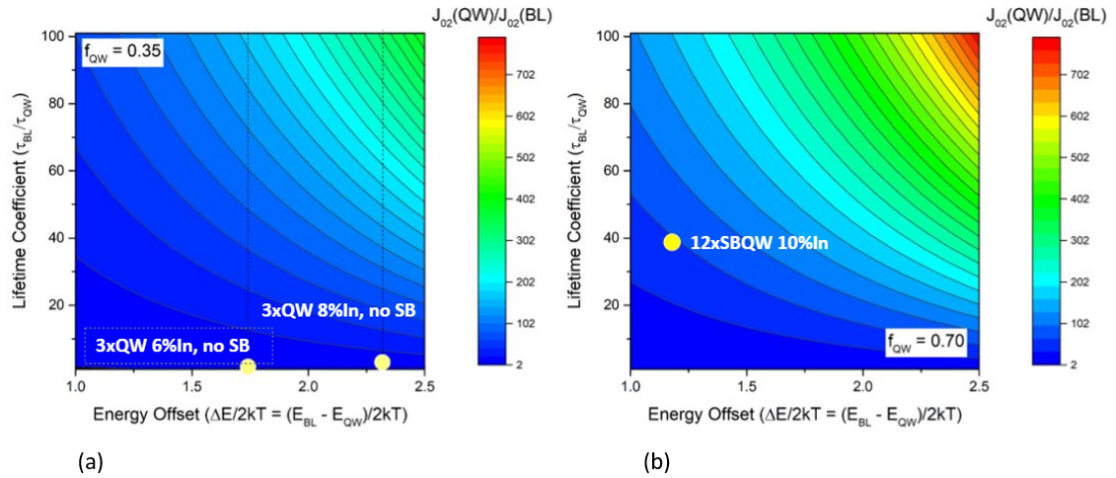
FIGURE 3.45: Non-radiative lifetime modulation factor due to added QWs compared to the bulk non-radiative lifetime calculated from Eq. 3.7 for the QW region volume fraction in the i-region of (a) 0.35 and (b) 0.70.

to the model, $12 \times$ SBQW 10%In structure has 40 times higher non-radiative recombination rate than an intrinsic GaAs (Fig. 3.45b) and in shallower QWs, the recombination rate increases by a factor of 1.5 and 2 times in 6%In and 8%In structures with no strain balancing (Fig. 3.45a).

3.4.6 Structural Analysis and Optimizations of the QW Superlattices

To investigate the origin of the deteriorated QW morphology leading to the dramatic non-radiative recombination increase, which becomes progressively influential in extended superlattices, XRD study confirming poor interfacial quality (Fig. 3.36) was accompanied by microscopic studies including atomic force microscopy (AFM) for step bunching analysis and cross-sectional TEM. The solar cell structures discussed in the previous chapters showing abnormal superlattice XRD were grown on the offcut substrates and the choice of the offcut for growing the devices is mainly determined by the desired growth modes and for managing ordering in ternary and quaternary materials (InGaP, InAlP, InAlGaP, etc.), so investigating the offcut influence on the growth of strained materials sequences specifically is an important step, since it can clearly affect

step bunching rate leading to the disruption of the 1D growth of the QWs and resulting in uncompensated opposite polarity strain zones propagating through the superlattice at an angle to the growth direction. Highly diffusion-driven, the step bunching process can also be controlled by a growth temperature, so QW growth temperature study was also conducted. The interface optimization study was also conducted by adjusting a switching sequence between the epitaxial precursors and/or adding interlayers to better manage cross-diffusion between the QW and SB layer species. In addition, a comparison between different types of GaAsP strain balancing ($GaAs_{0.68}P_{0.32}$ or $GaAs_{0.90}P_{0.10}$) was performed as well.

3.4.6.1 Switching Sequence and Interface Management Study

The first study within the optimization series comprised a set of 5 groups of samples that had different switching sequences as shown on Fig. 3.46a-e grown on on-axis ($0°$) and on $2° \rightarrow \langle 110 \rangle$ and $6° \rightarrow \langle 110 \rangle$ offcut (100)GaAs substrates resulting in total of 15 test structures. Each test structure intended for PL and XRD analysis had 10 periods of $In_{0.10}Ga_{0.90}As/GaAs_{0.68}P_{0.32}$ SBQWs and a 100 nm-thick GaAs capping layer, the offcuts correspond to the sample number indices, and GaAs interlayers are present only in selected switching sequence schemes (Fig. 3.46f). The labeled switching sequences replicate the reported processes as: "Nakano Optimized" [153] (Fig. 3.46b), "Samberg" [134], and "Nakano/Sugiyama" [154] (Fig. 3.46c) and their variants (Fig. 3.46d, e). All structures were grown at $650°$.

In Fig. 3.46, Interlayer corresponds to the GaAs inserts between the QW and strain balancing layers (here, Barriers), preparation for the barrier growth is Pre-flow of phosphine, and post-QW layer arsine is Post-flow, and hydrogen purge to desorb the trace species and prevent memory effect. "Nakano optimized" (Fig. 3.46b) features In purge
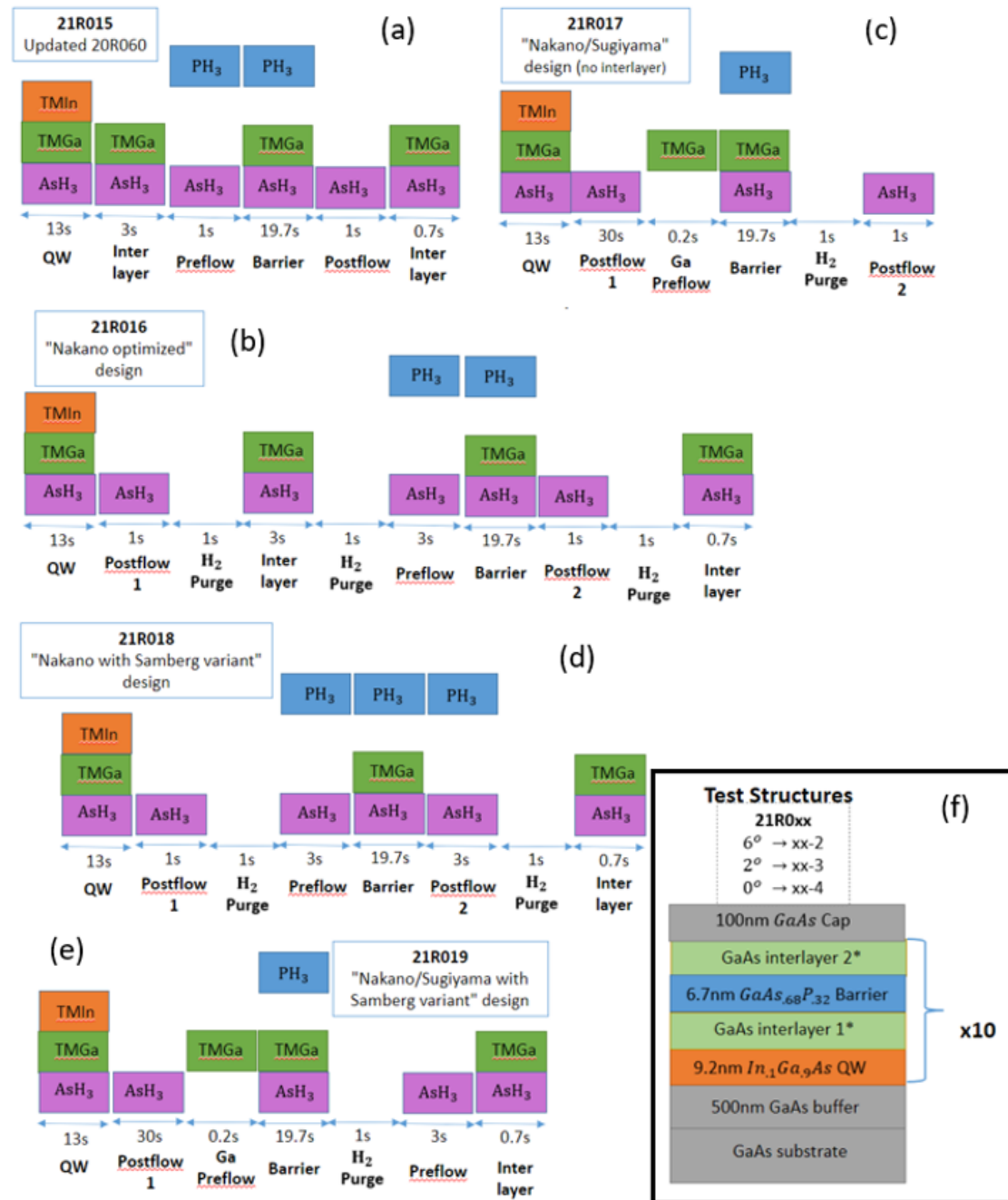
FIGURE 3.46: Flow switching sequences (a) RIT default, (b) "Nakano Optimized" [153], (c) "Nakano/Sugiyama" [154], (d) "Nakano with Samberg variant" [153, 134], (e) "Nakano/Sugiyama with Samberg variant" [154, 134] and (f) schematics of the test structure epitaxial layers. Sample numbers and indices after the dash correspond to the types of the switching sequences and offcut angles, respectively.
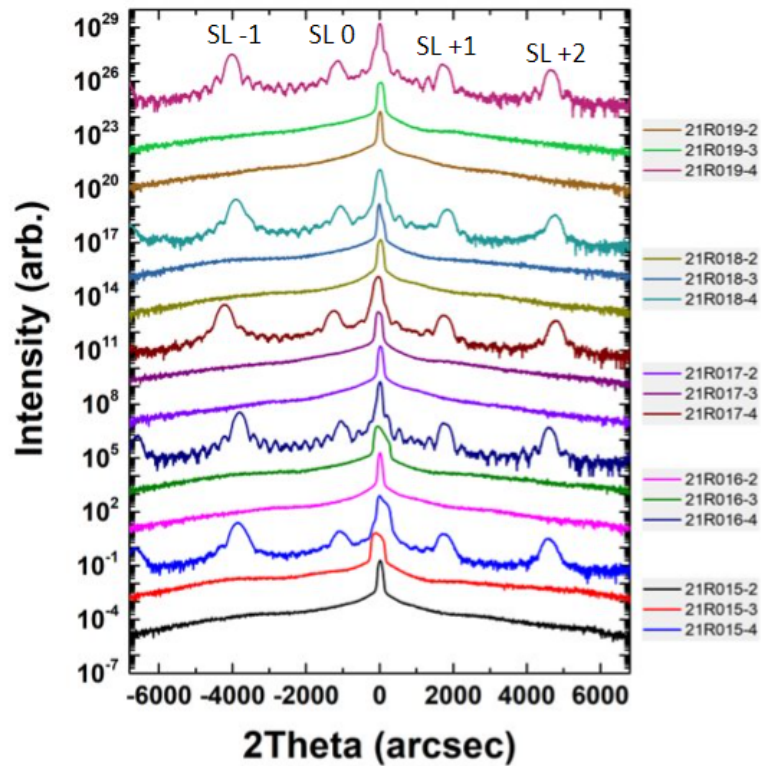
FIGURE 3.47: 2Theta/ω XRD spectra of the $10 \times$ In$_{0.10}$Ga$_{0.90}$As/GaAs$_{0.68}$P$_{0.32}$ SBQWs grown using various switching sequences and substrate offcuts as indicated in Fig. 3.46.

before GaAs barrier, H$_2$ purge between all, AsP before/after GaAsP, and GaAs barriers on both sides of strain-balancing layers. "Nakano/Sugiyama" design includes an In purge with AsH$_3$ before GaAsP and H$_2$ purge after GaAsP and no GaAs barriers altogether (Fig. 3.46c). "Nakano with Samberg variant" features In purge before the GaAs barrier, H$_2$ purge between all AsP before/after GaAsP, and GaAs barrier only after GaAsP strain balancing (Fig. 3.46d). The specifics for "Nakano/Sugiyama" sequence shown on Fig. 3.46e are In purge with AsH$_3$ before GaAsP, H$_2$ purge after GaAsP, and GaAs barrier after GaAsP. All of the approaches target manufacturing of the abrupt interfaces.

XRD spectra of the samples from the switching sequence series is shown on Figure 3.47. While superlattices grown on on-axis substrates clearly exhibit Pendellosung fringes (on-axis samples are labeled with the index - 4) and quantitative analysis can be performed

to compare relative interface roughness using Eq. 3.17, all offcut samples (indices - 3 and - 2), irrespective of the switching sequence, show absent or nearly absent superlattice signal. Based on the FWHM analysis of the SL peaks (only the first order peaks were considered) shown on the Figure 3.48a, "Nakano Optimized" switching sequence with GaAs interlayers on both sides of a QW and hydrogen purge was selected for all future optimization studies including growth temperature, SB composition, and offcut direction studies, as sample 21R016-4 showed the lowest FWHM of a SL peak (263 arcsec) closely comparing with the sample 21R019-4 ("Nakano/Sugiyama with Samberg variant", i.e., GaAs interlayer only after GaAsP) with SL peak FWHM of 265 arcsec. The optimized switching sequence allowed to reduce the SL peaks FWHM by 22% compared to the previously used RIT approach (21R015-4). Additionally, the oscillations resulting from higher order interference occurring in between the denoted (SL0, SL-1, etc.) fringes are most pronounced in the samples 21R016-4 and 21R019-4, while are almost vanished in the sample 21R015-4. By allocating the offset of the zero-order SL peak ($\Delta\theta_{SL0}$) from the Bragg peak (θ_{Bragg}) the ex-situ room-temperature strain in the QW structure $\Delta a/a$ can be calculated using differential Bragg's law as:

$$\frac{\Delta a}{a} = \Delta\theta_{SL0}cot(\theta_{Bragg}). \tag{3.18}$$

The SL period (thickness of a single QW plus SB unit) can be calculated as:

$$\mu = \frac{\lambda_{Cu,K_\alpha}}{\Delta\theta_{SL0}}(cos(\theta_{Bragg})^{-1}. \tag{3.19}$$

Figure 3.48b shows statistical data of XRD-extracted strain and period. Period fluctuations are natural due to the structural variations (one, two, or no 1 nm-thick GaAs
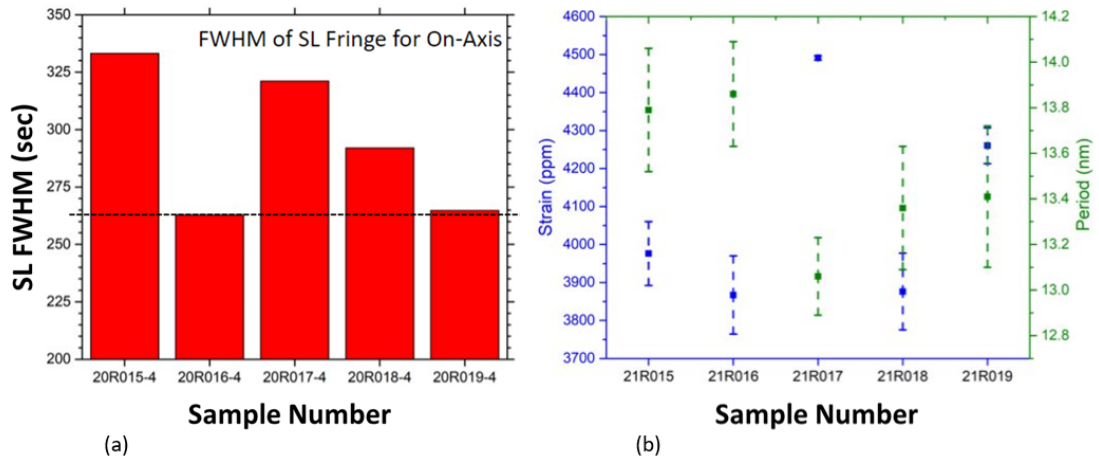
FIGURE 3.48: (a) FWHM of the first-order SL XRD peaks of the on-axis samples and (b) SL period and strain.

interlayers) and the values are close to the target: 9.2 nm InGaAs QW and 4.9 nm GaAsP SB resulting in 14.1 nm, plus GaAs interlayers where applies. Calibrations of the InGaAs and GaAsP composition and growth rate were initially performed on the 2° offcut substrates, so some thickness and stoichiometry deviations are possible during the growth on on-axis substrates, since step-flow growth was established. Those were thoroughly calibrated for the next sample sets. Relatively high compressive strain is likely a result of the layer thickness modulations suggesting that $GaAs_{0.68}P_{0.32}$ growth rate was lower on the exact substrate.

The expected interface refinement and recovery of the Pendellosung fringes in the offcut samples, however, did not follow, so the next approach involving excessive step bunching management was to investigate the impact of temperature. Another growth parameter, pressure, was included as well, as some authors report atmospheric pressure growth of high-quality InGaP/GaAsP superlattices [15], so increasing the reactor pressure from 100 mbar to 600 mbar was attempted. The 2Theta/Omega XRD spectra of the control samples, 21R016-3 and -4, grown at 650°C and 100 mbar pressure, of the low-temperature samples, 21R025-3 and -4, grown at 620°C and 100 mbar, and,

finally, the samples grown at elevated 600 mbar pressure and at $\sim$670°C which exceeded the target 650°C possibly due to the altered reactor pressure, 21R026-3 and -4. From comparison of the spectra of the on-axis samples (...-4), growth at elevated pressure and temperature resulted in lower compressive strain of 888 ppm compared to the other samples for which the extracted strain was 3867 ppm and 4694 ppm in 21R016-4 and 21R025-4, respectively. This can be a result of higher cracking efficiency of PH_3 and elevated phosphorous incorporation, since SL period remained nearly the same as in the low-temperature and low-pressure samples (13.62 nm vs. 13.82 nm and 13.86 nm, respectively). The inverse process can be leading to depleting strain balancing layer from P in the 620°C sample 21R025-4 which appears to be more compressive than 21R016-4. Additionally, from previous comparisons of the SL properties of $In_xGa_{1-x}As/GaAs$ strained QW superlattices and $In_xGa_{1-x}As/GaAs_{0.68}P_{0.32}$ strain-balanced QW structures (Fig. 3.36), incorporation of phosphorous-rich strain balancing layers results in removal of well-defined superlattices, so it is possible that phosphorous-poor strain balancing promoted some recovery of the Pendellosung fringes in sample 21R025-3, as can be seen in Fig. 3.49.

TEM imaging of the QW superlattice cross-section and AFM surface analysis along with the XRD spectra of the "Nakano Optimized" $10 \times In_{0.10}Ga_{0.90}As/GaAs_{0.68}P_{0.32}$ SBQWs are shown on Figure 3.50. Disruption of the superlattice growth with periodic thickness modulations featuring alternating regions with propagating opposite strain (strain causes film deformation resulting in the contrast) is seen in both offcut samples (Fig. 3.50b, c) compared to the on-axis structure (Fig. 3.50a). The AFM surface analysis of the 2° $\rightarrow \langle 110 \rangle$ sample (Fig. 3.50d) (the scan dimensions are 5 μm $\times$ 5 μm) shows atypical for thin film growth periodic bunching aligned along the growth terraces. To evaluate the height and calculate the number of monolayers (ML) the height profile was analyzed
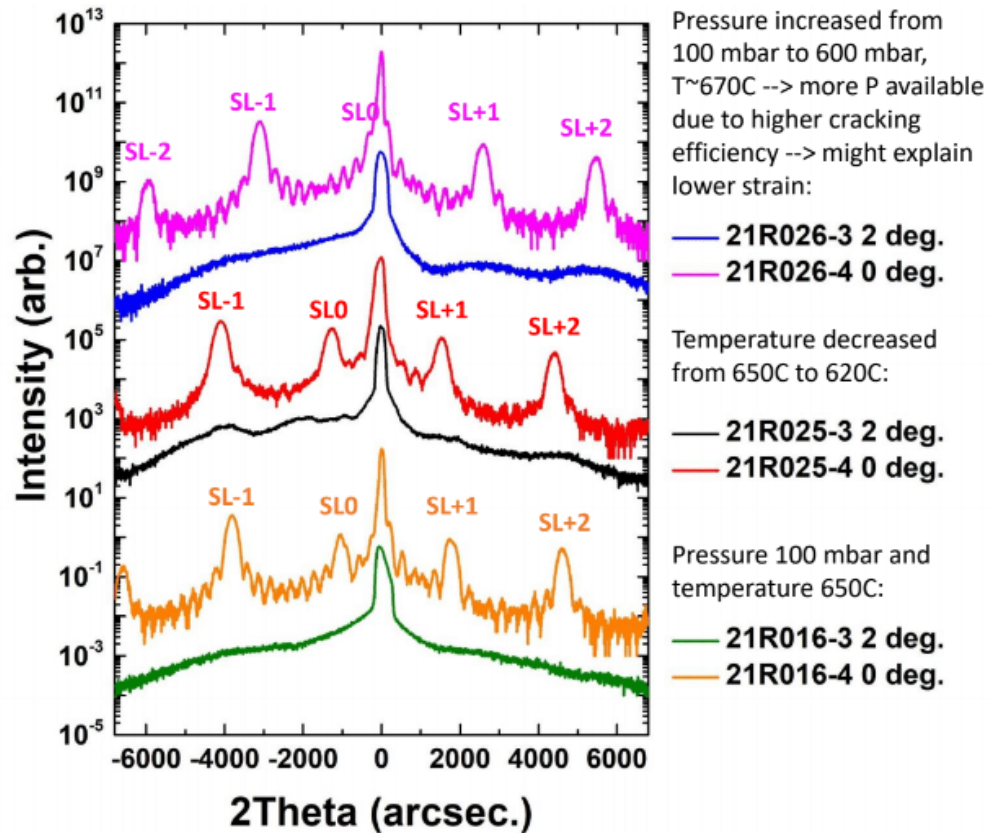
FIGURE 3.49: 2Theta/ω XRD spectra of the $10 \times \text{In}_{0.10}\text{Ga}_{0.90}\text{As}/\text{GaAs}_{0.68}\text{P}_{0.32}$ QWSLs grown on on-axis (...-4) and $2° \rightarrow \langle 110 \rangle$ (...-3) at 650°C and 100 mbar (21R016-3,4), at 620°C and 100 mbar (21R025-3,4), and at $\sim$670°C and 600 mbar (21R026-3,4; a simultaneous temperature increase likely occurred due to the pressure increase).

(Fig. 3.50e). The feature height measurement resulting in 5 - 10 nm height difference amplitude suggests that on average 4 ML per growth step in each QW and SB couple are aggregated. Lateral distortion of the superlattices on the offcut substrates result in broadened XRD SL features as Fig. 3.50f, since the signal is coming from the regions with varied thicknesses and angular orientation relatively to the substrate. A wavy growth commences in the first InGaAs layer and lateral thickness modulations are seen in TEM. Local compressive strain accumulation near the step edges and facet relaxation and preferential growth of strain balancing layers in the thin InGaAs regions cause formation of the regions with locally uncompensated opposite strain and aggravating thickness variations between the compressively strained bunched InGaAs and tensile GaAsP accumulation regions. This translates to the surface morphology observed in

AFM, and for the $2° \rightarrow \langle 110 \rangle$ sample the period of these features is up to 500 nm not necessarily following the individual terraces.

Correlating the structural properties and elevated non-radiative dark current, it becomes apparent that inclusion of propagating planes of superlattice stacking fault defects is responsible for lowering the carrier lifetimes and likely for the altered spectral properties of the nominally 9.2 nm $In_{0.10}Ga_{0.90}As/GaAs_{0.68}P_{0.32}$ QWs with strain balancing of 4.9 nm, given that the devices with comparable QW structures featuring 12-period superlattices reported in the previous section were grown on the $6° \rightarrow \langle 110 \rangle$ offcut (100)GaAs substrates with the immediate onset of the wavy growth which results in degeneration of strain balancing starting from the 5th period. It is expected, however, that using thicker (thermalization) strain balancing barriers would be beneficial for alleviating the strain balancing degeneration process due to non-uniform preferential growth leading to the formation of the alternating strain polarity growth regions, so in the next section this approach will be presented.

3.4.6.2 Strain Balancing Design for Lowered Non-Radiative Recombination in the QWs

As a first step, a test structure with 10 periods of $In_{0.10}Ga_{0.90}As/GaAs_{0.90}P_{0.10}$ capped with 10 nm GaAs was grown on $2° \rightarrow \langle 110 \rangle$ offcut substrate (Fig. 3.51a) for which strain balancing thickness of 17 nm was calculated using Eq. 3.1 and [149] (Fig. 3.51b). Carrier thermalization rates for both types of carriers shown on the Fig. 3.51b are calculated using the equation on the inset are given for the 32%P (red line) and 10%P (black line) SB barriers. This type of strain balancing structure is similar to the one reported by [15], yet featuring the GaAs interlayers and following the "Nakano Optimized" switching sequence. This test structure's spectral and morphological properties were compared
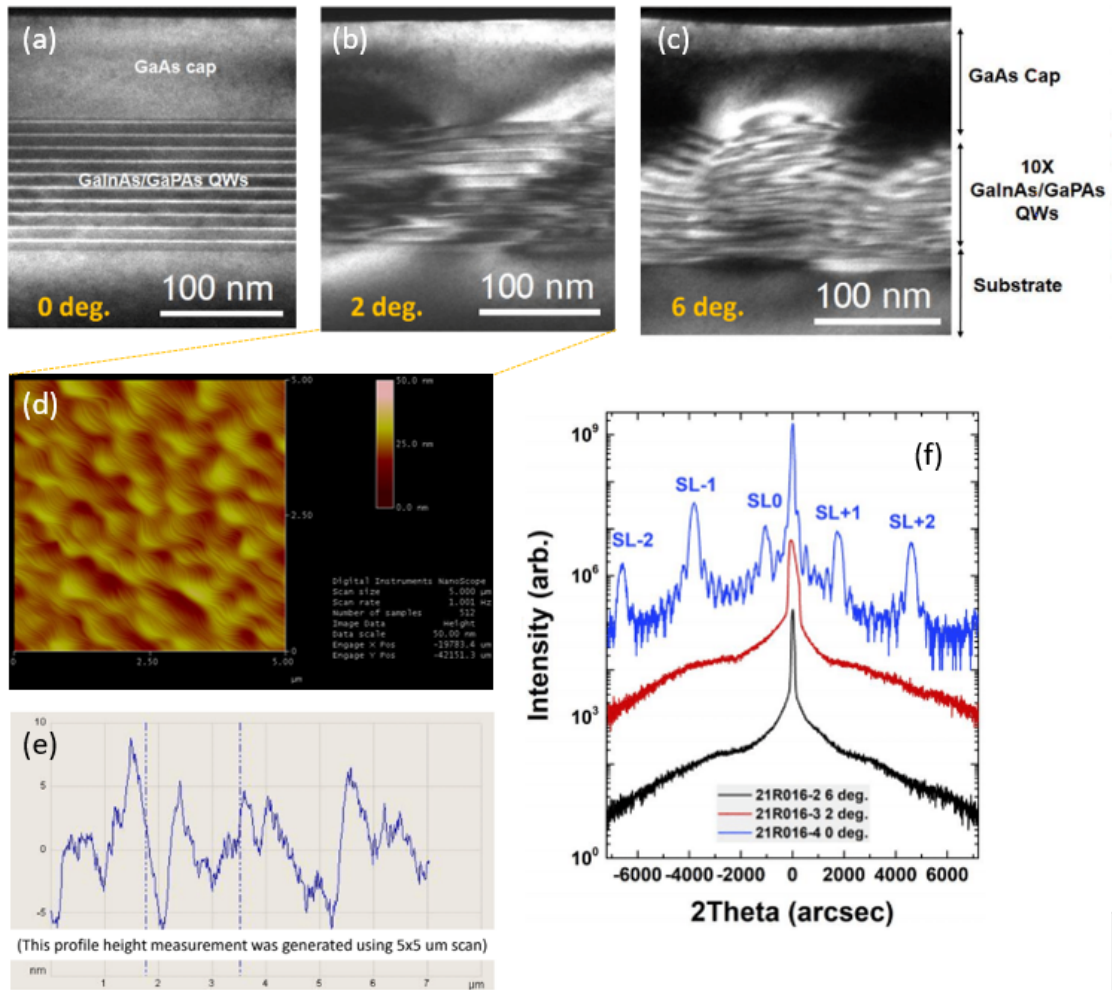
FIGURE 3.50: Cross-sectional TEM images of the "Nakano Optimized" $10 \times$ $In_{0.10}Ga_{0.90}As/GaAs_{0.68}P_{0.32}$ SBQWs grown at $650°$ on (a) on-axis, (b) $2° \rightarrow \langle 110 \rangle$, and (c) $6° \rightarrow \langle 110 \rangle$ offcut substrates. (d) AFM image of the $2° \rightarrow \langle 110 \rangle$ sample surface and (e) profile height analysis. (f) XRD spectra of the "Nakano Optimized" samples.

with the offcut samples from the previous series (21R016-3 and pressure and temperature studies, 21R026-3 and 21R025-3, respectively).

Figure 3.52a showing the 2Theta/Ω XRD spectra of the samples with thin, 32%P strain balancing grown under various conditions, i.e. changing pressure and temperature, and of the new $In_{0.10}Ga_{0.90}As/GaAs_{0.90}P_{0.10}$ $10 \times$ QW structure featuring the same switching sequence and grown at $650°C$ and 100 mbar. Qualitatively, presence of the SL fringes indicating the recovery of the planar QW growth can be observed in the low-phosphorous SB sample with the QW structure grown on the offcut substrate also enabling the SL
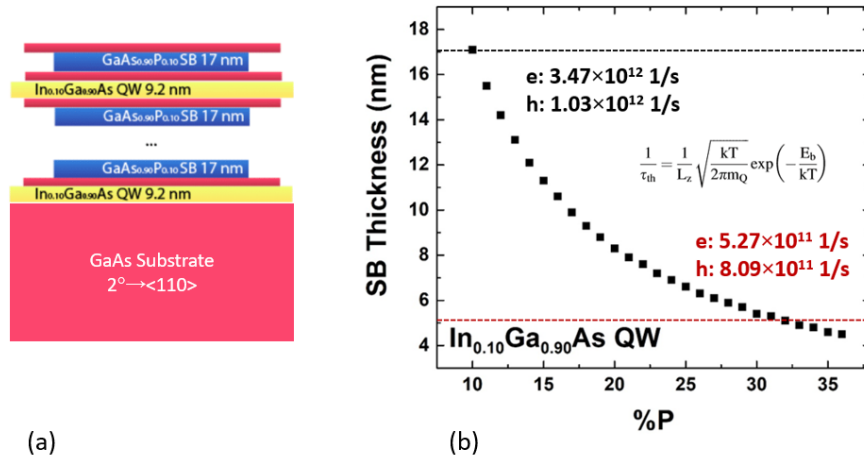
FIGURE 3.51: (a) QW test structure with 10%P 17 nm-thick GaAsP barriers and (b) calculated GaAs$_y$P$_{1-y}$ barrier thicknesses for each y%P satisfying the strain balancing condition for 9.2 nm-thick In$_{0.10}$Ga$_{0.90}$As QWs.

XRD characterization for extracting the SL period and *ex-situ* strain (Fig. 3.52b, c). Fig. 3.52b shows calculated statistical distribution of SL period of 28.8 ± 0.6 nm, while the nominal thickness of the QW and SB stack is 28.2 nm considering that the GaAs interlayers present on both sides of strain balancing are 1 nm each. Average strain shown on Fig. 3.52c is 423 ppm which is nearly 10 times lower compared to the switching sequence samples grown on on-axis substrates. This significant strain variation is likely a result of the growth rate inconsistencies due to the offcut. While FWHM of the SL fringes of 260 arcsec is comparable to that of the sample 21R016-4 grown on the on-axis substrate (263 arcsec), the Pendellosung fringes appear to have an onset of a subset superlattice in the sample 21R032-4 grown on 2° → ⟨110⟩ offcut substrate which is more prominently seen in the splitting of the SL+1 peak on Fig. 3.52 (blue line). This likely can be attributed to the periodic lateral non-uniformity.

The apparent recovery of the planar SL growth achieved by using 17 nm-thick phosphorous-poor strain balancing is accompanied with the changes in QW luminescent properties. PL spectra of the offcut samples with 32%P and 10%P strain balancing are shown on Fig. 3.53a. The notable increase in PL intensity is observed in the In$_{0.10}$Ga$_{0.90}$As/GaAs$_{0.90}$P$_{0.10}$
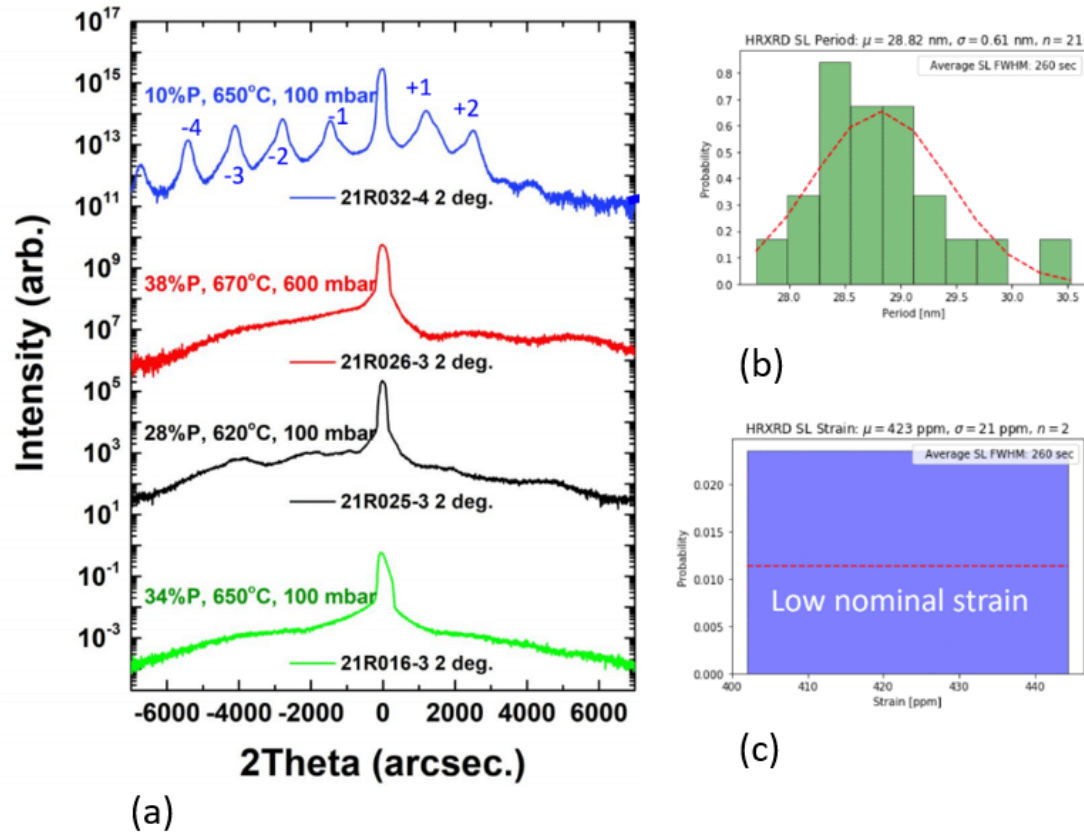
FIGURE 3.52: (a) 2Theta/ω XRD spectra of the "Nakano Optimized" switching sequence $10 \times$ QW samples with $GaAs_{0.68}P_{0.32}$ strain balancing grown at 650°C and 100 mbar, reduced T, increased T and pressure and of the sample with $GaAs_{0.90}P_{0.10}$ 17 nm-thick strain balancing grown at 650°C and 100 mbar. (b) Superlattice period statistical distribution calculated from the SL fringes analysis and (c) average strain.

structure indicating lowered non-radiative carrier loss. The QW PL peak position was extracted and plotted on Fig. 3.53b showing 10 nm PL peak red shift in the 10%P sample compared to the sample grown under the same conditions, but with 32%P strain balancing. The simulated QW emission wavelength for the ideal $In_{0.10}Ga_{0.90}As$ QW system was 948 nm not matching the measured value of 927 nm which based on the next**nano** corresponds rather to the predicted $In_{0.08}Ga_{0.92}As$ or to the QW structure with graded barriers. A blue shift of the PL peak of the QW structure grown at elevated pressure and unexpectedly increased growth temperature is observed as well, however, to establish the reason for this phenomenon, as well as to identify the reason for the QW peak intensity suppression additional calibrations of the individual films need to
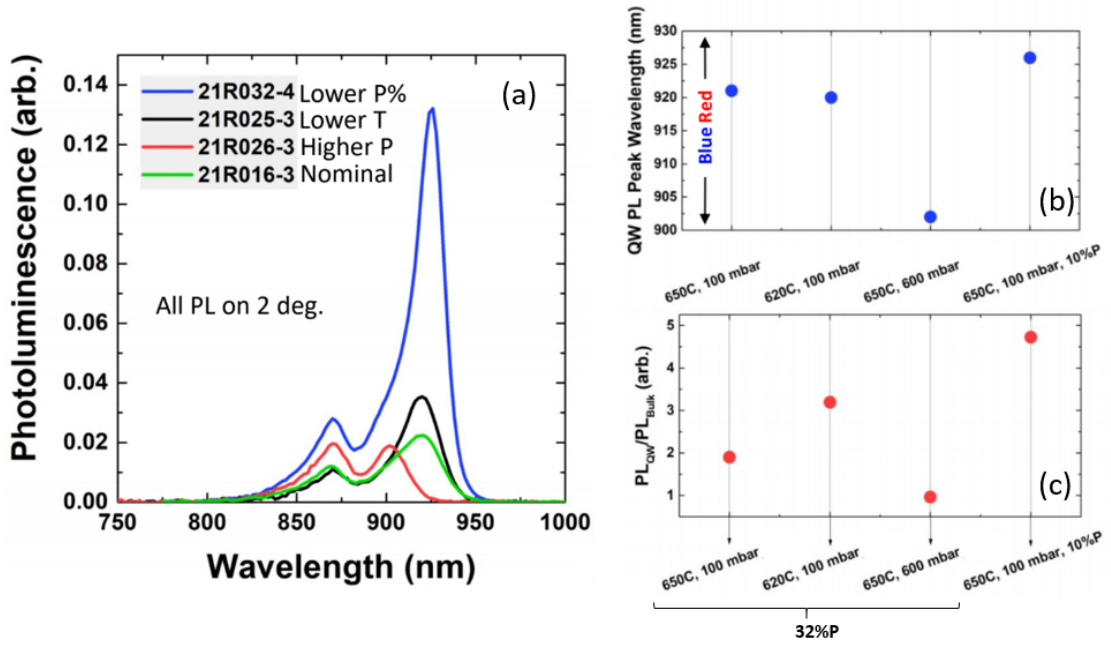
FIGURE 3.53: (a) PL spectra of the "Nakano Optimized" switching sequence $10 \times$ QW samples with GaAs$_{0.68}$P$_{0.32}$ strain balancing grown at 650°C and 100 mbar, reduced T, increased T and pressure and of the sample with GaAs$_{0.90}$P$_{0.10}$ 17 nm-thick strain balancing grown at 650°C and 100 mbar. (b) QW peak wavelength and (c) relative PL intensity of the QW peak normalized to the bulk GaAs PL intensity for each sample.

be performed (growth rate and composition), yet, since there was no observed benefit to using these growth conditions (in contrary, from a theoretical standpoint growth of the SLs at lowered temperatures is preferred), this work was not continued. Figure 3.53c shows the calculated ratios between the QW and bulk GaAs PL peak intensities. Both QW structures grown at 620°C and at 650°, but with GaAs$_{0.90}$P$_{0.10}$ SB resulted in higher QW-to-bulk PL intensity ratio compared to the nominal "Nakano Optimized" structure with 32%P strain balancing, however, while lowering the T_{growth} increased the PL by 1.7, the difference observed in the low-phosphorous strain balancing sample is more dramatic showing a PL enhancement by 2.6 compared to the 21R016-3 sample. Consequently, it would be quite interesting to investigate how this structure can be further improved if a combination of temperature and phosphorous-poor strain balancing is employed.

To assess the influence of the structural improvement on the electronic properties of the

QW regions with 32%P and with 10%P strain balancing layers, temperature-dependent PL spectroscopy analysis was carried out. PL spectra acquisition was performed at temperatures from 50 K to 300 K using He cryostat under 532 nm laser excitation. Using temperature-dependent PL peak intensity, $I(T)$, analysis expressed by Arrhenius behavior shown on Eq. 3.20 relative rate of non-radiative carrier ($C_i(32\%P)/C_i(10\%P)$) loss in the QW structures can be assessed [114]. The QW PL peak intensities dependent on temperature are plotted on Fig. 3.54. The calculated fit parameters, trap activation energy E_{a1} and relative non-radiative lifetime C_1 are 28 meV for each QW structure and 66 and 8 for the 32%P and 10%P QW structures, respectively, indicating 8.3 reduction in the non-radiative recombination rate in the QW structure with phosphorous-poor strain balancing.

$$I(T) \sim \frac{I(T_0)}{1 + \Sigma C_i exp \langle (-\frac{E_{ai}}{k_B T}) \rangle} \tag{3.20}$$

To rule out the InGaAs composition fluctuation concerns arising from the luminescent properties of the QW structures as one of the possible reasons for blue shifting of the QW PL peak, a plain 30 nm-thick InGaAs films were grown on $2° \rightarrow \langle 110 \rangle$ and $6° \rightarrow \langle 110 \rangle$ offcut substrates and properties of these samples were compared against the previously grown sample ($6° \rightarrow \langle 110 \rangle$ offcut) to identify any transient dependency of the TMIn pick-up efficiency. The InGaAs composition was studied by XRD spectra fitting and PL analysis. Figure 3.55a - c shows 2Theta/Ω XRD spectra of the nominally 30 nm-thick $In_{0.10}Ga_{0.90}As$ films and simulated spectra (Leptos) shown in grey with the appropriate simulation parameters (film composition and thickness) listed. Position of the XRD peaks resulting from compressively strained InGaAs films and period and position of the secondary interference fringes are used to extract the film parameters. Grown in
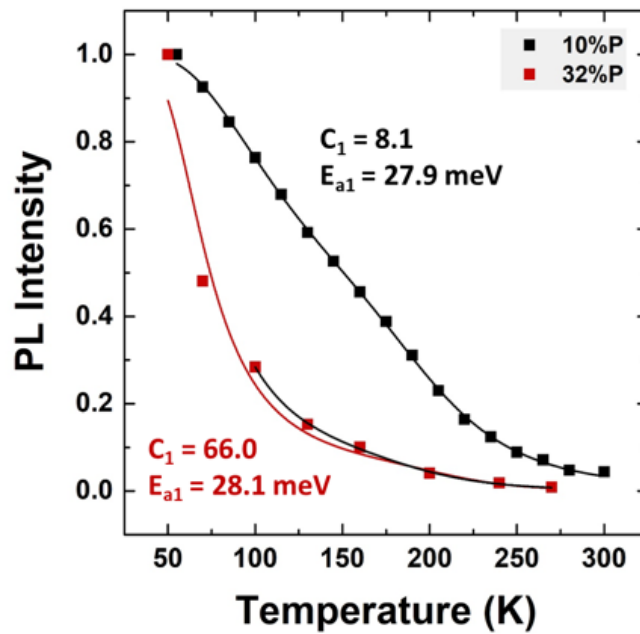
FIGURE 3.54: QW PL peak intensities dependent on the sample temperature. PL data of the $10 \times \text{In}_{0.10}\text{Ga}_{0.90}\text{As}/\text{GaAs}_{0.90}\text{P}_{0.10}$ SBQW is shown in black and $10 \times \text{In}_{0.10}\text{Ga}_{0.90}\text{As}/\text{GaAs}_{0.68}\text{P}_{0.32}$ SBQW in red. The lines are trend lines generated using fit parameters determined by Eq. 3.20.

2021, InGaAs films on both $2° \rightarrow \langle 110 \rangle$ and $6° \rightarrow \langle 110 \rangle$ offcuts are nearly identical with thicknesses of 29.4 nm and In content of 10.1% (Fig. 3.55a and b, respectively). Compared to the previous calibration sample with 31.5 nm-thick $\text{In}_{0.106}\text{Ga}_{0.894}\text{As}$ (Fig. 3.55c), reduction in both growth rate and In incorporation are observed that indeed can point to the lowered TMIn pick-up efficiency, however, the absolute 0.5%In reduction is insufficient to cause the blue shifting of the QW PL observed in SL structures, so it is likely that spectral properties of the QWs are mainly affected by the changes in quantum confinement due to the diffusion as was shown by next**nano** (Fig. 3.39). PL analysis of the uncapped InGaAs is not quite feasible due to the prevalence of the surface recombination (Fig. 3.55d), however, $2° \rightarrow \langle 110 \rangle$ sample exhibits a weak peak at 948 nm likely coming from $\text{In}_{0.10}\text{Ga}_{0.90}\text{As}$ film. The 2020 sample was grown on a p-type highly Zn-doped substrate that typically produces broadening towards IR due to parasitic recombination via impurity states, so analysis of the luminescence if peaks are
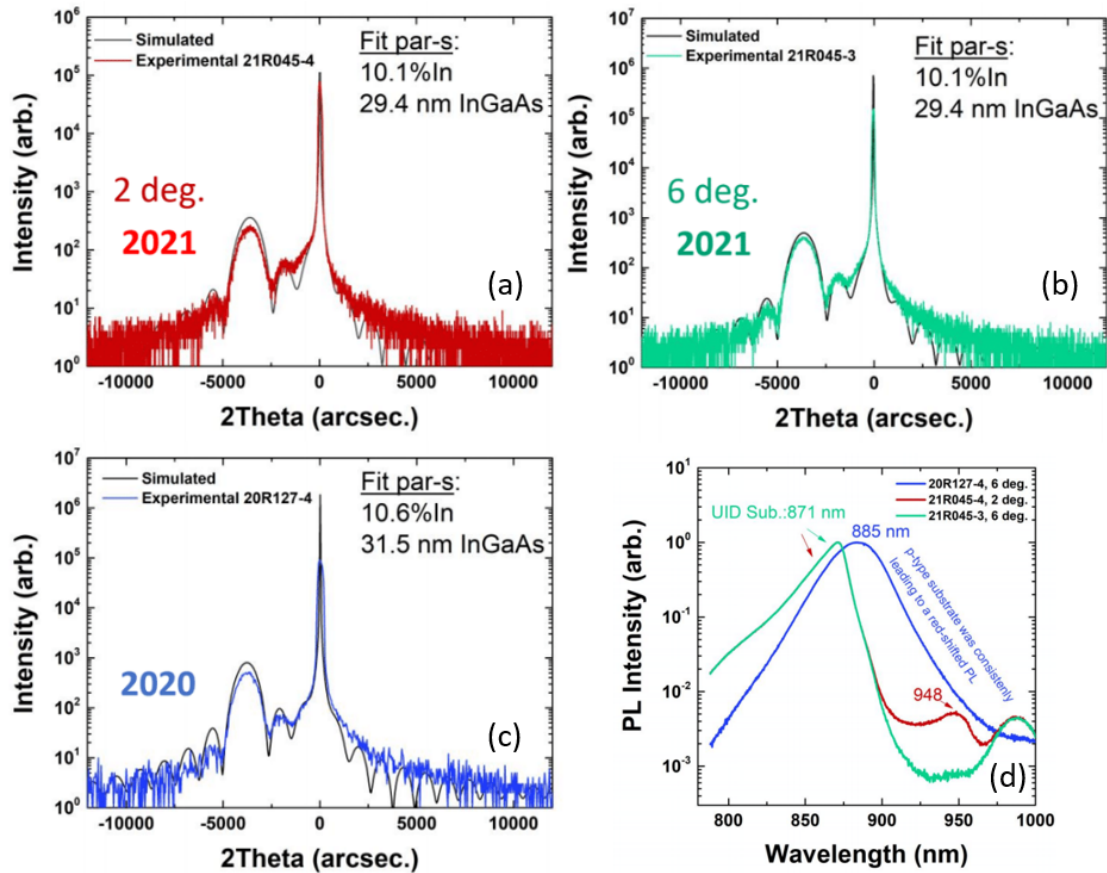
FIGURE 3.55: 2Theta/ω XRD spectra of the nominally 30 nm-thick $In_{0.10}Ga_{0.90}As$ films (exactly repeated growth recipes only adjusted to the relevant reactor temperature) grown on (a) $2° \rightarrow \langle 110 \rangle$ and (b) $6° \rightarrow \langle 110 \rangle$ offcut (100)GaAs substrates in 2021 and (c) $6° \rightarrow \langle 110 \rangle$ offcut substrate in 2020 (reference sample). Experimental curves are shown in color and simulated (Leptos) are shown in grey. Simulation parameters are listed in the insets. (d) PL spectra of the 2020 and 2021 InGaAs calibrations samples.

closely spaced is nearly impossible.

To address the drastic strain differences observed in the superlattices grown on on-axis substrates compared to the structures grown on $2° \rightarrow \langle 110 \rangle$ offcut a $GaAs_{0.10}P_{0.90}$ growth rate and composition calibration study was performed as well. XRD spectra of the nominally 50 nm-thick $GaAs_{0.90}P_{0.10}$ films grown on $2° \rightarrow \langle 110 \rangle$ offcut and on on-axis substrates are shown on Figure 3.56a and b, respectively. Fitting results (simulated curves are shown in grey) suggest that growth rate and phosphorous incorporation increase in on-axis-grown films compared to the GaAsP grown on offcut substrate (11.9%P vs. 10.7%P and 54 nm vs. 52 nm, respectively).
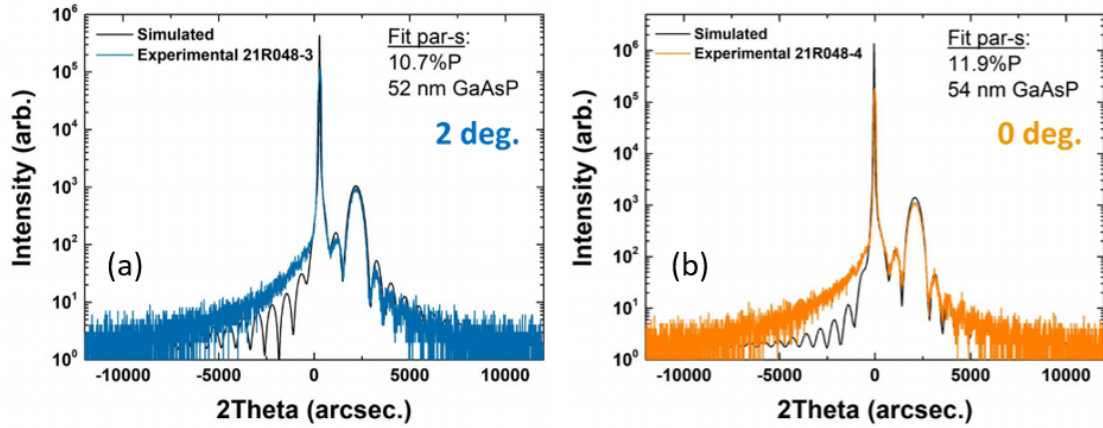
FIGURE 3.56: 2Theta/ω XRD spectra of the nominally 50 nm-thick GaAs$_{0.90}$P$_{0.10}$ films grown on (a) $2° \rightarrow \langle 110 \rangle$ offcut and (b) on-axis (100)GaAs substrates. Experimental curves are shown in color and simulated (Leptos) are shown in grey. Simulation parameters are listed in the insets.

The extended $25 \times$ In$_{0.10}$Ga$_{0.90}$As/GaAs$_{0.90}$P$_{0.10}$ superlattices were grown on $2° \rightarrow \langle 110 \rangle$ offcut and on on-axis (100)GaAs substrates (the schematics is shown on Fig. 3.57). The same switching sequence with GaAs interlayers (color-coded pink) were used. The XRD spectra of these structures are shown on Fig. 3.58. Sharp, high-intensity SL peaks are observed in on-axis sample (black line), while a more prominent double-peak feature is developed in the offcut sample (red line) with extended QW region compared to the 21R032-4 sample with only 10 periods of QWs. Using the Eq. 3.19 and 3.18, for each subset of SL peaks the corresponding period and strain can be extracted and are 28.4 nm and 1698 ppm and 27.8 nm and 169 ppm, respectively. On-axis SL sample's period and strain are 29.5 nm and 340 ppm. While FWHM of a double peak is not a representative measure (resulting in 411 arcsec), the FWHM of the SL peaks of on-axis sample is notably reduced compared to that of the samples with $10 \times$ In$_{0.10}$Ga$_{0.90}$As/GaAs$_{0.68}$P$_{0.32}$ SBQWs and is 69 arcsec.

Comparison between the $10 \times$ In$_{0.1}$Ga$_{0.9}$As/GaAs$_{0.9}$P$_{0.1}$ and $25 \times$ In$_{0.1}$Ga$_{0.9}$As/GaAs$_{0.9}$P$_{0.1}$ SL XRD spectra is shown on Fig. 3.59a and corresponding *in-situ* EpiTT curvature (green line with red lines shown as guides due to the noise in the original curve resulting
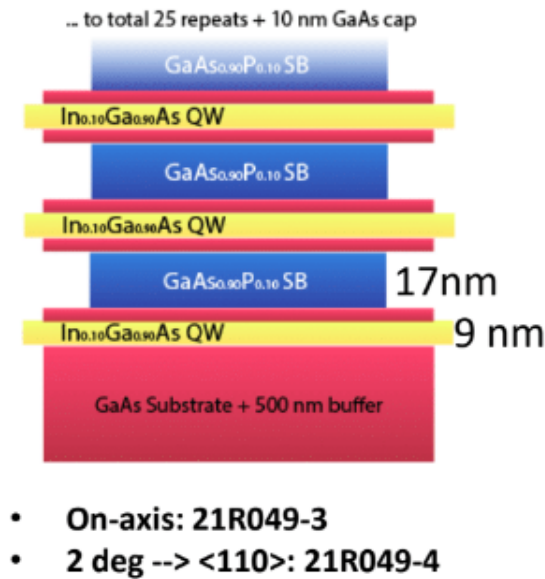
FIGURE 3.57: 25 × $In_{0.10}Ga_{0.90}As/GaAs_{0.90}P_{0.10}$ superlattice test structure with 1 nm-thick GaAs interlayers.

from instrumental issue) and reflectivity spectra (blue lines) are given on Fig. 3.59b and c for the 10 and 25 periods of QWs, respectively. In Fig. 3.59a, the grid lines are placed to allocate the coinciding peaks in each sample. EpiTT reflectivity curve in the 25 × SBQW starts descending more rapidly at 9th SL period and, more interestingly, this is the point where the type of strain suddenly switches from tensile to compressive (Fig. 3.59b). The curvature slope in the 21R032-4 sample with only 10 × SBQW periods is also lower (Fig. 3.59c), 0.0059 km^{-1}/s compared to ∼0.012 km^{-1}/s in the first 10 periods of 25 × SBQW structure (the approximation sign is used due to noise). This change might be a consequence of some growth adjustments (new temperature calibration, etc.). Flipping the type of strain in the extended SL can be well correlated with the observed bimodality in the XRD spectrum suggesting that some relaxation mechanism, also likely responsible for the wavy growth onset, is taking place, yet at the same time, a similar curvature change can be seen in the on-axis sample as well (Fig. 3.60). To claim that the partial relaxation and formation of a sub-superlattice due to offcut a TEM study is required.
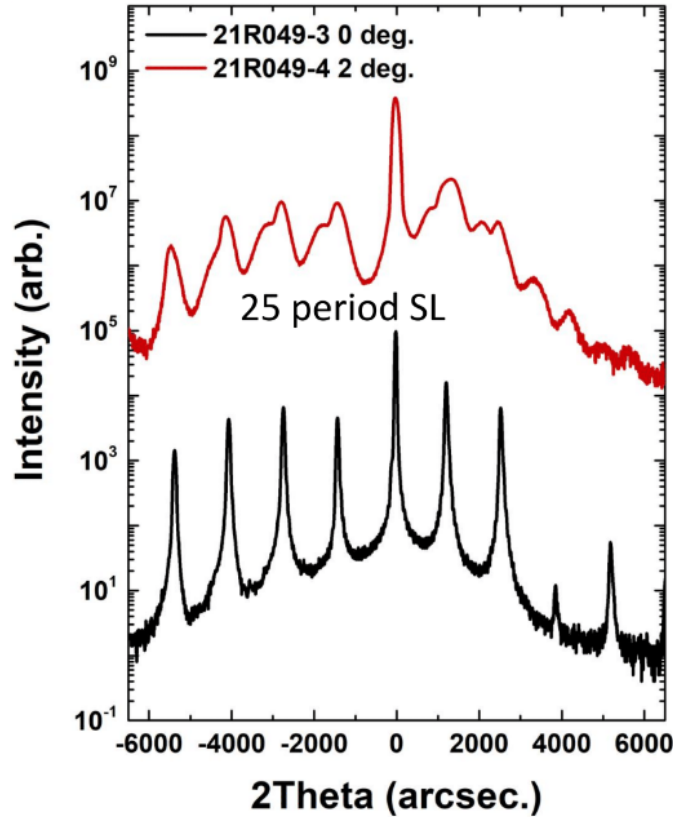
FIGURE 3.58: 2Theta/ω XRD spectra of $25 \times$ In$_{0.10}$Ga$_{0.90}$As/GaAs$_{0.90}$P$_{0.10}$ superlattice test structure with 1 nm-thick GaAs interlayers grown on on-axis substrate (black line) and on $2° \rightarrow \langle 110 \rangle$ offcut (red line).

Using low-phosphorous strain balancing barriers apparently led to the interface recovery and prevention of the formation of the periodic domains of opposite strain propagating through the superlattice, however, the origin of the superlattice subset with a different strain and period is to be investigated. Cross-sectional TEM images of the $25 \times$ In$_{0.10}$Ga$_{0.90}$As/GaAs$_{0.90}$P$_{0.10}$ grown on on-axis and on $2° \rightarrow \langle 110 \rangle$ offcut substrate are shown on Fig. 3.61a, b and c, d, respectively. Shown on Fig. 3.61a, morphology of the SL grown on on-axis substrate is pristine, similar to the structure with 32%P strain balancing (Fig. 3.50a), and from a closer analysis (Fig. 3.61b) thicknesses of QW and SB are 8.1 ± 0.7 nm and 14 ± 0.6 nm, respectively, with the distribution being a result of uniform interface roughness. The target values of the layers were 9.2 nm for the In$_{0.10}$Ga$_{0.90}$As QW and 17 nm for the GaAs$_{0.90}$P$_{0.10}$ SB, so elevated strain identified by XRD analysis in the on-axis samples can be attributed to the substantially reduced
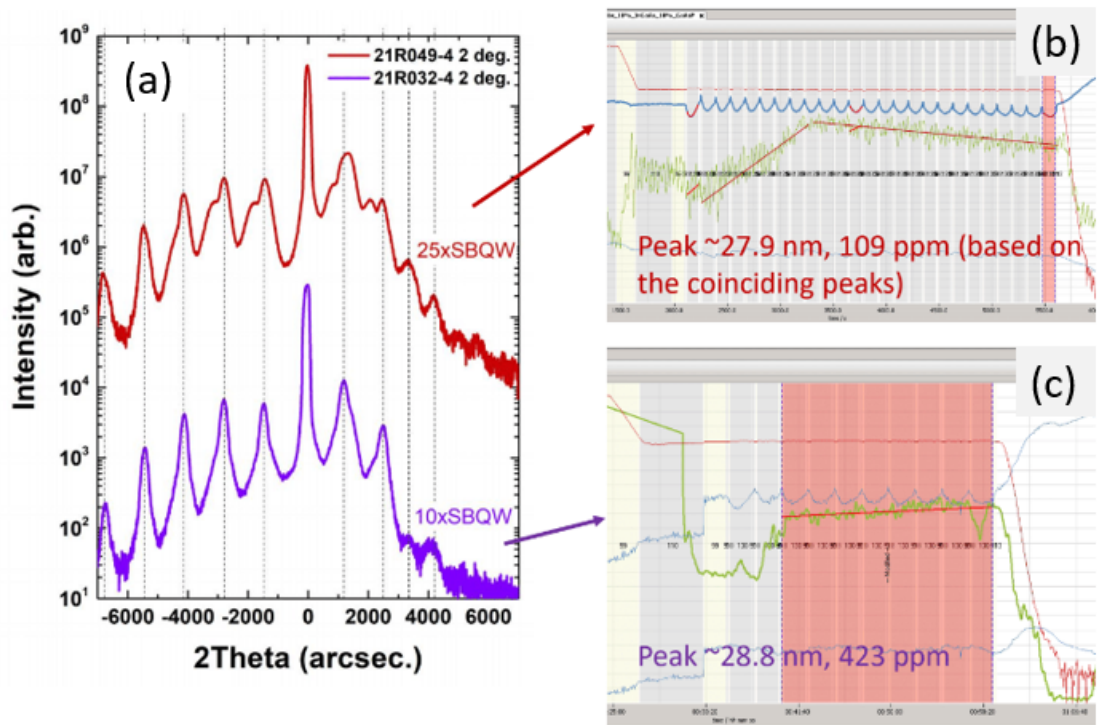
FIGURE 3.59: (a) 2Theta/ω XRD spectra of 10× and 25× In$_{0.10}$Ga$_{0.90}$As/GaAs$_{0.90}$P$_{0.10}$ superlattice test structures. EpiTT *in-situ* reflectivity and curvature of the (b) 25 × SBQW and (c) 10 × SBQW. Both are grown on 2° → ⟨110⟩ offcut substrates.

GaAsP growth rate. Analyzing the TEM images of the SL grown on the offcut substrate (Fig. 3.61c), multiplication of the ripples propagating at ∼30° to the growth plane is observed starting from 8th SL period which in turn must be associated with the change in EpiTT strain. Thickness modulations can be clearly seen in Fig. 3.61d. The QW layer thickness ranges from 8.8 nm to 14.6 nm (up to 5.8 nm difference within a period of 180 nm) and SB layer thickness changes from 14.0 nm to 21.3 nm ($\Delta t_{SB} = 7.3$ nm) reaching its minima and maxima where underlying QW thickness is at its maximum and minimum values. Another important observation is that while the interface coming from thin region of InGaAs to thickened GaAsP appears sharp, switching from bunched InGaAs to strain balancing is more diffuse. Presence of laterally spaced regions with periods of 30.1 nm (along the growth terraces) and 28.6 nm (at the steps) can explain the bi-modal XRD SL features.
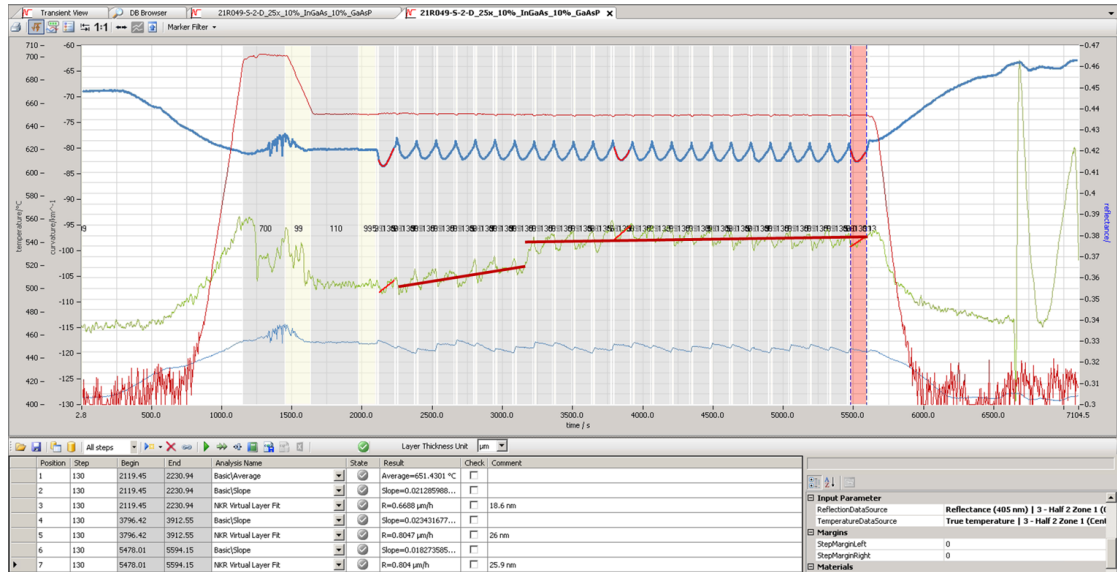
FIGURE 3.60: EpiTT *in-situ* reflectivity and curvature of the $25 \times$ SBQW grown on on-axis substrate.

The possible solutions, such as changing substrate offcut direction (for instance, the QW structures and QW solar cells shown in [15] are grown on $2° \rightarrow \langle 111 \rangle$B (100)GaAs substrates) and QW growth temperature, are investigated in the following section.

3.4.6.3 Influence of the Offcut and Growth Temperature on SL Morphology

First, the $25\times$ and $25\times$ In$_{0.10}$Ga$_{0.90}$As/GaAs$_{0.90}$P$_{0.10}$ superlattice test structures were repeated on alternative offcut substrates. It is notable that the bimodal behavior in XRD SL peaks appears to be suppressed in the $6° \rightarrow \langle 111 \rangle$A sample (Fig. 3.62a), while the XRD and EpiTT strain in this sample are the highest (Table 3.3). Compared to the QW structure grown on $2° \rightarrow \langle 110 \rangle$, $2° \rightarrow \langle 111 \rangle$B sample exhibits different SL period which is identified by the Pendellosung peaks offset in Fig. 3.62b, while degradation of the secondary SL peaks likely corresponding to the suppressed step bunching and thickness modulation is observed in $2° \rightarrow \langle 111 \rangle$A sample (Fig. 3.62c). An apparent structural improvement is well correlated with the luminescent properties with the highest relative intensity of the QW peak in the $2° \rightarrow \langle 111 \rangle$A sample (Fig. 3.63). Thus, offcut direction
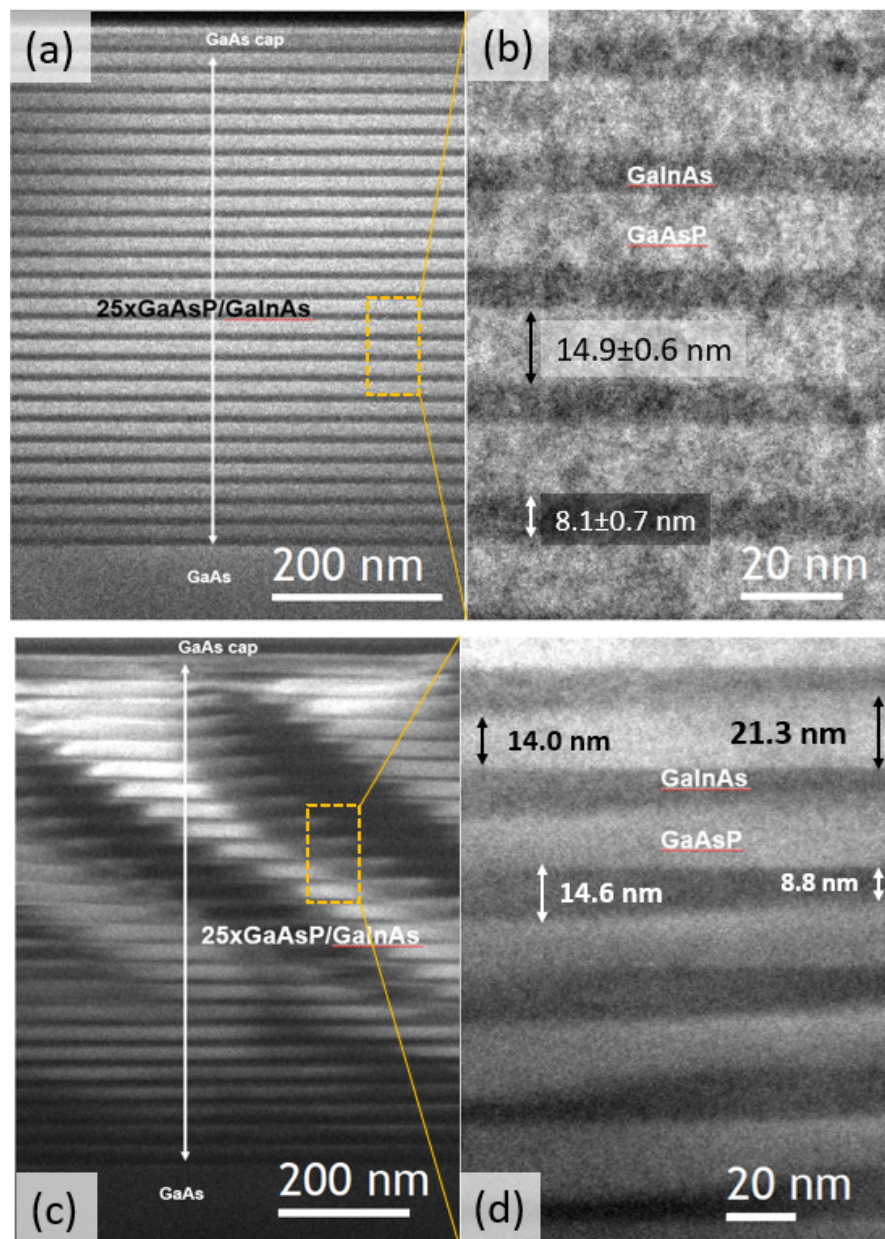
FIGURE 3.61: Cross-sectional TEM images of the $25\times$ $In_{0.10}Ga_{0.90}As/GaAs_{0.90}P_{0.10}$ superlattices grow on (a) on-axis substrate and on (c) $2° \rightarrow \langle 110 \rangle$ offcut substrate. Zoom-in images of the respective outlined regions are shown in (b) and (d), correspondingly. The average and local thicknesses are denoted where applies.
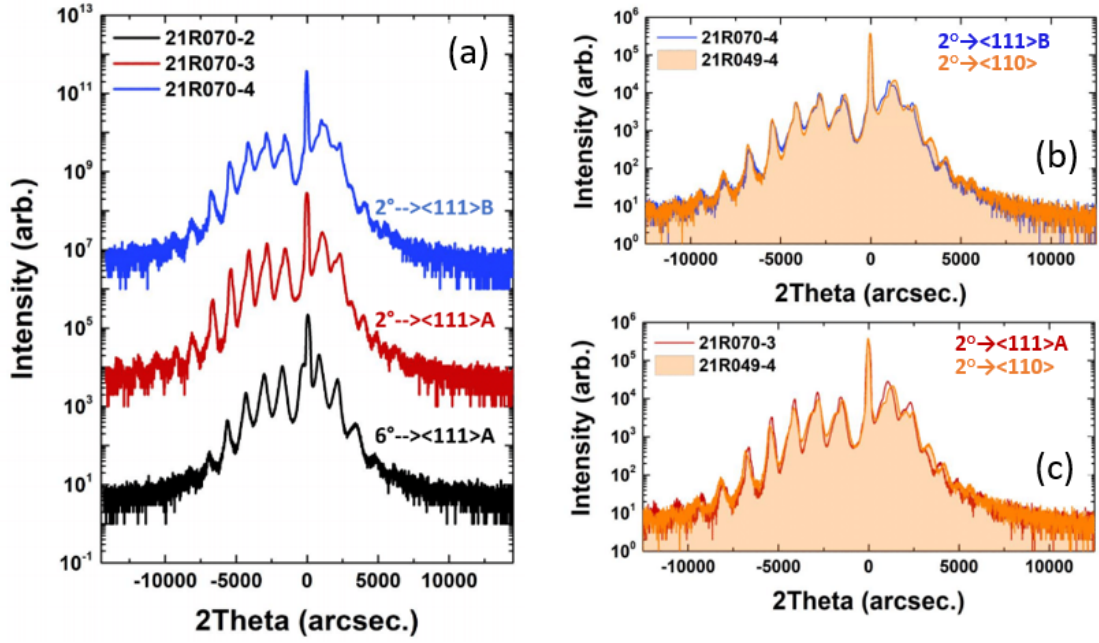
FIGURE 3.62: (a) 2Theta/ω XRD spectra of the 25× and 25× In$_{0.10}$Ga$_{0.90}$As/GaAs$_{0.90}$P$_{0.10}$ superlattice test structures grown on 2° → ⟨111⟩A (red), 2° → ⟨111⟩B (blue), and 6° → ⟨111⟩A (black) offcut substrates. Comparison between the 2° → ⟨110⟩ (orange shaded) and (b)2° → ⟨111⟩A and (c) 2° → ⟨111⟩B.

From XRD:	2° → ⟨111⟩B	2° → ⟨111⟩A	6° → ⟨111⟩A
Period, nm	28.7	29.1	29.7
Strain, ppm	667±391	902±42	1645±322
FWHM, arcsec	403	296	352
From EpiTT:	2° → ⟨111⟩B	2° → ⟨111⟩A	6° → ⟨111⟩A
ΔR	0.003	0.002	0.010
Strain, ppm	335	-579	827

TABLE 3.3: QW SL period, strain and peak FWHM extracted from XRD and reduction in reflectivity (ΔR) and strain extracted from curvature monitored with *in-situ* EpiTT.

was demonstrated to affect the step bunching rate and it was shown that using 2° → ⟨111⟩A (100)GaAs substrates is preferred for more uniform QW growth. Reduction in step bunching rate that is responsible for the development of the wavy growth and increased roughness is dependent on the incident flux of adatoms and also on the type and number of the available bonds that at the growth step, and the lateral growth rate exponentially depends on the activation energy of the adatom cite that scales with the number of As bonds [114].
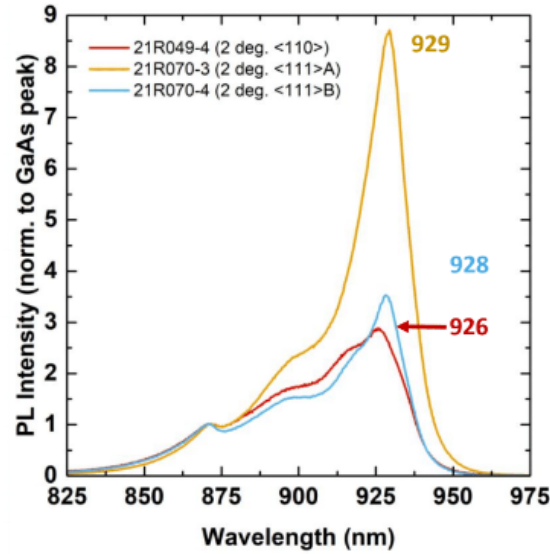
FIGURE 3.63: Normalized (to GaAs peak) PL spectra of the 25× and 25× $In_{0.10}Ga_{0.90}As/GaAs_{0.90}P_{0.10}$ superlattices grown on $2° → \langle 110 \rangle$ (red), $2° → \langle 111 \rangle A$ (yellow), and $2° → \langle 111 \rangle B$ (blue).

Next, an impact of the growth temperature, T_{growth} was studied. Figure 3.64a shows a comparison between the XRD spectra of the $2° → \langle 110 \rangle$ samples grown at 650°C and 600°C with a significant narrowing of the SL peaks in the low-temperature sample. Reduction of the SL peaks FWHM is observed as well as no sublattice is identified in the 600°C sample. XRD spectra of the QW structures grown at low T_{growth} on on-axis and on offcut substrates are shown on Fig. 3.64b with the corresponding FWHM of the first-order SL peaks denoted to the right. While no sublattice features are identified in neither sample, there is a clear variation in FWHM which is a metric of interface roughness. Normalized PL spectra are shown on Fig. 3.64c and clearly demonstrate ~1.8 times relative intensity improvement in $2° → \langle 110 \rangle$ and $2° → \langle 111 \rangle B$ samples compared to the PL of the QW structures grown at 650°C, yet PL signal appears to be suppressed in the $2° → \langle 111 \rangle A$ 600°C compared to its high-temperature counterpart making luminescent properties of the samples grown on 2° offcut substrates nearly identical.

A detailed analysis of the XRD parameters of the temperature study samples is shown on Fig. 3.65. It was expected that the interface roughness would increase in the 0°
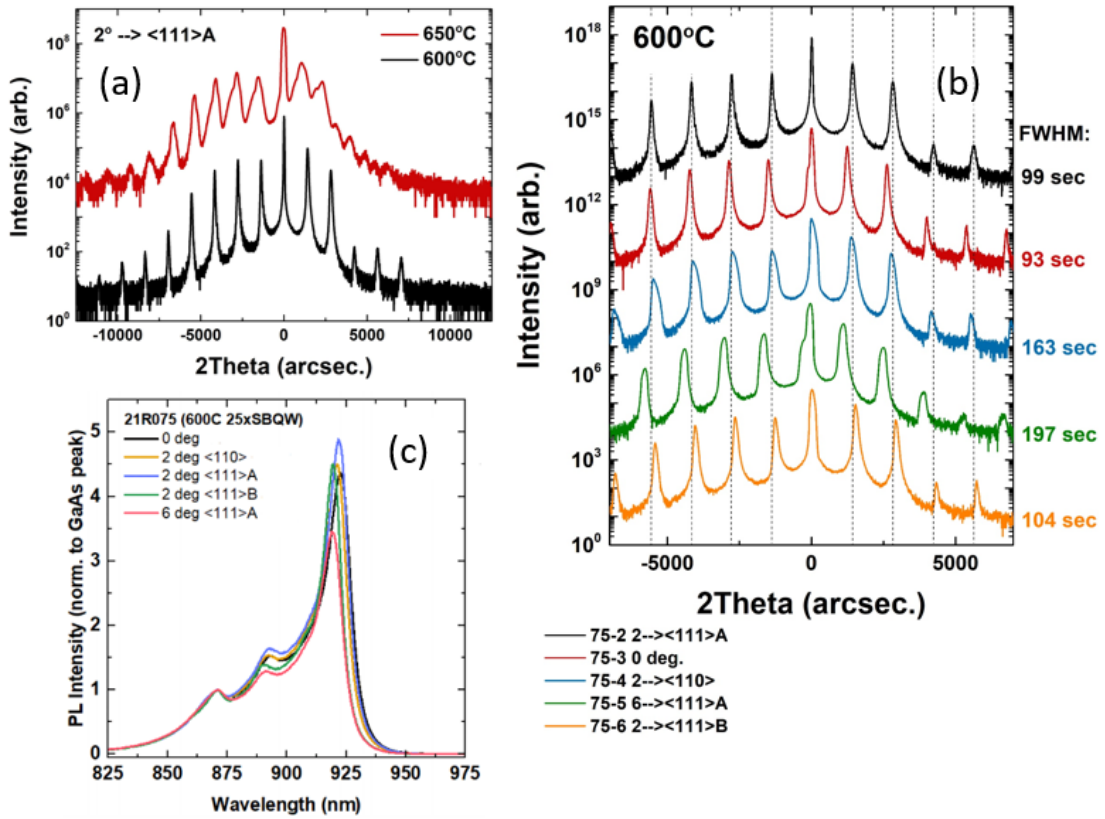
FIGURE 3.64: (a) 2Theta/ω XRD spectra of the 25× and 25× In$_{0.10}$Ga$_{0.90}$As/GaAs$_{0.90}$P$_{0.10}$ superlattice test structures grown on 2° → ⟨110⟩ at T_{growth}=650°C (red) and T_{growth}=600°C (black). (b) XRD spectra of the T_{growth}=600°C samples grown on on-axis (0°) and offcut substrates with FWHM of the first-order SL peaks denoted. (c) PL spectra of the corresponding structures normalized to the GaAs peak intensity.

sample due to reduced adatom diffusion suppressed by lowering the T_{growth}, yet in all

other samples a dramatic reduction in FWHM is observed (Fig. 3.65a). The average

XRD strain values dynamics shown on Fig. 3.65b is inconsistent between the samples.

First, type of strain is changed from compressive at 650°C to lightly tensile at 600°C

in the 2° samples irrespective of the offcut direction, while on-axis sample only shows

strain reduction by 100 ppm. The magnitude of the strain change in the offcut samples

is the lowest in the 2° → ⟨110⟩ sample and coincidentally, the SL period in this sample

is minimally affected as well compared to other samples (Fig. 3.65c). At the same time,

Fig. 3.65c demonstrates that better QW SL period control is achieved by switching to

600°C (the target period is 28.2 nm resulting from 9.2 nm-thick QW, double 1 nm-thick
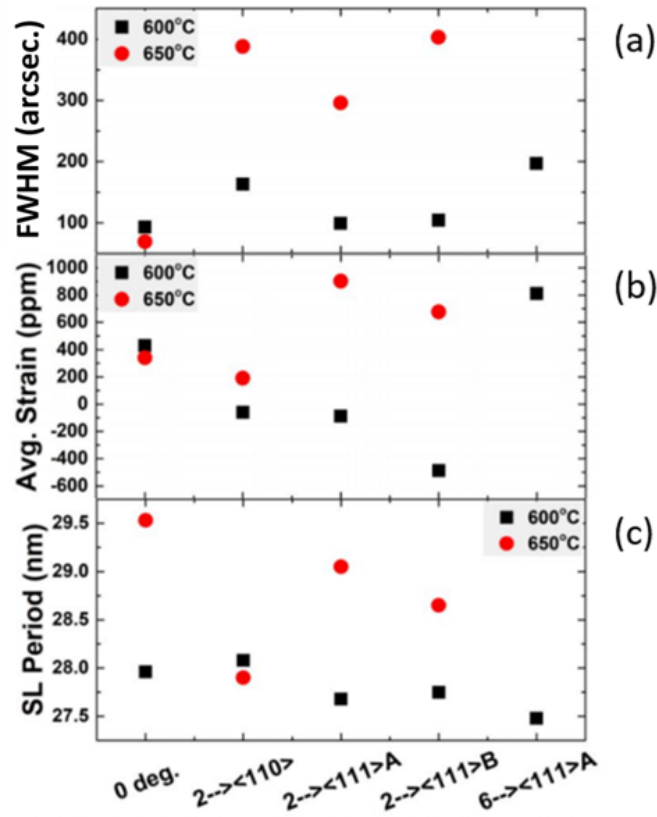
FIGURE 3.65: Breakdown of the XRD SL peak analysis: (a) first-order SL peak FWHM, (b) average strain, and (c) SL period (target is 28.2 nm) for the samples grown at 600°C (black) and 650°C (red) on various offcut substrates.

GaAs interlayers, and 17 nm strain balancing).

Reducing the T_{growth} was found to make a profound impact on the SL uniformity and in the next section properties of the devices with $12 \times \mathrm{In_{0.10}Ga_{0.90}As/GaAs_{0.90}P_{0.10}}$ grown at 650°C, providing a direct comparison with the $\mathrm{In_{0.10}Ga_{0.90}As/GaAs_{0.68}P_{0.32}}$ QW devices, and 600°C to investigate the influence of further SL refinement.

3.4.6.4 Influence of the QW Morphological Properties on Device Performance

Figure 3.66 shows a solar cell design featuring $6 \times$ and $12 \times \mathrm{In_{0.10}Ga_{0.90}As/GaAs_{0.90}P_{0.10}}$ QWs. These device structures were grown on the on-axis and on $2° \rightarrow \langle 110 \rangle$ substrates. The growth temperature was maintained at 650°C in the bulk of all devices,
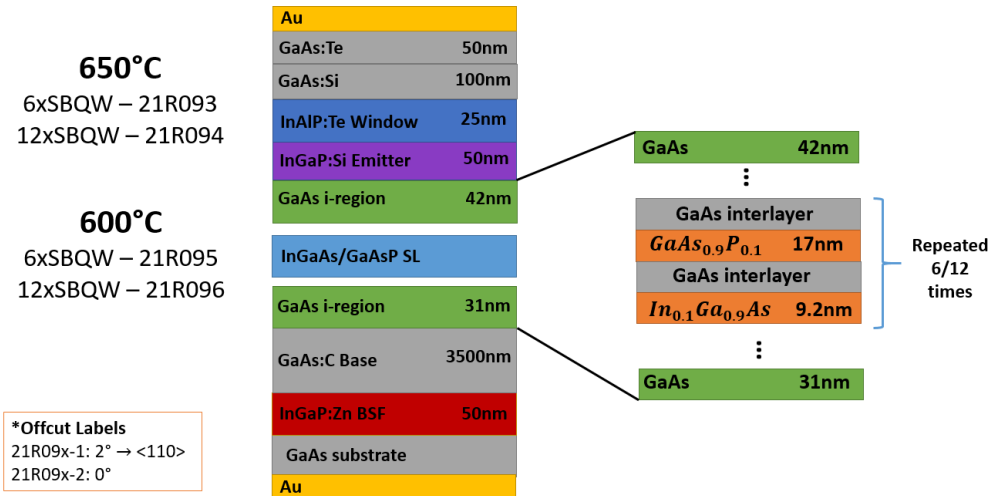
FIGURE 3.66: Design of the $6 \times$ or $12 \times \mathrm{In}_{0.10}\mathrm{Ga}_{0.90}\mathrm{As}/\mathrm{GaAs}_{0.90}\mathrm{P}_{0.10}$ QW solar cells and QW structure with the nomenclature of the samples dependent on the QW growth temperature and substrate offcut.

and QW layers were grown at either 600°C or 650°C. Compared to the previous solar cells with 4.9 nm-thick $\mathrm{GaAs}_{0.68}\mathrm{P}_{0.32}$ strain balancing, this set of devices had 17 nm-thick $\mathrm{GaAs}_{0.90}\mathrm{P}_{0.10}$ and "Nakano Optimized" precursor switching sequence throughout the QW layers.

In general, since this study is a preliminary work on developing a GaAs solar cell design that could be used as a part of dual- or triple-junction device, the optimization efforts should be placed on the samples grown on offcut substrates, however, 0° sample was included as well to establish a correlation between the spectral properties of solar cells and QW structure. EQE spectra of the $6 \times$ and $12 \times \mathrm{In}_{0.10}\mathrm{Ga}_{0.90}\mathrm{As}/\mathrm{GaAs}_{0.90}\mathrm{P}_{0.10}$ QW solar cells compared to the baseline device (no QWs) are shown on Fig. 3.67a. The drop in the window/emitter collection efficiency was attributed to the unintentional reduction in doping in these layers compared to the baseline that weakened the screening E-field at the front interface. As well, employed "Nakano Optimized" switching sequence for possible interface improvement in the emitter appeared to worsen the collection in the emitter. In the on-axis samples specifically, the further EQE reduction is likely due to the ordering effects in InGaP and InAlP that are highly sensitive to the offcut. In
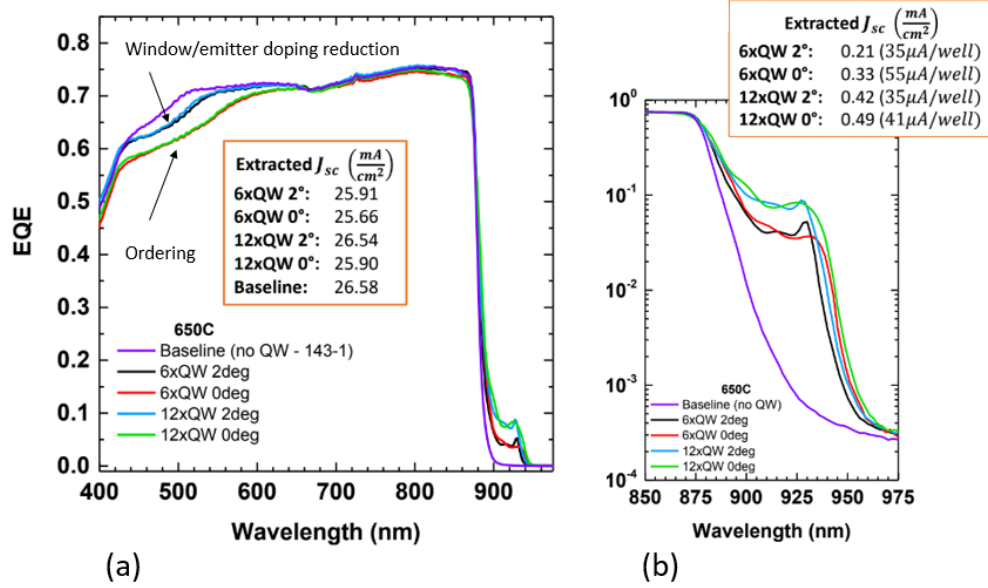
FIGURE 3.67: (a) EQE spectra of the baseline (no QW) and $6\times$ and $12\times$ $In_{0.10}Ga_{0.90}As/GaAs_{0.90}P_{0.10}$ QW solar cells grown on on-axis and on $2° \rightarrow \langle 110 \rangle$ substrates at $600°C$ or $650°C$ and (b) EQE of the QW region and QW J_{sc}.

more detail ordering in InGaP and InAlP is discussed in the subsequent chapter. By subtracting the baseline Urbach tail EQE and integrating spectral response modulated by the AM0 spectral irradiance over the QW absorption wavelength range (Fig. 3.67b), the current per QW was calculated. For the offcut samples, the current production in the QW region linearly scales with the number of QW periods.

Comparing the current per well results, the samples with phosphorous-poor strain balancing have up to 5 times higher J_{sc}/QW than the cells with 32%P strain balancing.

AM0 IV characteristics of the $In_{0.10}Ga_{0.90}As/GaAs_{0.90}P_{0.10}$ QW solar cells in comparison with the strained QW cell and $In_{0.10}Ga_{0.90}As/GaAs_{0.68}P_{0.32}$ QW solar cells are shown on Fig. 3.68. One major observation is the drop in J_{sc}, despite the superior spectral properties of $In_{0.10}Ga_{0.90}As/GaAs_{0.90}P_{0.10}$ QWs, primarily associated with the emitter and window layers deterioration in the 10%P QW cells (more pronounced in the on-axis samples), while in strained QW cell it is a result of nearly 1 μm thinner GaAs base. The 145 mV V_{oc} reduction in the $In_{0.10}Ga_{0.90}As/GaAs_{0.68}P_{0.32}$ QW solar cells observed with
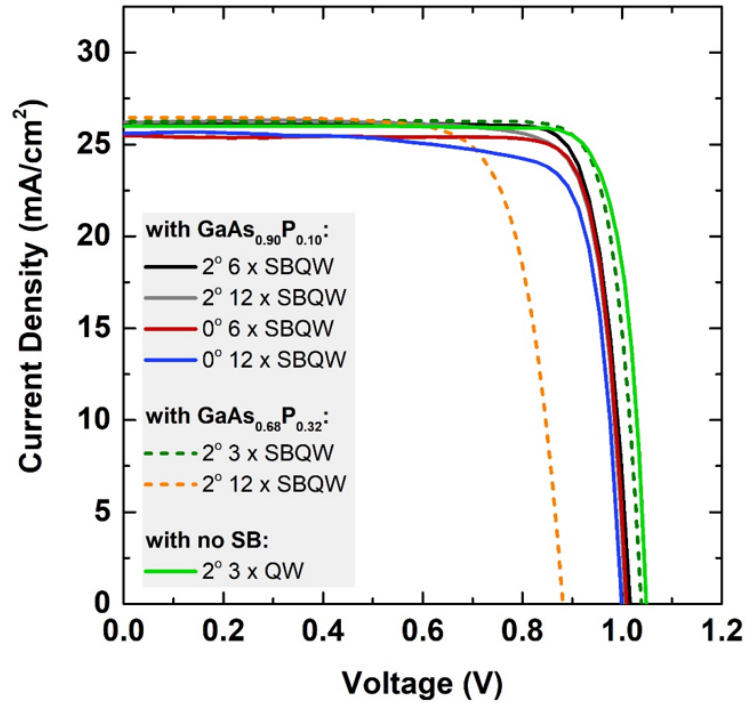
FIGURE 3.68: AM0 light IV curves of strained $3\times\text{In}_{0.06}\text{Ga}_{0.94}\text{As}/\text{GaAs}$, strain-balanced $3\times$ and $12\times\text{In}_x\text{Ga}_{1-x}\text{As}/\text{GaAs}_{0.68}\text{P}_{0.32}$ and $6\times$ and $12\times$ $\text{In}_{0.10}\text{Ga}_{0.90}\text{As}/\text{GaAs}_{0.90}\text{P}_{0.10}$ QW solar cells grown on the offcut and on-axis substrates.

increase in the QW number from 3 to 12 is not shown in the $\text{In}_{0.10}\text{Ga}_{0.90}\text{As}/\text{GaAs}_{0.90}\text{P}_{0.10}$ QW cells with 6 or 12 QWs which retain above 1.0 V V_{oc}.

3.4.7 Spectroscopic Analysis of the Strained QW Structures and Solar Cells

Considering the radiative recombination suppression in the QW solar cells and following the derivation of the QFLS in the QWs, the offset from the host material will increase due to the formation of low-energy states in the QWs, leading to enhanced absorption, and rapid (compared to the recombination rate) carrier escape from the QWs, which can be engineered by lowering the energy barriers for carrier thermalization or by thinning the strain balancing layers. From the EL-EQE reciprocity theorem expressed by Eq. 3.9, the relation between the measured and reciprocity-derived EL can be expressed in

terms of the front-surface radiative recombination probability in the QWs (important correction due to the anisotropic QW emission compared to the bulk material) weighted by the sum of the events that generated carriers can experience inside the QW region written in terms of carrier escape, R_{Escape}, and radiative, R_{Rad}, rates in a QW region:

$$\phi_{EL,QW}^{Measured} = \frac{R_{Rad,norm}}{R_{Escape} + R_{Rad,total}} \phi_{EL,QW}^{EQEReciprocity} \qquad (3.21)$$

Measured EL flux is coming from the front surface radiative recombination events that can be dominated by the carrier losses that are not taken into account in the reciprocity theorem and that cause the QFLS offset. Hence, we can relate the QFLS offset in the QW region with the carrier recombination or escape rates:

$$\frac{R_{Rad,norm}}{R_{Escape} + R_{Rad,total}} = exp\left(\frac{q\Delta V_F}{k_B T}\right) \qquad (3.22)$$

This equation can be rewritten to express the QFLS offset in a QW:

$$\Delta V_F = \frac{k_B T}{q} ln\left(\frac{R_{Rad,norm}}{R_{Escape} + R_{Rad,total}}\right) = -\frac{k_B T}{q} ln\left(\frac{R_{Escape} + R_{Rad,total}}{R_{Rad,norm}}\right), \qquad (3.23)$$

dependent on the radiative recombination rate (R_{Rad}) and total carrier escape. First, if radiative recombination rate is much greater than escape and anisotropy is not present, the QFLS offset becomes 0, since the fraction in brackets become 1 (this scenario is likely in the deep QWs such that thermal escape is suppressed, with a strong overlap between the electron and hole wave functions due to the electric field across the QW region being small and quantum confined Stark effect not observed, QWs are weakly strained), and,

due to the near-zero electric field, the tunneling escape rate is suppressed, in a pristine quality material, the QFLS offset will deepen in the sample dominated by the carrier escape:

$$R_{Escape} = R_{Th} + R_{Tun} = \tau_{Th}^{-1} + \tau_{Tun}^{-1}, \tag{3.24}$$

where τ_{Th} is thermal escape and τ_{Tun} is tunneling escape lifetimes that are defined by Eq. 3.2 and 3.3.

Now, moving on with the analysis, the assumption that the R_{rad} of the quantum wells that can be measured via EL is equivalent to the isotropic emission that can be collected from the bulk material is often not correct, since in strongly confined QWs or due to a high refractive index difference between the QW and the barriers, the QW emission can preferentially propagate in-plane and emit off of the solar cell edges. So in the QW systems where preferential emission direction can be a factor optically suppressing the front-surface emission (characterized by $R_{Rad,norm}$), the equation will take the following form:

$$\Delta V_F = \frac{k_B T}{q} ln \left(\frac{R_{Rad,norm}}{R_{Escape} + R_{Rad}} \right) = -\frac{k_B T}{q} ln \left(\frac{R_{Rad}}{R_{Rad,norm}} + \frac{R_{Escape}}{R_{Rad,norm}} \right). \tag{3.25}$$

Here we can see that in highly strained QWs, even if we ignore the escape and non-radiative recombination components, the QFLS will be less than in the host material.

Somewhat added complexity comes if we take into account the connectedness of the QWs and bulk material. Under light excitation, sub-bandgap generation is specific to the QWs

and optically excited carriers in the QWs, should they get successfully collected before they recombine, contribute to the J_{sc} of the solar cell, which is anticipated from a good QW-enhanced device. However, by injecting the carriers under applied forward bias and collecting the EL emission, we are observing the radiative recombination coming from the carriers that transit across the QW region , get captured, and recombine or escape out of the QW, which essentially requires the equation to be modified accordingly. In a QW solar cell system under dark operation, QWs serve as recombination centers for the carriers lowering the bulk QFLS by providing an additional recombination path for the carriers. This leads to the necessity of introducing the capture probability factor, $\sigma_{Capture}$, into the QFLS equation to account for the different origin of the carriers that contribute to the measured EL emission:

$$\Delta V_F = -\frac{k_B T}{q} ln \left(\sigma_{Capture} \left[\frac{R_{Rad}}{R_{Rad,front}} + \frac{R_{Escape}}{R_{Rad,front}} \right] \right) \qquad (3.26)$$

The reciprocity will hold if $\sigma_{Capture} \left[\frac{R_{Rad}}{R_{Rad,front}} + \frac{R_{Escape}}{R_{Rad,front}} \right] = 1$, so ignoring the anisotropy, this will mean that $\sigma_{Capture} R_{Escape}/R_{Rad} = 1$, i.e. assuming unity capture rate, the probability of carrier escape from the QWs should be in an equilibrium with the front-surface radiative recombination.

To determine how carrier escape relate to the QFLS offset the following study was performed. To understand the impact carrier escape can make on the QFLS offset in the QWs, recall the physical significance of the QFLS which indicates the quasi-stationary population of the energy states under non-equilibrium conditions, which in a bulk semiconductor is defined as $V_F = kT/q ln(np/(n_i^2))$, emptying the QW states by carrier escape is more likely for the states that provide the smallest energy barrier for the carriers, thus, deeper states are more likely to be QFLS-limiting inside the QWs. In
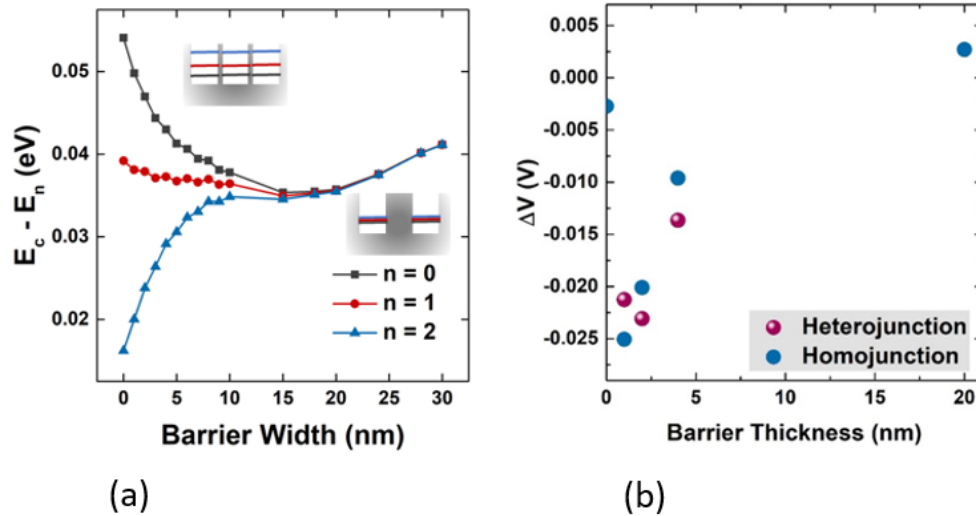
FIGURE 3.69: (a) Simulated (nextnano) electron energy levels in the $In_{0.08}Ga_{0.92}As$/GaAs strained QWs dependent on the GaAs barrier width; (b) measured QFLS offset extracted from the reciprocity relation dependent on the GaAs barrier width [131]

such system, carrier escape from the shallow states will result in an increase of the QFLS offset. This might explain the previously observed suppression of radiative efficiency of the QWs associated with stronger QFLS offset in the strongly coupled QWs, in which perturbed QW energy states split causing enhanced thermal escape rate [131].

Figure 3.69a shows a schematics of the electron energy states in the $In_{0.08}Ga_{0.92}As$/GaAs triple strained QWs. The energy offsets on the Y axis indicate energy barrier heights for the carriers excited to each state, and X axis indicates GaAs barrier thicknesses. It can be observed that stronger QW coupling (thinner GaAs barriers) is related to a higher splitting between the energy states and leads to formation of shallow (15 meV) and deep (50 meV) energy states compared to the isolated QW case resulting in a degenerate energy state ~40 meV below the conduction band (at barrier thicknesses over 15 nm). At barrier thickness of 4 nm, the electron barrier heights are 28 meV, 37 meV, and 42 meV, and as shown on Fig. 3.69b QFLS offset is 14 meV. With thinner, 2 nm-thick barriers, the electron energy states are splitting further apart, 20 meV, 38 meV, and 50 meV, corresponding to 22 meV QFLS offset.
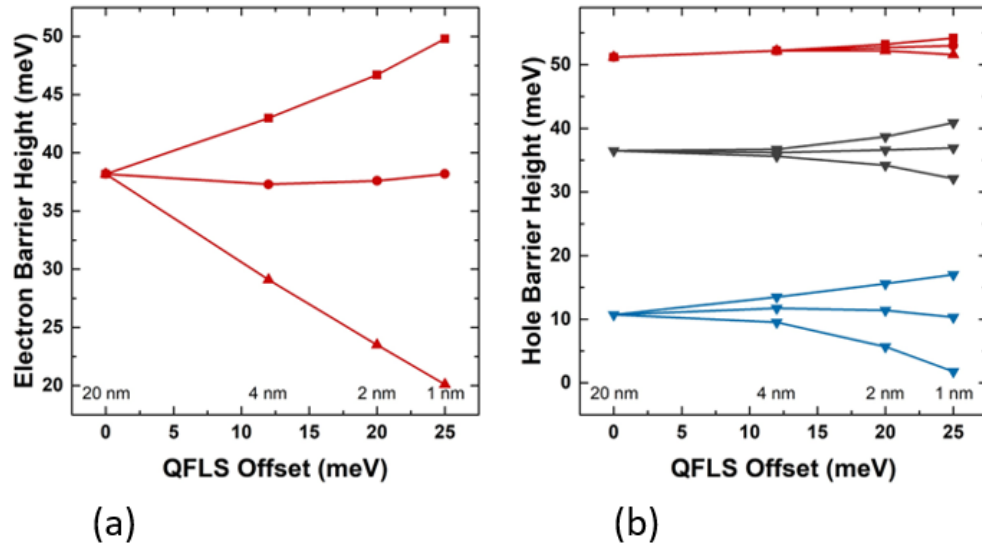
FIGURE 3.70: (a) Electron and (b) hole energy states in the QWs corresponding to the reciprocity-derived QFLS offset in the QW region. The associated GaAs barriers widths are annotated.

The thermal escape energy barrier height for hole and electron states in the $In_{0.08}Ga_{0.92}As$ QWs separated with varied thickness GaAs barriers (simulated in next**nano**) and associated QFLS offset calculated from the EL-EQE reciprocity are plotted on Fig. 3.70a and b, respectively. Quantum well coupling, as the barrier gets thinner, causes the degenerate energy states to split producing shallow and deep states. The hole band structure modulation is less dramatic than in electron states with the maximum splitting reaching 10 meV for the shallow energy state in the strongly coupled QWs (1 nm barrier) and only -5 meV for the deeper state. At the same time, the electron barrier lowering reaches 17 meV and deeper state is shifted down by 13 meV in the strongly coupled QWs. At the same time, QFLS offset increases by 25 meV. The analysis of how state splitting affects carrier escape rate is needed for both types of carriers.

Figure 83.71 shows carrier thermalization rate normalized to the rates corresponding to the highest QFLS offset (in strongly coupled QWs). The rates are calculated for each band structure using Eq. 7. Interestingly, linear relation between the QFLS offset and electron thermalization rate is established, corresponding to the observed electronic
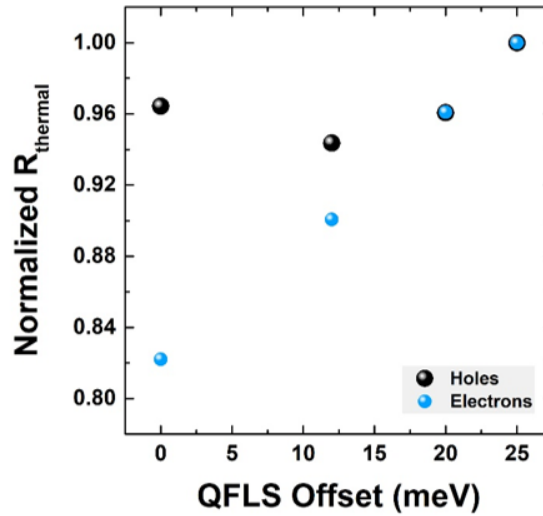
FIGURE 3.71: Normalized hole (black) and electron (light blue) thermalization rate for QFLS offset.

state splitting (Fig. 3.70a). For holes, the state splitting is smaller and hole effective masses are ∼8 times higher (for heavy holes), so their thermalization rate does not change much with QW coupling, hence, contribution of hole escape into QFLS offset is relatively insignificant compared to the electrons. Thus, it can be concluded that electron thermalization from the topmost energy state makes the lowest energy state dominating the radiative QFLS limit, since it is more likely to be populated and retain long-lived carriers. This might suggest that enhanced carrier escape rate in strongly coupled QWs is beneficial for efficient carrier collection and higher obtainable J_{sc}, yet will lower the V_{oc} by lowering the QFLS in the QW region due to the QFLS being largely determined by the lowest energy states. Coupling of QWs, on the one hand, provides a more efficient carrier escape due to the formation of low-barrier state, and on the other hand, formation of the deep state associated with the coupling lowers the QFLS relatively to the uncoupled QW with the same %In.

3.4.8 Parametric Predictions, Projections, and Suggestions for Dual Junction Solar Cell

Developing QW GaAs solar cells with retained V_{oc} and maximized current collection from the QW region is important for integration into multijunction device. While such device had not been implemented explicitly within the framework of the present report, collecting the existing parameters and trends and summarizing them to predict the properties of the dual-junction device is possible. In particular, empirical parameters of the top InGaP solar cell are available as indicated in the following chapter and, optimistic projections can be built using state-of-the-art reports demonstrating superior and, in principle, achievable performance of the InGaP solar cell. For the following illustrations, extrapolation of current was based on measured gain of J_{sc} per QW of 30 μA/cm^2 and progressive reduction of V_{oc} and fill factor corresponding to the QW structures with optimized interfaces and reduced impact of step bunching were assumed.

In principle, top InGaP sub-cell can be designed to produce $\sim$19 mA/cm^2 [15], so for 100 QWs with steady ΔJ_{sc} per QW, the current gain of up to 3 mA/cm^2. Figure 3.72 shows predicted efficiency of the 2J cell with increase in the bottom GaAs cell J_{sc} for different scenarios of fill factor including steady 89% (as was achieved in a 2J device with no QWs in GaAs subcell), 86% assuming the reduction due to inclusion of the QWs, and progressively changing fill factor. The maximum projected efficiency was 29.3% which can be further increased if bottom cell's voltage retention is achieved. Thus, it is crucial to improve both bulk GaAs and QW structural and electronic properties to achieve V_{oc} approaching 1 V, which can be possible if GaAs solar cell is operated in radiative limit with no QWs and only fundamental dark current increase is observed due to the QWs (due to the bandgap offset).
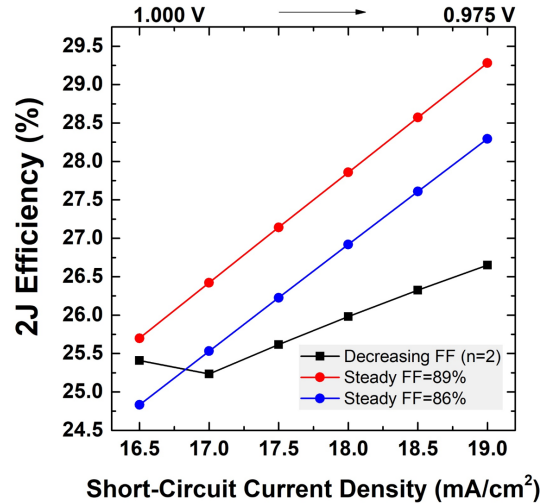
FIGURE 3.72: InGaP/GaAs dual junction solar cell efficiency projections with fixed fill factor values limited by the series resistance (89%) and retained at 86%, limited by the GaAs solar cell and not dependent on the number of QWs, as well as with progressively reducing fill factor as the QW number increases. V_{oc} of the InGaP sub-cell was fixed at 1.38 V and V_{oc} reduction in the GaAs sub-cell is shown on the top axis. The current gain per QW is 30 μA/cm^2.

With use of antimony as a surfactant for managing ordering in the top InGaP sub-cell and, possibly, alleviating step bunching in the QWs, this efficiency target can be achieved, however, junction design of the InGaP sub-cell can be adjusted (possibly also consider AlGaInP/InGaP heterojunction design). Reduction of the QW growth temperature from 650°C to 600°C was also found promising for managing step bunching. Adding DBR enabling up to 96% increase in the QW absorption and will allow to achieve the same current gain from 50 QWs as would be produced by 100 QWs with no DBR.

Chapter 4

Advances in Development of Quantum-Dot Enhanced Dual Junction InGaP/GaAs Solar Cells for CubeSat

4.1   Summary

Dual-junction $In_{0.49}Ga_{0.51}P$/GaAs (further, InGaP/GaAs, unless specified otherwise) solar cells were fully grown and fabricated on two types of offcut GaAs substrates (offcuts of 2° towards $\langle 110 \rangle$ and 6° towards $\langle 111 \rangle$A). For the purpose of accurate predictions of the 2J cell performance under changing parameters, the well-matched Sentaurus model was built. Incorporation of QDs into the bottom cell intrinsic region and layer optimizations for scaled-up devices (26.5 cm^2) are in progress, however, this report further shows the

accomplishments in these fields. The progress in development of the large-area 2J QD solar cells was reported [155, 156].

4.2   Motivation and Background

The goal of the CubeSat systems is to accelerate the introduction of the innovative space technology components. A CubeSat represents a small spacecraft (nanosatellite) that can accomodate a variety of functional units and enables a low-cost launch compared to the conventional satellite missions (https://www.cubesat.org). The work on developing quantum-dot-enhanced solar cells was a part of a CubeSat launch that was intended to demonstrate the capabilities of the nano-enhanced power components produced at RIT and compare them with commercially available power units in the space conditions. QD-enhanced solar cells for power harvesting, metal-free carbon-nanotube (CNT) conductors for power transmission, and CNT-enhanced lithium ion batteries for storage are the test components on the CubeSat. Development of the QD-enhanced 2J InGaP/GaAs solar cell was the objective of the current work (CNT wiring and batteries were developed by the collaborators) [156]. One of the requirements for the CubeSat solar cells was to target commercial cells parameters, hence, large-area solar cells development was important. For this work, ~ 27 cm^2 devices were fabricated as the end product.

For the space PV, radiation tolerance of the solar cells is important as the main environmental factor in space is presence of high-energy charged particles (electrons and protons) [157, 158]. The degradation of the solar cells under the incident flux of particles can be mathematically described in terms of the diffusion length:
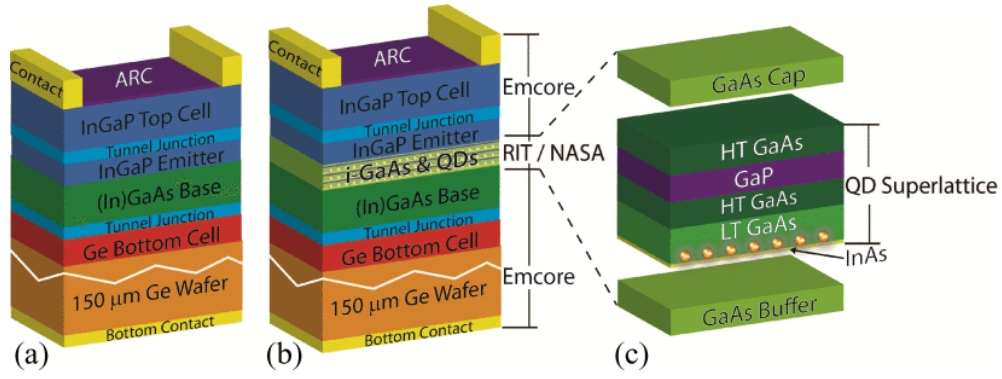
FIGURE 4.1: (a) Baseline solar cell (no QDs); (b) QD solar cell; (c) a single period of a QD superlattice including InAs QDs, GaAs barriers, and GaP strain compensation.

$$\frac{1}{L_\phi^2} = \frac{1}{L_0^2} + K_L\phi, \tag{4.1}$$

where L_0 is a minority carrier diffusion length in the material before exposure to the radiation, L_ϕ is a minority carrier diffusion length after exposure of the cell to the particle beam with fluence ϕ measured in number of 1MeV electrons with given energy per unit area, and K_L is a damage coefficient of the material [159]. In multijunction cells, J_{sc} reduction in the current-limiting subcell due to the radiation damage is an important issue to address. It is a GaAs subcell that gets most affected by the radiation and incorporation of the quantum structures. QDs or QWs can assist in offsetting the radiation-induced bulk carrier collection efficiency reduction as additional current generated in the quantum structures region does not experience radiation damage [160].

Adding InAs QW/QD system to the intrinsic region of the GaAs subcell was widely studied in terms of QD growth optimization, strain compensation, device layer design, and radiation tolerance [161, 32, 162]. The 3J InGaP/GaAs/Ge baseline and QD solar cell structures are shown on Fig. 4.1a and b, respectively. The QD structures incorporated in the intrinsic region of the middle cell represent InAs QDs, GaAs barriers, and GaP strain compensation (Fig. 4.1). The mechanism of InAs QDs formation on GaAs
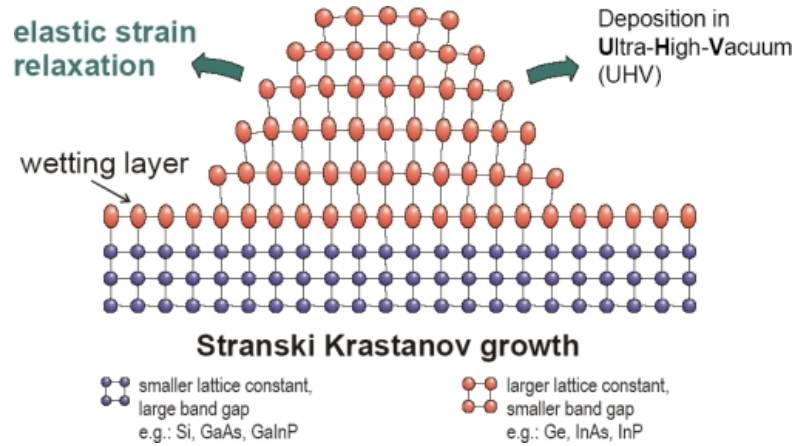
FIGURE 4.2: Stranski-Krastanov QD growth mechanism [171].

relies on the strong compressive strain accumulated in InAs material due to the lattice mismatch of 7.2% [163, 164]. Figure 4.2 shows the mechanism of a QD formation on the strongly-mismatched substrate via formation of a strained, monolayer-thick wetting layer and QD resulting from the further strain relaxation. Such growth mode requires relatively low growth temperatures ($\sim$ 450 - 490°C) to increase the number of QD nucleation centers and prevent an excessive migration of the adatoms along the growth plane contributing in QD coalescence via Ostwald ripening mechanism [165]. Due to the high vapor pressure of As, growth of the further high-temperature layers on top of the QDs can cause QD desorption, that is why overpressure of AsH$_3$ is necessary along with capping of the QDs with low-temperature GaAs as shown on Fig. 4.1c [166, 167]. Growth of InAs QDs on GaAs was previously optimized at RIT allowing to achieve uniform QD coverage with low degree of QD coalescence [168, 169, 170].

Radiation tolerance of the QD-enhanced solar cells was also investigated in comparison to the baseline devices and for different numbers of QD layers. The radiation hardness is typically characterized by the remaining factors of J_{sc}, V_{oc}, fill factor, and efficiency or power. Those are defined as a ratio between the parameter value after exposure to the radiation with certain fluence to the initial parameter value. Figure 4.3 shows
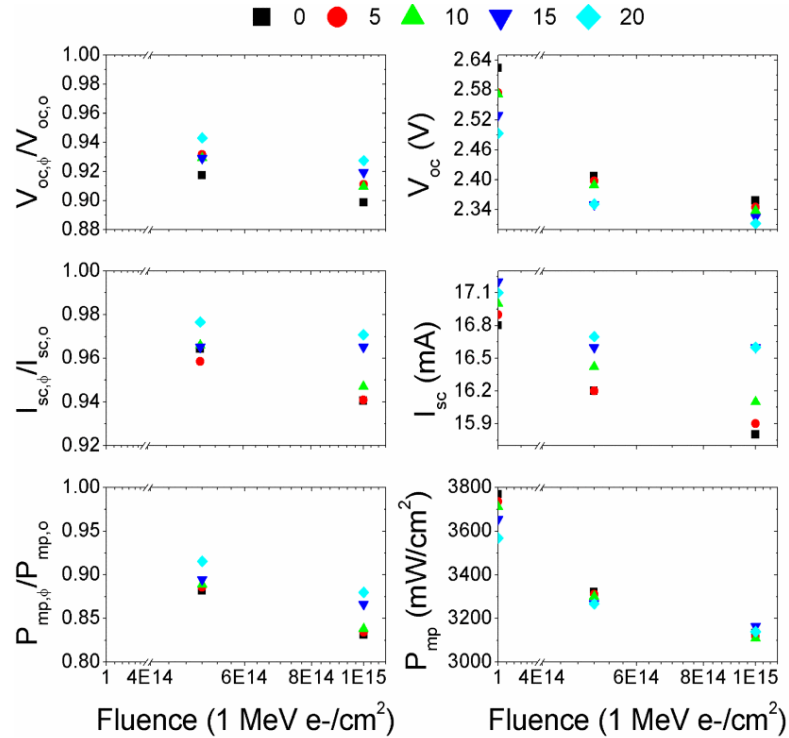
FIGURE 4.3: Radiation-induced decay of the 1 sun AM0 solar cell parameters: J_{sc}, V_{oc}, and power (remaining factors are shown in the left column and absolute values are given on the right). Color-coded are numbers of the QD superlattices, where 0 corresponds to the baseline[159].

the remaining J_{sc}, V_{oc}, and power as well as the absolute values of these parameters for various numbers of the QD superlattices (no QDs, 5×QDs, 10×QDs, 15×QDs, and 20×QDs). This family of plots illustrates that both relative and absolute end-of-life (i.e. after exposure to the 1 MeV 1E15 e-/cm^2 radiation) J_{sc} of the QD solar cells is higher than that of the baseline due to the extended absorption in the QDs and carrier collection in the QD region unaffected by the radiation. This reflects on the remaining power of the solar cells, P$_{mp,\phi}$/P$_{mp,0}$. Maximum achieved recovery of the end-of-life remaining power is 5% corresponding to the 20×QD solar cell compared to the baseline device. These observations are supported by other studies as well [172, 158, 45, 173].

4.3 Methods

Growth precursors and conditions and characterization tools described in Chapter 3, Methods section, apply for this section as well. EQE spectroscopy of the tandem cells requires light biasing of the subcells that are not being measured, such that DC current exceeds the AC signal produced by the excitation of the measured cell. For ensuring bottom GaAs cell is current limiting in the measurement, the InGaP subcell was illuminated with 470 nm LED, and for the InGaP EQE measurement, the GaAs cell was illuminated with a 750 nm LED light source.

InGaP with target In content of $\sim$49% was grown at 650°C, dopant precursors, DEZn and Si$_2$H$_6$ were used for p-type top cell base and n-type emitter, respectively. Wide-bandgap rear window layer in the top cell was realized with quaternary Al$_{0.27}$In$_{0.48}$Ga$_{0.25}$P alloy followed by the highly Zn-doped (2.1×10^{18} 1/cm^3) 30 nm-thick GaAs-lattice-matched InGaP. The choice of the wide-bandgap (2.19 eV) quaternary window layer composition was driven by a couple of factors. Having higher minority electron barrier at the rear interface of the top solar cell is beneficial for preventing interface recombination. At the same time, further increase in the bandgap achievable by increasing an Al fraction in the alloy, could lead to poorer incorporation of p-type Zn dopant. Second, some wide-bandgap AlInGaP compositions have indirect bandgap which makes it more challenging to establish the bandgap value by standard PL measurement. Thus, the Al$_{0.27}$In$_{0.48}$Ga$_{0.25}$P composition was targeted and successfully implemented. Other layer characteristics including thicknesses and doping are shown on the device scheme (Fig. 4.4). Modeling of the solar cells was performed using Sentaurus Device using optical constants of the active materials measured by ellipsometry on RIT-produced epitaxial films.

Layer	Thickness	Doping
Ni/Au		
n-GaAs:Si/Te contact	100+50 nm	5e18/2e19
n-window AlInP	20 nm	2e19
n-emitter InGaP:Si	70 nm	1e18
i-InGaP	10 nm	UID
p-base InGaP:Zn	400 nm	1e17
p-bsf InGaP:Zn	30 nm	2e18
p-bsf InAlGaP:Zn	30 nm	1e18
p++ AlGaAs:C	10 nm	2e19
i-GaAs	2 nm	UID
n++ GaAs:Te	10 nm	2e19
n+ AlGaAs:Si	10 nm	1e18
n-fsf InAlP	25 nm	1e19
n-emitter InGaP:Si	50 nm	2e18
i-GaAs	100 nm	UID
p-base GaAs:C	3100 nm	1e17
p-bsf InGaP	100 nm	1e18
p-buffer GaAs:Si	100 nm	1e18
Substrate p-GaAs		
Au/(Zn)/Au annealed		

(a)

Layer	Thickness	Doping
Ni/Au		
n-GaAs:Si/Te contact	100+50 nm	5e18/2e19
n-window AlInP	20 nm	2e19
n-emitter InGaP:Si	70 nm	1e18
i-InGaP	10 nm	UID
p-base InGaP:Zn	400 nm	1e17
p-bsf InGaP:Zn	30 nm	2e18
p-bsf InAlGaP:Zn	30 nm	1e18
p++ AlGaAs:C	10 nm	2e19
i-GaAs	2 nm	UID
n++ GaAs:Te	10 nm	2e19
n+ AlGaAs:Si	10 nm	1e18
n-fsf InAlP	25 nm	1e19
n-emitter InGaP:Si	50 nm	2e18
i-GaAs	33 nm	UID
QD SL	~120 nm	UID
i-GaAs	33 nm	UID
p-base GaAs:C	3100 nm	1e17
p-bsf InGaP	100 nm	1e18
p-buffer GaAs:Si	100 nm	1e18
Substrate p-GaAs		
Au/(Zn)/Au annealed		

(b)

FIGURE 4.4: Dual-junction InGaP/GaAs (a) baseline and (b) QD solar cell structures.

For the QD device, InAs quantum dots were grown in the intrinsic region of the bottom GaAs subcell via the Stranski-Krastanov growth mode [164]. AsH$_3$ and tertiarybutylarsine, TBAs, were tested as precursors for low-temperature QDs growth ($\sim$450°)[159]. The use of TBAs was considered due to the lower cracking temperature allowing better control over the QD thickness and coalescence, however, the final set of the QD solar cells was grown using AsH$_3$. Since Stranski-Krastanov QD growth mechanism relies on the build up of compressive strain allowing formation of the discrete QD islands on the substrate surface when critical thickness corresponding to the mismatch between InAs and GaAs is exceeded, to mitigate the overall residual strain, GaP strain compensation layers were placed between the layers of QDs capped with GaAs [166, 174, 175].

Tunnel junction [3, 93] test structures were separately grown and fabricated first to evaluate their applicability for 1 sun operation (peak current density of the tunnel junction

Layer	Material:Dopant	Thickness (nm)	Doping (1/cm³)
Contact Layer	GaAs:C	200	2e19
Buffer	GaAs:Zn	10	1e18
Top Cell BSF	In$_{0.48}$Ga$_{0.52}$P:Zn	50	1e18
TJ "Emitter"	Al$_{0.30}$Ga$_{0.70}$As:C	10	2e19
TJ "UID"	GaAs	2	UID
TJ "Base"	GaAs: Te	10	-2e19
TJ Diffusion Barrier	Al$_{0.3}$Ga$_{0.7}$As:Si	10	-1e18
Bottom Cell Window	In$_{0.49}$Al$_{0.51}$P:Si	25	-8e17
Bottom Heterojunction Cell Emitter	In$_{0.48}$Ga$_{0.52}$P:Si	50	-2e18
Epi Buffer	GaAs:Si	300	-1e18
Substrate	GaAs	350000	-1e19
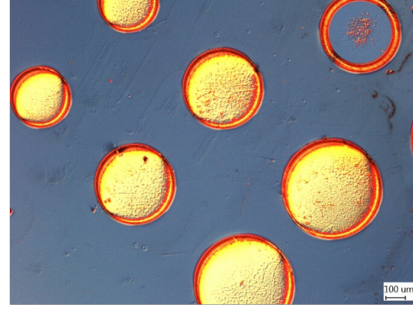
(a) **(b)**

FIGURE 4.5: (a) Tunnel diode layer structure and (b) optical microscopy top view image of the fabricated structures.

must exceed the limiting J$_{sc}$ of the 2J cell). The tunnel diode structures were grown on GaAs substrates along with the bottom and top cell window and back-surface field layers, respectively. The devices were mesa-isolated on the substrate by self-aligned etch against Au contacts to define the diode active areas (the largest devices were 0.0019 cm^2). The full structure and optical microscopy image of the transparent thinned hetero-tunnel diodes fabricated in circular diodes are shown on Fig. 4.5.

Both baseline and QD cells were fabricated using standard III-V processing techniques (manual processing including UV lithography patterning for defining the metal grids and active areas combined with wet etch for mesa-isolating devices using selective III-V compound etchants) in 1 cm^2 devices (test structures) and in 26.5 cm^2 solar cells grown on 4-inch substrates with 2° towards ⟨110⟩ offcut intended to be integrated onto the CubeSat as a power supply unit. Metallization of the solar cells contacts was performed via electroplating using Zn and Au combination for the rear-side annealed p-type contacts and Ni and Au for the n-type front contacts, where Ni seed layer serves as an adhesion for Au. Characterization of two-terminal monolithic 2J devices is more complicated than that of the 1J solar cells due to the unaccessibility of the individual cells for measuring

their electrical parameters directly. However, spectroscopy techniques (EQE and EL) coupled with the electrical testing can be used for extracting the individual sub-cells V$_{oc}$'s using the reciprocity relation and for finding the approximate individual J$_{sc}$'s of the subcells for their quality evaluation. Similarly to that described in Chapter 5, the reciprocity relation was written for the diodes (top and bottom cells) connected in series as a system of equations, such that V$_{oc}^{top}$ and V$_{oc}^{bot}$ can be calculated from the relative spectral irradiance of the biased cells under the injection current corresponding to the 1 sun integrated J$_{sc}$'s of the subcells and near-bandedge EQE:

$$EL_{top} = BB \times EQE_{top} \times exp\Big(\frac{qV_{top}}{k_BT}\Big) \tag{4.2}$$

and

$$EL_{bot} = BB \times EQE_{bot} \times exp\Big(\frac{qV_{bot}}{k_BT}\Big) \tag{4.3}$$

while considering that thus extracted voltages normalized by the setup calibration constant are related as:

$$V_{top} + V_{bot} = V_{oc}. \tag{4.4}$$

Relative EL was used for this calculation, such that the EL$_{top}$ and EL$_{bot}$ were related as the ratio between the EL peak intensities that are representative of the absolute irradiance corrected by a coefficient.

4.4 Results and Discussion

The final 2J solar cells, both without and with QDs, feature a transparent tunnel diode structure with p++ $Al_{0.30}Ga_{0.70}As$:C "emitter" and n++ GaAs:Te "base", both with thicknesses of 10 nm and intrinsic, 2 nm-thick GaAs layer serving for mitigation of Te memory effect [176, 177]. In addition, the final set of the 2J cells comprises heterojunction bottom GaAs cell with InGaP emitter and InAlP window layers for reduced non-radiative dark current [131]. The n+ AlGaAs diffusion barrier is placed underneath the tunnel diode to prevent the out-migration of dopant species from highly doped tunnel diode layer. Ordering effects in low-doped InGaP material causing the bandgap shift were taken into account as well [178, 179, 180]. While elevated doping of InGaP with Zn can partially address the ordering effects, as well as adjustments of other growth parameters (III/V ratio and growth temperature), using larger offcut substrates for the tandem growth [181] was found to resolve the issue without requiring any further calibration of the growth regime.

The transparent tunnel diode design was partially inherited from the previously performed studies [182]. Figure 4.6 shows the current-voltage characteristic of the tunnel diodes collected from 19 devices yielding the average peak current density of 14 A/cm^2. The voltage drop across the tunnel diodes was not exceeding 50 μV in the current range corresponding to the expected 1 sun J$_{sc}$ of the tandem cell reaching up to 16.5 mA/cm^2 under AM0 illumination with anti-reflective coating. These specifications allowed this tunnel diode structure to be adapted for the RIT 2J solar cell without any further adjustments as it is expected to provide reliable operation under 1 sun use.

The first optimization step that led to the increased the rear-side collection in the top InGaP cell was development of a 2.19 eV $In_{0.48}Al_{0.27}Ga_{0.25}P$ (henceforth to be referred
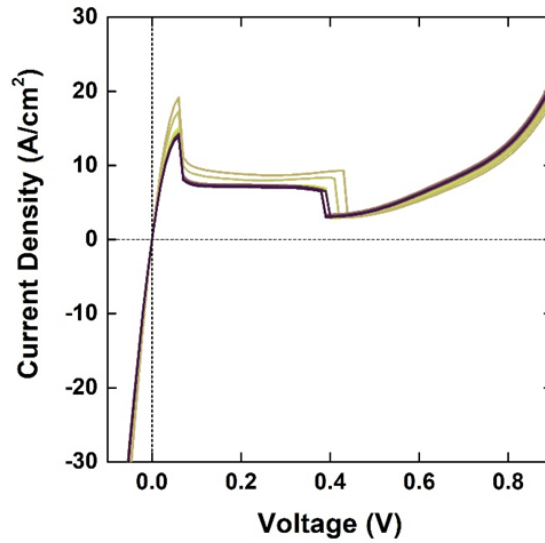
FIGURE 4.6: Family of the J-V characteristics of the AlGaAs/GaAs tunnel diodes.

as InAlGaP) back-surface field (BSF) in addition to the previously used highly-doped InGaP:C. Figure 4.7 shows the overlayed EQE spectra of 1J test InGaP solar cells with 600 nm-thick base with InGaP and bi-layer InAlGaP and InGaP BSF (the bi-layer BSF is shown on Fig. 4.4). The purpose of using dual BSF was to initially establish an electric field at the homointerface between InGaP base and highly-doped InGaP BSF and further enhance minority carrier repulsion by introducing an energy barrier. An integration of the spectral response of these solar cells modulated with the AM0 spectrum irradiance (Eq. 4.5 analogous to the Eq. 2.25) yields total gain of ~ 1 mA/cm^2 by switching to the distributed BSF including creation of the minority-carrier barrier by adding heterojunction and additional electric field established at the p-type InGaP base and p+ InGaP BSF layer (base doping is 5×10^{16} 1/cm^3) allowing to repel electrons from the rear interface of the solar cell increasing collection probability that directly reflects on the spectral response and J$_{sc}$.

$$J_{sc,EQE} = \int_{\lambda_1}^{\lambda_2} \frac{q\lambda}{hc} I_{AM0}(\lambda) EQE(\lambda) d\lambda. \tag{4.5}$$
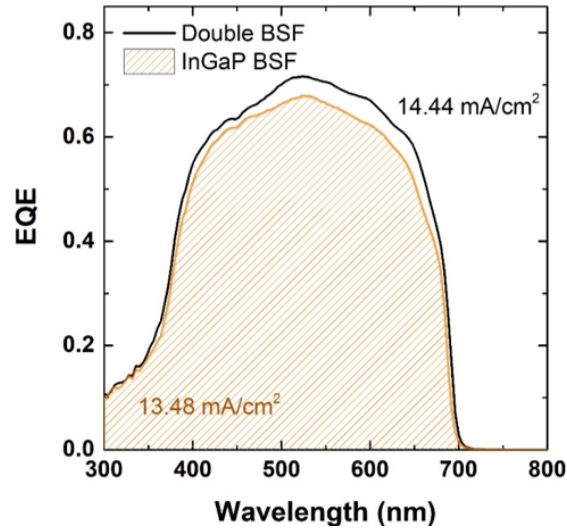
FIGURE 4.7: EQE spectra of the 1J InGaP solar cells with single-layer InGaP BSF (orange shadowing) and combination of InAlGaP and InGaP BSF (black line) with integrated 1 sun AM0 J$_{sc}$.

Significant overproduction of current in the top cell compared to the bottom cell is not favorable for the optimal efficiency of the tandem cell as bottom cell becomes strongly current-limiting reducing the resulting current output. The initial design of the top cell with 600 nm-thick absorbing top cell base was developed first in 2018 and was found to be not optimal requiring a reduction in the base thickness due to the overproduction of current by the top cell by 3.3 mA/cm^2 comparatively to the bottom GaAs cell. Figure 4.8 shows the EQE spectra of the top and bottom cells with the integrated J$_{sc}$'s corresponding to the 600 nm-thick top base. While current mismatch of $\sim$ 0.5 mA/cm^2 would be preferred for the baseline device allowing to identify the current density gain achieved with addition of QDs, the discrepancy between the currents of 3.3 mA/cm^2, as indicated by the integrated J$_{sc}$ values, is unacceptable, so further adjustments in the top cell were required. Making the bottom cell current-limiting is important for the test purposes to be able to directly measure the current gain achievable with adding quantum structures. The difference between the 2018 and new 2019 devices is in transitioning to the heterojunction bottom cell that immediately reflected in higher EQE in the bottom GaAs cell (the heterojunction bottom cell design is the same as in [131]). Another
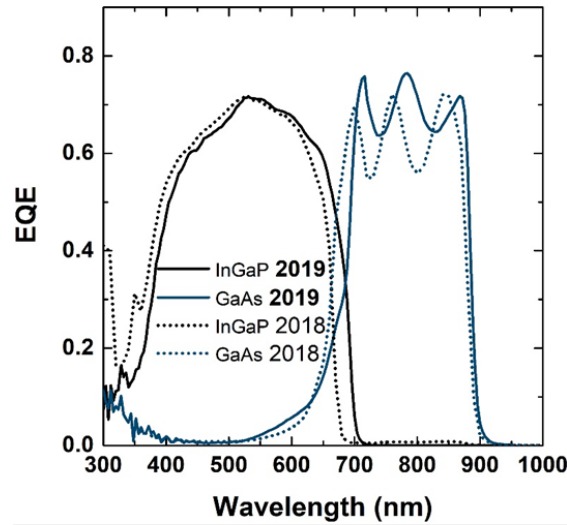
Integrated J$_{sc}$:
J$_{sc}$(InGaP) = 14.83 mA/cm^2
J$_{sc}$(GaAs) = 11.51 mA/cm^2

FIGURE 4.8: EQE spectra of the top cells with 600 nm-thick base and bottom cells with the integrated J$_{sc}$'s denoted for the 2019 devices (solid lines).

nuance that is notable in the spectra on Fig. 4.8 is the band edge offset in the top cell.
This is attributed to the changing the substrate offcut from 6° in 2018 to 2° in 2019.
The magnitude of the band edge red shift is 50 meV corresponding to so-called 50 meV
anomaly [178] caused by the ordering in InGaP. This also promotes an increase in the
J$_{sc}$, along with the reduction in V$_{oc}$, and needs to be taken into account.

Top cell base thickness was optimized for the InGaP material grown 2° offcut substrate.
Experimental results were used to predict the current and base thickness relation (Fig.
4.9). The experimentally obtained optical constants were used. With minority elec-
trons in the base, the change in their lifetime in the nanoseconds range did not have
a significant impact on the EQE shape due to high mobility in low-doped base (μ_e =
2722 cm^2/V-s). Based on the simulation study, for the next set of samples, InGaP base
thickness was reduced to 400 nm. Figure 4.10 shows EQE spectra of the baseline 2J

(a)   **(b)**
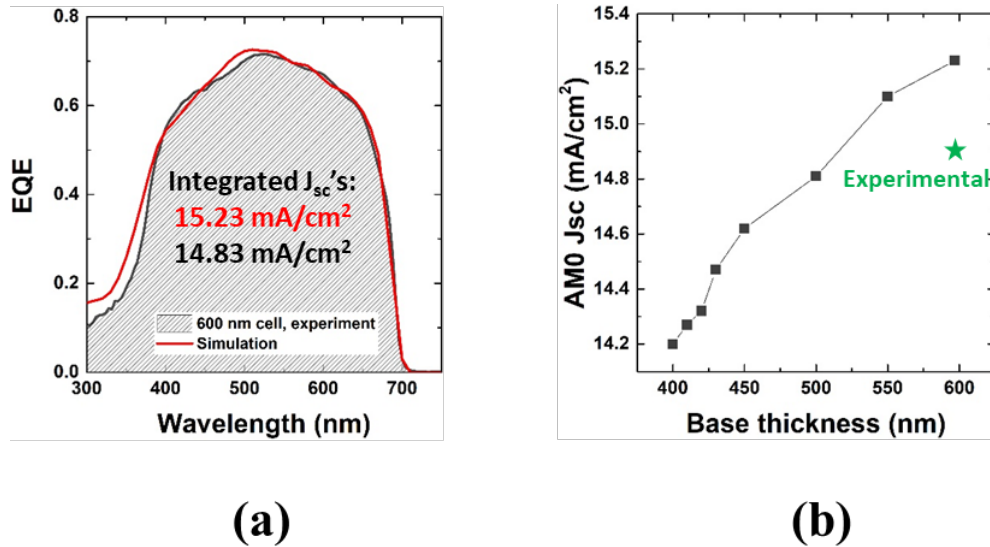
FIGURE 4.9: (a) Modeled and experimental EQE spectra of the InGaP cell with 600 nm-thick base; (b) dependency of the 1 sun J$_{sc}$ on the base thickness. Green star denotes the experimental value and the line is added as an eye guide.

subcells and 2J with QDs in the bottom cell. One can notice that close-to-target current mismatch between the baseline top (12.44 mA/cm^2) and bottom (11.85 mA/cm^2) is achieved. With the QD device, however, short-circuit response in the top cell is degraded reducing the integrated J$_{sc}$ down to 11.76 mA/cm^2. At the same time, the current density gain from adding QDs to the bottom cell achieved 0.11 mA/cm^2. The possible reason for the degradation of the top cell can be elevated front surface recombination velocity, since long-wavelength EQE corresponding to the base response is preserved as high as in the baseline device. Thus, problems with either InAlP window or InGaP emitter can be suspected. This has not been investigated yet, since more global issue with incorporating QDs in the bottom cell was observed.

One-sun illumination J-V measurements of the baseline and QD devices were performed and representative J-V characteristics are shown on Figure 4.12 with extracted parameters listed on the graph inset. On average, the drop of V$_{oc}$ in the QD cells is ~200 mV. In addition, there is a visible knee occurring near maximum power point influencing the fill factor (drops by 8%), since neither series resistance component, nor shunt are visibly
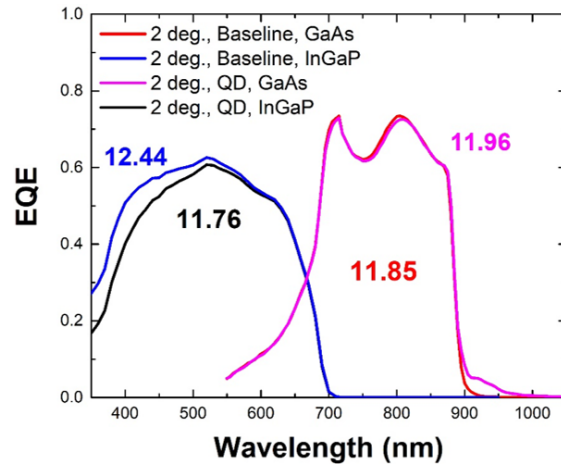
FIGURE 4.10: EQE spectra of the 2J top and bottom subcells (baseline and with QD) of the devices grown on 2° offcut substrates with thinned top cell base. Numbers correspond to the extracted integrated 1 sun J$_{sc}$'s and color-coded for each cell.
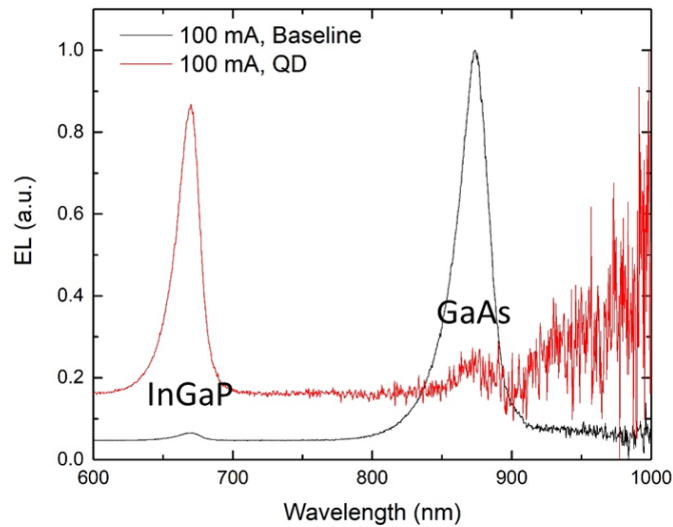
FIGURE 4.11: EL spectra of the baseline (black) and QD (red) solar cells measured at 100 mA/cm^2 injection current density.

changed. To identify whether the top or the bottom cell are responsible for the voltage reduction, an EL study was performed. Despite the degradation in the top cell EQE, the EL spectroscopy revealed severe reduction in radiative emission intensity specifically from the bottom GaAs cell. Figure 4.11 shows EL spectra of the tandem baseline and QD cells with the bulk InGaP and GaAs peaks denoted.

While for the baseline, V$_{oc}^{top}$ extracted from reciprocity was 1.366 V and V$_{oc}^{bot}$ was 1.014 V, under near-one-sun injection, only the signal from the InGaP cell could be resolved and to
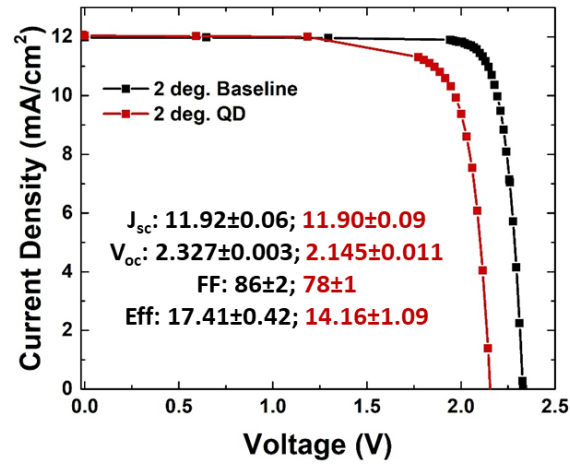
FIGURE 4.12: 1 sun AM0 illuminated J-V characteristics of the baseline (black) and QD (red) 2J cells. Electrical parameters measured for the assortment of 12 devices per wafer are listed as an inset.

obtain reliable signal from the bottom cell and QDs, the injection current density had to be increased. Upon this, however, the magnitude of the top cell signal saturates the CCD detector, thus any comparative quantitative analysis becomes impossible. Qualitatively, this shows that some inferior process in the bottom cell space-charge region causes an increase in non-radiative recombination under applied forward bias. The possible reason for it can be a distortion in the crystalline structure in the QD superlattice layers leading to the non-radiative loss of carriers. In addition to the EL analysis, EQE spectroscopy can be performed under bias to assess the wavelength-resolved carrier collection efficiency under different band alignment regimes the same way as described in Chapter 3. The only modification that needs to be made for measuring tandem devices is a simultaneous use of light bias.

Voltage-biased EQE measurements were performed on the QD solar cell in the range of applied voltages from -1.8 V to 1.8 V (maximum power point voltage of the tandem is 1.85 V). Measurements under forward bias are limited by the diode switch-on point. Figure 4.13a shows EQE spectra collected from the GaAs bottom cell of the tandem with QDs. While the signal from the QDs remains stable under applied bias,an apparent

drop in the base region occurs. For comparison, the EQE values measured from the baseline and QD device at the wavelength of 860 nm is plotted in dependency on the applied voltage and are shown on Figure 4.13b. The rapid decline in the bulk collection efficiency in the QD cell is observed even under small forward bias dropping by 15% near maximum power point, while baseline cell retains stable GaAs base collection up to 2 V. To possibly establish the reason causing the decline in the EQE in the QD cell and reduction in the V$_{oc}$, the offset in the EQE under forward bias and under short-circuit condition was investigated as a function of wavelength (Fig. 4.13c, d). It can be noticed that the reduction in spectral response under positive bias increases at longer wavelengths corresponding to the higher absorption depth. This behavior can be explained by shrinking of the space-charge region making dependency on the diffusion length of electrons generated at the rear side of the base stronger.

This observation, however, does not provide an insight for the dramatic reduction in EL and V$_{oc}$ and flattening of the J-V curve near maximum power point in the QD device. Both of the phenomena indicate that some source of enhanced non-radiative recombination might be present in the depletion region where QDs are located. Similar effects were previously observed in the QW cells [148] and were attributed to the unintentional i-region doping causing electric field reduction impacting the carrier transport across the QWs. On the other hand, dark current measurement of the tandem baseline and QD devices (Fig. 4.14) might reveal that voltage-dependent recombination in the QDs can play the role in degrading the QD cells performance. Alignment of the QD minibands can induce tunneling of charge carriers resulting in resonant tunneling favoring thermal carrier escape as they tunnel from deeper to shallow levels [183]. The local peaks occurring in the QD cell's dark current at 0.35 V, 1.22 V, and 1.79 V might be the evidence of the carrier tunneling transitions. Another possible cause for the voltage reduction in the
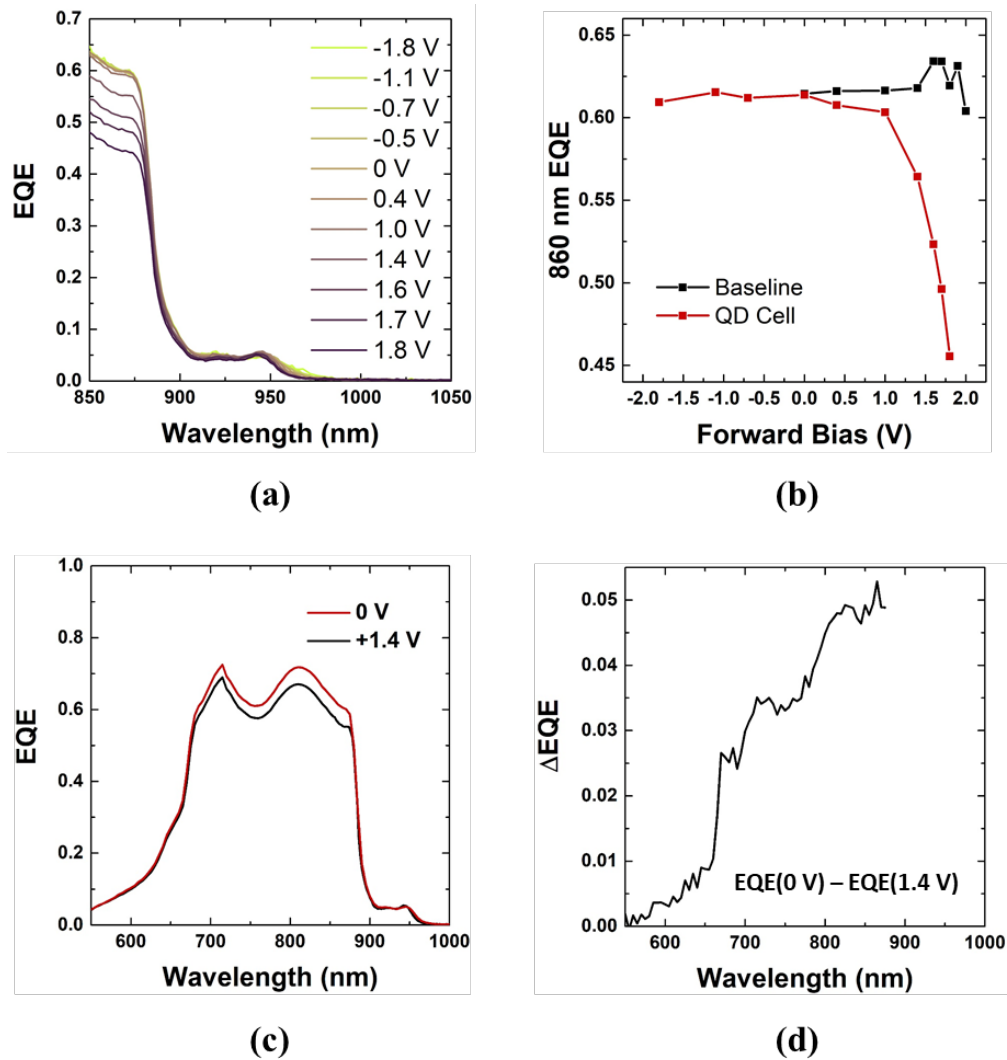
FIGURE 4.13: (a) EQE spectra of the bottom GaAs subcell with QDs under applied bias ranging from -1.8 V to +1.8 V; (b) comparison between EQE of the baseline cell (black) and QD cell collected at 860 nm under varied applied voltages; (c) full EQE spectra of the bottom subcell with QDs under short-circuit condition and under applied +1.4 V; (d) extracted from (c), wavelength-specific difference in EQE of unbiased QD cell and QD cell under 1.4 V bias.

bottom cell can be the heterojunction. However, further investigations or solid simulations of the devices are required to make a solid conclusion on the definitive mechanism of QD cell performance degradation.

Fabricated on 2-inch substrates, the record AM0 efficiency of the 2J solar cell was achieved from the baseline device grown on 6° offcut substrate and was 25.0% after depositing a bi-layer ARC (ZnS and MgF$_2$) which is 0.65% higher than the identical
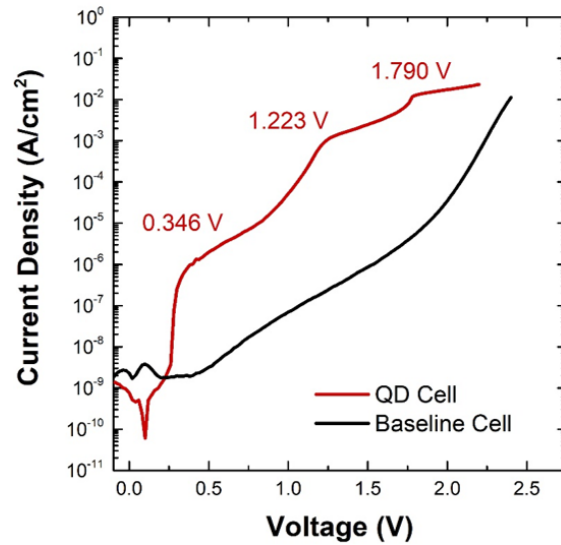
FIGURE 4.14: Dark current measurements of the baseline 2J cell (black) and QD tandem (red). The numbers represent the voltages corresponding to the local peaks.
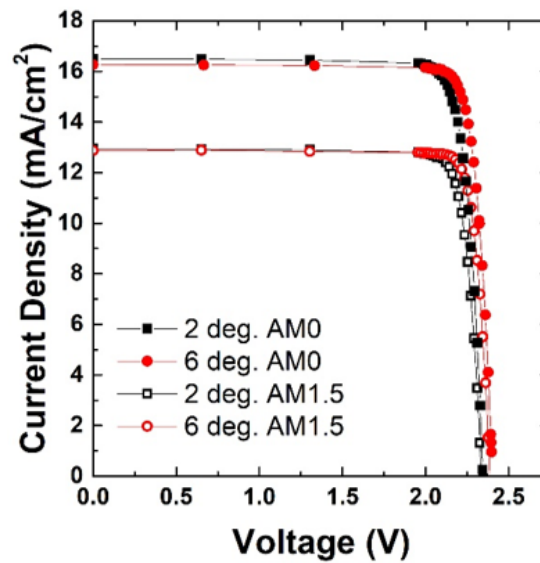
FIGURE 4.15: AM0 (solid points) and AM1.5G (open points) illumination J-V curves of the tandem baseline solar cells grown on 2° (black) and 6° (red) offcut substrates.

device grown on the 2° offcut substrate due to the InGaP subcell voltage reduction by 50 mV (Fig. 4.15).

The scaled-up 26.7 cm^2 cells were grown on 4-inch substrates (2°). Figure 4.16 shows the mask layout used for fabricating these cells (2 large cells per wafer and smaller test structures). For the large cells, grid spacing is 673 μm, grid finger width is 8 μm, while height of the electroplated grid fingers can vary between 2μm to 4 μm. In addition to the
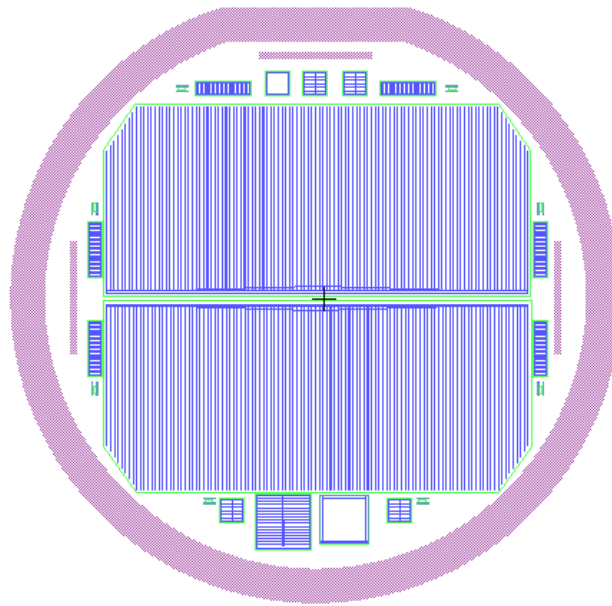
FIGURE 4.16: The lithography mask layout for 26.7 cm^2 cells.

metal contacts, top conductive epitaxial layers can contribute into the series resistance, however, their parameters remained unchanged in the large-area device. Measurements of the large cells under illumination yielded unexpected results. Figure 4.17a shows 1 sun AM0 J-V curves of the large-area baseline (black)and QD (red) cells. In the baseline device, an increased series resistance is present which could indicate that the height of the grid fingers is smaller than implied by the lateral design and can be a result of irregularity in electroplating process. QD cells do not exhibit this problem, although both types of devices suffer from leakage as seen in the low-bias range (the light J-V curve is not flat near J_{sc}). EL emission from the top InGaP subcell (luminesces at 675 nm) is shown on Fig. 4.17b illustrating the uniformity in the emission across the solar cell area and suggesting areal manufacturing consistency and low lateral series resistance.

Comparison of the electrical parameters of large and small (0.25 cm^2) area baseline and QD solar cells was performed. The maximum power output was from the QD cell and was 650 mW corresponding to the J$_{sc}$ of 16.44 mA/cm^2, V$_{oc}$ of 2.146 V, and fill factor of 69%. While baseline device had 200 mV higher V$_{oc}$, as well as previously made 1
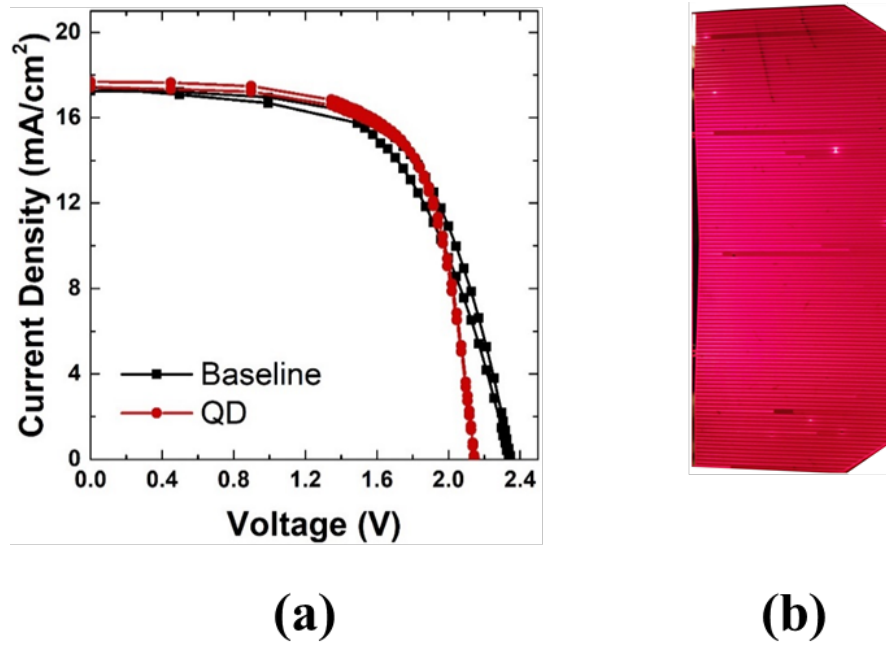
FIGURE 4.17: (a) 1-sun AM0 illumination J-V curves of the baseline (black) and QD
(red) large-area cells; (b) visible electroluminescence from the top InGaP subcell (two
injection points).

cm^2 test cells, the gain in fill factor and J$_{sc}$ (measured under illumination, ΔJ$_{sc}$ = 0.29

mA/cm^2) allowed QD cell to show better overall performance. For both devices, small

cells had fill factors of 80% (baseline) and 76% (QD). This discrepancy can indicate

the lateral conduction or probing to be a problem for the larger devices, while overall

record fill factor of reduced-area devices being 10% smaller than that of standard cells

(typically, 89%) can indicate a presence of a rear contact issue.

EQE spectroscopy also was performed on this set of devices and is shown on Fig. 4.18.

QD device shows broadband reduction in the top InGaP cell EQE, while bulk GaAs

subcell EQE remains almost unchanged. Degradation of the top cell can be caused by

residual strain induced by the QD superlattice. A closer look at the QD region (Fig.

4.18b) gives an estimate of the integrated J$_{sc}$ gain of 0.25 mA/cm^2 due to QDs that

matches well with the measured currents.

While scale-up of the 2J cells still requires some considerations (possibly checking the

(a) **(b)**
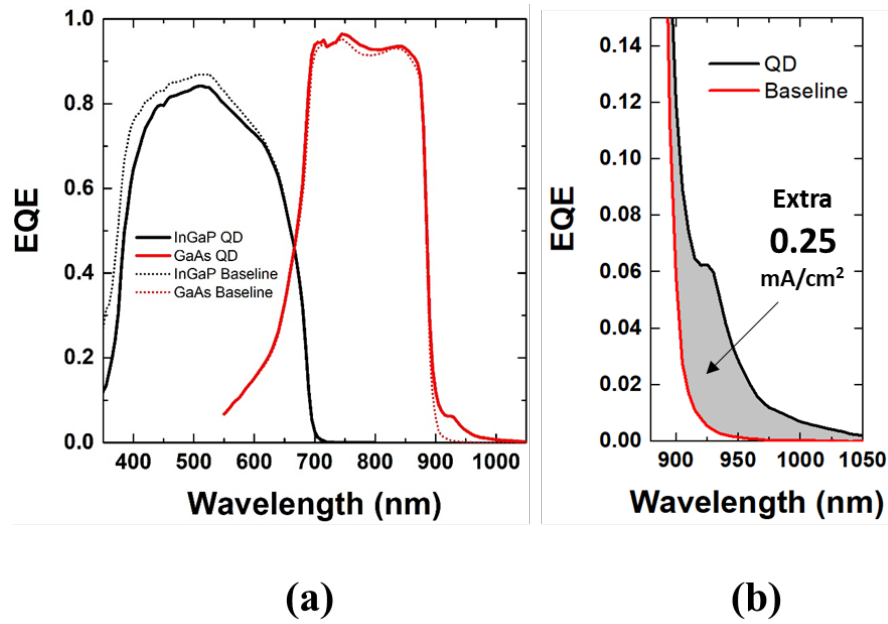
FIGURE 4.18: (a) EQE spectra of the InGaP and GaAs subcells of the baseline (dotted line) and QD (solid line) solar cells grown on 4-inch substrates; (b) QD EQE region (black) over the baseline (red) EQE tail and integrated spectral response J$_{sc}$ gained from adding the QDs.

uniformity of epitaxy and calibration of the heating elements, improving the electroplating uniformity and enabling rear alloyed contact for realizing acceptable series resistance), there was a significant progress made on developing the dual junction solar cells. Some refinements that are currently in work include achieving closer lattice matching of InGaP for top cell voltage enhancement and solving ordering problem either by moving to larger-offcut substrates or carrying out temperature and precursor flow calibrations to achieve disordered 1.89 eV InGaP on 2° GaAs. Additional design modifications can include switching to the rear-side emitter configuration and targeting higher front window doping for minimization of surface impact. However, the successful implementation of the tunnel diode and established growth and characterization techniques open up possibilities for producing high-efficiency multijunction devices at RIT.

Chapter 5

Single-Junction In$_{0.18}$Ga$_{0.82}$As Metamorphic Solar Cells for Low-Cost Photovoltaics

5.1 Motivation and Background

Metamorphic epitaxial growth is the growth of fully relaxed material on a substrate with considerable structural difference, typically a large lattice mismatch. Misfit strain is deliberately relieved by the formation of dislocations at the interface or at multiple interfaces in a graded structure, away from the active areas of the device. Since any generated threading segment contributes only marginally to strain relaxation but detrimentally acts as a non-radiative recombination center, the density of threading dislocations is to be minimized by eliminating kinetic barriers to dislocation glide, e.g., compositional inhomogeneity and high surface roughness. In photovoltaics (PV), metamorphic epitaxy enables the integration of absorbing materials with a wider energy bandgap

range than lattice-matched systems offer, allowing for a more optimized partitioning of the solar spectrum [18], [184]. Inverted metamorphic multijunction solar cells hold efficiency record under concentrated light [185], [186]. On the other hand, overcoming the limitations imposed by lattice mismatch can contribute to the III-V photovoltaics cost reduction by allowing for the low-cost alternative epitaxial substrates. For example, integration of III-V-based device systems onto silicon has been developing for decades yielding new technological possibilities in photonics [187],[188], and photovoltaics [23].

While development of the metamorphic buffers or metamorphic grading (MMG) is described in detail in [189] the part of the study dedicated to the design and characterization of the single-junction metamorphic 1.16 eV In$_{0.18}$Ga$_{0.82}$As solar cells is presented in this work. A comprehensive study of the device performance in dependence on the GaAs(001) substrate offcut and grading scheme is carried out using electroluminescence analysis for establishing relation between the threading dislocations density in the metamorphic material and electrical parameters of the devices.

5.2   Methods

1.1 eV In$_{0.18}$Ga$_{0.82}$As solar cell structures lattice-matched to metamorphic In$_{0.18}$Ga$_{0.82}$As on GaAs(001) were fabricated by MOCVD using an Aixtron Closed Coupled Showerhead^{ő} 3x2" reactor. III-V layers were grown using trimethylgallium (TMGa) and trimethylindium (TMIn) as group III precursors, and either arsine (AsH$_3$) or phosphine (PH$_3$) as group V precursors. Initially, five types of GaAs(001) substrates were explored aiming at achieving the highest quality In$_{0.18}$Ga$_{0.82}$As template for the subsequent integration of Al: on-axis, 2° to [110], 2° to $\langle 111 \rangle$ A, 2° to $\langle 111 \rangle$ B, and 6° to $\langle 111 \rangle$ A. Prior to growth the substrates were annealed for 5 min under AsH$_3$ at 700°C to desorb the native oxide.

For each substrate type, 5×300 nm, 10×300 nm and 5×600 nm In$_x$Ga$_{1-x}$As MMGs with x increasing in identical steps up to 22 at% were grown. The grading rate was 1.05% misfit/μm for the first structure and 0.53% misfit/μm for the other two. The top In$_{0.22}$Ga$_{0.78}$As film, which is +1.58% lattice-mismatched to GaAs, overshoots the target In$_{0.18}$Ga$_{0.82}$As composition to compensate for residual coherency strain [190]. The growth temperature was 600°C for the 5×300 nm and 10×300 nm series, and 600 and 650°C for the 5×600 nm specimens. MMG heterostructures were overgrown with an unstrained In$_{0.18}$Ga$_{0.82}$As Fall Back Layer (FBL) in the 1-3 μm range at 650°C to isolate active regions of the device from defects. Real temperature, as well as reflectivity at 405, 633 and 950 nm, and curvature were monitored in situ with a LayTec EpiCurve$^{\ddot{o}}$ TT sensor. The reactor pressure was 100 mbar throughout the growth process.

One cm^2 In$_{0.18}$Ga$_{0.82}$As solar cells were manufactured by standard III-V fabrication technology and the devices were mesa-isolated with the mesa etch terminated at the metamorphic buffer fallback layer. No antireflective coating was deposited to enable an investigation of the structural and design effects on the devices operation specifically. 1-sun AM1.5 Global illumination J-Vs were measured by a two-zone TS Space Systems solar simulator (RIT NanoPower Research Laboratories) calibrated using InGaP and GaAs reference solar cells. External quantum efficiency measurements were performed using Newport IQE-200 Quantum Efficiency Measurement System. Electroluminescence analysis was done with OceanOptics^{TM} spectrometers calibrated for the absolute irradiance measurements using broad-range light source.

5.3   Results and Discussion

Two p-i-n solar cell designs differing in the emitter thicknesses proposed for this work are depicted on Fig. 5.1(a). Increasing thickness of the p-type emitter, t, was intended to enhance carrier generation rate and collection. Provided that electrons are the minority carriers in the emitter, an increase in thickness allows to take advantage of their significantly higher mobility and diffusion length as compared to holes. Selected emitter dimensions resulted from a series of simulations performed in TCAD Sentaurus Device, Synopsys^{TM} software. To ensure validity of the modelling, the minority carrier lifetimes were reduced relatively to the lattice matched In$_{0.18}$Ga$_{0.82}$As to take degradation of the metamorphic material into account. The optimal value of the emitter thickness extracted from the simulation in terms of short-circuit current density (J_{sc}) and conversion efficiency was around 500 nm which determined the additional design of the solar cells. However, this leads to the reduction in open-circuit voltage (V_{oc}) as the depth of junction increases making diffusivity of the charge carriers critical, specifically in highly defective samples. The gain in fill factor is expected from the cells with thicker emitter as the cross-section area of the lateral path for charge carriers in the emitter increasing proportionally to t^2 leads to the reduction of series resistance which is influential at small thicknesses.

Based on the preceding optimization of the metamorphic buffers for In$_{0.18}$Ga$_{0.82}$As on GaAs substrates two grading schemes, 5×600 nm and 10×300 nm, were preferred for the following growth of the solar cell structures to supposedly provide reduced non-radiative losses and thus promote higher open-circuit voltage. As also deduced from the structural analysis, the use of offcut substrates is favored for high-quality In$_{0.18}$Ga$_{0.82}$As growth, so 2° towards $\langle 110 \rangle$, 6° towards $\langle 111 \rangle$A, and 6° towards $\langle 110 \rangle$ offcut substrates
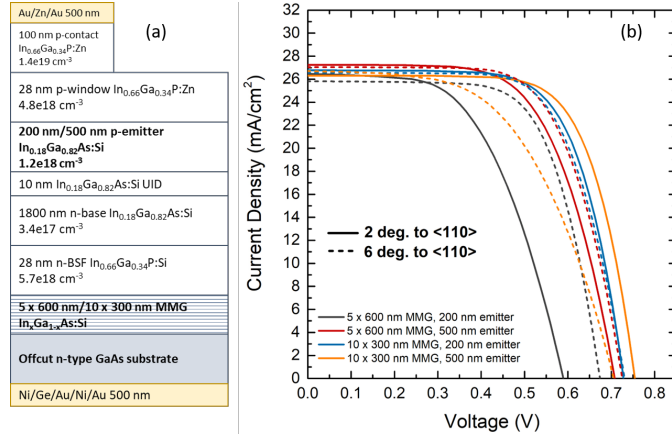
FIGURE 5.1: (a) Scheme of the solar cell structure designs: with 5 × 600 nm and 10 × 300 nm MMG buffers and with emitter thicknesses of 200 nm and 500 nm. (b) 1 sun AM1.5G illuminated J-V curves of the solar cells grown on the (100) GaAs substrates with 2° → ⟨110⟩ (solid lines) and 6° → ⟨110⟩ (dashed lines) offcuts.

were selected. The one-sun $J - V$ measurements were performed under AM1.5G illumination. The illuminated $J - V$ characteristics are shown on Fig. 5.1(b). Obtained electrical parameters are summarized in Table 5.5. Ranging from 9.10% to 13.53%, the maximum achieved average efficiency is attributed to the 10 × 300 nm MMG buffer sample with 500 nm-thick emitter; the averaging was performed for for 12 1 cm^2 × 1 cm^2 solar cells fabricated on the single 2-inch wafer. The best device also features the highest V_{oc} of 0.748±0.010 V. The fill factors of the solar cells in all groups are below 70% due to the series resistance (R_{series}) which is caused by thin Au contacts (500 nm), however, the best device's fill factor is the highest - 69 ± 2%. Deposition of thicker contacts would allow to push the efficiency up to ∼ 17%. From comparison of the samples with finely graded buffers and two different emitter thicknesses, J_{sc} did not show an increase expected for the sample with the thicker absorber. This could indicate that it might be minority-carrier-diffusion-length-limited and an enhancement in generation is inhibited by the presence of the defects. However, the expected trend holds for the samples grown on the 5 × 600 nm buffers with an increase in average J_{sc} by 0.4 mA/cm^2 and 1.3 mA/cm^2 for the solar cells grown on the substrates with 2° to ⟨110⟩ and 6° to
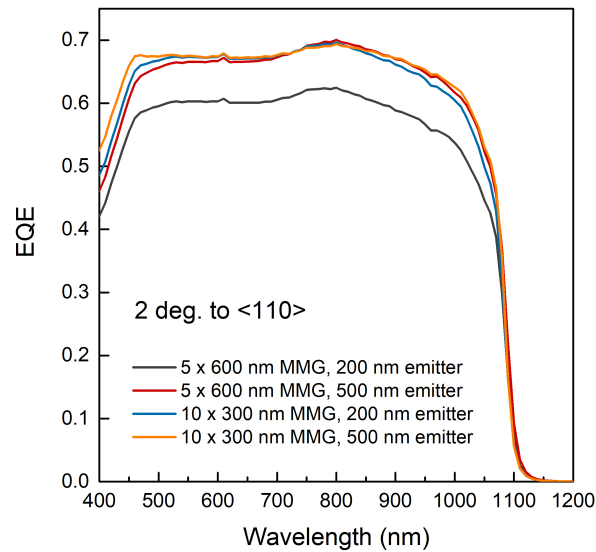
FIGURE 5.2: External quantum efficiency (EQE) spectra of the solar cells grown on the $2° \rightarrow \langle 110 \rangle$ substrate offcut; the spectra shown for the cells with 200 nm and 500 nm-thick emitters and grown on the metamorphic buffers with coarse and fine grading.

$\langle 110 \rangle$ offcuts respectively.

External quantum efficiency (EQE) spectra of the samples with 200 nm and 500 nm emitter layer and grown on the buffers with coarse and fine grading, while the substrate offcuts are the same, $2°$ to $\langle 110 \rangle$, are given of Fig. 5.2. The gain in carrier collection in the long-wavelength range due to the increased emitter thickness was calculated from spectral response and was 0.25 mA/cm^2 for the devices grown on the 10×300 nm MMG. At the same time, the difference between measured J_{sc}'s was only 0.02 mA/cm^2.

Using quantum efficiency and electroluminescence reciprocity Rau theorem[126], external radiative efficiency (ERE) of the solar cells was also investigated. ERE is determined as the ratio between radiatively emitted and injected currents when solar cell is forward biased operating as an LED and thus radiative and non-radiative current densities, non-radiative offset of the V_{oc} can be derived. The limiting efficiency of the solar cell, as shown by Shockley-Queisser model, is achieved when the device is radiative-recombination limited making ERE a unified method for evaluating the ideality of the single junction solar

cells [191]. Another reason for using ERE as an additional characterization tool was to possibly avoid the impact of sidewall chemical exposure upon mesa and contact etching while evaluating the performance of the solar cells in order to obtain the parameters dependent only on the bulk and surface properties of the material. This can be enabled considering that the electrolminescence spectra were collected from the near-bus-bar region located closely to the current injection point. Figure 5.3 shows the distribution of the V_{oc}'s averaged for the individual 1 cm $\times$ 1 cm solar cells across the wafers with the ERE of the solar cells. ERE was calculated for the solar cells having the highest V_{oc} among each group of samples featuring the same substrate offcut, grading, and emitter thickness. The ERE data for the 5 $\times$ 600 nm MMG and 200 nm emitter sample is estimated based on the extrapolation of the emitted current in dependency on the injection current towards low injection currents, thus it is not shown as a real value. Both V_{oc} and ERE are exhibiting the same trends with varying solar cell structural and design properties which can be evidence that the conversion efficiencies of the solar cells are inhibited by the non-radiative lifetime suppression due to the crystalline defects. However, the highest achieved ERE for this series of MMG In$_{0.18}$Ga$_{0.82}$As solar cells is only 0.013%. For comparison, ERE calculated for lattice-matched GaAs single-junction solar cells with 27.6% (Alta, Alta Devices) and 26.4% (ISE, Fraunhofer Institute for Solar Energy Systems) efficiencies is 22.5% and 1.26% respectively [192].

$$\phi_{EL}(E) = \phi_{BB}(E)EQE(E)exp\left(\frac{qV}{kT}\right) \tag{5.1}$$

Acquiring the radiative and non-radiative dark current components by fitting of the dark J-V curves was challenging as the diode equation ideality factor parameters $n_1 = 1$ and $n_2 = 2$ corresponding to the recombination in quasi-neutral and space-charge regions
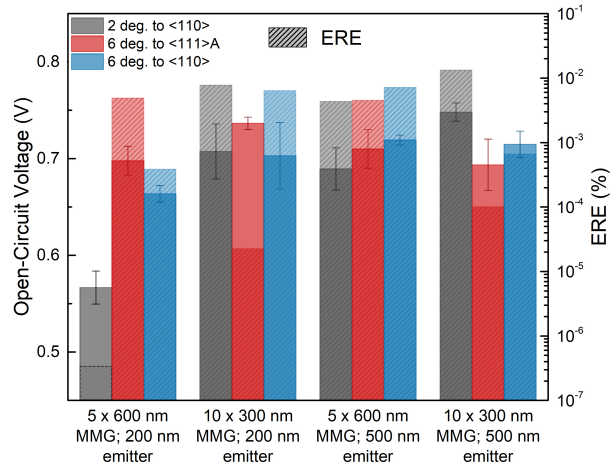
FIGURE 5.3: Measured V_{oc} of the solar cells (solid bars) and ERE calculated for the solar cells with the highest V_{oc} (patterned bars). An estimated ERE value for the $5 \times$ 600 nm MMG and 200 nm emitter sample is depicted with the dashed line.

were not clearly resolved - the logarithmic J-V curves exhibit non-linear behavior in the low-level injection forward-bias regime and high leakage current, as indicated by the measurements in reverse-bias regime (Fig. 5.4(a)). In addition, it can be seen from comparison of $J_{sc} - V_{oc}$ and dark $J - V$ behavior that series resistance R_{series} becomes impactful even at low voltages, below 0.6 V (Fig. 5.4(b)). Thus, in order to establish J_{01} and J_{02} saturation current components the Rau's reciprocity relation (Equation 5.1) was used, specifically since 1 sun solar cells operation is dominated by the non-radiative component.

The sample with the lowest $V_{oc} = 0.576$ V did not show pronounced EL signal at the injection current densities below 200 mA/cm^2, so the extrapolation of the data towards low injection currents yielded inaccurate values for the radiative current component attributed to $n = 1$, so this sample's results were excluded from the dataset. The radiative J_{01} component for the rest of the solar cells was found to be in the order of $10^{-18} - 10^{-19}$ A/cm^2 and the results including n_1 ideality factors, and J_{02} for each sample are summarized in Table 5.5. Saturation currents J_{02} were calculated using Equation 5.2
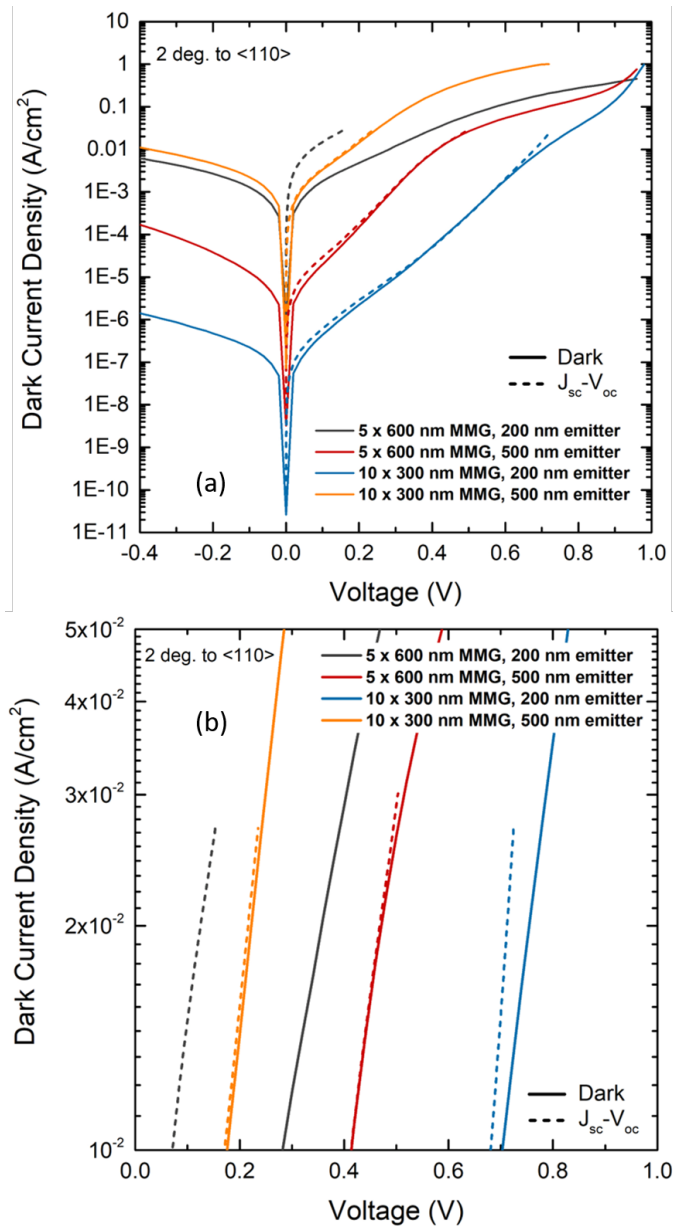
FIGURE 5.4: Dark current measurements of the solar cells grown on 2° to ⟨110⟩ offcut substrates (solid lines) and $J_{sc} - V_{oc}$ curves (dashed lines)(a). Forward bias $J_{sc} - V_{oc}$ and dark $J - V$ measurements results (b).

where R_{series} correction ($J_{inj}R_{series}$)is not included, since EL data was collected near the injection point, which reduces the impact of R_{series} caused by the metal contacts and lateral resistance. Along with the non-radiative V_{oc} offset, these values are shown on the diagram (Fig. 5.6).

	5 × 600 nm MMG, 200 nm			5 × 600 nm MMG, 500 nm			10 × 300 nm MMG, 200 nm			10 × 300 nm MMG, 500 nm		
	Substrate Offcut											
	2°→<110>	6°→<111>A	6°→<110>	2°→<110>	6°→<111>A	6°→<110>	2°→<110>	6°→<111>A	6°→<110>	2°→<110>	6°→<111>A	6°→<110>
	Measured under 1 Sun AM1.5G Illumination											
J_{sc}, mA/cm²	26.5	26.4	25.6	26.9	26.0	26.9	26.8	26.7	26.5	26.5	26.2	26.3
V_{oc}, V	0.567	0.698	0.664	0.689	0.710	0.719	0.707	0.737	0.703	0.748	0.694	0.715
FF, %	61	62	66	62	67	65	66	65	64	69	59	65
Eff., %	9.10	11.43	11.32	11.55	12.33	12.55	12.42	12.68	11.90	13.53	10.80	12.21
	Extracted from EL-EQE Reciprocity Relation											
ERE, %	~3.4×10⁻⁷	4.9×10⁻³	3.9×10⁻⁴	4.4×10⁻³	4.5×10⁻³	7.2×10⁻³	7.8×10⁻³	2.3×10⁻⁵	6.4×10⁻³	1.3×10⁻²	1.0×10⁻⁴	6.6×10⁻⁴
n_1		1.01	0.93	1.01	0.98	1.00	0.99	0.95	1.09	0.97	0.99	1.01
J_{01}, A/cm²		1.11×10⁻¹⁸	8.30×10⁻²⁰	1.11×10⁻¹⁸	4.62×10⁻¹⁹	6.99×10⁻¹⁹	6.05×10⁻¹⁹	1.48×10⁻¹⁹	7.16×10⁻¹⁸	3.70×10⁻¹⁹	5.82×10⁻¹⁹	1.01×10⁻¹⁸
J_{02}, A/cm²		2.01×10⁻⁸	6.80×10⁻⁸	2.00×10⁻⁸	2.05×10⁻⁸	1.75×10⁻⁸	1.71×10⁻⁸	1.84×10⁻⁸	1.69×10⁻⁸	1.24×10⁻⁸	2.18×10⁻⁸	5.34×10⁻⁸

FIGURE 5.5: Table 1: n_1 ideality factors and J_{01}, J_{02} saturation current densities extracted from EL-EQE reciprocity relation.
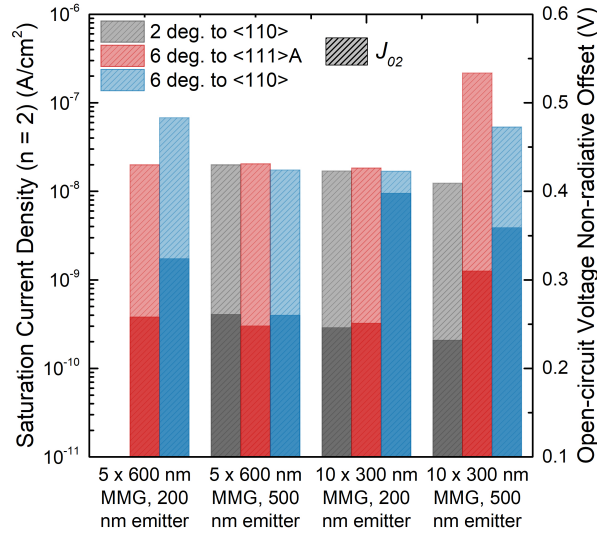
FIGURE 5.6: J_{02} saturation current densities (patterned bars) and V_{oc} non-radiative offset (solid bars) calculated from the EL-EQE reciprocity.

$$J_{02} = \left[J_{inj}(V_{oc}) - J_{01}exp\left(\frac{qV_{oc}}{n_1kT}\right) \right] exp\left(-\frac{qV_{oc}}{n_2kT} \right) \tag{5.2}$$

TRPL spectroscopy of the double heterostructure (DH) of In$_{0.66}$Ga$_{0.34}$P/In$_{0.18}$Ga$_{0.82}$As/In$_{0.66}$Ga$_{0.34}$P used for structural analysis allowed to evaluate photoluminescence decay times to be ranging from 18 ns to 34.5 ns corresponding to the radiative recombination on the shallow Si impurities. These values were used as reference parameters for the lifetimes and TDD evaluation. Considering Auger recombination rate negligible in low injection

regime with the Auger coefficient being in the order of 10^{-30}cm^{6}s^{-1} [193], the effective recombination rate can be approximated as:

$$\frac{1}{\tau_{Eff}} = \frac{1}{\tau_{Rad}} + \frac{1}{\tau_{SRH}}$$ (5.3)

where τ_{SRH} can be written as a sum of lattice-matched and lattice-mismatched components:

$$\frac{1}{\tau_{SRH}} = \frac{1}{\tau_{SRH_0}} + \frac{1}{\tau_{TD}}$$ (5.4)

In metamorphic materials, effective minority carrier lifetime is dominated by non-radiative lifetime component corresponding to the recombination on the threading dislocations as their density exceeds critical value of $\sim 10^5 - 10^6$ cm^{-2} [16], thus based on the extracted lifetimes the threading dislocation density was found [194]:

$$TDD = \frac{4}{\pi^3 (MCLD)^2}$$ (5.5)

At the same time, for such materials minority carrier lifetimes, effectively τ_{TD}, are proportionally related to the ERE η, non-radiative current density, and TDD[16, 191]:

$$\frac{\eta_1}{\eta_2} = \frac{\tau_1}{\tau_2} = \frac{J_{02_2}}{J_{02_1}} = \frac{TDD_2}{TDD_1}$$ (5.6)

Considering that the lifetime of minority holes in the n-type base is imiting, since their mobility is an order of magnitude smaller than that of electrons in the emitter [193], their

diffusion length is critical for calculating the TDD, as TDD determines the efficiency of collection of holes from the 1.8 μ-thick base.

5.4   Conclusion

Fully relaxed In$_{0.18}$Ga$_{0.82}$As templates, theoretically lattice-matched to Al via coincidence lattice epitaxy, were fabricated by MOCVD on GaAs(001) using In$_x$Ga$_{1-x}$As metamorphic buffers featuring an overshoot layer to x = 21 at%. Different grade designs, different substrate offcut angles / directions, and two growth temperatures, 600°C and 650°C, were studied. By combining HRXRD, AFM and PL, it was inferred that, within the space of parameters explored, accommodating the 1.3% misfit to GaAs in either 10 layers of 300 nm or 5 layers of 600 nm and employing either 2° to $\langle 111 \rangle$B or 6° to $\langle 111 \rangle$A substrates yield MMGs of the highest quality. The 3 μm unstrained fall back layer exhibits RMS roughness of a few nm over (40×40) μm^2. The integration of Al on such a template via MOCVD was not successful. Nor TMAl nor TTBAl produced crystalline Al films in the temperature range (600-650)°C, owing to undesired incorporation of carbon from the metal-organic precursor, which does not fully dissociate in absence of AsH$_3$. To overcome this issue, thermal evaporation of Al was attempted at the cost of exposing to air first the In$_{0.18}$Ga$_{0.82}$As fall back layer and then the metal film. No epitaxial registry of the evaporated Al to the template was observed. The metal grows polycrystalline with (111)- and (001)-oriented domains. Upon re-introduction into the MOCVD reactor for the growth of In$_{0.66}$Ga$_{0.34}$P / In$_{0.18}$Ga$_{0.82}$As / In$_{0.66}$Ga$_{0.34}$P DH, the Al film converts to AlAs during the ramp up and bake in AsH$_3$. Compared to the control DH without Al interlayer, the DH on Al is $\sim$ 10 times rougher and emits red-shifted PL with $\sim$ 103 times lower intensity.

In$_{0.18}$Ga$_{0.82}$As solar cell devices with p-on-n polarity were MOVPE grown on the templates with two grading schemes, 5×600 nm and 10×300 nm prepared on the (100) GaAs offcut substrates and their electrical performance was assessed in dependency on the grading slope, substrate offcut, and thickness of the p-type emitter. The highest photoconversion efficiency solar cell was achieved using $2°$ to $\langle 110 \rangle$ offcut substrate reaching maximum efficiency of 14.16% under 1 sun AM1.5G enabled by both high fill factor and V_{oc} indicating low impact of the defects. The evaluation of the minority charge carriers lifetimes and TDD was performed for the whole set of samples based on the TRPL carried out on the test DH, EL, and EQE spectroscopy. Using these techniques, the minimal threading dislocation density in the In$_{0.18}$Ga$_{0.82}$As grown metamorphically on GaAs was calculated to be $\sim 8.1 \times 10^5$ cm^{-2}, whereas calculated for the devices with the low ERE and efficiency, the TDD was much higher, up to $\sim 3 \times 10^7$ cm-2. Combined, structural and device characterization show that 1.12 eV InGaAs can be grown metamorphically on (100) GaAs substrates using 2∘ offcut towards $\langle 110 \rangle$ and 1.8% per step grading scheme.

Chapter 6

Products

6.1 Journal Articles

Baboli, M.A., Abrand, A., Burke, R.A., **Fedorenko, A.**, Wilhelm, T.S., Polly, S.J., Dubey, M., Hubbard, S.M. and Mohseni, P.K., 2021. Mixed-dimensional InAs nanowire on layered molybdenum disulfide heterostructures via selective-area van der Waals epitaxy. Nanoscale Advances, 3(10), pp.2802-2811.

Fedorenko, A., Baboli, M.A., Mohseni, P.K. and Hubbard, S.M., 2019. Design and Simulation of the Bifacial III-V-Nanowire-on-Si Solar Cell. MRS Advances, 4(16), pp.929-936.

Welser, R.E., Polly, S.J., Kacharia, M., **Fedorenko, A.**, Sood, A.K. and Hubbard, S.M., 2019. Design and Demonstration of High-Efficiency Quantum Well Solar Cells Employing Thin Strained Superlattices. Scientific reports, 9(1), pp.1-10.

Kum, H., Dai, Y., Aihara, T., Slocum, M.A., Tayagaki, T., **Fedorenko, A.**, Polly, S.J., Bittner, Z., Sugaya, T. and Hubbard, S.M., 2018. Two-step photon absorption in InP/InGaP quantum dot solar cells. Applied Physics Letters, 113(4), p.043902.

6.2 Conference Presentations (Oral)

Fedorenko, A., Polly, S.J., Bogner, B.M., Hubbard, S.M., 2021, June. Enhancing Open-Circuit Voltage and Efficiency of Shallow In$_x$Ga$_{1-x}$As Quantum Well GaAs Solar Cells. In 2021 48th IEEE Photovoltaic Specialists Conference (PVSC). IEEE.

Fedorenko, A., Abrand, A., Mohseni, P. and Hubbard, S., 2020, June. Multi-Terminal Dual-Junction GaAs$_{0.73}$P$_{0.27}$/In$_{0.22}$Ga$_{0.78}$As Nanowire Solar Cell: An Integrated Approach to Simulation. In 2020 47th IEEE Photovoltaic Specialists Conference (PVSC) (pp. 1472-1475). IEEE.

Fedorenko, A., Baboli, M.A., Mohseni, P.K. and Hubbard, S.M., 2019, June. Towards High-Efficiency Triple-Junction Bifacial III-V Nanowire-on-Silicon Solar Cells: Design Approaches Enabling the Concept. In 2019 IEEE 46th Photovoltaic Specialists Conference (PVSC) (pp. 3191-3194). IEEE.

Hubbard, S.M., Kacharia, M., **Fedorenko, A.**, Polly, S.J., Welser, R. and Sood, A.K., 2019, June. Thin-Barrier Strained Quantum Well Superlattice Solar Cells. In 2019 IEEE 46th Photovoltaic Specialists Conference (PVSC) (pp. 0756-0759). IEEE.

A. Fedorenko, M. A. Baboli, P. K. Mohseni, S. M. Hubbard, "Design and Simulation of Bifacial III-V Nanowire Arrays on Silicon. " Materials Research Society (MRS) Meeting, Fall, 2018

A. Fedorenko, S. J. Polly, Z. S. Bittner, R. P. Raffaelle, and S. M. Hubbard, "Quantum-Dot Enhanced Tandem Solar Cells for CubeSat Nano-Enabled Space Power System." 25th Space Photovoltaic Research and Technology Conference (SPRAT), 2018

Polly, S. J., Dann, M., **Fedorenko, A.**, Hubbard, S. M., Landi, B., Schauerman, C., Ganter, M. and Raffaelle, R. P., 2018, June. Development of a Nano-Enabled Space Power System. In 2018 IEEE 7th World Conference on Photovoltaic Energy Conversion (WCPEC)(A Joint Conference of 45th IEEE PVSC, 28th PVSEC & 34th EU PVSEC) (pp. 3389-3391). IEEE.

Bibliography

[1] Armin Richter, Martin Hermle, and Stefan W Glunz. Reassessment of the limiting efficiency for crystalline silicon solar cells. IEEE journal of photovoltaics, 3(4):1184–1191, 2013.

[2] Kunta Yoshikawa, Hayato Kawasaki, Wataru Yoshida, Toru Irie, Katsunori Konishi, Kunihiro Nakano, Toshihiko Uto, Daisuke Adachi, Masanori Kanematsu, Hisashi Uzu, et al. Silicon heterojunction solar cell with interdigitated back contacts for a photoconversion efficiency over 26%. Nature Energy, 2(5):17032, 2017.

[3] Jenny Nelson. The physics of solar cells. World Scientific Publishing Company, 2003.

[4] J Scott Ward, Timothy Remo, Kelsey Horowitz, Michael Woodhouse, Bhushan Sopori, Kaitlyn VanSant, and Paul Basore. Techno-economic analysis of three different substrate removal and reuse strategies for iii-v solar cells. Progress in Photovoltaics: Research and Applications, 24(9):1284–1292, 2016.

[5] Sneha A Kulkarni, Tom Baikie, Pablo P Boix, Natalia Yantara, Nripan Mathews, and Subodh Mhaisalkar. Band-gap tuning of lead halide perovskites using a sequential deposition process. Journal of Materials Chemistry A, 2(24):9221–9225, 2014.

[6] Giles E Eperon, Samuel D Stranks, Christopher Menelaou, Michael B Johnston, Laura M Herz, and Henry J Snaith. Formamidinium lead trihalide: a broadly tunable perovskite for efficient planar heterojunction solar cells. Energy & Environmental Science, 7(3):982–988, 2014.

[7] Nam Joong Jeon, Jun Hong Noh, Woon Seok Yang, Young Chan Kim, Seungchan Ryu, Jangwon Seo, and Sang Il Seok. Compositional engineering of perovskite materials for high-performance solar cells. Nature, 517(7535):476, 2015.

[8] Wanyi Nie, Hsinhan Tsai, Reza Asadpour, Jean-Christophe Blancon, Amanda J Neukirch, Gautam Gupta, Jared J Crochet, Manish Chhowalla, Sergei Tretiak, Muhammad A Alam, et al. High-efficiency solution-processed perovskite solar cells with millimeter-scale grains. Science, 347(6221):522–525, 2015.

[9] Konrad Domanski. The Quest for Stability of Perovskite Solar Cells: Understanding Degradation, Improving Lifetimes and Towards Experimental Standards. PhD thesis, Ecole Polytechnique Fédérale de Lausanne, 2018.

[10] Juan Bisquert and Emilio J Juarez-Perez. The causes of degradation of perovskite solar cells, 2019.

[11] John Simon, Kevin L Schulte, Nikhil Jain, Steve Johnston, Michelle Young, Matthew R Young, David L Young, and Aaron J Ptak. Upright and inverted single-junction gaas solar cells grown by hydride vapor phase epitaxy. IEEE Journal of Photovoltaics, 7(1):157–161, 2016.

[12] RR King, DC Law, KM Edmondson, CM Fetzer, GS Kinsey, H Yoon, RA Sherif, and NH Karam. 40% efficient metamorphic gainp/ gainas/ ge multijunction solar cells. Applied physics letters, 90(18):183516, 2007.

[13] Masafumi Yamaguchi, Tatsuya Takamoto, and Kenji Araki. Super high-efficiency multi-junction and concentrator solar cells. Solar energy materials and solar cells, 90(18-19):3068–3077, 2006.

[14] Richard R King. Multijunction cells: Record breakers. Nature Photonics, 2(5):284, 2008.

[15] Myles A Steiner, Ryan M France, Jeronimo Buencuerpo, John F Geisz, Michael P Nielsen, Andreas Pusch, Waldo J Olavarria, Michelle Young, and Nicholas J Ekins-Daukes. High efficiency inverted gaas and gainp/gaas solar cells with strain-balanced gainas/gaasp quantum wells. Advanced Energy Materials, 11(4):2002874, 2021.

[16] CL Andre, JJ Boeckl, DM Wilt, AJ Pitera, ML Lee, EA Fitzgerald, BM Keyes, and SA Ringel. Impact of dislocations on minority carrier electron and hole lifetimes in gaas grown on metamorphic sige substrates. Applied physics letters, 84(18):3447–3449, 2004.

[17] CL Andre, DM Wilt, AJ Pitera, Minjoo Lawrence Lee, EA Fitzgerald, and SA Ringel. Impact of dislocation densities on n+/ p and p+/ n junction gaas diodes and solar cells on sige virtual substrates. Journal of applied physics, 98(1):014502, 2005.

[18] Christopher JK Richardson and Minjoo Larry Lee. Metamorphic epitaxial materials. MRS Bulletin, 41(3):193–198, 2016.

[19] Tyler J Grassman, Mark R Brenner, Maria Gonzalez, Andrew M Carlin, Raymond R Unocic, Ryan R Dehoff, Michael J Mills, and Steven A Ringel. Characterization of metamorphic gaasp/si materials and devices for photovoltaic applications. IEEE Transactions on Electron Devices, 57(12):3361–3369, 2010.

[20] TJ Grassman, JA Carlin, C Ratcliff, DJ Chmielewski, and SA Ringel. Epitaxially-grown metamorphic gaasp/si dual-junction solar cells. In 2013 IEEE 39th Photovoltaic Specialists Conference (PVSC), pages 0149–0153. IEEE, 2013.

[21] MR Lueck, CL Andre, AJ Pitera, ML Lee, EA Fitzgerald, and SA Ringel. Dual junction gainp/gaas solar cells grown on metamorphic sige/si substrates with high open circuit voltage. IEEE Electron Device Letters, 27(3):142–144, 2006.

[22] Karen Derendorf, Stephanie Essig, Eduard Oliva, Vera Klinger, Tobias Roesener, Simon P Philipps, Jan Benick, Martin Hermle, Michael Schachtner, Gerald Siefer, et al. Fabrication of gainp/gaas//si solar cells by surface activated direct wafer bonding. IEEE Journal of Photovoltaics, 3(4):1423–1428, 2013.

[23] Romain Cariou, Jan Benick, Frank Feldmann, Oliver Höhn, Hubert Hauser, Paul Beutel, Nasser Razek, Markus Wimplinger, Benedikt Bläsi, David Lackner, et al. Iii–v-on-silicon solar cells reaching 33% photoconversion efficiency in two-terminal configuration. Nature Energy, 3(4):326, 2018.

[24] Romain Cariou, Jan Benick, Paul Beutel, Nasser Razek, Christoph Flötgen, Martin Hermle, David Lackner, Stefan W Glunz, Andreas W Bett, Markus Wimplinger, et al. Monolithic two-terminal iii–v//si triple-junction solar cells with 30.2% efficiency under 1-sun am1. 5g. IEEE Journal of Photovoltaics, 7(1):367–373, 2016.

[25] Frank Dimroth, Tobias Roesener, Stephanie Essig, Christoph Weuffen, Alexander Wekkeli, Eduard Oliva, Gerald Siefer, Kerstin Volz, Thomas Hannappel, Dietrich Häussler, et al. Comparison of direct growth and wafer bonding for the fabrication of gainp/gaas dual-junction solar cells on silicon. IEEE Journal of Photovoltaics, 4(2):620–625, 2014.

[26] G Kästner and U Gösele. Stress and dislocations at cross-sectional heterojunctions in a cylindrical nanowire. Philosophical Magazine, 84(35):3803–3824, 2004.

[27] Thomas Mårtensson, C Patrik T Svensson, Brent A Wacaser, Magnus W Larsson, Werner Seifert, Knut Deppert, Anders Gustafsson, L Reine Wallenberg, and Lars Samuelson. Epitaxial iii- v nanowires on silicon. Nano Letters, 4(10):1987–1990, 2004.

[28] Erik PAM Bakkers, Magnus T Borgström, and Marcel A Verheijen. Epitaxial growth of iii-v nanowires on group iv substrates. Mrs Bulletin, 32(2):117–122, 2007.

[29] Katsuhiro Tomioka, Tomotaka Tanaka, Shinjiro Hara, Kenji Hiruma, and Takashi Fukui. Iii–v nanowires on si substrate: selective-area growth and device applications. IEEE Journal of Selected Topics in Quantum Electronics, 17(4):1112–1129, 2010.

[30] Frank Dimroth, Matthias Grave, Paul Beutel, Ulrich Fiedeler, Christian Karcher, Thomas ND Tibbits, Eduard Oliva, Gerald Siefer, Michael Schachtner, Alexander Wekkeli, et al. Wafer bonded four-junction gainp/gaas//gainasp/gainas concentrator solar cells with 44.7% efficiency. Progress in Photovoltaics: Research and Applications, 22(3):277–282, 2014.

[31] Peter A Iles. Evolution of space solar cells. Solar Energy Materials and Solar Cells, 68(1):1–13, 2001.

[32] Seth Hubbard, Christopher Bailey, Stephen Polly, Cory D Cress, John Andersen, David V Forbes, and Ryne P Raffaelle. Nanostructured photovoltaics for space power. Journal of Nanophotonics, 3(1):031880, 2009.

[33] Sudersena Rao Tatavarti, Zachary S Bittner, A Wibowo, Michael A Slocum, George Nelson, Hyun Kum, S Phillip Ahrenkiel, and Seth M Hubbard. Epitaxial lift-off (elo) of ingap/gaas/ingaas solar cells with quantum dots in gaas middle sub-cell. Solar Energy Materials and Solar Cells, 185:153–157, 2018.

[34] Masafumi Yamaguchi, Tatsuya Takamoto, Kenji Araki, and Nicholas Ekins-Daukes. Multi-junction iii–v solar cells: current status and future potential. Solar Energy, 79(1):78–85, 2005.

[35] JF Geisz, Sarah Kurtz, MW Wanlass, JS Ward, A Duda, DJ Friedman, JM Olson, WE McMahon, TE Moriarty, and JT Kiehl. High-efficiency ga in p/ ga as/ in ga as triple-junction solar cells grown inverted with a metamorphic bottom junction. Applied Physics Letters, 91(2):023502, 2007.

[36] C Youtsey, J Adams, R Chan, V Elarde, G Hillier, M Osowski, D McCallum, H Miyamoto, N Pan, C Stender, et al. Epitaxial lift-off of large-area gaas thin-film multi-junction solar cells. In CS Mantech Conference, pages 23–26, 2012.

[37] Victor Christopher Elarde, Haruki Miyamoto, Ray Chan, Chris Stender, Chris Youtsey, Jessica GJ Adams, Andree Wibowo, Rao Tatavarti, Mark Osowski, and Noren Pan. Fabrication and applications of high-efficiency, lightweight, multi-junction solar cells by epitaxial liftoff. ECS Transactions, 66(7):89–93, 2015.

[38] Brittany L Smith, Michael A Slocum, Zachary S Bittner, Yushuai Dai, George T Nelson, Staffan D Hellstroem, Rao Tatavarti, and Seth M Hubbard. Inverted growth evaluation for epitaxial lift off (elo) quantum dot solar cell and enhanced absorption by back surface texturing. In 2016 IEEE 43rd Photovoltaic Specialists Conference (PVSC), pages 1276–1281. IEEE, 2016.

[39] Keith Barnham, Ian Ballard, Jenny Barnes, James Connolly, Paul Griffin, Benjamin Kluftinger, Jenny Nelson, Ernest Tsui, and Alexander Zachariou. Quantum well solar cells. Applied Surface Science, 113:722–733, 1997.

[40] Ryne P Raffaelle, Stephanie L Castro, Aloysius F Hepp, and Sheila G Bailey. Quantum dot solar cells. Progress in Photovoltaics: Research and Applications, 10(6):433–439, 2002.

[41] Ryne P Raffaelle, Samar Sinharoy, John Andersen, David M Wilt, and Sheila G Bailey. Multi-junction solar cell spectral tuning with quantum dots. In 2006 IEEE 4th World Conference on Photovoltaic Energy Conference, volume 1, pages 162–166. IEEE, 2006.

[42] Christopher G Bailey, David V Forbes, Ryne P Raffaelle, and Seth M Hubbard. Near 1 v open circuit voltage inas/gaas quantum dot solar cells. Applied Physics Letters, 98(16):163105, 2011.

[43] DB Bushnell, NJ Ekins-Daukes, KWJ Barnham, JP Connolly, JS Roberts, G Hill, R Airey, and M Mazzer. Short-circuit current enhancement in bragg stack multi-quantum-well solar cells for multi-junction space cell applications. Solar energy materials and solar cells, 75(1-2):299–305, 2003.

[44] Alexandre Freundlich. Multi-quantum well tandem solar cell, April 16 2002. US Patent 6,372,980.

[45] Christopher Kerestes, Stephen Polly, David Forbes, Christopher Bailey, Adam Podell, John Spann, Pravin Patel, Benjamin Richards, Paul Sharps, and Seth Hubbard. Fabrication and analysis of multijunction solar cells with a quantum dot (in) gaas junction. Progress in Photovoltaics: Research and Applications, 22(11):1172–1179, 2014.

[46] Yushuai Dai, Stephen Polly, Staffan Hellström, Kristina Driscoll, David V Forbes, Seth M Hubbard, Paul J Roland, and Randy J Ellingson. Effects of electric field on thermal and tunneling carrier escape in inas/gaas quantum dot solar cells. In

Physics, Simulation, and Photonic Engineering of Photovoltaic Devices III, volume 8981, page 898106. International Society for Optics and Photonics, 2014.

[47] Roger E Welser. Thick-well quantum-structured solar cells: design criteria for nano-enhanced absorbers. In Physics, Simulation, and Photonic Engineering of Photovoltaic Devices II, volume 8620, page 86201C. International Society for Optics and Photonics, 2013.

[48] Roger E Welser, Ashok K Sood, Ramesh B Laghumavarapu, Diana L Huffaker, David M Wilt, Nibir K Dhar, and Kimberly A Sablon. The physics of high-efficiency thin-film iii-v solar cells. In Solar Cells—New Approaches and Reviews, pages 247–277. InTech, 2015.

[49] Roger E Welser, Ashok K Sood, Jay S Lewis, Nibir K Dhar, Priyalal Wijewarnasuriya, and Roy L Peters. Development of iii-v quantum well and quantum dot solar cells. International Journal of Engineering Research and Technology, 9:29–44, 2016.

[50] Nicklas Anttu and HQ Xu. Coupling of light into nanowire arrays and subsequent absorption. Journal of nanoscience and nanotechnology, 10(11):7183–7187, 2010.

[51] Sudha Mokkapati and Chennupati Jagadish. Review on photonic properties of nanowires for photovoltaics. Optics express, 24(15):17345–17358, 2016.

[52] KM Azizur-Rahman and RR LaPierre. Wavelength-selective absorptance in gaas, inp and inas nanowire arrays. Nanotechnology, 26(29):295202, 2015.

[53] RR LaPierre, ACE Chia, SJ Gibson, CM Haapamaki, J Boulanger, R Yee, P Kuyanov, J Zhang, N Tajik, N Jewell, et al. Iii–v nanowire photovoltaics: review of design for high efficiency. physica status solidi (RRL)–Rapid Research Letters, 7(10):815–830, 2013.

[54] Ningfeng Huang, Chenxi Lin, and Michelle L Povinelli. Broadband absorption of semiconductor nanowire arrays for photovoltaic applications. Journal of Optics, 14(2):024004, 2012.

[55] Nicklas Anttu. Shockley–queisser detailed balance efficiency limit for nanowire solar cells. Acs Photonics, 2(3):446–453, 2015.

[56] Jos EM Haverkort, Erik C Garnett, and Erik PAM Bakkers. Fundamentals of the nanowire solar cell: optimization of the open circuit voltage. Applied Physics Reviews, 5(3):031106, 2018.

[57] Alessandro Cavalli, Alain Dijkstra, Jos EM Haverkort, and Erik PAM Bakkers. Nanowire polymer transfer for enhanced solar cell performance and lower cost. Nano-Structures & Nano-Objects, 16:59–62, 2018.

[58] Ningfeng Huang, Chenxi Lin, and Michelle L Povinelli. Limiting efficiencies of tandem solar cells consisting of iii-v nanowire arrays on silicon. Journal of Applied Physics, 112(6):064321, 2012.

[59] Brendan A Wood, Paul Kuyanov, Martin Aagesen, and Ray R LaPierre. Gaasp nanowire-on-si tandem solar cell. Journal of Photonics for Energy, 7(4):042502, 2017.

[60] Long Wen, Xinhua Li, Zhifei Zhao, Shaojiang Bu, XueSong Zeng, Jin-hua Huang, and Yuqi Wang. Theoretical consideration of iii–v nanowire/si triple-junction solar cells. Nanotechnology, 23(50):505202, 2012.

[61] RR LaPierre, M Robson, KM Azizur-Rahman, and P Kuyanov. A review of iii–v nanowire infrared photodetectors and sensors. Journal of Physics D: Applied Physics, 50(12):123001, 2017.

[62] Frank J Effenberger and Abhay M Joshi. Ultrafast, dual-depletion region, in-gaas/inp pin detector. Journal of lightwave technology, 14(8):1859–1864, 1996.

[63] Sudha Mokkapati, Dhruv Saxena, HH Tan, and C Jagadish. Optical design of nanowire absorbers for wavelength selective photodetectors. Scientific reports, 5:15339, 2015.

[64] Kwanyong Seo, Munib Wober, Paul Steinvurzel, Ethan Schonbrun, Yaping Dan, Tal Ellenbogen, and Kenneth B Crozier. Multicolored vertical silicon nanowires. Nano letters, 11(4):1851–1856, 2011.

[65] Pinyun Ren, Wei Hu, Qinglin Zhang, Xiaoli Zhu, Xiujuan Zhuang, Liang Ma, Xiaopeng Fan, Hong Zhou, Lei Liao, Xiangfeng Duan, et al. Band-selective infrared photodetectors with complete-composition-range inasxp1-x alloy nanowires. Advanced Materials, 26(44):7444–7449, 2014.

[66] Baomin Wang and Paul W Leu. Tunable and selective resonant absorption in vertical nanowires. Optics letters, 37(18):3756–3758, 2012.

[67] KM Azizur-Rahman and RR LaPierre. Optical design of a mid-wavelength infrared insb nanowire photodetector. Nanotechnology, 27(31):315202, 2016.

[68] Johannes Svensson, Nicklas Anttu, Neimantas Vainorius, B Mattias Borg, and Lars-Erik Wernersson. Diameter-dependent photocurrent in inassb nanowire infrared photodetectors. Nano letters, 13(4):1380–1385, 2013.

[69] Linus C Chuang, Michael Moewe, Chris Chase, Nobuhiko P Kobayashi, Connie Chang-Hasnain, and Shanna Crankshaw. Critical diameter for iii-v nanowires grown on lattice-mismatched substrates. Applied Physics Letters, 90(4):043115, 2007.

[70] GE Cirlin, VG Dubrovskii, IP Soshnikov, NV Sibirev, Yu B Samsonenko, AD Bouravleuv, JC Harmand, and F Glas. Critical diameters and temperature domains for mbe growth of iii–v nanowires on lattice mismatched substrates. physica status solidi (RRL)–Rapid Research Letters, 3(4):112–114, 2009.

[71] Nicolas Chateau and Jean-Paul Hugonin. Algorithm for the rigorous coupled-wave analysis of grating diffraction. JOSA A, 11(4):1321–1331, 1994.

[72] MG Moharam, Eric B Grann, Drew A Pommet, and TK Gaylord. Formulation for stable and efficient implementation of the rigorous coupled-wave analysis of binary gratings. JOSA a, 12(5):1068–1076, 1995.

[73] MG Moharam, Drew A Pommet, Eric B Grann, and TK Gaylord. Stable implementation of the rigorous coupled-wave analysis for surface-relief gratings: enhanced transmittance matrix approach. JOSA A, 12(5):1077–1086, 1995.

[74] Wook Lee and F Levent Degertekin. Rigorous coupled-wave analysis of multilayered grating structures. Journal of Lightwave Technology, 22(10):2359–2363, 2004.

[75] Evgeny Popov and Michel Nevière. Maxwell equations in fourier space: fast-converging formulation for diffraction by arbitrary shaped, periodic, anisotropic media. JOSA A, 18(11):2886–2894, 2001.

[76] Elias N Glytsis and Thomas K Gaylord. Three-dimensional (vector) rigorous coupled-wave analysis of anisotropic grating diffraction. JOSA A, 7(8):1399–1420, 1990.

[77] Hwi Kim, Il-Min Lee, and Byoungho Lee. Extended scattering-matrix method for efficient full parallel implementation of rigorous coupled-wave analysis. JOSA A, 24(8):2313–2327, 2007.

[78] Mingming Jiang, Theodor Tamir, and Shuzhang Zhang. Modal theory of diffraction by multilayered gratings containing dielectric and metallic components. JOSA A, 18(4):807–820, 2001.

[79] Chung-Hsiang Lin, K Ming Leung, and Theodor Tamir. Modal transmission-line theory of three-dimensional periodic structures with arbitrary lattice configurations. JOSA A, 19(10):2005–2017, 2002.

[80] Sadao Adachi. Refractive indices of iii–v compounds: Key properties of ingaasp relevant to device design. Journal of Applied Physics, 53(8):5863–5869, 1982.

[81] Anna H Trojnar, Christopher E Valdivia, Khalifa M Azizur-Rahman, Ray R LaPierre, Karin Hinzer, and Jacob J Krich. Optimization of gaas nanowire solar cell efficiency via optoelectronic modeling. In 2015 IEEE 42nd Photovoltaic Specialist Conference (PVSC), pages 1–6. IEEE, 2015.

[82] Kyozaburo Takeda, Nobuo Matsumoto, Akihito Taguchi, Hiroyuki Taki, Eiji Ohta, and Makoto Sakata. Hole mobility of gaas, gap, and gaas 1- x p x mixed-compound semiconductors. Physical Review B, 32(2):1101, 1985.

[83] Hannah J Joyce, Jennifer Wong-Leung, Chaw-Keong Yong, Callum J Docherty, Suriati Paiman, Qiang Gao, H Hoe Tan, Chennupati Jagadish, James Lloyd-Hughes, Laura M Herz, et al. Ultralow surface recombination velocity in inp nanowires probed by terahertz spectroscopy. Nano letters, 12(10):5325–5330, 2012.

[84] J Plá, M Barrera, and F Rubinelli. The influence of the ingap window layer on the optical and electrical performance of gaas solar cells. Semiconductor Science and Technology, 22(10):1122, 2007.

[85] Zhe Li, Yesaya C Wenas, Lan Fu, Sudha Mokkapati, Hark Hoe Tan, and Chennupati Jagadish. Influence of electrical design on core–shell gaas nanowire array solar cells. IEEE Journal of Photovoltaics, 5(3):854–864, 2015.

[86] Jae Cheol Shin, Ari Lee, Parsian Katal Mohseni, Do Yang Kim, Lan Yu, Jae Hun Kim, Hyo Jin Kim, Won Jun Choi, Daniel Wasserman, Kyoung Jin Choi, et al. Wafer-scale production of uniform inas y p1−y nanowire array on silicon for heterogeneous integration. ACS nano, 7(6):5463–5471, 2013.

[87] Mohadeseh A Baboli, Michael A Slocum, Hyun Kum, Thomas S Wilhelm, Stephen J Polly, Seth M Hubbard, and Parsian K Mohseni. Improving pseudo-van der waals epitaxy of self-assembled inas nanowires on graphene via mocvd parameter space mapping. CrystEngComm, 21(4):602–615, 2019.

[88] Han Wang, Xianglei Liu, Liping Wang, and Zhuomin Zhang. Anisotropic optical properties of silicon nanowire arrays based on the effective medium approximation. International Journal of Thermal Sciences, 65:62–69, 2013.

[89] Anastasiia Fedorenko, Mohadeseh A Baboli, Parsian K Mohseni, and Seth M Hubbard. Design and simulation of the bifacial iii-v-nanowire-on-si solar cell. MRS Advances, 4(16):929–936, 2019.

[90] Dick van Dam, Niels JJ van Hoof, Yingchao Cui, Peter J van Veldhoven, Erik PAM Bakkers, Jaime Gomez Rivas, and Jos EM Haverkort. High-efficiency nanowire solar cells with omnidirectionally enhanced absorption due to self-aligned indium–tin–oxide mie scatterers. ACS nano, 10(12):11414–11419, 2016.

[91] Darin Madzharov, Rahul Dewan, and Dietmar Knipp. Influence of front and back grating on light trapping in microcrystalline thin-film silicon solar cells. Optics express, 19(102):A95–A107, 2011.

[92] Tatsuo Saga. Advances in crystalline silicon solar cell technology for industrial mass production. npg asia materials, 2(3):96–102, 2010.

[93] Simon M Sze and Kwok K Ng. Physics of semiconductor devices. John wiley & sons, 2006.

[94] AJ Standing, S Assali, JEM Haverkort, and EPAM Bakkers. High yield transfer of ordered nanowire arrays into transparent flexible polymer films. Nanotechnology, 23(49):495305, 2012.

[95] Katherine E Plass, Michael A Filler, Joshua M Spurgeon, Brendan M Kayes, Stephen Maldonado, Bruce S Brunschwig, Harry A Atwater, and Nathan S Lewis. Flexible polymer-embedded si wire arrays. Advanced Materials, 21(3):325–328, 2009.

[96] J Tatebayashi, G Mariani, A Lin, RF Hicks, and DL Huffaker. Optical characteristics of gainp/gap double-heterostructure core-shell nanowires embedded in polydimethylsiloxane membranes. Applied Physics Letters, 96(25):253101, 2010.

[97] Nicklas Anttu, Vilgailė Dagytė, Xulu Zeng, Gaute Otnes, and Magnus Borgström. Absorption and transmission of light in iii–v nanowire arrays for tandem solar cell applications. Nanotechnology, 28(20):205203, 2017.

[98] Nicklas Anttu, Alireza Abrand, Damir Asoli, Magnus Heurlin, Ingvar Åberg, Lars Samuelson, and Magnus Borgström. Absorption of light in inp nanowire arrays. Nano Research, 7(6):816–823, 2014.

[99] VJ Logeeswaran, Jinyong Oh, Avinash P Nayak, Aaron M Katzenmeyer, Kristin H Gilchrist, Sonia Grego, Nobuhiko P Kobayashi, Shih-Yuan Wang, A Alec Talin, Nibir K Dhar, et al. A perspective on nanowire photodetectors: current status, future challenges, and opportunities. IEEE Journal of selected topics in quantum electronics, 17(4):1002–1032, 2011.

[100] Simon Fafard. Solar cell with epitaxially grown quantum dot material, January 4 2011. US Patent 7,863,516.

[101] NJ Ekins-Daukes, KWJ Barnham, JP Connolly, JS Roberts, JC Clark, G Hill, and M Mazzer. Strain-balanced gaasp/ingaas quantum well solar cells. Applied Physics Letters, 75(26):4195–4197, 1999.

[102] M Mazzer, KWJ Barnham, IM Ballard, A Bessiere, A Ioannides, DC Johnson, MC Lynch, TND Tibbits, JS Roberts, G Hill, et al. Progress in quantum well solar cells. Thin Solid Films, 511:76–83, 2006.

[103] Hassanet Sodabanlu, Shaojun Ma, Kentaroh Watanabe, Masakazu Sugiyama, and Yoshiaki Nakano. Impact of strain accumulation on ingaas/gaasp multiple-quantum-well solar cells: direct correlation between in situ strain measurement and cell performances. Japanese Journal of Applied Physics, 51(10S):10ND16, 2012.

[104] Masakazu Sugiyama, Yunpeng Wang, Hiromasa Fujii, Hassanet Sodabanlu, Kentaroh Watanabe, and Yoshiaki Nakano. A quantum-well superlattice solar cell for enhanced current output and minimized drop in open-circuit voltage under sunlight concentration. Journal of Physics D: Applied Physics, 46(2):024001, 2012.

[105] Yunpeng Wang, Yu Wen, Masakazu Sugiyama, and Yoshiaki Nakano. Ingaas/gaasp strain-compensated superlattice solar cell for enhanced spectral response. In 2010 35th IEEE Photovoltaic Specialists Conference, pages 003383–003385. IEEE, 2010.

[106] Kasidit Toprasertpong, Hiromasa Fujii, Yunpeng Wang, Kentaroh Watanabe, Masakazu Sugiyama, and Yoshiaki Nakano. Carrier escape time and temperature-dependent carrier collection efficiency of tunneling-enhanced multiple quantum well solar cells. IEEE Journal of Photovoltaics, 4(2):607–613, 2013.

[107] Warakorn Yanwachirakul, Hiromasa Fujii, Kasidit Toprasertpong, Kentaroh Watanabe, Masakazu Sugiyama, and Yoshiaki Nakano. Effect of barrier thickness on carrier transport inside multiple quantum well solar cells under high-concentration illumination. IEEE Journal of Photovoltaics, 5(3):846–853, 2015.

[108] Hiromasa Fujii, Yunpeng Wang, Yoshiaki Nakano, and Masakazu Sugiyama. Effects of quantum wells position and background doping on the performance of multiple quantum well solar cells. In 2011 37th IEEE Photovoltaic Specialists Conference, pages 002609–002611. IEEE, 2011.

[109] Chunge Hou, Yonggang Zou, Haizhu Wang, Xinying Wang, Ying Xu, Quhui Wang, Zhifang He, Jie Fan, Linlin Shi, Li Xu, et al. Tailoring strain and lattice relaxation characteristics in ingaas/gaasp multiple quantum wells structure with phosphorus doping engineering. Journal of Alloys and Compounds, 770:517–522, 2019.

[110] Myles A Steiner, Collin D Barraugh, Chase W Aldridge, Isabel Barraza Alvarez, Daniel J Friedman, Nicholas J Ekins-Daukes, Todd G Deutsch, and James L Young. Photoelectrochemical water splitting using strain-balanced multiple quantum well photovoltaic cells. Sustainable Energy & Fuels, 3(10):2837–2844, 2019.

[111] Martin A Green. Prospects for photovoltaic efficiency enhancement using low-dimensional structures. Nanotechnology, 11(4):401, 2000.

[112] Hiromasa Fujii, Kentaroh Watanabe, Masakazu Sugiyama, and Yoshiaki Nakano. Effect of quantum well on the efficiency of carrier collection in ingaas/gaasp multiple quantum well solar cells. Japanese Journal of Applied Physics, 51(10S):10ND04, 2012.

[113] Geoffrey K Bradshaw, C Zachary Carlin, Joshua P Samberg, Nadia A El-Masry, Peter C Colter, and Salah M Bedair. Carrier transport and improved collection in thin-barrier ingaas/gaasp strained quantum well solar cells. IEEE Journal of Photovoltaics, 3(1):278–283, 2012.

[114] Hailiang Dong, Jing Sun, Shufang Ma, Jian Liang, Taiping Lu, Xuguang Liu, and Bingshe Xu. Influence of substrate misorientation on the photoluminescence and structural properties of ingaas/gaasp multiple quantum wells. Nanoscale, 8(11):6043–6056, 2016.

[115] Hassanet Sodabanlu, Yunpeng Wang, Kentaroh Watanabe, Masakazu Sugiyama, and Yoshiaki Nakano. Growth of ingaas/gaasp multiple quantum well solar cells on mis-orientated gaas substrates. Journal of Applied Physics, 115(23):233104, 2014.

[116] L Nasi, C Ferrari, A Lanzi, L Lazzarini, R Balboni, G Clarke, M Mazzer, C Rohr, P Abbott, and KWJ Barnham. Wavy growth onset in strain-balanced ingaas multi-quantum wells. Journal of crystal growth, 274(1-2):65–72, 2005.

[117] Masakazu Sugiyama, Hiromasa Fujii, Takumi Katoh, Kasidit Toprasertpong, Hassanet Sodabanlu, Kentaroh Watanabe, Diego Alonso-Álvarez, Nicholas J Ekins-Daukes, and Yoshiaki Nakano. Quantum wire-on-well (wow) cell with long carrier lifetime for efficient carrier transport. Progress in Photovoltaics: Research and Applications, 24(12):1606–1614, 2016.

[118] Hiromasa Fujii, Yunpeng Wang, Kentaroh Watanabe, Masakazu Sugiyama, and Yoshiaki Nakano. Compensation doping in ingaas/gaasp multiple quantum well solar cells for efficient carrier transport and improved cell performance. Journal of Applied Physics, 114(10):103101, 2013.

[119] Guilherme Matos Sipahi, R Enderlein, LMR Scolfaro, JR Leite, ECF Da Silva, and A Levine. Theory of luminescence spectra from δ-doping structures: Application to gaas. Physical Review B, 57(15):9168, 1998.

[120] A Mark Fox, David AB Miller, Gabriela Livescu, JE Cunningham, and William Y Jan. Quantum well carrier sweep out: relation to electroabsorption and exciton saturation. IEEE journal of quantum electronics, 27(10):2281–2295, 1991.

[121] OY Raisky, WB Wang, RR Alfano, CL Reynolds Jr, DV Stampone, and MW Focht. Resonant enhancement of the photocurrent in multiple-quantum-well photovoltaic devices. Applied physics letters, 74(1):129–131, 1999.

[122] PS Klemmer, Yu A Mityagin, MP Telenkov, KK Nagaraja, DA Elantsev, and Sh Amiri. Resonant tunneling in gaas/algaas quantum well system for solar photovoltaics. Superlattices and Microstructures, 140:106472, 2020.

[123] JGJ Adams, BC Browne, IM Ballard, James Patrick Connolly, NLA Chan, A Ioannides, W Elder, PN Stavrinou, KWJ Barnham, and NJ Ekins-Daukes. Recent results for single-junction and tandem quantum well solar cells. Progress in Photovoltaics: research and applications, 19(7):865–877, 2011.

[124] Neal G Anderson. Ideal theory of quantum well solar cells. Journal of applied physics, 78(3):1850–1861, 1995.

[125] Stephen P Bremner, Richard Corkish, and Christiana B Honsberg. Detailed balance efficiency limits with quasi-fermi level variations [qw solar cell]. IEEE Transactions on electron Devices, 46(10):1932–1939, 1999.

[126] Uwe Rau. Reciprocity relation between photovoltaic quantum efficiency and electroluminescent emission of solar cells. Physical Review B, 76(8):085303, 2007.

[127] Gerardo L Araújo and Antonio Martí. Absolute limiting efficiencies for photovoltaic energy conversion. Solar energy materials and solar cells, 33(2):213–240, 1994.

[128] Jenny Nelson, Jenny Barnes, Nicholas Ekins-Daukes, Benjamin Kluftinger, Ernest Tsui, Keith Barnham, C Tom Foxon, Tin Cheng, and John S Roberts. Observation of suppressed radiative recombination in single quantum well pin photodiodes. Journal of applied physics, 82(12):6240–6246, 1997.

[129] NJ Ekins-Daukes, JM Barnes, KWJ Barnham, JP Connolly, M Mazzer, JC Clark, R Grey, G Hill, MA Pate, and JS Roberts. Strained and strain-balanced quantum well devices for high-efficiency tandem solar cells. Solar Energy materials and Solar cells, 68(1):71–87, 2001.

[130] JGJ Adams, JS Roberts, G Hill, NJ Ekins-Daukes, and KWJ Barnham. Directional emission in strain-balanced quantum well solar cells. In 2009 34th IEEE Photovoltaic Specialists Conference (PVSC), pages 000071–000075. IEEE, 2009.

[131] Roger E Welser, Stephen J Polly, Mitsul Kacharia, Anastasiia Fedorenko, Ashok K Sood, and Seth M Hubbard. Design and demonstration of high-efficiency quantum well solar cells employing thin strained superlattices. Scientific Reports, 9(1):1–10, 2019.

[132] A Bessiere, JP Connolly, KWJ Barnham, IM Ballard, DC Johnson, M Mazzer, G Hill, and JS Roberts. Radiative recombination in strain-balanced quantum well solar cells. In Conference Record of the Thirty-first IEEE Photovoltaic Specialists Conference, 2005., pages 679–682. IEEE, 2005.

[133] Kentaroh Watanabe, Yunpeng Wang, Hassanet Sodabanlu, Masakazu Sugiyama, and Yoshiaki Nakano. Strain effect for different phosphorus content of ingaas/gaasp super-lattice in gaas p–i–n single junction solar cell. Journal of crystal growth, 401:712–716, 2014.

[134] Joshua P Samberg, Hamideh M Alipour, Geoffrey K Bradshaw, C Zachary Carlin, Peter C Colter, James M LeBeau, NA El-Masry, and Salah M Bedair. Interface properties of ga (as, p)/(in, ga) as strained multiple quantum well structures. Applied Physics Letters, 103(7):071605, 2013.

[135] ShaoJun Ma, Yunpeng Wang, Hassanet Sodabanlu, Kentaroh Watanabe, Masakazu Sugiyama, and Yoshiaki Nakano. Effect of hetero-interfaces on in situ wafer curvature behavior in ingaas/gaasp strain-balanced mqws. Journal of crystal growth, 352(1):245–248, 2012.

[136] Yu Wen, Yunpeng Wang, Kentaroh Watanabe, Masakazu Sugiyama, and Yoshiaki Nakano. Effect of gaas step layer thickness in ingaas/gaasp stepped quantum-well solar cell. In 2012 IEEE 38th Photovoltaic Specialists Conference (PVSC) PART 2, pages 1–6. IEEE, 2012.

[137] Yu Wen, Yunpeng Wang, and Yoshiaki Nakano. Suppressed indium diffusion and enhanced absorption in ingaas/gaasp stepped quantum well solar cell. Applied Physics Letters, 100(5):053902, 2012.

[138] T Marschner, S Lutgen, M Volk, W Stolz, EO Göbel, NY Jin-Phillipp, and F Phillipp. Strain-induced changes in epitaxial layer morphology of highly-strained iii/v-semiconductor heterostructures. Superlattices and microstructures, 15(2):183, 1994.

[139] K Hiramoto, T Tsuchiya, M Sagawa, and K Uomi. Multistep formation and lateral variation in the in composition in ingaas layers grown by metalorganic vapor phase epitaxy on (001) vicinal gaas substrates. Journal of crystal growth, 145(1-4):133–139, 1994.

[140] J Tersoff, YH Phang, Zhenyu Zhang, and MG Lagally. Step-bunching instability of vicinal surfaces under stress. Physical review letters, 75(14):2730, 1995.

[141] SR Coriell, AA Chernov, BT Murray, and GB McFadden. Step bunching: generalized kinetics. Journal of Crystal Growth, 183(4):669–682, 1998.

[142] Masanori Shinohara and Naohisa Inoue. Behavior and mechanism of step bunching during metalorganic vapor phase epitaxy of gaas. Applied physics letters, 66(15):1936–1938, 1995.

[143] F Cappelluti, D Kim, M van Eerden, AP Cédola, T Aho, G Bissels, F Elsehrawy, J Wu, H Liu, P Mulder, et al. Light-trapping enhanced thin-film iii-v quantum dot solar cells fabricated by epitaxial lift-off. Solar Energy Materials and Solar Cells, 181:83–92, 2018.

[144] Chung-Yu Hong, Yi-Chin Wang, Mu-Min Hung, Yu-Chih Su, Jia-Ling Tsai, Yu-Chen Lin, Chao-Ming Tung, Min-An Tsai, Guo-Chung Ghi, and Peichen Yu. Photovoltaic characteristics of multiple quantum well solar cells with distributed bragg reflector and selective filters. In 2016 IEEE 43rd Photovoltaic Specialists Conference (PVSC), pages 1273–1275. IEEE, 2016.

[145] CJR Sheppard. Approximate calculation of the reflection coefficient from a stratified medium. Pure and Applied Optics: Journal of the European Optical Society Part A, 4(5):665, 1995.

[146] Braxton Osting. Bragg structure and the first spectral gap. Applied Mathematics Letters, 25(11):1926–1930, 2012.

[147] DC Johnson, IM Ballard, KWJ Barnham, JP Connolly, M Mazzer, Aurélie Bessière, C Calder, G Hill, and JS Roberts. Observation of photon recycling in strain-balanced quantum well solar cells. Applied Physics Letters, 90(21):213505, 2007.

[148] Hiromasa Fujii, Kasidit Toprasertpong, Kentaroh Watanabe, Masakazu Sugiyama, and Yoshiaki Nakano. Carrier collection efficiency in multiple quantum well solar cells. In Physics, Simulation, and Photonic Engineering of Photovoltaic Devices II, volume 8620, page 86201F. International Society for Optics and Photonics, 2013.

[149] SJ Polly, CG Bailey, AJ Grede, DV Forbes, and SM Hubbard. Calculation of strain compensation thickness for iii–v semiconductor quantum dot superlattices. Journal of Crystal Growth, 454:64–70, 2016.

[150] Carissa N Eisler, Matthew T Sheldon, and Harry A Atwater. Enhanced performance of small gaas solar cells via edge and surface passivation with trioctylphosphine sulfide. In 2012 38th IEEE Photovoltaic Specialists Conference, pages 000937–000940. IEEE, 2012.

[151] M Paillard, X Marie, E Vanelle, T Amand, VK Kalevich, AR Kovsh, AE Zhukov, and VM Ustinov. Time-resolved photoluminescence in self-assembled inas/gaas quantum dots under strictly resonant excitation. Applied Physics Letters, 76(1):76–78, 2000.

[152] L Tapfer and K Ploog. X-ray interference in ultrathin epitaxial layers: a versatile method for the structural analysis of single quantum wells and heterointerfaces. Physical Review B, 40(14):9802, 1989.

[153] ShaoJun Ma, Yunpeng Wang, Hassanet Sodabanlu, Kentaroh Watanabe, Masakazu Sugiyama, and Yoshiaki Nakano. Optimized interfacial management for ingaas/gaasp strain-compensated superlattice structure. Journal of crystal growth, 370:157–162, 2013.

[154] Takayuki Nakano, Tomonari Shioda, Naomi Enomoto, Eiji Abe, Masakazu Sugiyama, Yoshiaki Nakano, and Yukihiro Shimogaki. Precise structure control of gaas/ingap hetero-interfaces using metal organic vapor phase epitaxy and its abruptness analyzed by stem. Journal of crystal growth, 347(1):25–30, 2012.

[155] Jeremiah S McNatt. 25th space photovoltaic research and technology conference. 2019.

[156] Stephen J Polly, Martin Dann, Anastasiia Fedorenko, Seth Hubbard, Brian Landi, Christopher Schauerman, Matthew Ganter, and Ryne Raffaelle. Development of a nano-enabled space power system. In 2018 IEEE 7th World Conference on Photovoltaic Energy Conversion (WCPEC)(A Joint Conference of 45th IEEE PVSC, 28th PVSEC & 34th EU PVSEC), pages 3389–3391. IEEE, 2018.

[157] J Feynman and SB Gabriel. High-energy charged particles in space at one astronomical unit. IEEE Transactions on Nuclear Science, 43(2):344–352, 1996.

[158] Christopher Kerestes, David Forbes, Christopher G Bailey, John Spann, Benjamin Richards, Paul Sharps, and Seth Hubbard. Radiation effects on quantum dot enhanced solar cells. In Physics, Simulation, and Photonic Engineering of Photovoltaic Devices, volume 8256, page 82561I. International Society for Optics and Photonics, 2012.

[159] Christopher Kerestes, Cory D Cress, Benjamin C Richards, David V Forbes, Yong Lin, Zac Bittner, Stephen J Polly, Paul Sharps, and Seth M Hubbard. Strain effects on radiation tolerance of triple-junction solar cells with inas quantum dots in the gaas junction. IEEE journal of Photovoltaics, 4(1):224–232, 2013.

[160] Seth Hubbard and Ryne Raffaelle. Boosting solar-cell efficiency with quantum-dot-based nanotechnology. SPIE Newsroom, 2010.

[161] Cory D Cress, Christopher G Bailey, Seth M Hubbard, David M Wilt, Sheila G Bailey, and Ryne P Raffaelle. Radiation effects on strain compensated quantum dot solar cells. In 2008 33rd IEEE Photovoltaic Specialists Conference, pages 1–6. IEEE, 2008.

[162] Christopher Kerestes, David V Forbes, Zac Bittner, Stephen Polly, Yong Lin, Benjamin Richards, Paul Sharps, and Seth Hubbard. Strain effects on radiation tolerance of quantum dot solar cells. In 2012 38th IEEE Photovoltaic Specialists Conference, pages 002792–002796. IEEE, 2012.

[163] J-Y Marzin, J-M Gérard, A Izraël, D Barrier, and G Bastard. Photoluminescence of single inas quantum dots obtained by self-organized growth on gaas. Physical review letters, 73(5):716, 1994.

[164] JX Chen, Alexander Markus, Andrea Fiore, U Oesterle, RP Stanley, JF Carlin, Romuald Houdre, M Ilegems, L Lazzarini, L Nasi, et al. Tuning inas/gaas quantum dot properties under stranski-krastanov growth mode for 1.3 μm applications. Journal of applied physics, 91(10):6710–6716, 2002.

[165] Peter W Voorhees. The theory of ostwald ripening. Journal of Statistical Physics, 38(1-2):231–252, 1985.

[166] Koichi Yamaguchi, Kunihiko Yujobo, and Toshiyuki Kaizu. Stranski-krastanov growth of inas quantum dots with narrow size distribution. Japanese Journal of Applied Physics, 39(12A):L1245, 2000.

[167] GD Lian, J Yuan, LM Brown, GH Kim, and DA Ritchie. Modification of inas quantum dot structure by the growth of the capping layer. Applied physics letters, 73(1):49–51, 1998.

[168] Seth Martin Hubbard, Ryne Raffaelle, Ross Robinson, Christopher Bailey, David Wilt, David Wolford, William Maurer, and Sheila Bailey. Growth and characterization of inas quantum dot enhanced photovoltaic devices. MRS Online Proceedings Library Archive, 1017, 2007.

[169] Seth M Hubbard, David Wilt, Sheila Bailey, Daniel Byrnes, and Ryne Raffaelle. Omvpe grown inas quantum dots for application in nanostructured photovoltaics. In 2006 IEEE 4th World Conference on Photovoltaic Energy Conference, volume 1, pages 118–121. IEEE, 2006.

[170] Seth M Hubbard, Chelsea Plourde, Zac Bittner, Christopher G Bailey, Mike Harris, Tim Bald, Mitch Bennett, David V Forbes, and Ryne Raffaelle. Inas quantum dot enhancement of gaas solar cells. In 2010 35th IEEE Photovoltaic Specialists Conference, pages 001217–001222. IEEE, 2010.

[171] Jana Drbohlavova, Vojtech Adam, Rene Kizek, and Jaromir Hubalek. Quantum dots—characterization, preparation and usage in biological systems. International journal of molecular sciences, 10(2):656–673, 2009.

[172] Edward W Taylor. The role of nanostructures and quantum dots in detectors and solar cells for radiation hardened space applications. In Photonics for Space Environments XI, volume 6308, page 630807. International Society for Optics and Photonics, 2006.

[173] Zachary S Bittner, Michael A Slocum, George T Nelson, Rao Tatavarti, and Seth M Hubbard. Novel inas/gaas qd subcell design for radiation hard 3-j elo imm solar cell. In 2016 IEEE 43rd Photovoltaic Specialists Conference (PVSC), pages 3421–3424. IEEE, 2016.

[174] Chelsea R Mackos, David V Forbes, Stephen Polly, Adam Podell, Yushuai Dai, Christopher G Bailey, and Seth M Hubbard. Gaas substrate misorientation and the effect on inas quantum dot critical thickness. In 2011 37th IEEE Photovoltaic Specialists Conference, pages 002633–002638. IEEE, 2011.

[175] David V Forbes, Seth M Hubbard, Christopher Bailey, Stephen Polly, John Andersen, and Ryne Raffaelle. Iii-v quantum dot enhanced photovoltaic devices. In Next Generation (Nano) Photonic and Cell Technologies for Solar Energy Conversion, volume 7772, page 77720C. International Society for Optics and Photonics, 2010.

[176] M Kamp, G Mörsch, J Gräber, and H Lüth. Te doping of gaas using diethyltellurium. Journal of applied physics, 76(3):1974–1976, 1994.

[177] I García, I Rey-Stolle, B Galiana, and C Algora. Analysis of tellurium as n-type dopant in gainp: Doping, diffusion, memory effect and surfactant properties. Journal of crystal growth, 298:794–799, 2007.

[178] Tohru Suzuki, Akiko Gomyo, Sumio Iijima, Kenichi Kobayashi, Seiji Kawata, Isao Hino, and Tonao Yuasa. Band-gap energy anomaly and sublattice ordering in gainp and algainp grown by metalorganic vapor phase epitaxy. Japanese journal of applied physics, 27(11R):2098, 1988.

[179] G Attolini, C Bocchi, F Germini, C Pelosi, A Parisini, L Tarricone, R Kudela, and S Hasenohrl. Effects of inhomogeneities and ordering in ingap/gaas system grown by movpe. Materials chemistry and physics, 66(2-3):246–252, 2000.

[180] Osamu Ueda, Masahiko Takikawa, Junji Komeno, and Itsuo Umebu. Atomic structure of ordered ingap crystals grown on (001) gaas substrates by metalorganic chemical vapor deposition. Japanese journal of applied physics, 26(11A):L1824, 1987.

[181] L Francesio, P Franzosi, M Caldironi, L Vitali, M Dellagiovanna, A Di Paola, F Vidimari, and S Pellegrino. Investigation of the cationic ordering in ingap/gaas epilayers grown by low-pressure, metal organic vapour phase epitaxy. Materials Science and Engineering: B, 28(1-3):219–223, 1994.

[182] I García, I Rey-Stolle, and C Algora. Performance analysis of algaas/gaas tunnel junctions for ultra-high concentration photovoltaics. Journal of Physics D: Applied Physics, 45(4):045101, 2012.

[183] Andenet Alemu and Alexandre Freundlich. Resonant thermotunneling design for high-performance single-junction quantum-well solar cells. IEEE Journal of Photovoltaics, 2(3):256–260, 2012.

[184] Tyler J Grassman, Andrew M Carlin, Krishna Swaminathan, Chris Ratcliff, Javier Grandal, Limei Yang, Michael J Mills, and Steven A Ringel. Expanding the palette: Metamorphic strategies over multiple lattice constant ranges for extending the spectrum of accessible photovoltaic materials. In Photovoltaic Specialists Conference (PVSC), 2011 37th IEEE, pages 003375–003380. IEEE, 2011.

[185] Wolfgang Guter, Jan Schöne, Simon P Philipps, Marc Steiner, Gerald Siefer, Alexander Wekkeli, Elke Welser, Eduard Oliva, Andreas W Bett, and Frank Dimroth. Current-matched triple-junction solar cell reaching 41.1% conversion efficiency under concentrated sunlight. Applied Physics Letters, 94(22):223504, 2009.

[186] Arthur Cornfeld and Benjamin Cho. Four junction inverted metamorphic multi-junction solar cell with two metamorphic layers, June 27 2017. US Patent 9,691,929.

[187] Henrique F Santana, Giovanni B de Farias, Alexandre P Freitas, Diogo A Motta, and Wilson Carvalho Junior. Design of a 80-nm tunable hybrid iii/v-on-silicon laser. In Microwave and Optoelectronics Conference (IMOC), 2017 SBMO/IEEE MTT-S International, pages 1–5. IEEE, 2017.

[188] Ruijun Wang, Anton Vasiliev, Muhammad Muneeb, Aditya Malik, Stephan Sprengel, Gerhard Boehm, Markus-Christian Amann, Ieva Šimonytė, Augustinas Vizbaras, Kristijonas Vizbaras, et al. Iii–v-on-silicon photonic integrated circuits for spectroscopic sensing in the 2–4 μm wavelength range. Sensors, 17(8):1788, 2017.

[189] Alessandro Giussani, Michael A Slocum, Seth M Hubbard, Nathan Smaglik, Nikhil Pokharel, and S Phillip Ahrenkiel. Integration of thin al films on in 0.18 ga 0.82 as metamorphic grade structures for low-cost iii-v photovoltaics. In 2017 IEEE 44th Photovoltaic Specialist Conference (PVSC), pages 2514–2519. IEEE, 2017.

[190] SP Ahrenkiel, MW Wanlass, JJ Carapella, RK Ahrenkiel, SW Johnston, and LM Gedvilas. Optimization of buffer layers for lattice-mismatched epitaxy of $ga_xin_{1-x}as/inas_yp_{1-y}$ double-heterostructures on inp. Solar energy materials and solar cells, 91(10):908–918, 2007.

[191] Kan-Hua Lee, Kenji Araki, Li Wang, Nobuaki Kojima, Yoshio Ohshita, and Masafumi Yamaguchi. Assessing material qualities and efficiency limits of iii–v on silicon solar cells using external radiative efficiency. Progress in Photovoltaics: Research and Applications, 24(10):1310–1318, 2016.

[192] Martin A Green. Radiative efficiency of state-of-the-art photovoltaic cells. Progress in Photovoltaics: Research and Applications, 20(4):472–476, 2012.

[193] M Niemeyer, J Ohlmann, AW Walker, P Kleinschmidt, R Lang, T Hannappel, F Dimroth, and D Lackner. Minority carrier diffusion length, lifetime and mobility in p-type gaas and gainas. Journal of Applied Physics, 122(11):115702, 2017.

[194] Masafumi Yamaguchi and Chikara Amano. Efficiency calculations of thin-film gaas solar cells on si substrates. Journal of applied physics, 58(9):3601–3606, 1985.